

University of Windsor

## Scholarship at UWindor

---

Electronic Theses and Dissertations

Theses, Dissertations, and Major Papers

---

9-21-2018

### An Investigation of Premixed and Lean Combustion in Engines

Shouvik Dev

*University of Windsor*

Follow this and additional works at: <https://scholar.uwindsor.ca/etd>

---

#### Recommended Citation

Dev, Shouvik, "An Investigation of Premixed and Lean Combustion in Engines" (2018). *Electronic Theses and Dissertations*. 7513.

<https://scholar.uwindsor.ca/etd/7513>

This online database contains the full-text of PhD dissertations and Masters' theses of University of Windsor students from 1954 forward. These documents are made available for personal study and research purposes only, in accordance with the Canadian Copyright Act and the Creative Commons license—CC BY-NC-ND (Attribution, Non-Commercial, No Derivative Works). Under this license, works must always be attributed to the copyright holder (original author), cannot be used for any commercial purposes, and may not be altered. Any other use would require the permission of the copyright holder. Students may inquire about withdrawing their dissertation and/or thesis from this database. For additional inquiries, please contact the repository administrator via email ([scholarship@uwindsor.ca](mailto:scholarship@uwindsor.ca)) or by telephone at 519-253-3000ext. 3208.

AN INVESTIGATION OF PREMIXED AND LEAN COMBUSTION IN  
ENGINES

By

Shouvik Dev

A Dissertation  
Submitted to the Faculty of Graduate Studies  
through the Department of Mechanical, Automotive, and Materials Engineering  
in Partial Fulfillment of the Requirements for  
the Degree of Doctor of Philosophy at the  
University of Windsor

Windsor, Ontario, Canada

2018

© 2018 Shouvik Dev

An Investigation of Premixed and Lean Combustion in Engines

By

Shouvik Dev

APPROVED BY:

---

C. R. Koch, External Examiner  
University of Alberta

---

X. Nie  
Department of Mechanical, Automotive, and Materials Engineering

---

D. Ting  
Department of Mechanical, Automotive, and Materials Engineering

---

J. Tjong  
Department of Mechanical, Automotive, and Materials Engineering

---

M. Zheng, Advisor  
Department of Mechanical, Automotive, and Materials Engineering

August 31, 2018

## DECLARATION OF ORIGINALITY

I hereby certify that I am the sole author of this thesis and that no part of this thesis has been published or submitted for publication.

I certify that, to the best of my knowledge, my thesis does not infringe upon anyone's copyright nor violate any proprietary rights and that any ideas, techniques, quotations, or any other material from the work of other people included in my thesis, published or otherwise, are fully acknowledged in accordance with the standard referencing practices. Furthermore, to the extent that I have included copyrighted material that surpasses the bounds of fair dealing within the meaning of the Canada Copyright Act, I certify that I have obtained a written permission from the copyright owner(s) to include such material(s) in my thesis and have included copies of such copyright clearances to my appendix.

I declare that this is a true copy of my thesis, including any final revisions, as approved by my thesis committee and the Graduate Studies office, and that this thesis has not been submitted for a higher degree to any other University or Institution.

## ABSTRACT

Spark ignited internal combustion engines are expected to continue to be the mainstay for the passenger cars and light duty trucks for the next few decades. It is understood that to conform to the stringent fuel efficiency legislations as well as meet the regulated exhaust emission limits, combustion technology must evolve significantly. It is imperative to develop a deeper understanding of the fundamental engine processes such as air intake, fuel-air interaction, and ignition so that avenues for incremental improvements may be explored.

With this broad objective, the present study focuses on spark ignition engines in which premixed and lean (air in excess) charge of fuel and air can be burned efficiently. Studies have indicated that under these conditions, it is possible to simultaneously reduce the oxides of nitrogen (NO<sub>x</sub>), while keeping the carbon monoxide (CO) and unburned hydrocarbons (UHCs) at low levels. The in-cylinder turbulence plays a major role in the fuel-air mixture preparation. When this mixture ignites, the combustion may propagate through what is known as a premixed turbulent flame. Turbulence is beneficial since it enhances the mass burning rate. This is particularly critical in lean burn engines in which it is difficult to complete the combustion within the extremely short time scales typical of modern engines. Excess turbulence however, may lead to flame quenching.

In order to investigate the conditions leading up to and the propagation of the turbulent flame itself, analytical and empirical studies are performed. Tests are conducted on a constant volume combustion chamber with optical access to provide insight into the combustion characteristics of lean mixtures subject to turbulence. Fundamental studies on premixed flame propagation are performed with a variety of fuels at different equivalence

ratios with different fuels. Impacts of engine operating conditions such as air-fuel ratio, exhaust gas recirculation, engine load, fuels, and ignition strategies on the flame initiation and development are investigated in detail on a research engine test setup. Chemical simulation and computational fluid dynamics (CFD) tools are used to supplement the understanding of the results. Finally, an attempt is made to comprehensively understand the combined effects of in-cylinder flow and fuel reactivity on premixed and lean combustion.

## DEDICATION

This dissertation is dedicated to the amazing family I am blessed with.

My mother Sumita, my father Manoj, and my sister Mohima

My wife Teodora, our daughter Emma, and my mother-in-law Voichita.

## ACKNOWLEDGEMENTS

I am deeply grateful to my advisor, Dr. Ming Zheng. His guidance, wisdom, support, and encouragement have not only made this work possible but have also contributed immensely to my professional development.

I would also like to thank the members of my dissertation committee for their time and valuable comments – Dr. C. R. Koch, Dr. X. Nie, Dr. D. Ting, and Dr. J. Tjong,

I consider myself very fortunate to be a member of the Clean Combustion Engine Laboratory, University of Windsor. I would like to thank all my present and past colleagues – Dr. Meiping Wang, Dr. Shui Yu, Dr. Xiao Yu, Dr. Prasad Divekar, Dr. Kelvin Xie, Qingyuan Tan, Zhenyi Yang, Hua Zhu, Navjot Sandhu, Divyanshu Purohit, Mark Ives, Simon Leblanc and Linyan Wang. I would also like to acknowledge the help I received from Ye Chang. This work has been brought to fruition only because of their unconditional assistance and honest feedback.

I would like to thank Convergent Science and Ansys for the use of their simulation suite and post processing software respectively. The research at the Clean Combustion Engine Laboratory is sponsored by the NSERC Industrial Research Chair program, NSERC Collaborative Research and development Program, Ontario Center of Excellency – VIP II program, Ford Motor Company of Canada Ltd., and the University of Windsor.

I am especially grateful to my wife and my best friend, Teodora. I couldn't have asked for a better companion for the journey of life. This endeavor was made possible due to the relentless support of her and the rest of my family. This dissertation is dedicated to them.



TABLE OF CONTENTS

DECLARATION OF ORIGINALITY ..... iii

ABSTRACT ..... iv

DEDICATION ..... vi

ACKNOWLEDGEMENTS ..... vii

LIST OF TABLES ..... xii

LIST OF FIGURES ..... xiii

LIST OF APPENDICES ..... xviii

LIST OF SYMBOLS AND ABBREVIATIONS ..... xix

**INTRODUCTION** ..... 1

    ■ Dissertation Outline ..... 1

    ■ Research Motivation ..... 4

    ■ Research Objective ..... 9

    ■ Spark Ignited Lean Combustion ..... 10

    ■ Premixed Turbulent Flames ..... 13

        ■ Premixed turbulent combustion in a CVCC ..... 17

        ■ Premixed turbulent combustion in engines ..... 21

    ■ Relevant Flame Detection Techniques ..... 23

        ■ Shadowgraph imaging ..... 23

        ■ Ion current sensing ..... 24

**LITERATURE REVIEW** ..... 27

■	Premixed Lean Combustion in SI Engines .....	27
■	Modifying Charge Reactivity.....	31
■	Effect of temperature .....	32
■	Effect of fuel property.....	34
■	RESEARCH TOOLS AND METHODS .....	38
■	Constant Volume Combustion Chamber (CVCC).....	38
■	Creation of air motion.....	40
■	Estimation of flame area .....	42
■	Research Engine Platform.....	43
■	Ion Current Measurement System.....	49
■	Shock Tube Setup.....	52
■	COMBUSTION CHAMBER FLAME PROPAGATION STUDIES..	54
■	Validation of Ion Current Signal in CVCC.....	54
■	Flame Propagation Study in Optical Chamber.....	59
■	Flame imaging analysis.....	59
■	Pressure and ion current analysis .....	66
■	Fuel Effect: A Comparison between Methane, Propane and DME .....	72
■	Directed Flow on Spark Gap.....	78
■	Shock Accelerated Flame.....	84
■	CHARGE REACTIVITY IMPACT ON ENGINE COMBUSTION...	89

■	Effect of Modifying Intake Flow .....	89
■	Test Matrix and Baseline Combustion Results .....	92
■	Excess Air Ratio Effect .....	99
■	Temperature Effect.....	108
■	Extending Lean Limit of DME HCCI.....	114
■	Summary of Engine Test Results.....	118
■■■■■	<b>ANALYSIS OF CHARGE REACTIVITY AND FLOW FIELDS ...</b>	<b>119</b>
■	Chemical Simulations .....	119
■	Gasoline surrogate SI combustion .....	121
■	Ethanol SI combustion .....	126
■	Intake temperature effect .....	130
■	DME HCCI combustion .....	136
■	In-cylinder Flow-field Simulations .....	141
■	Simulation parameters .....	141
■	Effect of intake flow rate on in-cylinder flow field .....	146
■	Flow profile in the spark plug vicinity.....	152
■■■■■	<b>CONCLUSIONS AND FUTURE WORK.....</b>	<b>156</b>
■	Combustion Chamber Flame Propagation Studies.....	156
■	Charge Reactivity Impact on Engine Combustion.....	158
■	Simulation Studies for Combustion Chemistry and In-cylinder Flow Field.....	160

■ Chemical simulations.....	160
■ In-cylinder flow-field simulations .....	161
■ Recommendations for Future Work.....	162
REFERENCES .....	163
APPENDIX A: Specifications of Key Equipment.....	175
APPENDIX B: Pressure Signal Based Combustion Metrics.....	177
APPENDIX C: Ion Current Signal Processing Method .....	179
APPENDIX D: Validation and Input Parameters – CHEMKIN .....	183
APPENDIX E: Validation and Input Parameters – Converge.....	192
APPENDIX F: Copyright Permissions.....	200
VITA AUCTORIS .....	201
LIST OF PUBLICATIONS .....	202

## LIST OF TABLES

Table 1-1. Impact of SI ICE operating variables on ignition and flame.....	13
Table 2-1. Property of test fuels.....	35
Table 3-1. Phantom V7.3 camera settings .....	43
Table 3-2: Yanmar NFD-170 specifications.....	47
Table 4-1. Experimental conditions for shock tube test .....	85
Table 5-1. Engine Test Conditions .....	92
Table 5-2. Summary of CA5, CA50 and Combustion Duration.....	98
Table 5-3. Impact summary of experimental variables .....	118
Table 6-1. Parameters for CHEMKIN simulations.....	121
Table 6-2. Converge simulation parameters .....	143

## LIST OF FIGURES

Figure 1-1. Dissertation outline .....	3
Figure 1-2. CAFE or equivalent historic trends and projections of passenger vehicles .....	5
Figure 1-3 Energy density of liquid fuels in comparison to lithium-ion battery .....	6
Figure 1-4 Impact of lean burn on engine performance .....	7
Figure 1-5 Laminar burning velocity of ethanol-air mixtures .....	8
Figure 1-6. General scheme of research .....	10
Figure 1-7. Zones of stable, misfire and partial burn combustion .....	11
Figure 1-8. Simplified representation of SI combustion.....	12
Figure 1-9: Premixed turbulent flame ball.....	15
Figure 1-10. Maximum initial pressure and temperature in surveyed literature.....	20
Figure 1-11: Maximum initial pressure and $\lambda$ in surveyed literature.....	21
Figure 1-12. Shadowgraph image of flame in a CVCC.....	24
Figure 1-13. Fundamental concept of ion current measurement .....	25
Figure 2-1. Indicated thermal efficiency under super-lean conditions .....	31
Figure 2-2. Example of effect of $T_{\text{initial}}$ on the misfire lean limit.....	33
Figure 3-1. Experimental setup of CVCC.....	39
Figure 3-2. Multi-pole spark plug of 14 mm metric thread size.....	40
Figure 3-3. Motor for driving fan inside CVCC (Inset: Speed sensor) .....	41
Figure 3-4. Estimating flame area using binary images .....	42
Figure 3-5. Location of ion current probes on cylinder head .....	44
Figure 3-6. Image of cylinder head.....	46
Figure 3-7. Helical insert .....	46

Figure 3-8: Schematic setup of research engine platform .....	48
Figure 3-9: Ion current circuit used for this research.....	50
Figure 3-10. Typical engine ion current signal profiles and cylinder pressure .....	51
Figure 3-11. Shock tube schematic.....	53
Figure 4-1. Ion current signal validation at $\lambda=1.0$ with methane as fuel .....	56
Figure 4-2. Ion current signal validation at $\lambda=1.4$ with propane as fuel.....	57
Figure 4-3. Ion current signal validation at $\lambda=1.6$ with DME as fuel.....	58
Figure 4-4. Image frames from methane combustion at $\lambda=1.0$ .....	60
Figure 4-5. Flame area calculation of methane-air flames at varying $\lambda$ .....	61
Figure 4-6. Image frames from propane combustion at $\lambda=1.0$ .....	63
Figure 4-7. Image frames from DME combustion at $\lambda=1.0$ .....	64
Figure 4-8. Flame area calculation of propane-air flames at varying $\lambda$ .....	65
Figure 4-9. Flame area calculation of DME-air flames at varying $\lambda$ .....	65
Figure 4-10. Air-methane flames – pressure traces (top) & ion probe signal (bottom)....	69
Figure 4-11. Air-propane flames – pressure traces (top) & ion probe signals (bottom)...	70
Figure 4-12. Air-DME flames – pressure traces (top) & ion probe signals (bottom).....	71
Figure 4-13. Image frames from combustion at $\lambda=1.4/1.6$ - quiescent condition.....	73
Figure 4-14. Image frames from combustion at $\lambda=1.4/1.6$ - charge motion condition.....	75
Figure 4-15. Flame area calculation at $\lambda=1.0$ .....	76
Figure 4-16. Flame area calculation at $\lambda=1.4/1.6$ .....	76
Figure 4-17. $t_5$ based on pressure at $\lambda=1.0$ .....	77
Figure 4-18. $t_5$ based on pressure at $\lambda=1.4/1.6$ .....	78
Figure 4-19. Stretching of the discharge channel under flow .....	79

Figure 4-20. Discharge current vs. time at different gap velocities.....	80
Figure 4-21. Discharge current manipulation using current control.....	82
Figure 4-22. Combustion with directed flow – effect of current control.....	83
Figure 4-23. Flame area using current control at 25 m/s directed flow .....	84
Figure 4-24. Driver and driven section pressure profiles .....	86
Figure 4-25. Ion and pressure signal profiles for $\lambda=1.4$ and $p_{\text{initial}}=2.0$ bar abs .....	87
Figure 4-26. Flame speed estimation from ion current signal .....	88
Figure 5-1. COV of IMEP without and with insert at varying $\lambda$ .....	90
Figure 5-2. CA5 without and with insert at varying $\lambda$ .....	91
Figure 5-3. CA50 without and with insert at varying $\lambda$ .....	91
Figure 5-4. Pressure and HRR at $\lambda=1.0$ for test fuels .....	94
Figure 5-5. Pressure and HRR at $\lambda=1.2$ for test fuels .....	95
Figure 5-6. Pressure and HRR at $\lambda=1.4$ for test fuels .....	96
Figure 5-7. Pressure and HRR at $\lambda=1.6$ for test fuels .....	97
Figure 5-8. CA5 (top) and combustion duration (bottom) at 313 K.....	100
Figure 5-9. CA50 (top) and CA95 (bottom) at 313 K .....	102
Figure 5-10. NO <sub>x</sub> emission (top) and CO emission (bottom) at 313 K.....	104
Figure 5-11. Indicated thermal efficiency at 313 K.....	105
Figure 5-12. Scatter of ion current peak position – plug and auxiliary probe .....	106
Figure 5-13. Ion signal peak difference for gasoline combustion at 313 K.....	107
Figure 5-14. Intake heating (gasoline): CA5 (top) and combustion duration (bottom)..	109
Figure 5-15. Intake heating (ethanol): CA5 (top) and combustion duration (bottom) ...	110
Figure 5-16. Ion signal peak difference for gasoline combustion with intake heating...	111



Figure 5-17. $T_{\text{intake}}$ effect on NO <sub>x</sub> emission (top) and CO emission (bottom) .....	112
Figure 5-18. COV of IMEP – changing $\lambda$ and $T_{\text{intake}}$ .....	113
Figure 5-19. Effect of increasing $\lambda$ on CD and COV of IMEP for DME .....	115
Figure 5-20. Effect of increasing $\lambda$ on CA5 and CA50 for DME .....	116
Figure 5-21. Effect of increasing $\lambda$ on NO <sub>x</sub> and CO emissions for DME .....	117
Figure 6-1. Gasoline surrogate – Cylinder pressure, temperature & $Y_{\text{C}_8\text{H}_{18}}$ .....	122
Figure 6-2. Gasoline surrogate – $Y_{\text{OH}}$ , $Y_{\text{H}}$ , $Y_{\text{H}_2\text{O}}$ , and $Y_{\text{CH}_3}$ .....	124
Figure 6-3. Gasoline surrogate – $Y_{\text{C}_4\text{H}_8}$ , $Y_{\text{C}_3\text{H}_6}$ , $Y_{\text{CH}_4}$ and $Y_{\text{CO}}$ .....	125
Figure 6-4. Ethanol – Cylinder pressure, temperature & $Y_{\text{C}_2\text{H}_5\text{OH}}$ .....	126
Figure 6-5. Ethanol – $Y_{\text{OH}}$ , $Y_{\text{H}}$ , $Y_{\text{H}_2\text{O}}$ , and $Y_{\text{CH}_3}$ .....	128
Figure 6-6. Ethanol – $Y_{\text{C}_2\text{H}_4}$ , $Y_{\text{CH}_4}$ , $Y_{\text{CH}_2\text{O}}$ and $Y_{\text{CO}}$ .....	129
Figure 6-7. $T_{\text{intake}}$ effect (gasoline) – Cylinder pressure, temperature & $Y_{\text{C}_8\text{H}_{18}}$ .....	131
Figure 6-8. $T_{\text{intake}}$ effect (gasoline) – $Y_{\text{OH}}$ , $Y_{\text{H}}$ , $Y_{\text{H}_2\text{O}}$ , and $Y_{\text{CH}_3}$ .....	132
Figure 6-9. $T_{\text{intake}}$ effect (gasoline) – $Y_{\text{C}_4\text{H}_8}$ , $Y_{\text{C}_3\text{H}_6}$ , $Y_{\text{CH}_4}$ and $Y_{\text{CO}}$ .....	134
Figure 6-10. $T_{\text{intake}}$ effect (ethanol) – $Y_{\text{C}_2\text{H}_4}$ , $Y_{\text{CH}_4}$ , $Y_{\text{CH}_2\text{O}}$ and $Y_{\text{CO}}$ .....	135
Figure 6-11. DME – Cylinder pressure, temperature & $Y_{\text{CH}_3\text{OCH}_3}$ .....	137
Figure 6-12. DME – $Y_{\text{OH}}$ , $Y_{\text{H}}$ , $Y_{\text{H}_2\text{O}}$ , and $Y_{\text{CH}_3}$ .....	139
Figure 6-13. DME – $Y_{\text{CH}_3\text{O}}$ , $Y_{\text{CH}_4}$ , $Y_{\text{CH}_2\text{O}}$ and $Y_{\text{CO}}$ .....	140
Figure 6-14. Converge geometry input showing the main features and boundaries .....	142
Figure 6-15. Effect of cell size on turbulent velocity and swirl ratio .....	144
Figure 6-16. Viewing planes for the CFD results .....	145
Figure 6-17. Flow field comparison at 325 °CA between MAF of 4.2 and 5.4 g/s .....	148
Figure 6-18. Flow field comparison at 335 °CA between MAF of 4.2 and 5.4 g/s .....	149

Figure 6-19. Flow field comparison at 345 °CA between MAF of 4.2 and 5.4 g/s.....	150
Figure 6-20. Flow field comparison at 355 °CA between MAF of 4.2 and 5.4 g/s.....	151
Figure 6-21. Detailed flow field in the spark vicinity at 5.4 g/s for gap plane .....	153
Figure 6-22. Detailed flow field in the spark vicinity at 5.4 g/s for ground plane .....	154

## LIST OF APPENDICES

APPENDIX A: Specifications of Key Equipment.....	175
APPENDIX B: Pressure Signal Based Combustion Metrics.....	177
APPENDIX C: Ion Current Signal Processing Method .....	179
APPENDIX D: Validation and Input Parameters – CHEMKIN .....	183
APPENDIX E: Validation and Input Parameters – Converge.....	192
APPENDIX F: Copyright Permissions.....	200

## LIST OF SYMBOLS AND ABBREVIATIONS

<i>Greek Symbols</i>		<i>Unit</i>
$\lambda$	Excess air ratio	[-]
$\phi$	Equivalence ratio	[-]
$\gamma$	Ratio of specific heats – $C_p$ and $C_v$	[-]
$\mu F$	Microfarad	
$\mu m$	Micrometer	
$\mu s$	Microsecond	
$\rho$	Fluid density	[kg/m <sup>3</sup> ]
$\rho_F$	Density of fuel at steady state temperature	[kg/m <sup>3</sup> ]
<i>Non-Greek Symbols and Abbreviations</i>		
BDC	Bottom dead center	
°CA	Degree crank angle	
CA5	Crank angle for 5% of mass fraction burned	[°CA]
CA50	Crank angle for 50% of mass fraction burned	[°CA]
CA95	Crank angle for 95% of mass fraction burned	[°CA]
CD	Combustion duration	[°CA]

$C_p$	Molar specific heat at constant pressure for a gas mixture	[J/mol.K]
$C_v$	Molar specific heat at constant volume for a gas mixture	[J/mol.K]
CAFE	Corporate average fuel economy	
CARB	California Air Resources Board	
CFD	Computational fluid dynamics	
CI	Compression ignition	
CN	Cetane number	[-]
CO	Carbon monoxide	
CO <sub>2</sub>	Carbon dioxide	
COV	Coefficient of variation	
CPU	Central processing unit	
CR	Compression ratio	[-]
CVCC	Constant volume combustion chamber	
DAQ	Data acquisition	
DI	Direct injection	
DME	Dimethyl ether	
EGR	Exhaust gas recirculation	

EPA	Environmental Protection Agency	
Exp	Experimental	
fps	Frames per second	
FPGA	Field programmable gated array	
HC	Hydrocarbon	
HCCI	Homogeneous charge compression ignition	
HRR	Heat release rate	[J/°CA]
HTR	High temperature reaction	
ICE	Internal combustion engine	
ITE	Indicated thermal efficiency	[%]
IMEP	Indicated mean effective pressure	[bar]
J	Joule	
<i>K</i>	Flame stretch	[s <sup>-1</sup> ]
K	Kelvin	
LED	Light emitting diode	
LTR	Low temperature reaction	
mm	Millimeter	

ms	Millisecond	
m/s	Meters per second	
mol	Mole	
<i>Ma</i>	Markstein Number	[-]
MAF	Mass air flow	[g/s]
MFB	Mass fraction burned	[-]
ON	Octane number	[-]
$p_{int}$	Engine intake charge pressure	[bar]
$p_{initial}$	Chamber intake pressure	[bar]
ppm	Parts per million	
PFI	Port fuel injection	
PIV	Particle image velocimetry	
PM	Particulate matter	
PWM	Pulse width modulation	
NI	National Instruments	
NMHC	Non-methane hydrocarbon	
NO <sub>x</sub>	Oxides of nitrogen – NO and NO <sub>2</sub>	

RPM	Revolutions per minute	
RNG	Renormalized-group	
RT	Real time	
Sim	Simulation	
SI	Spark ignition	
STD	Standard deviation	
t	Time	[ms]
$T_{\text{intake}}$	Engine intake charge temperature	[K]
$T_{\text{initial}}$	Chamber initial temperature	[K]
TCI	Transistor coil ignition (system)	
TDC	Top dead center	
TKE	Turbulence kinetic energy	
u	Fluctuating component of velocity of turbulent flow field	[m/s]
u'	Root mean square of u (above)	[m/s]
U	Mean component of velocity of turbulent flow field	[m/s]
VDC	Voltage direct current	[volts]
Y	Mole fraction	[-]



## **INTRODUCTION**

Spark ignited, reciprocating internal combustion engines are the mainstay of light duty vehicles for passenger and goods transport. Improving the efficiency and reducing the emissions of such engines continue to be the focus of extensive research. In this chapter, a context is offered for the work undertaken by the author in this research domain. First, an outline of the dissertation is presented followed by the research objectives. Thereafter, the background, associated challenges and trends of this research are described with the aid of relevant literature.

### **Dissertation Outline**

The dissertation consists of seven chapters and appendices. It is divided into five main sections as illustrated in Figure 1-1. The first section consists of Chapters 1 to 2. In Chapter 1, the author introduces the topic, states the research objectives and motivations, and describes the relevant background of the research. A detailed literature review is presented in Chapter 2. In the second section, consisting of Chapter 3, the author provides a detailed description of the empirical tools and methods used to execute the research plan.

The third section consists of Chapters 4 and 5 in which the author describes the empirical results of this research. In Chapter 4, the author expounds on the combustion tests in a constant volume combustion chamber (CVCC) with optical access to estimate flame propagation speed and measure ionization current magnitude. The effects of fuel, fuel concentration, and charge<sup>1</sup> motion are explained. The effect of directed charge flow on a conventional spark discharge is described as well. High speed flames are generated using a shock tube and the flame speeds are estimated using ion current probes. The engine test

<sup>1</sup>Charge is defined here as a homogeneous mixture of fuel and air

results are presented in Chapter 5 in which different methods of changing charge reactivity are investigated.

The fourth section consists of the numerical simulations performed to analyze the empirical results in further detail (Chapter 6). Zero-dimensional chemical kinetic simulations are used to determine how fuel concentration and temperature may affect the inherent chemistry of the combustion. Three-dimensional computational fluid dynamics (CFD) simulations are performed to estimate the in-cylinder flow-field especially the region near the spark plug.

The fifth and final section of this dissertation comprises of the research outcomes and additional information provided in the references and appendices. In Chapter 7, the author provides a summary of the research conducted, lists the main conclusions, and proposes future work. The specifications of the critical equipment used in this research are presented in Appendix-A together with the measurement uncertainties. Formulae for pressure-based combustion metrics along with different related statistics are summarized in Appendix-B. The author has developed MATLAB codes to process the ionization current data from the combustion chamber and engine test setups which are provided in Appendix-C. Validation of the simulation parameters by comparison with empirical results is presented in Appendix-D. Input parameters of the three-dimensional flow field simulation are listed in Appendix-E. Copyright permissions for non-original material are listed in Appendix-F.

<b>RESEARCH OBJECTIVES AND LITERATURE REVIEW</b>	<b>Chapter-1</b> <b>Introduction</b> <input type="checkbox"/> Research motivation <input type="checkbox"/> Research objectives <input type="checkbox"/> Literature review	<b>Chapter-2</b> <b>Literature Review</b> <input type="checkbox"/> Premixed lean combustion <input type="checkbox"/> Effect of charge motion <input type="checkbox"/> Effect of fuel reactivity
<b>TEST SETUP AND METHODS</b>	<b>Chapter-3</b> <b>Research Tools and Methods</b> <input type="checkbox"/> Constant volume combustion chamber test setup <input type="checkbox"/> Single cylinder research engine test setup <input type="checkbox"/> Ion current measurement system development <input type="checkbox"/> Data processing methods	
<b>EMPIRICAL INVESTIGATION</b>	<b>Chapter-4</b> <b>Combustion Chamber Flame Propagation Studies</b> <input type="checkbox"/> Validate ion current system on optical chamber <input type="checkbox"/> Investigate effect of fuel, excess air ratio and charge motion on flame propagation <input type="checkbox"/> Study impact of directed flow on spark discharge channel <input type="checkbox"/> Demonstrate high speed flame measurement in a shock tube  <b>Chapter-5</b> <b>Charge Reactivity Impact on Engine Combustion</b> <input type="checkbox"/> Increase stability of lean combustion by modifying intake flow <input type="checkbox"/> Investigate the effect of modifying charge reactivity by changing fuel, excess air ratio and intake temperature	
<b>NUMERICAL ANALYSIS</b>	<b>Chapter-6</b> <b>Analysis of Charge Reactivity and Flow Fields</b> <input type="checkbox"/> Analyze the chemical mechanism of test fuels through chemical kinetic simulation to identify differences <input type="checkbox"/> Estimate the in-cylinder flow field through CFD simulation under engine test conditions	
<b>RESEARCH OUTCOMES AND ADDITIONAL INFORMATION</b>	<b>Chapter-7</b> <b>Conclusions</b> <input type="checkbox"/> Summary of Results <input type="checkbox"/> Conclusions <input type="checkbox"/> Proposed Future Work <b>References</b>	<b>Appendices</b> <input type="checkbox"/> Specifications of measuring equipment <input type="checkbox"/> Details of pressure and ion signal processing <input type="checkbox"/> Simulation parameters and validation curves

Figure 1-1. Dissertation outline

## ■ Research Motivation

In North America, the passenger vehicle and light truck market is dominated by gasoline fueled, spark ignition engines (SI) [1]. Originally, the fuel efficiency improvement of passenger vehicles was primarily driven by governmental regulations to tackle uncertainties related to oil supply and prices [2]. In United States of America (USA), these regulations were enacted under the Corporate Average Fuel Economy (CAFE) standards, with each manufacturer's vehicle fleet mandated to meet them [2]. Eventually, greenhouse gas (GHG) emissions were also brought under the purview of the CAFE standards. Canadian standards are closely aligned with USA's standards [3-4]. Moreover, major automotive markets such as China and the European Union (EU) have similar standards. Consequently, the fuel economy of passenger vehicles has steadily improved (Figure 1-2) and this improvement is projected to continue in the future provided there are no major policy changes. The CAFE and other equivalent standards have therefore incentivized manufacturers to continuously improve the fuel efficiency of their vehicle fleets. Separate regulations have also curbed vehicular pollutant emissions.

In recent years, battery electric vehicles (BEVs) have received significant attention [5-6] due to their absence of tailpipe emissions. If sufficient BEVs can be sold, manufacturers would also be able to meet the CAFE standards. However, two of the biggest concerns with BEVs from a consumer's perspective are the driving range and the charging time. Gasoline fueled vehicles typically have longer driving ranges and shorter refuelling times [7]. In Figure 1-3, the energy densities (lower heating values) of gasoline, dimethyl ether (DME) and ethanol are plotted together with practical energy density of lithium ion (Li-ion) batteries used in automotive applications [8-15]. DME and ethanol are shown since they

are relevant to the research presented in this manuscript. One cause for the low energy density of a conventional Li-ion battery is the fact that the battery carries all the reactants and products of the chemical reaction. A reasonable compromise could be gasoline-battery hybrid electric vehicles (HEVs) which leverage certain advantages of BEVs and gasoline fueled vehicles.

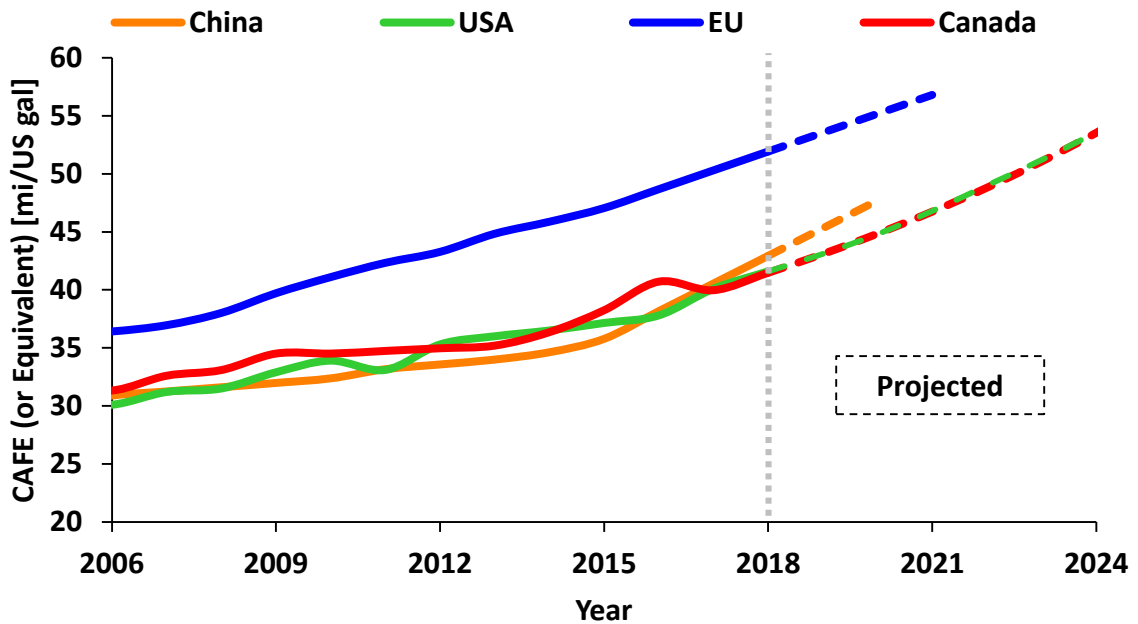


Figure 1-2. CAFE or equivalent historic trends and projections of passenger vehicles [1]

Hence, given the ubiquity of gasoline fueled SI engines, incremental improvements in their fuel efficiency can make significant environmental and societal impacts. Different methods and combinations thereof have been studied to improve SI engine efficiency [16]. One such method is the premixed lean-burn SI engine in which a mixture of fuel and excess air is combusted [17-21]. In lean-burn engines, air is in excess, meaning that after complete combustion of the fuel, there is oxygen remaining in the exhaust.

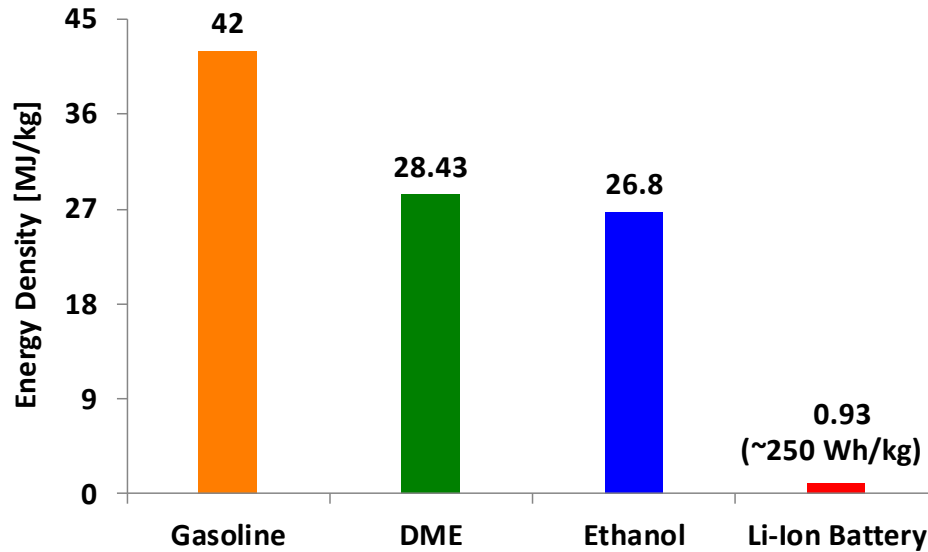


Figure 1-3 Energy density of liquid fuels in comparison to lithium-ion battery

In theory, a lean burn engine should have higher thermal efficiency because the excess air increases the specific heat ratio of the in-cylinder charge and decreases the dissociation and heat transfer losses. Consequently, this should improve the fuel efficiency. The impact of lean combustion on engine performance is summarized in Figure 1-4. In this figure, the fuel consumption, power, and regulated emissions – nitrogen oxide and nitrogen dioxide (hereafter referred to as NO<sub>x</sub>), carbon monoxide (CO), and (unburned) hydrocarbon (HC) are plotted against the excess air ratio, denoted by the Greek letter  $\lambda$ .

Excess air ratio ( $\lambda$ ) is defined by the following equation –

$$\lambda = \frac{\text{Actual air to fuel ratio}}{\text{Stoichiometric air to fuel ratio}} \quad 1.1$$

The stoichiometric air-fuel ratio can be calculated from the molecular formula of the fuel (or equivalent molecular formula in case of mixtures such as gasoline). This is applicable for the condition of complete combustion of the fuel with full utilization of the air. The

actual air-fuel ratio can be determined by direct measurement of the air flow rate and the fuel flow rate and multiplying each by the density of air and density of fuel respectively. When  $\lambda < 1$ , the combustion is deemed to be rich. When  $\lambda > 1$ , the combustion is deemed to be lean.  $\lambda = 1$  corresponds to stoichiometric combustion. Conventional gasoline SI engines typically operate around the stoichiometric condition.

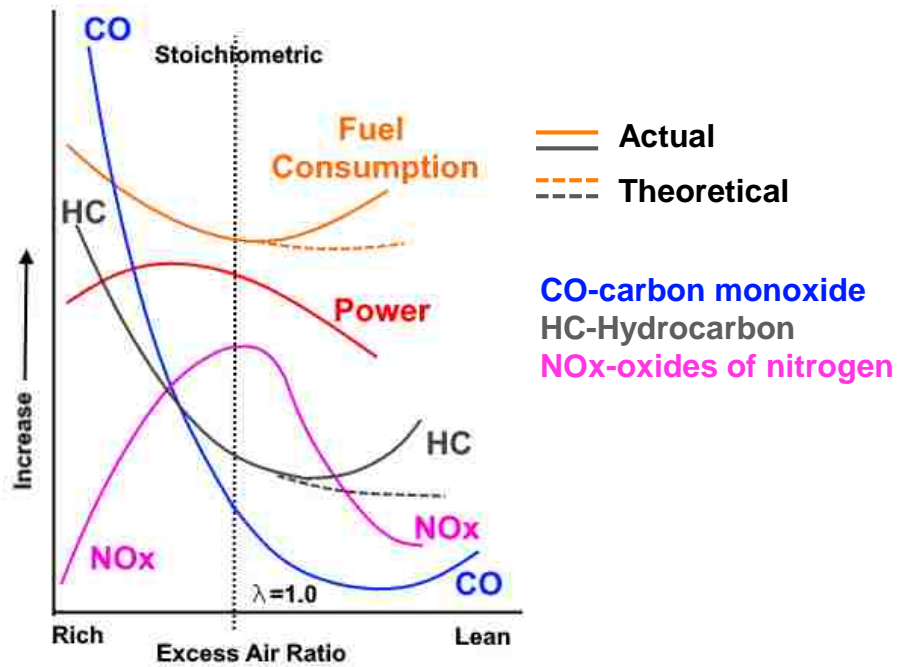


Figure 1-4 Impact of lean burn on engine performance (adapted from [17])

As illustrated in Figure 1-4, with increasing  $\lambda$  (increasing leanness of the charge), in theory, the fuel consumption and the HC emissions should decrease, but in practice, the opposite happens when the air fuel mixture is too lean – a so called ‘lean limit’ is reached. The NOx and CO emissions however, show a decreasing trend with increasing  $\lambda$ . Extension of the lean limit therefore, may help achieve lower NOx, HC and CO emissions, and yet maintain or improve fuel efficiency.

One reason for the lean limit is the decrease in the laminar burning velocity with increasing  $\lambda$  [22-26]. Due to the lowered burning velocity, combustion may be incomplete. This can explain the rise in the HC emissions and the drop in the fuel efficiency. For example, laminar burning velocities of ethanol-air mixtures at different excess air ratios and initial pressures are plotted in Figure 1-5 based on tests conducted in a constant volume combustion chamber (CVCC) [25]. Additionally, increase in initial pressure also decreases the laminar burning velocity.

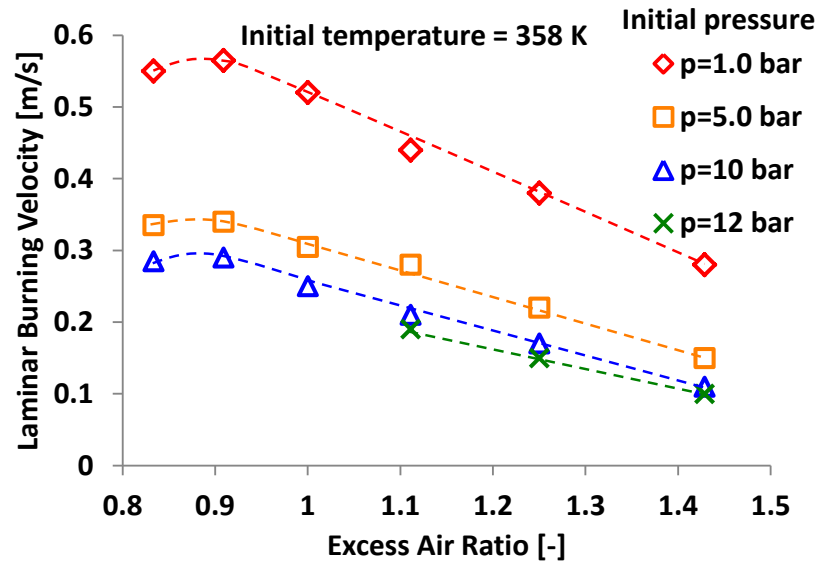


Figure 1-5 Laminar burning velocity of ethanol-air mixtures [25]

One means to counteract the reduction in the burning velocity is to enhance the in-cylinder flow field [27-28]. In SI engines, regardless of whether they operate under lean burn or not, the flame propagation rate is increased through turbulence. In lean burn engines however, this assumes greater significance since the completion of combustion is even more challenging. This turbulence is typically generated by features of the engine design such as the design of the intake manifold, or the piston bowl [29].



## ■ Research Objective

The primary objective of this research is to study the premixed and lean combustion relevant to a spark ignition engine operating under low load and low speed to understand the fundamental effects of certain operational parameters. The first is the charge motion which would affect the flame propagation. Organizing the charge motion under lean conditions is especially critical for timely completion of combustion in an engine. The second is the reactivity of the air-fuel charge itself. The modulation of the charge reactivity will be performed in the following ways – type of fuel, air-fuel ratio, and initial temperature of the charge. According to the author's search, this is the first comprehensive study on the combined effects of in-cylinder flow and fuel reactivity on premixed and lean combustion in an SI engine.

The objective will be achieved through a combination of empirical and computational tools and methods. The fundamental effect of flow on the flame propagation will be studied through controlled tests in a constant volume combustion chamber (CVCC) with optical access. Emphasis will be on effect of flow on the spark discharge and initial flame kernel formation as well as the overall flame propagation. Additionally, tests will be conducted on a spark ignition engine under low load and low speed condition. Impact of intake flow modulation and air-fuel mixture reactivity control will be highlighted. Furthermore, the engine test conditions will be subject to numerical analysis to further the knowledge of underlying flow and chemical phenomena. Simulations of engine combustion conditions will be performed through detailed chemical kinetic analysis. The in-cylinder flow field will be estimated through use of computational fluid dynamics (CFD) simulation. The general scheme of the research is illustrated in Figure 1-6.

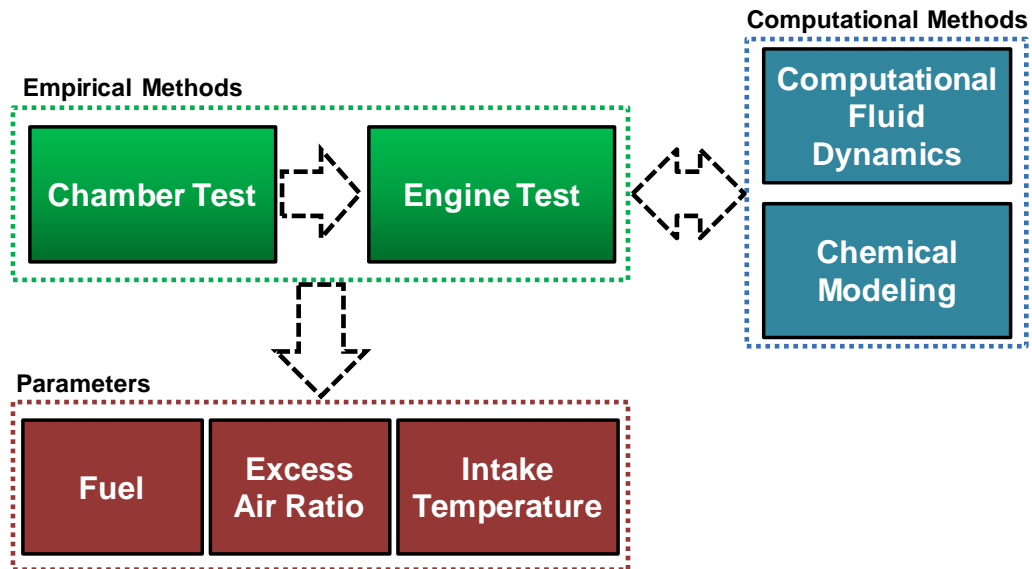


Figure 1-6. General scheme of research

## ■ Spark Ignited Lean Combustion

Lean combustion for SI engines as a concept has existed for more than a hundred years [30]. In the 1970s, automotive companies such as General Motors and Toyota published research on lean burn SI engines [19-20]. It is believed that some of this interest was caused by the shortage and cost of petroleum fuels during that time [18]. As explained in Section 1.2, the benefits of lean combustion can be diminished by the practical considerations such as lowering of flame speeds.

Quader presented a qualitative relationship between spark timing and excess air ratio which further defined the challenges of lean combustion [31]. At any  $\lambda$ , if the ignition timing is advanced or retarded from the maximum brake torque (MBT) timing, there is an ignition limit or a partial burn limit respectively for the timing (Figure 1-7). The ignition limit is the start of the misfire zone. Advancing the timing further would cause misfire – either the charge will not ignite, or even if it does, the flame will be blown out. After the partial burn

limit, retarding combustion further causes incomplete combustion, and consequently, a decrease in the engine load. Between these two limits is the stable zone of combustion. As the  $\lambda$  increases, the ignition and partial burn limits converge, thereby decreasing the range of stable spark timings possible. The  $\lambda$  corresponding to the point where the ignition and partial burn limits converge marks the start of the misfire or the partial burn zone [18]. The intention would be to move this further right (direction of arrow) which extends the stable zone further as  $\lambda$  is increased.

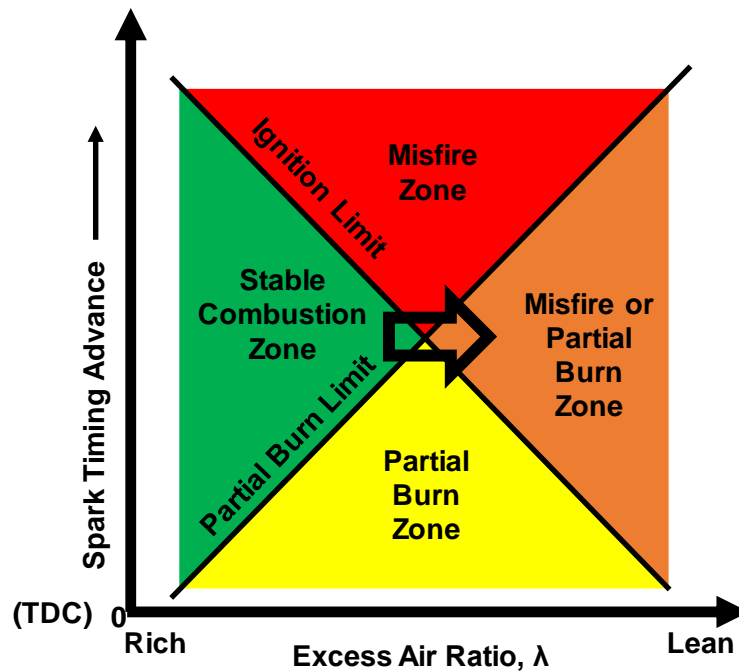


Figure 1-7. Zones of stable, misfire and partial burn combustion (based on [31])

In this context, two other relevant terms must be defined. The first is the lower flammability limit which is a property of the fuel and varies with pressure and temperature. It is defined by ASTM as “the minimum concentration of a combustible substance that is capable of propagating a flame in a homogeneous mixture of the combustible and a gaseous oxidizer under the specified conditions of test” [32]. Therefore, this is the highest  $\lambda$  at a given

pressure and temperature at which a flame can propagate. The second term is the lean ignition limit which is defined as “minimum external energy which must be supplied to a critical volume to raise the mixture to its minimum ignition temperature” [18]. This is related to the energy delivered to the spark gap which in turn is affected by parameters such as the coil charging duration and the length of the spark gap.

The combustion in an SI engine with a premixed charge, can be visualized in a simplified manner as shown in Figure 1-8. If the spark energy is at or above the lean ignition limit, ignition will occur, and a flame kernel may be formed. If the fuel concentration in the charge is above the lower flammability limit, the flame kernel may expand, and eventually propagate.

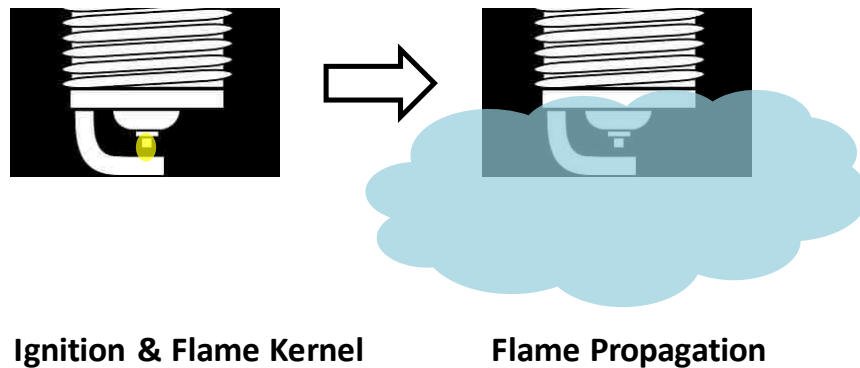


Figure 1-8. Simplified representation of SI combustion

In an SI engine environment with a premixed charge, the ignition and the subsequent flame propagation are therefore two of the main stages of combustion. The type of impact (positive/negative/no impact) of some engine operating variables on ignition and flame propagation are summarized in Table 1-1.

Table 1-1. Impact of SI ICE operating variables on ignition and flame (based on [31])

<b>Operating Variable</b>	<b>Impact on ignition</b>	<b>Impact on flame propagation</b>
Increasing spark energy	Positive	No/negligible
Increasing compression ratio	Positive	Positive
Increasing charge motion	Negative	Positive
Increasing charge dilution	Negative	Negative
Increasing flame propagation distance	No/negligible	Negative

During lean combustion, with reduced flame speeds, flame propagation becomes a challenge [18]. One way to address this is to increase the charge motion through bulk motion (swirl/tumble) and/or turbulence. However, increasing the charge motion may have a negative impact on the ignition. Moreover, increasing charge dilution typically has a negative effect on both ignition and flame propagation. Hence, research in lean combustion attempts to address some of these challenges. A summary of premixed lean combustion engine research is provided in Chapter 2.

### ■ Premixed Turbulent Flames

In an internal combustion engine, in-cylinder flows are characterized by turbulence. The turbulence plays a major role in the fuel air mixture preparation, and subsequent combustion. Eddies move in random directions to enhance mixing of fuel and air across adjacent fluid layers [33]. When the fuel-air mixture ignites, the combustion propagates through what is known as turbulent flame. Unlike a laminar flame, whose velocity can be characterized by the fuel, oxidizer and transport properties such as thermal conductivity, viscosity and thermal diffusivity, turbulent burning velocity is harder to resolve. It is not a well-defined quantity and results vary between one experimental setup to the next.

Turbulence can be defined as the fluctuating component of the velocity which is added to the mean velocity of a viscous flow. In a physical sense, the velocity and pressure inside a turbulent flow keeps varying with irregularity and the fluctuations are characterized by high frequencies. In a qualitative sense, these fluctuations would affect the surface area of the flame by producing a corrugated flame front and increase the energy transfer as well as the flame speed. Mixing due to enhanced convection can promote further burning of the unburned mixture.

Damkohler was the first to study turbulent premixed flame propagation [34]. He identified two limiting cases based on magnitude of scale of turbulence as compared to thickness of the laminar premixed flame, and for large scale turbulence, assumed interaction between turbulent premixed flame front and turbulence flame front to be purely kinematic.

The Damkohler number (Da) is used to characterize turbulent flames –

$$Da = \frac{T_{flow}}{T_{chem}} \quad 1.2$$

which, is the ratio of the characteristic turbulence time scale ( $T_{flow}$ ) and the characteristic chemical time scale ( $T_{chem}$ ). For large values of Da, the chemical time scale would be small, which in turn would imply that the chemical reactions are fast relative to the flow and not significantly affected by the turbulence.

In an internal combustion engine, a spherical flame may be encountered given by the Figure 1-9 (adapted from [33]). The innermost wavy line represents the flame front at time,  $t=0$ . Let the burned mixture be contained in a spherical volume or radius,  $r_m$ . Over an infinitely small step in time,  $dt$ , the unburned mixture enclosed by next corrugated line is burned.

This volume is given by the volume of a spherical shell with inside diameter  $r_m$ , and wall thickness  $dr_{um}$ .

The turbulent flame speed ( $S_t$ ) is equal to,

$$S_t = \frac{dr_{um}}{dt} \quad 1.3$$

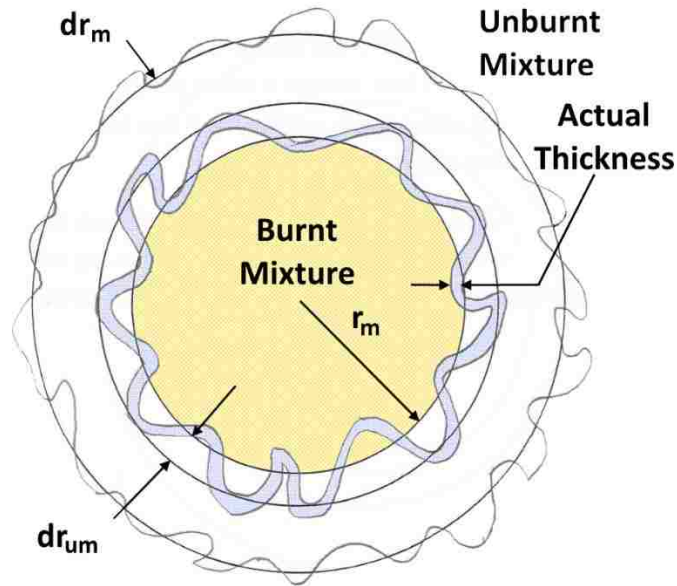


Figure 1-9: Premixed turbulent flame ball (adapted from [33])

One of the most common ways of characterizing turbulence is to define the turbulence root mean square velocity denoted by  $u'$  in this manuscript.  $u'$  is also sometimes referred to as the turbulence intensity, but in this manuscript, the definitions are as follows.

The velocity at any point,  $U$  can be expressed as the sum of the mean velocity component  $\bar{U}$  and the fluctuating component  $u$ . The equation is –

$$U = \bar{U} + u \quad 1.4$$

So,  $u'$  is the root mean square of the fluctuating component  $u$ . The turbulence intensity ( $I$ ) is given by the following ratio –

$$I = \frac{u'}{\bar{U}} \quad 1.5$$

Turbulence can be visualized as an assortment of eddies of different sizes. The largest eddies are of the order of the geometry of the chamber and their size is given by the integral length ( $\Lambda$ ). The size of the smallest eddies is given by the Kolmogorov length ( $\eta$ ).

A turbulent flame increases the rate of burning compared to a laminar flame due to an increase in the surface area characterized by the corrugations or wrinkling as shown in Figure 1-9. Again, the heat transfer rate and convective transport of active species due to the turbulence can increase the burning velocity. Furthermore, turbulence can enhance the mixing of the burned and the unburned gas such that the reaction becomes homogeneous. Two terms will be defined at this point which are relevant to the evaluation of flames – flame stretch rate, and Markstein Number. Flame stretch rate is defined as the change in frontal area of a flame with respect to time [35]. It is given by the relation –

$$K = \frac{d(\ln A)}{dt} \quad 1.6$$

Where  $A$  is flame surface area and  $t$  is time [35].

Finally, the Markstein number is defined as follows [36] –

$$Ma = \frac{\text{Markstein Length}}{\text{Characteristic Laminar Flame Thickness}} \quad 1.7$$



A higher Markstein length typically indicates a greater impact of flame stretching on the localized burning velocity. It can be calculated for the burned and the unburned gas [36].

The flame stretch rate and the Markstein number can be determined experimentally.

Two other definitions will be given here for future reference. The ‘turbulent burning velocity’ is defined as the “velocity which when multiplied by a defined flame surface area and the unburned gas density gives the mass rate of burning” [37]. The flame (propagation) speed is “a measure of how fast the flame is traveling with respect to a fixed point of reference” [38].

### ■ Premixed turbulent combustion in a CVCC

One of the ways to study flame propagation in engine like conditions is to use constant volume combustion chambers (CVCCs). A summary of CVCC research for flame propagation studies is provided in this section since a CVCC was used in this research as well. One way to generate turbulence in a CVCC is using a fan which can stir the charge inside the chamber [37]. The turbulent combustion in a CVCC can be divided into four stages [38]. It is assumed that the gas phase, homogeneous, premixed charge is ignited by a spark. The stages are as follows –

#### Stage-I

The first stage is characterized by chemical reactions beginning at the spark surface without any perceptible change in the pressure. The flame accelerates as a primarily laminar flame whose acceleration would depend on the fuel-air ratio, temperature, density, and loss of heat. At this stage, the unburned mixture may be compressed so the expansion of the burned mixture is isobaric.

## Stage-II

As the flame front expands further away from the spark plug, the flame velocity is essentially a sum of the expansion velocity and the laminar burning velocity. Both pressure and temperature increase in the chamber since with the expanding flame front, the burned as well as the unburned gases get compressed.

## Stage-III

At this stage, the flame has approached a turbulent flame with marginal change in flame area with increase in the flame radius.

## Stage-IV

As the flame front approaches the walls of the chamber, the burning velocity decreases which is accompanied by a decrease in the flame velocity.

Herweg *et al* used a CVCC to study the initial flame kernel formation [39]. The initial flame speed was similar to the laminar flame speed when turbulence intensities were low. The laminar flame chemistry controlled the flame kernel formation. Increasing turbulence intensity increased the initial flame speed. The turbulent burning velocity during the flame kernel formation was significantly lower than a fully developed flame. Bradley *et al* made a review of premixed turbulent velocity measurements in combustion bombs and burners [37]. They found that when turbulent velocity was measured in a fan-stirred bomb, the entire flame surface was exposed to mostly isotropic turbulence under constant pressure conditions. Limited data was available at high pressures and temperatures which are more relevant to engine operation conditions. Ohigashi *et al* performed premixed turbulent

combustion tests in a chamber using a fast-moving perforated plate for generating turbulence [40]. Increasing the turbulence intensity increased the extents of the combustion region. When turbulence was weak ( $u' < 0.1$  m/s), the initial flame front resembled a laminar flame, but the flame front wrinkled subsequently.

Moriyoshi *et al* studied the combustion characteristics of homogeneous and stratified charge using propane and methane [41]. For homogeneous charge, it was found that turbulence enhanced combustion at any excess air ratio. The effect of turbulence was especially enhanced for methane-air charges. Lee and Ryu researched flame propagation and combustion characteristics of liquified petroleum gas (LPG) in a CVCC without charge motion [42]. They concluded that excess air ratio had a greater impact on flame propagation speed than the initial pressure and temperature of the unburned gas. Flame propagation speed increased with increasing temperature of the unburned gas and decreased with increasing pressure of the unburned gas.

Bradley *et al* discussed the importance of selecting the reference radii in turbulence velocity measurements, the effect of Markstein number, and studied the turbulent flames of different fuels such as ethanol, propane and methane [43-46]. They also proposed the use of spherical flames to determine the stretch free burning velocity and Markstein length.

Haq *et al* studied laminar and turbulent flames in a CVCC at initial pressures of 1 and 5 bar for methane and iso-octane fuels [47]. Planar laser induced fluorescence of the OH radical (PLIF-OH) was used to study the flame structure. Disturbances during the ignition process were found to manifest in laminar flames in the form of dents or cusps. The shape of the cusp varied with type of fuel, excess air ratio, and pressure. Flame curvature increased when pressure was increased from 1 to 5 bar. Jiang *et al* studied the relationship

that minimum spark ignition energy had with premixed and lean combustion [48]. They found that the minimum spark ignition energy increased with increasing intensity of turbulence. Sayama *et al* used a high swirl chamber in which the flow velocity in the spark gap was 65 m/s. When the charge became leaner, it became increasingly difficult for the flame to remain attached to the spark plug and it tended to be blown-off [49]. The turbulent flame itself will also affect the turbulence in a chamber or engine. In a review published by Lipatnikov *et al*, it was stated that premixed flames can substantially affect a turbulent velocity field [50]. Moreover, predicting such effects is difficult especially if the root mean square of the turbulence velocity and the laminar flame speed are of the same order. The maximum initial pressure and maximum initial temperature in the surveyed literature for CVCCs is summarized in Figure 1-10. The corresponding maximum excess air ratio in the surveyed literature for CVCCs is summarized in Figure 1-11. This is based on the author's limited search only.

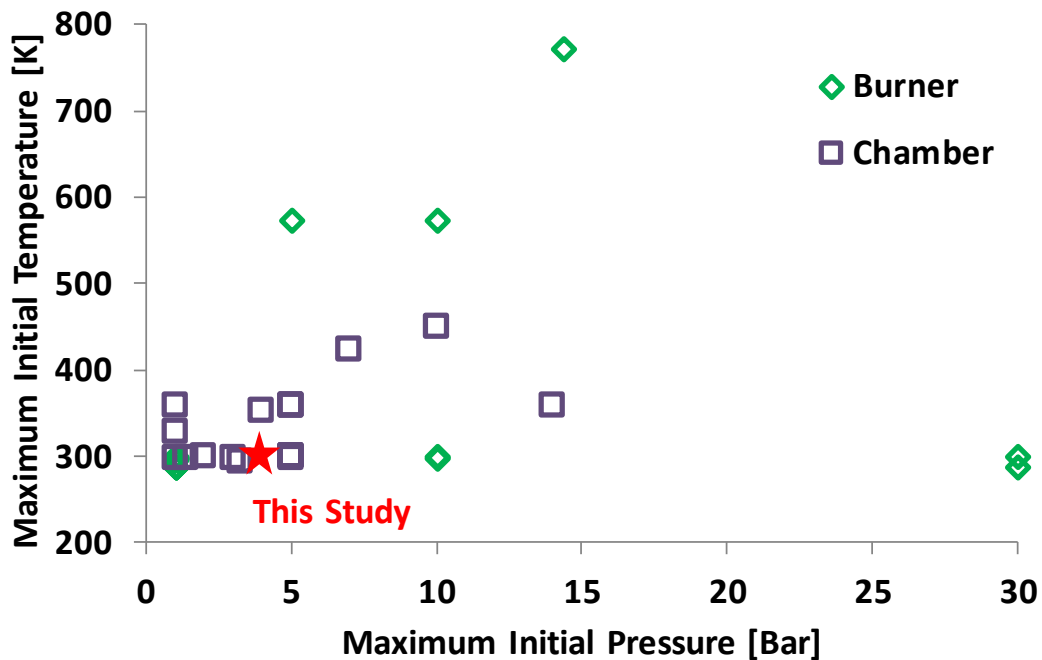


Figure 1-10. Maximum initial pressure and temperature in surveyed literature

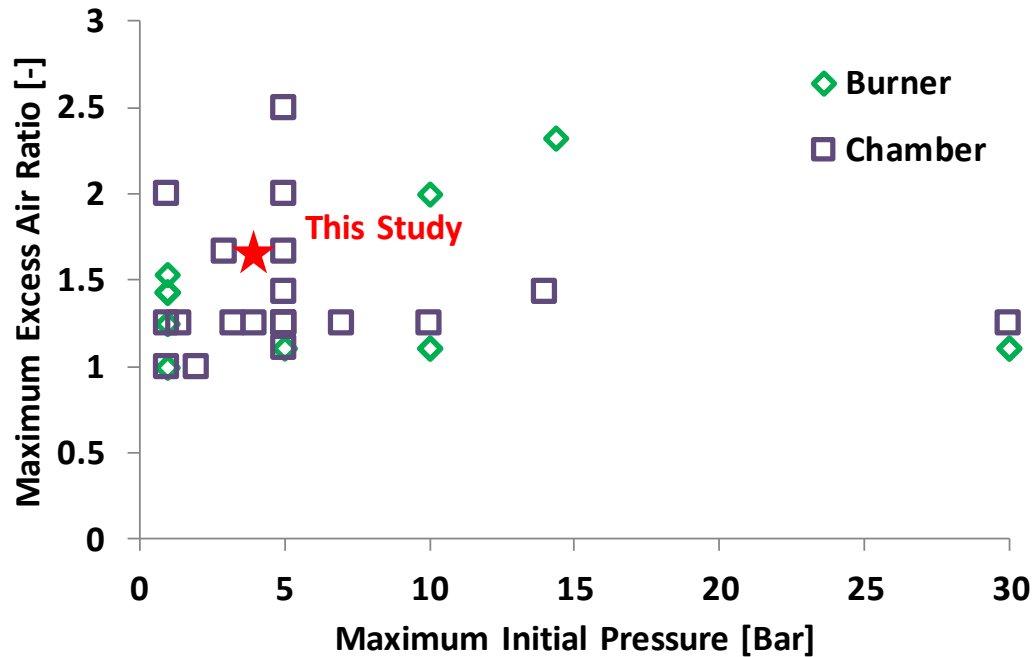


Figure 1-11: Maximum initial pressure and  $\lambda$  in surveyed literature

### ■ Premixed turbulent combustion in engines

In this sub-section, a summary of research on premixed turbulent combustion in engines is provided. Under motoring condition, the root mean square of fluctuating velocity,  $u'$  can be influenced by several operating parameters. Typically, increasing engine speed, volumetric efficiency, or intake swirl causes a linear increase in the  $u'$  [38]. The effects of compression ratio, throttling and charge dilution with exhaust gas recirculation (EGR) on the  $u'$  are either marginal or there are no effects. Under firing conditions, the turbulent burning velocity is strongly correlated to the engine speed and the intake swirl due to the in-cylinder turbulence [38].

Brequisny *et al* studied early stages of flame propagation in an optical engine at different engine speeds using different fuels. The fuels ranked in order of decreasing combustion duration were methane, propane, butane and iso-octane, which corresponded to their ranks

according to the Markstein lengths [51]. Moreover, it was observed that at small flame radii, the global flame stretch rate increased for all fuels. Premixed fuel–air flame propagation was investigated in a single-cylinder, spark-ignited, four-stroke optical test engine using high-speed imaging by Ihracska *et al* [52]. The results indicated that gasoline and isooctane had similar flame propagation behavior with axial flame speeds of the order of ~0-20 m/s. The initial flame propagation speed at the start of ignition was very high (~50 m/s) and then the flame contracted (negative velocity) due to endothermic dissociation of the fuel molecules and formation of radicals. Subsequently, the flame speed became positive again.

Ikeda *et al* discussed flame speed measurement in a V-8 racing engine with four valves and a pent roof cylinder head [53]. An infrared sensor was used to measure the amount of laser light absorption by the fuel and determine the flame arrival timing. A micro Cassegrain (MC) sensor was used to measure the chemiluminescence inside the cylinder after arrival of the flame. The flame propagation speed increased with engine speed. From 10000 to 16000 rpm, the flame propagation speed increased from 20 to 32 m/s. However, the flame speed normalized with mean piston speed remained constant. At high speeds, flame propagation speed was affected by the fluid dynamics of the cylinder flow.

Mounaïm-Rousselle *et al* used an optically accessible boosted (1.3 bar absolute) spark ignited single cylinder engine run at 1200 rpm and medium load using simulated EGR [54]. The laminar burning velocity,  $S_L$  was calculated and the turbulent burning velocity,  $S_T$ , was obtained from measurement. The ratio of  $S_T$  and  $S_L$  decreased with increasing burned mass fraction which indicated a decrease in the flame corrugation. Charge dilution was found to increase this ratio – indicating an increase in the flame corrugation.

Le Coz made a study of cycle to cycle variations in SI engines caused by the in-cylinder flow field [55]. Four variables of consequence were identified – intensity of the high frequency turbulence in the charge, low frequency velocity of the charge before ignition (swirl/tumble), spark duration (from discharge current), and spark breakdown period. The cyclic variations of the large-scale flow field controlled the stability of lean combustion. These effects and evolution of the large-scale flow field have been researched extensively [42, 56-59]. The spark glow duration was a characteristic of the in-cylinder flow field near the plug since it was distorted by the flow field. This impact of the flow field on the spark discharge has been confirmed by others [27, 60].

## ■ Relevant Flame Detection Techniques

This section provides a background summary of the flame detection techniques used in this research – shadowgraph imaging and ion current sensing. Each sub-section provides a description of the technique followed by brief overview of results and applications.

### ■ Shadowgraph imaging

Shadowgraph imaging has been a standard laboratory tool for more than a century [61]. The underlying theory of this technique is based on geometrical optics and diffraction effects. The refractive index of a medium is related to its density. The sensitivity of this technique is proportional to the second derivative of the refractive index. This makes it suitable for measuring density changes in high speed compressible fluid flows [62]. Shadowgraph measures the deflection and the displacement of a single uniform incident light beam [63]. When the light ray passes through a region where there is a gradient of refractive index, it gets bent. When there is no change in refractive index, the light ray

maintains its path. Convergence and divergence of these light rays cause the image to have light and dark regions corresponding to the gradients in density in the medium under investigation. Different configurations of the shadowgraph system are possible. The shadowgraph imaging configuration relevant to this research is the Z-type system which consists of two parabolic telescope mirrors, a light source, and a high-speed camera. The experimental setup is illustrated in Figure 3-1. A sample shadowgram (image obtained from shadowgraphy) from this system is shown in Figure 1-12.

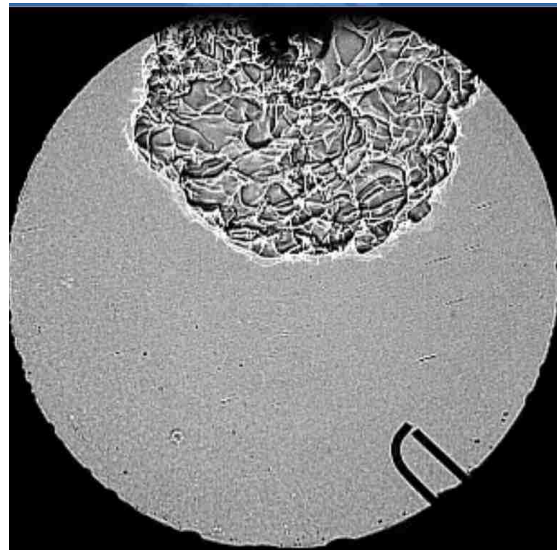


Figure 1-12. Shadowgraph image of flame in a CVCC

### ■ Ion current sensing

Ion sensing is based on the ability of the ionized gas to conduct electricity. In its simplest form, an ion sensing probe consists of two electrodes, and is placed in a volume of interest where ionized species are expected (Figure 1-13). A voltage bias (typically direct current) is provided across the electrodes. When ionized gas such as in the flame front passes between the electrodes, the circuit is completed by ions present in the reacting gas. This ion current is detected by measuring the voltage drop across a resistor in series.



Typical ionic species in engine combustion include  $\text{H}_3\text{O}^+$ ,  $\text{OH}^-$ ,  $\text{H}^+$ , and  $\text{CH}^+$  radicals. The ion sensing method is used in some production engines for combustion diagnostics especially misfire and knock detection [64-65]. The spark plug is generally used as the ion sensing probe in production engines.

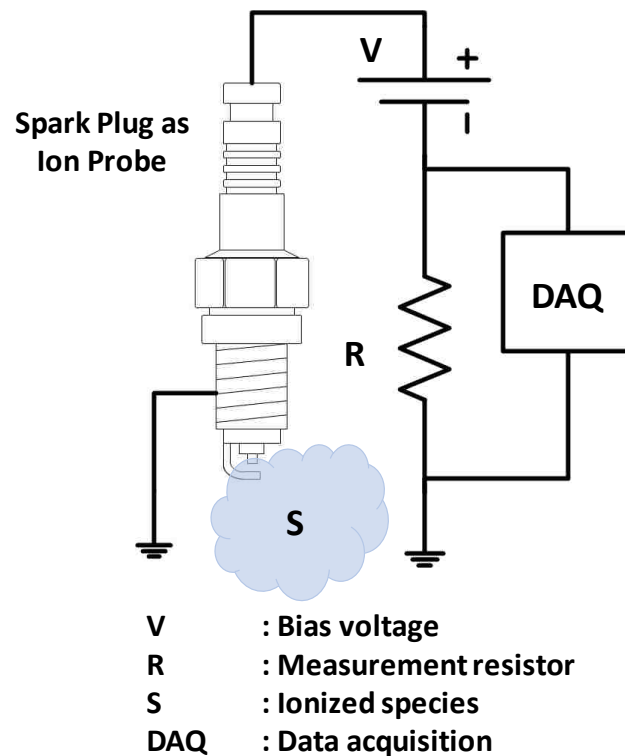


Figure 1-13. Fundamental concept of ion current measurement

The use of ion current for combustion detection and analysis in SI engines is well established [65-78]. Andersson and Eriksson used ion current measurement in an SI direct injection engine for combustion stability control [66]. The ignition phase ion signal was excluded, and the remaining signal was integrated similar to the cumulative heat release calculation. At the maximum brake torque timing (MBT), the ion signal variation was lowest, and the signal integral value was the highest. Using ion current to detect knock, misfire and incomplete combustion are widely reported in literature and used in racing and

production applications [67-73]. The ion current magnitude is typically highest when the charge is stoichiometric or slightly rich ( $\lambda \leq 1$ ) [74-75].

Correlating the ion signal to the pressure signal has also been researched. Gürbüz used an ion current sensor which was integrated into a fast response thermocouple [76]. The author reported various correlations between in-cylinder pressure-based combustion parameters, local gas temperature, and ion current. Gao *et al* found good agreement between the timing of the post flame peak of the ion current, and the timing of peak of the pressure. The peak of ion current increased with load [77].

Einewall *et al* made a comparison between lean combustion with excess air and exhaust gas recirculation (EGR) diluted combustion through the measurement of ion current [78]. EGR dilution at stoichiometric conditions produced a stronger ion current signal when compared to lean conditions. Ion current detection for homogeneous charge compression ignition (HCCI) combustion has also been reported. For instance, Dong *et al* concluded that in gasoline and ethanol fueled HCCI engines, the ion production was dominated by temperature [79]. They integrated the ion signal and compared the phasing of ion signal (Ion50) with the combustion phasing (CA50). It was found that the difference between the Ion50 and CA50 changed with  $\lambda$  and the type of fuel used. Mehresh *et al.* demonstrated that the ion signal could not only be a surrogate for the pressure signal but could also be used to detect cycle-by-cycle variation [64].

## LITERATURE REVIEW

In this chapter, the author presents a literature review on premixed lean combustion in engines and the effects of charge reactivity modulation using different fuels and temperatures. This chapter is divided into two sections. In the first section, the author provides a general review of premixed lean combustion in SI engines. The second section is a discussion on the effect of modifying charge reactivity.

### Premixed Lean Combustion in SI Engines

An introduction to spark ignited lean combustion has been provided in Sections 1.2 and 1.4. A further discussion from literature is provided in this section to explain the benefits and challenges associated with premixed lean combustion in SI engines. A few definitions are in order. The start of combustion is defined as CA5, which is the crank angle for the 5% mass burned fraction (MFB). The MFB is derived from the heat release rate (HRR) which is again calculated from the pressure signal. Additionally, CA10, CA50, and CA90 represent crank angles corresponding to 10%, 50% and 90% of MFB.

Second law of thermodynamics analysis by Farrell *et al* provided further evidence of higher engine efficiency with lean combustion due to reduced exhaust and in-cylinder heat losses, and pumping losses [80]. However, it was estimated that lean burn operation increased ‘combustion irreversibilities’, a measure of entropy production and consequently, indicated a decrease of capability to do work. The combustion irreversibility could be reduced by increasing the reaction temperatures.

Studies in engines with optical access have revealed certain characteristics of flame propagation under lean conditions. Aleiferis *et al* observed that the 3-dimensional structure

of the flame ( $\lambda=1.47$ , iso-octane) varied between each engine cycle in terms of size, shape and location [27]. The flame kernel was not spherical which indicated that the large-scale features of the flow-field, rather than the turbulence were more influential. Moreover, the tumble motion caused convection of the kernel out of the spark gap. This phenomenon advanced the CA5. Arcoumanis *et al* attempted to quantify the tumble generating capacity of a four-valve pent roof engine with optical access [81]. The flame was observed to be turbulent and asymmetric from the early stages and stretched in the direction of the mean flow. In an additional study, Arcoumanis *et al* further confirmed the strong correlation between flame development and the velocity field near the spark plug [82]. Increasing the mean flow velocity and the turbulence intensity tended to decrease the combustion duration.

Le *et al* used high speed particle image velocimetry (PIV) to measure the flow field and capture the flame propagation simultaneously [83]. The flame generated turbulence was higher for stoichiometric operating conditions than lean conditions. Again, lean flames grew as a “highly turbulent structure” and flame front propagation was slowest into the regions where the turbulence and flow velocity were the lowest. Further studies by Aleiferis *et al* suggested that the cyclic variability in the early flame development stage caused variability in the CA5 [84]. The flame growth speeds decreased when they were plotted as a function of flame radius from the piston crown plane of view. Moreover, the flame typically preserved its shape while growing. Lee *et al* confirmed the decrease in flame speed with increasing  $\lambda$  in a liquified petroleum gas (LPG) fueled SI engine [85]. However, HC emissions and the IMEP variation increased with increasing  $\lambda$ . By increasing the in-cylinder swirl motion, the CA50 was advanced but the overall burn duration was increased marginally. The measured flame speed had a linear positive correlation with the

corresponding laminar flame speed at the experimental pressures and temperatures. Kang *et al* also studied the characteristics of tumble motion on lean combustion and observed that the turbulence intensity increased near TDC when the tumble was enhanced [86]. The enhancement of tumble decreased the combustion duration, but also increased the cyclic variation in peak pressure due to the higher turbulence near TDC.

A major disadvantage of lean combustion is the inability to use a three-way catalyst due to the presence of oxygen in the exhaust. Einewall *et al* made a comparison of lean combustion and stoichiometric combustion with EGR and a three-way catalyst using natural gas as the fuel [87]. Higher CO emissions and lower efficiency were reported for stoichiometric combustion with EGR in comparison to those for lean combustion. The three-way catalyst can be used for stoichiometric combustion with EGR, but the  $\lambda$  must be controlled in a very narrow range ( $\pm 0.01\%$ ) for acceptable trade-off between NO<sub>x</sub> reduction and CO oxidation. One of the downsides of lean combustion was the limited window of ignition timing, which limited load extension. Similar comparisons between lean combustion and stoichiometric combustion with EGR by Lumsden *et al* [88] and Inge *et al* [89] suggested that lean combustion was better for improving fuel efficiency. However, Lumsden *et al* recommended that the increase in HC emissions and decrease in combustion stability associated with lean combustion could be compensated by enhancing intake flow. Kharas *et al.* studied the implications of lean combustion on the engine after-treatment [90]. They proposed a system which consisted of a durable lean NO<sub>x</sub> catalyst placed upstream of a suitable three-way catalyst. Hydrocarbons in the exhaust reduced NO<sub>x</sub> in the lean NO<sub>x</sub> catalyst, and the hydrocarbons and CO were subsequently oxidized in the three-way catalyst. A combination of lean combustion and EGR was presented by

Ratnak *et al* [91]. Using high intake swirl, 95 Research Octane Number (RON) gasoline, and lean combustion with EGR, an indicated thermal efficiency of 48.2% at ~5 bar IMEP was demonstrated.

One challenge for lean combustion as mentioned previously is the combustion stability with increasing  $\lambda$ . This is highlighted in Figure 2-1 (based on report presented by [92]) which shows a plot of indicated thermal efficiency vs. excess air ratio. The range of the data is also shown with error bars. It is evident that when  $\lambda$  increases (especially  $\lambda > 2$ ), the combustion variability increases significantly with high chances of misfire. Ishii *et al* concluded that the cyclic variation in IMEP was affected by initial combustion speed, maximum fuel MFB, and the fraction of fuel which burned later in the expansion stroke [93]. The authors chose 60 degrees after compression TDC as the starting point for determining this 'late burn' fraction. 7% to 20% of the supplied fuel could be burned during this later period. Moreover, when the initial combustion was slow, the maximum MFB was smaller, and the late burn fraction was higher. Takagi *et al* observed a negative correlation between NO<sub>x</sub> emissions and cyclic variability (given by the coefficient of variation (COV) of IMEP) [94]. This observation was attributed to the decreasing mean flame temperature with increasing  $\lambda$ . Furthermore, with increasing  $\lambda$ , the COV of IMEP and HC emissions increased due to higher number of misfires or partial burn cycles.

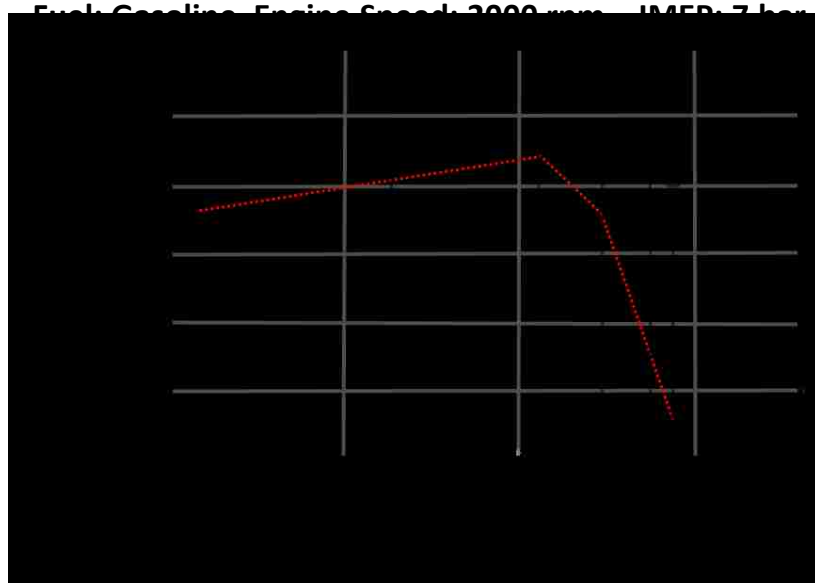


Figure 2-1. Indicated thermal efficiency under super-lean conditions (adapted from [92])

A reason for increasing cyclic variability (or decreasing combustion stability) is the extended combustion duration. Under lean operation, Jung *et al* demonstrated the use of a multi-coil ignition system which increased the effective spark discharge energy to advance the CA5 [95]. By advancing the ignition timing and the CA5, the authors were able to advance the CA50 which consequently shortened the combustion duration (defined by CA10 to CA90). In a related study, the Jung and Iida increased the discharge energy and tumble motion to demonstrate a lean limit of  $\lambda=1.9$  [60]. The duration of spark timing (ST) to CA5 was shortened as well. There was a positive correlation between ST-CA5 duration and the CA10-CA90 duration.

### ■ Modifying Charge Reactivity

In this dissertation, the author employed three methods of modifying charge reactivity – modifying the excess air ratio, fuel, and temperature of the unburned gas.

Since the effects of modifying the excess air ratio have been discussed in the preceding sections, the temperature and the fuel property effects on premixed lean combustion will be elaborated on in the following sub-sections.

### ■ Effect of temperature

The general effect of increasing the inlet charge temperature is extension of the lean limit [96-99]. The lean limit reported in literature depends on how combustion stability is defined by the authors. For instance, Hanabusa *et al* defined the unstable combustion as having a COV of IMEP greater than 6%. [96]. When the in-cylinder temperature was increased by increasing the compression ratio (13.2:1) and the intake temperature (373 K), the lean limit could be extended to  $\lambda \approx 1.9$ . The NO<sub>x</sub> emissions were low even with intake heating at the leanest condition.

Badr *et al* made a parametric study on misfiring and knocking combustion in SI gasoline engines [97]. Again, the increase in intake temperature was expected to extend the lean limit due to increase of the reaction rate. This was the dominant phenomenon. However, increase in the intake temperature also caused an increase in the heat loss which tended to decrease the lean limit, especially at the higher engine speeds tested (more than 1500 rpm) and at intake heating temperatures below 343 K. The effect of intake temperature on a propane fueled engine with a compression ratio of 10:1 is shown in Figure 2-2 (adapted from [97]). The y-axis is the equivalence ratio, which is the reciprocal of excess air ratio  $\lambda$  ( $=1/\phi$ ). Therefore, decreasing equivalence ratio means increasing  $\lambda$ .



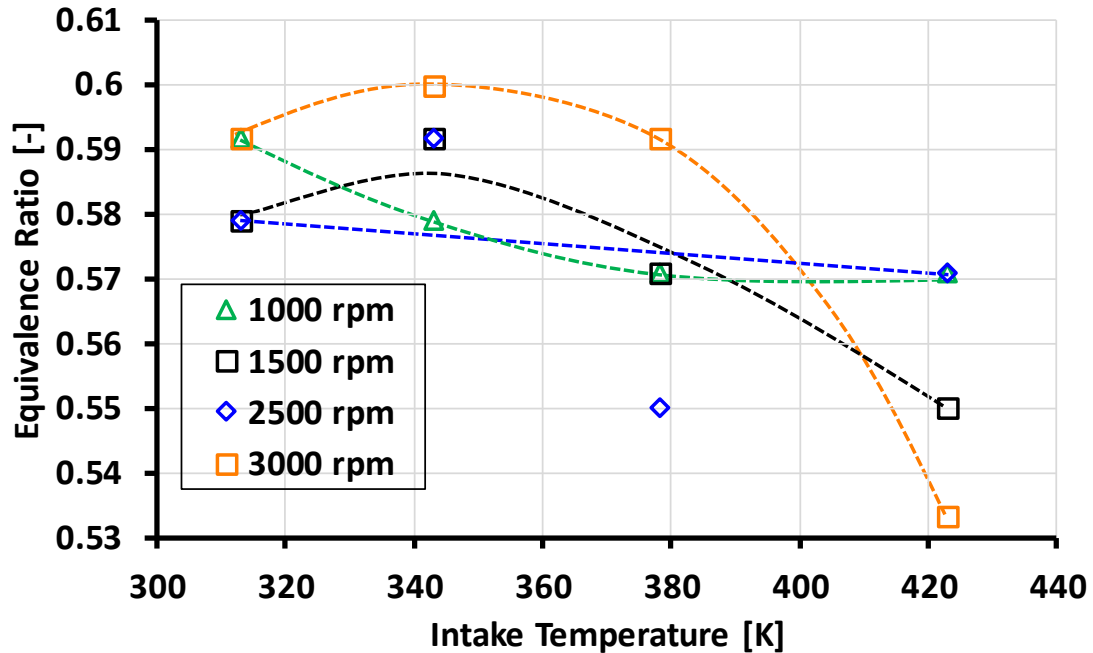


Figure 2-2. Example of effect of  $T_{initial}$  on the misfire lean limit (adapted from [97])

Russ observed that the increase in intake temperature from 302 K to 364 K led to a decrease in the knock limited spark advance (KLSA) [98]. For every 7 K increase in intake temperature, the spark timing had to be retarded by 1 °CA from the KLSA timing. An approximate relation for the effect of intake temperature on the octane number (ON) requirement for the fuel was discussed as well – an increase of 1 ON for the fuel for every 7 K of increase intake temperature to maintain KLSA. Sjöberg *et al* researched the combined effects of intake heating and multi-pulse transient plasma ignition using E85 fuel (blend of 85% ethanol, 15% gasoline by volume) under lean conditions [99]. An increase in the intake temperature of 40 K with additional heating was found to make a significant effect on the lean limit since the spark timing could be retarded. The increase in flame speeds was predicted to be caused by two factors – higher intake charge temperature and the enhanced compression heating of the charge prior to the late spark timing.

## ■ Effect of fuel property

The fuel is expected to be one of the key factors in charge reactivity. The properties of fuels used in this research are listed in Table 2-1. Gaseous fuels – methane, propane, and DME were used for the CVCC tests, and liquid fuels – gasoline, ethanol and DME were used for the engine tests. DME was unique in the sense that it behaved as a gas below 5 bar gauge pressure and as liquid above that pressure. Consequently, it could be used in the chamber as a gaseous fuel and as a liquid fuel in the engine by controlling the fuel pressurization. Some unique properties of the fuels will be highlighted. Methane has a comparatively lower reactivity with respect to the other fuels based on the high octane number and close to zero cetane number. Propane's octane number is in a similar range as gasoline. Gasoline's properties can vary over a wide range since it is a mixture, and subject to seasonal and regional variations. The oxygenated fuels, DME and ethanol have the same molecular weight but based on the differences in their octane and cetane numbers, their reactivities are expected to be dissimilar. DME and ethanol have smaller lower heating values (LHVs) compared to the conventional hydrocarbon fuels such as gasoline. DME has the highest cetane number which indicates its propensity for auto-ignition. Its auto ignition temperature is also the lowest of all the test fuels. Finally, ethanol has the highest latent heat of vaporization, which indicates that evaporation of the fuel droplets would produce significant charge cooling compared to the other liquid test fuels.

Table 2-1. Property of test fuels (sourced from [8-11])

	<b>Methane</b>	<b>Propane</b>	<b>Di-methyl Ether (DME)</b>	<b>Gasoline*</b>	<b>Ethanol</b>
Mol. Wt. [g/mol]	16.043	44.09	46.07	~100	46.07
Boiling Point [°C]	-161.5	-42	-25.1	30-190	78.2
Latent heat of vapor. [kJ/kg]	512	426	464	305	920
Vapor pressure @25 °C [bar]	621	9.3	6.1	0.28	0.079
Auto-ignition temp. [°C]	537	457	235	280-486	363
Research Octane number [-]	>127	96	<20	90-100	109
Cetane Number [-]	~0	~5	55-60	~16	~5-8
Lower Heating Value [MJ/kg]	50	46.36	28.43	42.5	26.7

\* Values for comparison

Some background information on ethanol and DME lean combustion will be presented here since they were used in the engine tests. Aleiferis *et al* made a comprehensive comparison of flame propagation between gasoline, iso-octane, methane, ethanol, and butanol fuels in an optical engine under  $\lambda=1.0/1.2$  [100]. At  $\lambda=1.0$ , they observed that the flame growth was fastest for ethanol (~10-13 m/s at 1500 rpm), followed by butanol, gasoline and iso-octane. Methane's initial flame growth was slow, but the overall flame development was completed within a similar period to the alcohol fuels (ethanol and butanol). At  $\lambda=1.2$ , the trends remained same. The flame stretch was also estimated, and the order was as follows – methane, ethanol, butanol, iso-octane, and gasoline. Faster flame speeds were observed for fuels which had lower Markstein numbers and vice-versa. Moxey *et al* reported similar results in their comparison of gasoline, iso-octane, ethanol and E10 (blend of 90% ethanol and 10% iso-octane by volume) [101]. Ethanol flame propagation was the fastest, followed by gasoline and iso-octane. E10 was the slowest which indicated

that blending ethanol did not provide any benefit in terms of increasing flame propagation speed. The faster burning of ethanol was attributed to the marginally higher laminar flame speed which was deemed to be the more dominant in the initial flame development. Moreover, for all fuels, with increasing flame size, the wrinkled depth of the flame increased as well [102]. In a separate study, the detachment of the flame centroid from the spark plug was also studied [103]. The displacement speed of this centroid was of the order of the velocity field around the plug during ignition timing ( $\sim 3$  m/s for this case). E85 (blend of 85% ethanol and 15% gasoline by volume) had a higher displacement speed than gasoline. However, in this study [103] and others for example [104], owing to its composition, gasoline may have a flame speed greater than ethanol under certain conditions. Tests by Costa *et al* using hydrous ethanol suggested that the lean limit for their setup was  $\lambda=1.4$  [105]. The combustion was deemed unstable when COV of IMEP exceeded 3%. With increasing  $\lambda$ , the NO<sub>x</sub>, HC, and CO emissions decreased till the lean limit was reached. Arcoumanis *et al* made a review of the potential of DME to be used as an alternative for diesel in compression ignition (CI) engines [106]. The main feature of DME is its high cetane number which allows it to auto-ignite easily. DME can be derived from sustainable means and is non-toxic [106-107]. Since DME is mostly seen as a fuel for CI engines, according to the author's search, there is very limited research on SI combustion. Shi *et al* for instance, studied the effects of spark timing on combustion and emission of gasoline-DME blends under lean conditions in an SI engine [108]. DME combustion was characterized by the low temperature reactions which shortened the CA<sub>10</sub>-CA<sub>90</sub> duration. It was possible to reduce the NO<sub>x</sub> and HC emissions by suitably adjusting the ignition timing. Ying *et al* made a comparison of port injected (PFI) and direct injected (DI) DME

under HCCI operation [109]. Engine operation under a wide range of load (0.5 to 8 bar brake mean effective pressure) was demonstrated. The peak pressure and peak heat release rate were lower for HCCI-DI compared to those for HCCI-PFI. With increasing DI fuel quantity, and decreasing PFI fuel quantity, there were three main observations. First, the start of the second stage heat release was retarded (first stage was a result of low temperature reactions). Second, the NO<sub>x</sub> increased at low loads and decreased at high loads. Third, the HC and CO emissions decreased. In a numerical analysis with experimental validation, Kong concluded that the low temperature heat release of DME drove the auto-ignition of the fuel [110].

In the context of this research, DME HCCI is implemented to contrast the high reactivity of DME fuel with SI combustion of lower reactivity fuels such as ethanol and gasoline. Furthermore, DME HCCI combustion may not need intake heating to increase the lean limit unlike gasoline and ethanol due to its higher reactivity.

## **RESEARCH TOOLS AND METHODS**

In this chapter, the author describes the tools and methods used for the empirical research. There were two main research platforms used – a constant volume combustion chamber with optical access and shadowgraph imaging, and a single cylinder research engine. Additionally, the author developed an ion current detection system for use on both the research platforms. A shock tube setup was also used to simulate higher flame speeds. The following sections describe these setups and the methods associated with processing the data from each setup.

### **Constant Volume Combustion Chamber (CVCC)**

The ion signal validation tests were performed on a constant volume combustion chamber setup with optical access (Figure 3-1) which will hereafter be referred to as CVCC. A second purpose of the CVCC was to study the flame propagation for the air-fuel mixtures of the three gaseous test fuels – methane, propane and DME. The working volume of the CVCC was 2.6 liters with optical access of 80 mm diameter. The inner structure of the vessel was cylindrical with a diameter of 150 mm and length of 115 mm. The test fuel and air were supplied to an Environics 4040 gas divider which provided precise control of the excess air ratio of the charge. The charge was then pressurized using a diaphragm pump and routed into the CVCC. Charge filling and exhaust were performed through 3/8-inch diameter ports. The chamber pressure was recorded using a flush mounted Swagelok S Model dynamic pressure sensor (Model PTI-S-NG5000-22AQ) with a range of 0-344.7 bar (0-5000 psi). High speed shadowgraph imaging of the flame propagation was performed through a system consisting of a white LED light, two parabolic mirrors, and a Vision Research Phantom V7.3 high speed camera with Nikon 105 mm f/2.8 lens.

The spark discharge was provided through an ignition power drive consisting of an ignition coil controlled by an insulated gate bipolar transistor (IGBT) chip. This chip was driven by an in-house developed electronic driver circuit. The ignition command was generated by a National Instruments (NI) real-time (RT) and field-programmable gate array (FPGA) setup. This control signal was isolated from the rest of the system by means of optical isolation. The secondary cable from the coil was passed through a Pearson 411 wide-band current monitor probe to measure the discharge current. All signals were measured with Picoscope 4824 digital oscilloscope. Detailed specifications of the oscilloscopes used in this research are provided in Appendix-A. The multi-pole spark plug developed at the Clean Combustion Engine Laboratory was installed on the top of the chamber. Details of this invention can be found in [111].

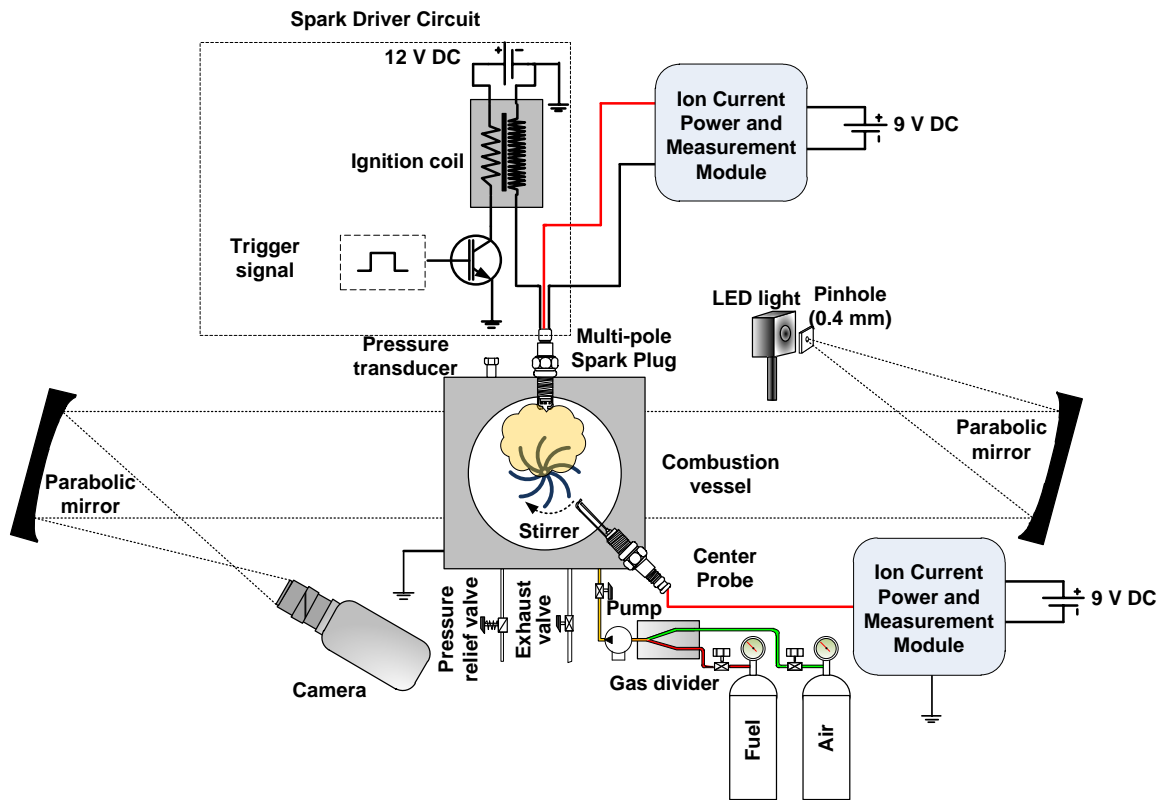


Figure 3-1. Experimental setup of CVCC

The multi-pole spark plug in the given configuration consisted of three independent electrodes as show in Figure 3-2. The spark plug thread was specified as M14 – metric thread of 14 mm diameter with 1.25 mm pitch. One electrode was connected to the spark discharge circuit for igniting the mixture. The spark gap was 0.86 mm. The remaining two were used for ion current detection. An second ion probe was installed from the bottom of the chamber and this probe extended into the optical viewport. This probe was a modified non-resistive spark plug with extended electrodes. In this way, ion current detection was enabled at two locations – in the vicinity of the spark plug, and in the central region of the CVCC.



Figure 3-2. Multi-pole spark plug of 14 mm metric thread size

### ■ Creation of air motion

An additional feature of the chamber was the ability to stir the air-fuel charge in the CVCC. This was done by driving a 3.0-inch diameter, 10-blade fan installed in the chamber. The other end of the fan shaft was connected to a SDP/SI magnetic coupling (S50DCM-24H08). The entire assembly was mounted on two high speed ball bearings (~5000 rpm). The magnetic coupling was used to avoid the complexities associated with sealing a rotating shaft for high pressure. The fan shaft was driven by the driver shaft through the other half of the magnetic coupling. The driver shaft was connected to a Ryobi router motor



(model R163G). The speed of the router motor was controlled by a rheostat-based fan speed controller. To ensure consistency between the data points, the driver shaft rotational speed was monitored. A rotor magnet was installed on the shaft and the passage of the magnetic pole over each rotation of the shaft was picked up by a Hall Effect sensor (Littelfuse Inc. 55110-3M-03-A). The fan shaft was mounted perpendicular to the optical path. An image of this installation is shown in Figure 3-3.



Figure 3-3. Motor for driving fan inside CVCC (Inset: Speed sensor)

The torque transmission ability of the magnetic coupling was limited to 1 Nm. Based on this limitation, the fan was tested at different speeds and charge pressures in the CVCC. An initial pressure of 4 bar gauge was chosen for the CVCC tests since this was close to the cylinder pressure in the ignition timing window for the engine test setup. At this pressure, a fan speed of 1200 rpm was found to be stable. The magnetic coupling was also able to maintain a connection in order to keep driving the fan in the chamber. This speed of 1200 rpm is lower than most of the fan speeds reported in literature for fan stirred CVCCs. Based on an estimation given in [48], a fan running at 20 Hz ( $f$ ) frequency (1200 rpm) can generate turbulence with a fluctuating velocity of  $\sim 0.92$  m/s. Consequently, any

turbulence, if generated, may be weak. The author did not have the means to measure and verify if any turbulence was produced. Therefore, future references to the fan use will be termed as ‘charge motion’.

### ■ Estimation of flame area

The shadowgraph image frames obtained from the high-speed camera are used to determine the flame area over time. The Phantom camera records a video in its proprietary format – cine. Each frame of the video is converted to grayscale bitmap images. The images are then processed into binary images using a MATLAB code originally developed in the author’s laboratory. The flame area is represented by white coloured pixels while the remainder of the image is converted to black coloured pixels (Figure 3-4). This judgement is made for each pixel based on a brightness threshold value. Through calibration, the area of each pixel is determined. This area is multiplied by the number of white pixels to estimate the flame area. The camera settings are summarized in Table 3-1.

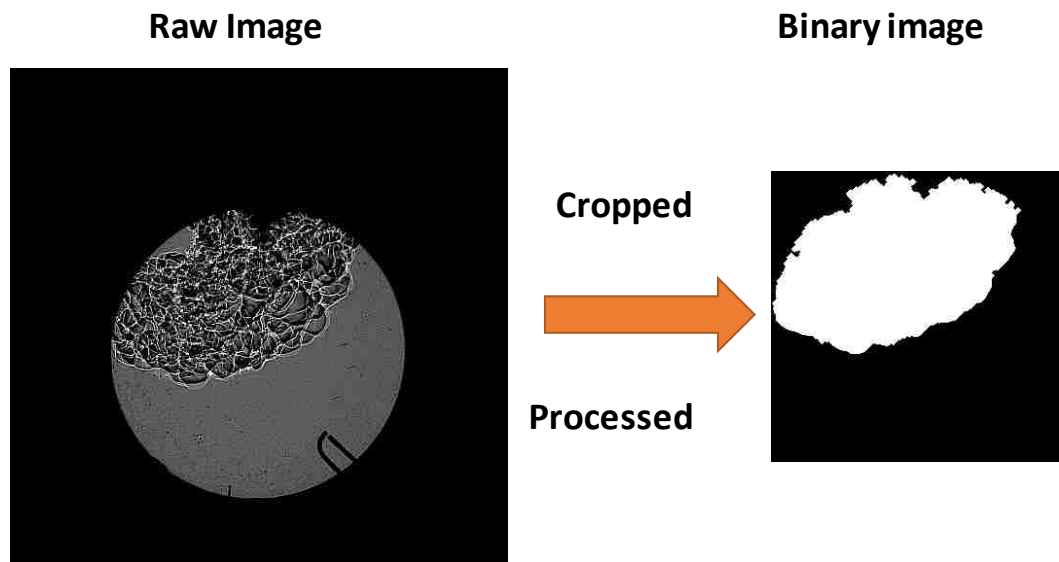


Figure 3-4. Estimating flame area using binary images

Table 3-1. Phantom V7.3 camera settings

<b>Sample rate</b>	11527 frames per second
<b>Exposure</b>	7 $\mu$ s
<b>Resolution</b>	512 X 512 pixels
<b>Trigger</b>	External, spark command

## ■ Research Engine Platform

The research engine platform was based around a Yanmar NFD170 single cylinder, four-stroke, horizontal configuration, industrial grade, diesel engine. Specifications of the engine are listed in Table 3-2. This engine was heavily modified for spark ignition research. The ignition, fuel management, and air management systems were controlled independently. A schematic overview of the research engine platform is shown in Figure 3-8. The original diesel injector was replaced with a spark ignition system. The ignition power drive was identical to the one used for the CVCC tests. Again, the multi-pole spark plug was used for spark discharge as well as ion current measurement near the spark discharge location. Ion current signal from this location will hereafter be termed as the ‘plug probe’. An additional ion probe was installed on the cylinder head and was based on a modified M8 spark plug. This probe will hereafter be referred to as the ‘auxiliary probe’. The location of the ion current probes and the pressure transducer are shown in Figure 3-5 and Figure 3-6. The distance between the two ion probe locations was ~25.6 mm. Ion current signals were measured using a Picoscope 4425 oscilloscope.

A water-cooled Kistler pressure transducer (model 6043A60) was installed on the cylinder head and coupled with a Kistler 5010B charge amplifier. The pressure data was

synchronized at a resolution of 0.1 °CA through an optical shaft encoder (Gurley Precision Instruments) mounted on the crankshaft. The manifold pressure was measured using a Kistler piezo-resistive type absolute pressure transducer (model 4075A10). In-cylinder and manifold pressure were recorded for 200 consecutive cycles for each data point. An auxiliary liquid cooling system (FEV Coolant Conditioning Unit) maintained the engine coolant temperature at 80 °C. The cooling unit was also used to preheat the engine before the start of the tests. An auxiliary lubrication system circulated the engine oil under controlled pressure and temperature. The stock piston was replaced with a customized piston which reduced the stock compression ratio (17.8:1) to 9.2:1. The engine was coupled to a 40 horsepower General Electric direct current (DC) dynamometer (model 26G215) which was operated through a Dyne Systems Dyn-Loc IV digital dynamometer controller.

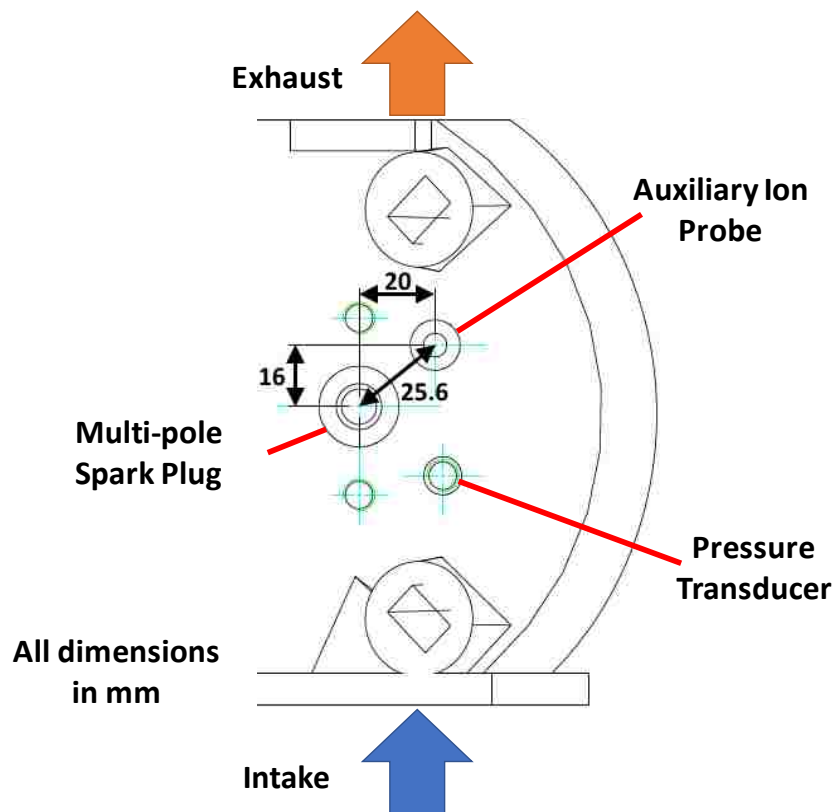


Figure 3-5. Location of ion current probes on cylinder head

Given the engine load level and the air flow rate requirements for this research, no intake boost was necessary. All tests were carried out under normally aspirated intake conditions. A Roots (5M175) mass air flow meter was installed just before the intake surge tank to measure the intake charge quantity. This engine was also equipped with an EGR loop though use of EGR was outside the scope of this research. The EGR loop consisted of an EGR cooler (using municipal water) and an EGR flow control valve.

A throttle valve, and a solenoid four-hole port fuel injector were installed upstream of the intake valve in the intake manifold, and an exhaust oxygen sensor was installed on the exhaust manifold just downstream of the exhaust valve. The main controls for the intake charge dilution were the throttle opening (to set the mass air flow (MAF) rate of the engine), and the opening duration of the solenoid fuel injector. Gasoline (pump octane 89) and anhydrous ethanol were supplied to the engine at 4 bar gauge injection pressure through an in-house developed fuel injection system. Gasoline and ethanol fuel flow rates were measured with an Ono Sokki FP-213 flow meter. Since DME is a gas below 5 bar gauge pressure and normal temperature, it was handled differently. DME was filled into a day tank from the main storage tank. This DME in the day tank was then pressurized to 7 bar gauge using nitrogen gas. To further ensure that DME remains a liquid in the fuel line, a section of the fuel line was kept immersed into an ice bath upstream of the injector to lower DME's temperature.

There were two additional features added to the intake air path of the engine. The first was the heater coil downstream of the throttle valve which was used to increase the temperature of the incoming air. This heater was controlled by an Omega CN2110 series temperature controller which used feedback from a K-type thermocouple inserted into the intake flow

downstream of the heater. The second feature was a helical insert (Figure 3-7) installed downstream of the heater and was used to enhance the intake flow field. Details of the development work related to this insert can be found in [29]. The insert was found to improve combustion stability under lean conditions and was therefore used for majority of this research.

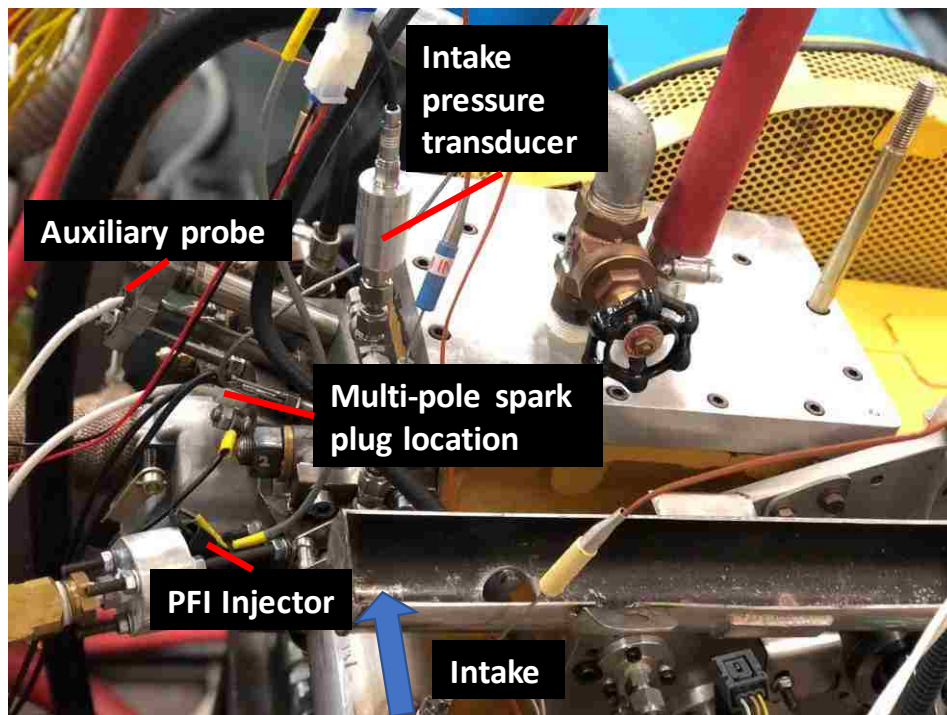


Figure 3-6. Image of cylinder head



Figure 3-7. Helical insert (adapted from [29])

Certain engine exhaust species were measured using different types of gas analyzers manufactured by California Analytical Instruments (CAI). Each analyzer was based on a certain detection technology. Oxygen (O<sub>2</sub>) was measured with a paramagnetic oxygen detector. Carbon monoxide and carbon dioxide were measured with a non-dispersive infrared (NDIR) analyzer. NO<sub>x</sub> was measured with a chemiluminescence detector. Hydrocarbon was measured with a flame ionization detector. Detailed specifications of the analyzers, including the measurement uncertainties, are provided in Appendix-A.

The critical data acquisition and control applications were performed using National Instruments (NI) RT-FPGA hardware. An array of sensors and actuators were integrated using the NI data acquisition and control system. Windows-based PC systems were used for overall test control and data management. More details of the hardware can be found in Appendix A and in [112].

Table 3-2: Yanmar NFD-170 specifications

Displacement volume	857 cm <sup>3</sup>
Bore	102 mm
Stroke	105 mm
Connecting rod length	165 mm
Compression ratio	9.2:1
Engine Speed	1300 rpm
Injection system	Port injection
Injection pressure	4 bar gauge (gasoline/ethanol) 7 bar gauge (DME)
Ignition system	Spark ignition

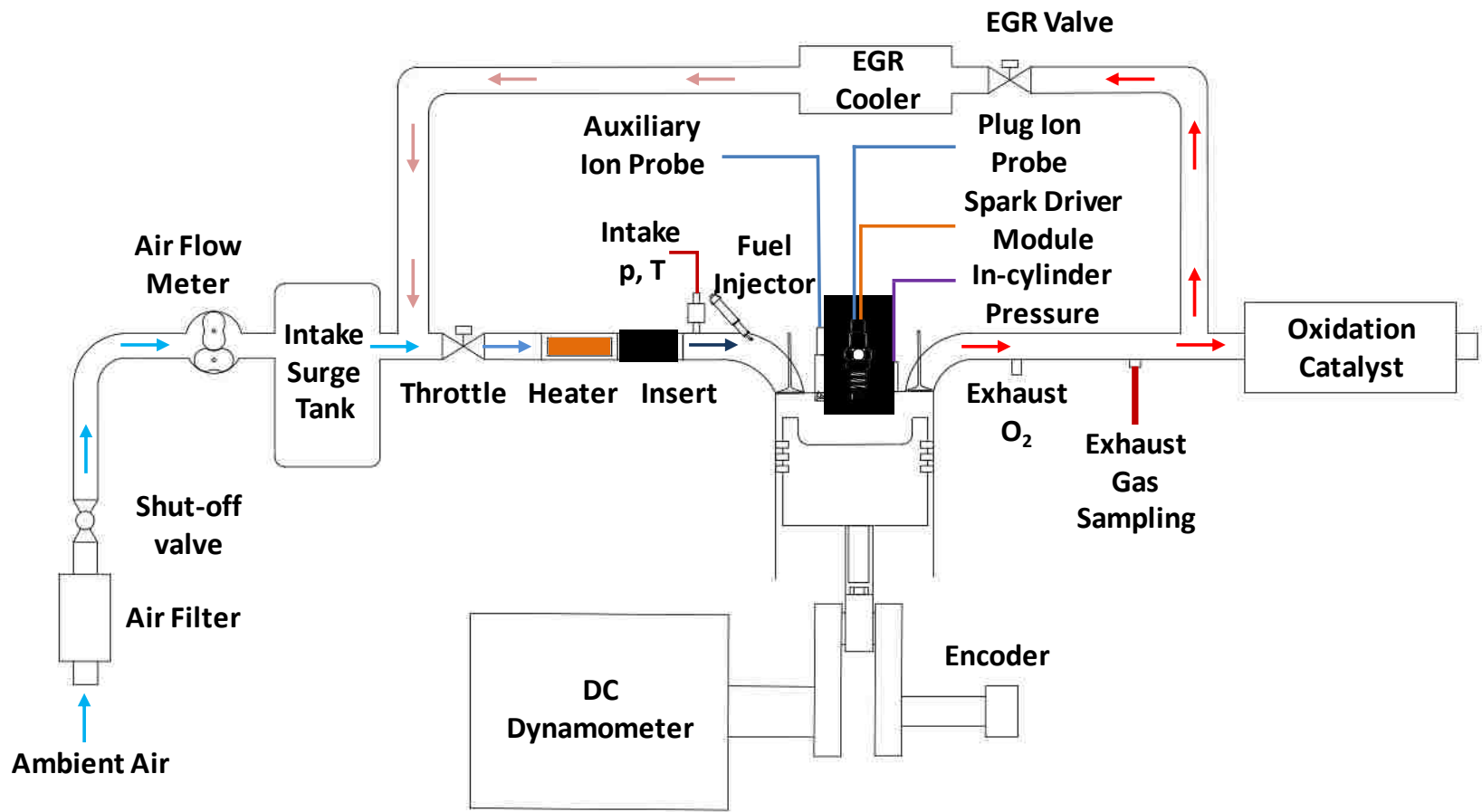


Figure 3-8: Schematic setup of research engine platform



## ■ Ion Current Measurement System

The ion current measurement system was developed by the author for detecting combustion and estimating flame propagation speeds. The concept of ion current measurement in IC engines is well-established and has been in use in research as well as product domains for more than two decades (Chapter 1). The ion current measurement system developed here therefore draws from published research. The author's own experience in improving the ion current signal quality has been incorporated in the measurement circuit as well.

One of the main drawbacks of using a conventional spark plug for ion current measurement in an SI engine is the inability to measure the ion current during the breakdown and the glow phase of the spark discharge. The use of the multi-pole plug overcomes this challenge since one central electrode can be used for the breakdown, and the remaining two can be used for ion current measurement near the spark kernel. The author has published a comparison previously between using conventional spark plug and a multi-pole plug for ion current detection [75]. As stated previously, the research presented in this dissertation incorporates a multi-pole plug (plug probe) as well as a conventional plug (central/auxiliary probe) for ion current measurement at two locations in either of the experimental setups.

The ion current measurement circuit is shown in Figure 3-9 for the plug probe and the auxiliary probe. An input voltage of 9 V from a PP3 alkaline cell was provided to an isolated negative biased DC-DC converter (XP Power EMCO A05N-12). The DC-DC converter amplified the voltage to 600 V. A 1000 V diode was used to prevent current from the system from flowing back into the DC-DC converter. A 0.5  $\mu$ F capacitor was used to provide a stable voltage supply. For the plug probe, each of the central electrodes acted

as one of the ends of the gap which detected ions between themselves. Therefore, the system was electrically isolated not just from the spark breakdown circuit but from the engine ground as well.

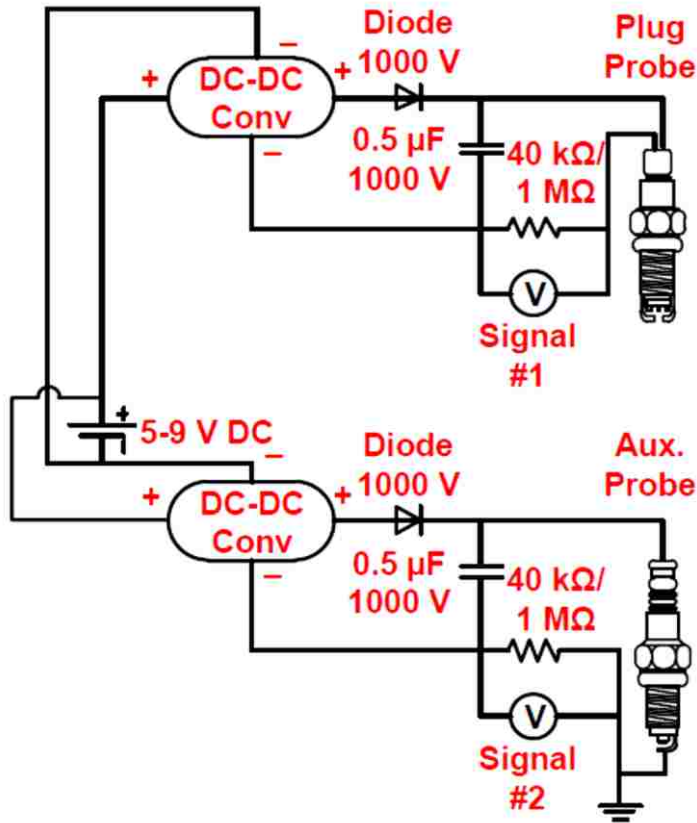


Figure 3-9: Ion current circuit used for this research

For the auxiliary probe, one end of the probe was the common ground of the engine as the modified spark plug was installed on the cylinder head. This was the main reason why the negatively biased DC-DC converter had to be used so that current from the ground flowed into the measurement resistor. When ionized species completed the circuit, the current passed through the measurement resistor. The measurement resistor was 40 kΩ for chamber tests. For engine tests, a higher resistance of 1 MΩ was used since it was the best compromise in terms of signal detection and noise from the circuit. Each of the plug probe

and the auxiliary probe circuits could be operated as independent circuits with their own power supply.

An example of the ion signal profiles from the engine are shown in Figure 3-10 along with the in-cylinder pressure trace for reference. After the ignition, the ion signal is expected to constitute of the flame front (propagation) phase and the post flame phase [66]. During the post flame phase, the ion signal can also be high due to the presence of ions produced due to thermal ionization. The locations of the first peak of the plug probe signal and the first peak of the auxiliary probe signal are determined through post-processing (Appendix C). The period between these two peaks is used to calculate the parameter  $T_{ion\_diff}$ . This can be regarded as a rough estimation of the time it takes for the flame to propagate between the two probe locations.

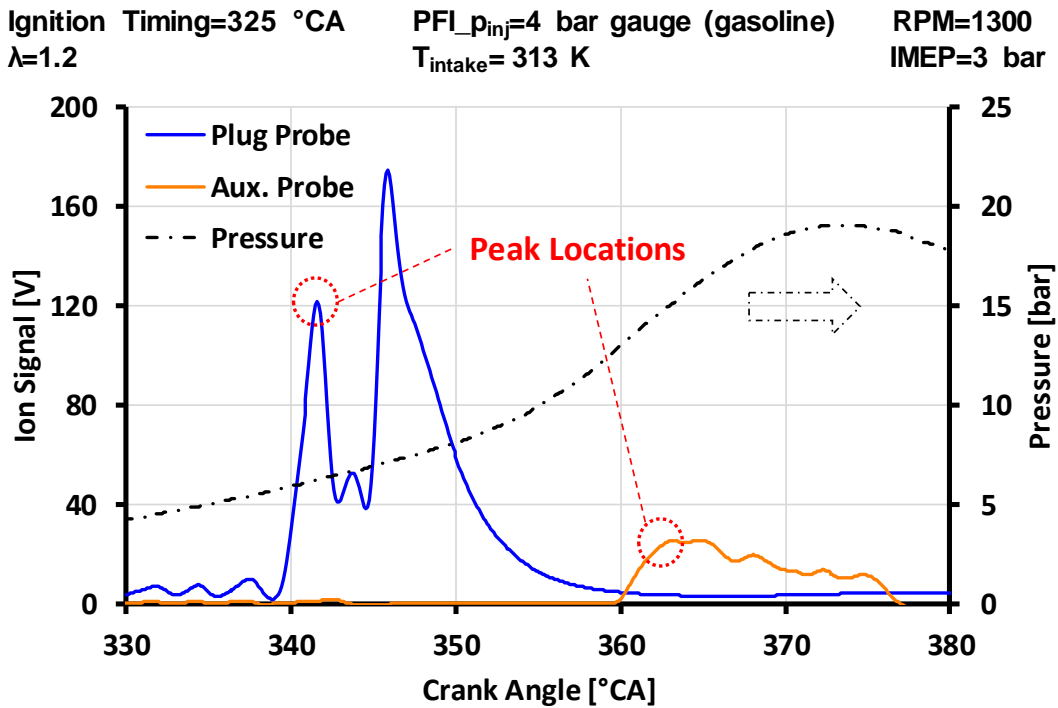


Figure 3-10. Typical engine ion current signal profiles and cylinder pressure

## ■ Shock Tube Setup

The shock tube was used to generate a shockwave which could potentially create conditions for flames propagating at speeds higher than what may be achieved in the CVCC. The shock tube schematic is shown in Figure 3-11. It consisted of a 480 mm long driver section and a 360 mm driven section which was open to the atmosphere. The material of construction of the shock tube was alloy steel (SAE 4340) with an inner diameter of 23.8 mm and a wall thickness of 12.5 mm. At this relatively low internal diameter, a major limitation of this shock tube is that the boundary layer effects may cause significant deviation from ideal shock tube theory [116]. The diaphragm consisted of heavy duty aluminum foil with a thickness of ~0.048 mm. Instrumentation consisted of two piezoresistive pressure transducers (Kistler 4075A10) and two ion current probes – one of each in the driver and the driven section. The ion current probes were modified K-type thermocouples. The ion current overall circuit layout was identical to the previously described one (Figure 3-9). The bias voltage was 250 VDC and the measurement resistance was 1 M $\Omega$ .

The air-methane charge was filled into the driver section at an initial pressure of 1.5/1.75/2.0 bar. A spark discharge was used to ignite the mixture in the driver section. When the charge ignited, the pressure in the driver section increased causing the diaphragm to burst. The burst pressure ratio varied between ~3-4 bar for the given test conditions. The burst of the diaphragm caused a shockwave to propagate in the driven section followed by the gas interface. Since the fuel in the driver section may not have been completely consumed, a flame may propagate from the driver section into the driven section which could be detected by the ion current probes.

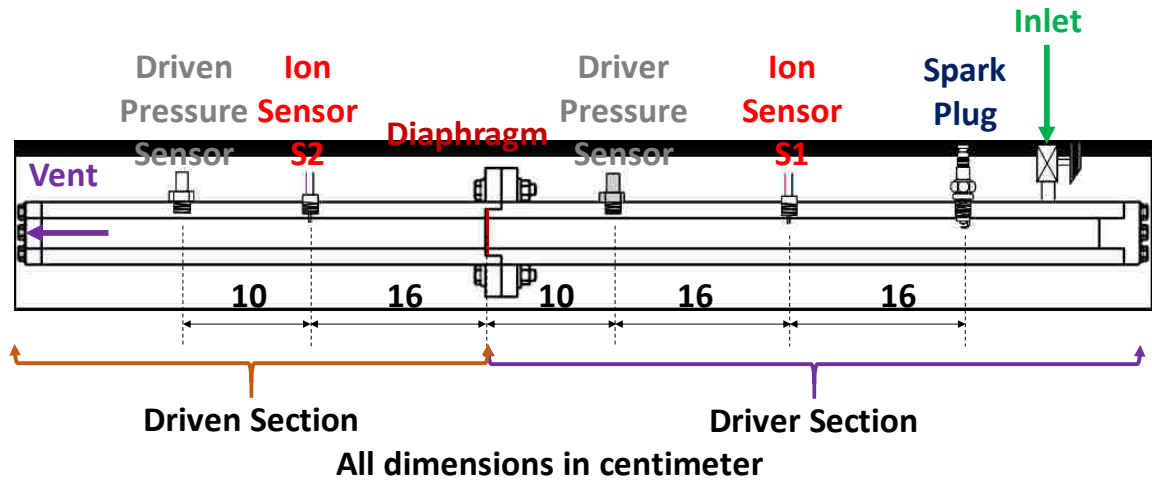


Figure 3-11. Shock tube schematic

## ■■■■■ COMBUSTION CHAMBER FLAME PROPAGATION STUDIES

In this chapter, the author presents the results for tests conducted in a constant volume combustion chamber (CVCC) with optical access. High speed imaging and concurrent measurement of ion current are carried out to observe the flame propagation under different excess air ratios with and without charge motion. The first section describes the validation of the ion current measurement system through high speed imaging. The second and third sections present analyses of the flame images, pressure and the ion current signals. The fourth section describes an investigation on the effect of directed flow on the spark gap. The final section presents a study on higher speed methane-air flames using a shock tube.

### ■■■ Validation of Ion Current Signal in CVCC

The validation of the ion current signal is carried out using high speed shadowgraph imaging in a CVCC. The purpose of these tests is to verify if the ion current signal corresponds to the flame front propagation in the chamber. As explained in Chapter 3, two locations of ion current measurements are used which are visible through the optical windows. The first location is within the perimeter of the multi-pole spark plug and the spark gap can be seen in the images (right side of the plug). The second location is closer to the center of the chamber. The first location captures the ion signal at the initial stage of the flame kernel, while the second location measures the ion signal when the flame is further developed.

Three conditions are discussed in this section for purpose of demonstrating the wide applicability of ion current measurement for different test fuels at various excess air ratios. The ion signals for methane fuel at  $\lambda$  of 1.0, and propane at 1.4 are shown in Figure 4-1

and Figure 4-2 respectively. The ion signals for DME at  $\lambda$  of 1.6 are shown in Figure 4-3. The corresponding secondary current profile is also shown in the figures. Since the coil charging duration is 5 ms, the spark breakdown occurs at around the 5 ms mark from the trigger (at 0 ms) for all cases discussed in this section and Sections 4.2 and 4.3.

For all cases, the ion signal profile corresponds to the physical phenomena of the flame propagation. For instance, in Figure 4-1, the first rise in the multi-pole ion current probe signal is observed at the 7 ms mark, which is within the glow phase of the spark discharge. Ion current measurement during the glow phase is typically not possible when a conventional spark plug is used for spark discharge as well as ion current probing. The ion signal reaches a peak at approximately 8.8 ms at which point, the flame is still located within the measurement volume of the multi-pole plug. Subsequently, the ion current magnitude reduces and remains constant till the 20 ms mark. This could be the result of the thermal ionization since the flame front has already passed this location. Finally, when the flame front reaches the central probe at 45 ms, there is a rise in the ion signal. Subsequently, the ion current measurement system is validated for different equivalence ratios and fuels. The ion current signal profiles of propane for instance at  $\lambda=1.4$  (Figure 4-2) also directly correlate to the flame propagation though the magnitudes and the time instances are different. Since the multi-pole plug is non-resistive, some effects of the noise from the spark discharge are observed on the ion signals although the multi-pole probe is isolated from the common ground. This is especially important for  $\lambda=1.6$  cases when the ion concentration and combustion temperature would be expected to be lowest. The result for DME at  $\lambda=1.6$  is shown in Figure 4-3. The flame front propagation is drastically slower than the methane  $\lambda=1.0$  case. The ion current magnitude is also lower.

Medium: Air-Methane  
 $\lambda=1.0$   
 $p_{\text{initial}} = 4 \text{ bar absolute}$   
 $T_{\text{initial}} = 300 \text{ K}$   
 $V_{\text{ion}} = 600 \text{ V}$   
 $R_{\text{ion}} = 40 \text{ k}\Omega$

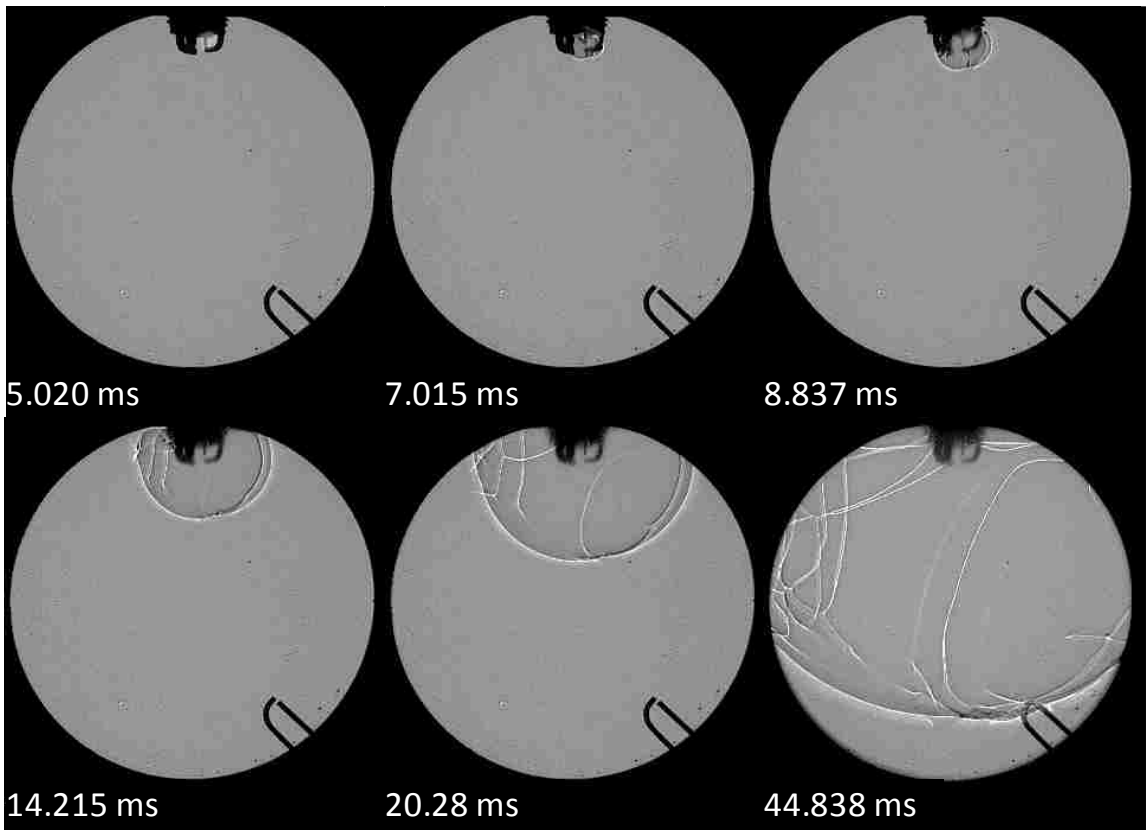
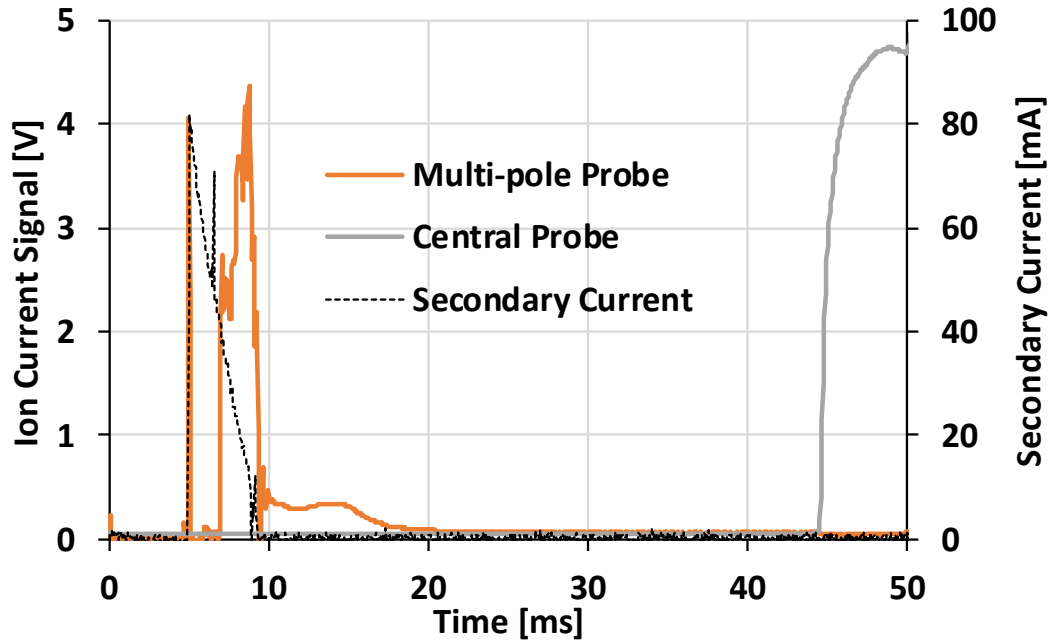


Figure 4-1. Ion current signal validation at  $\lambda=1.0$  with methane as fuel



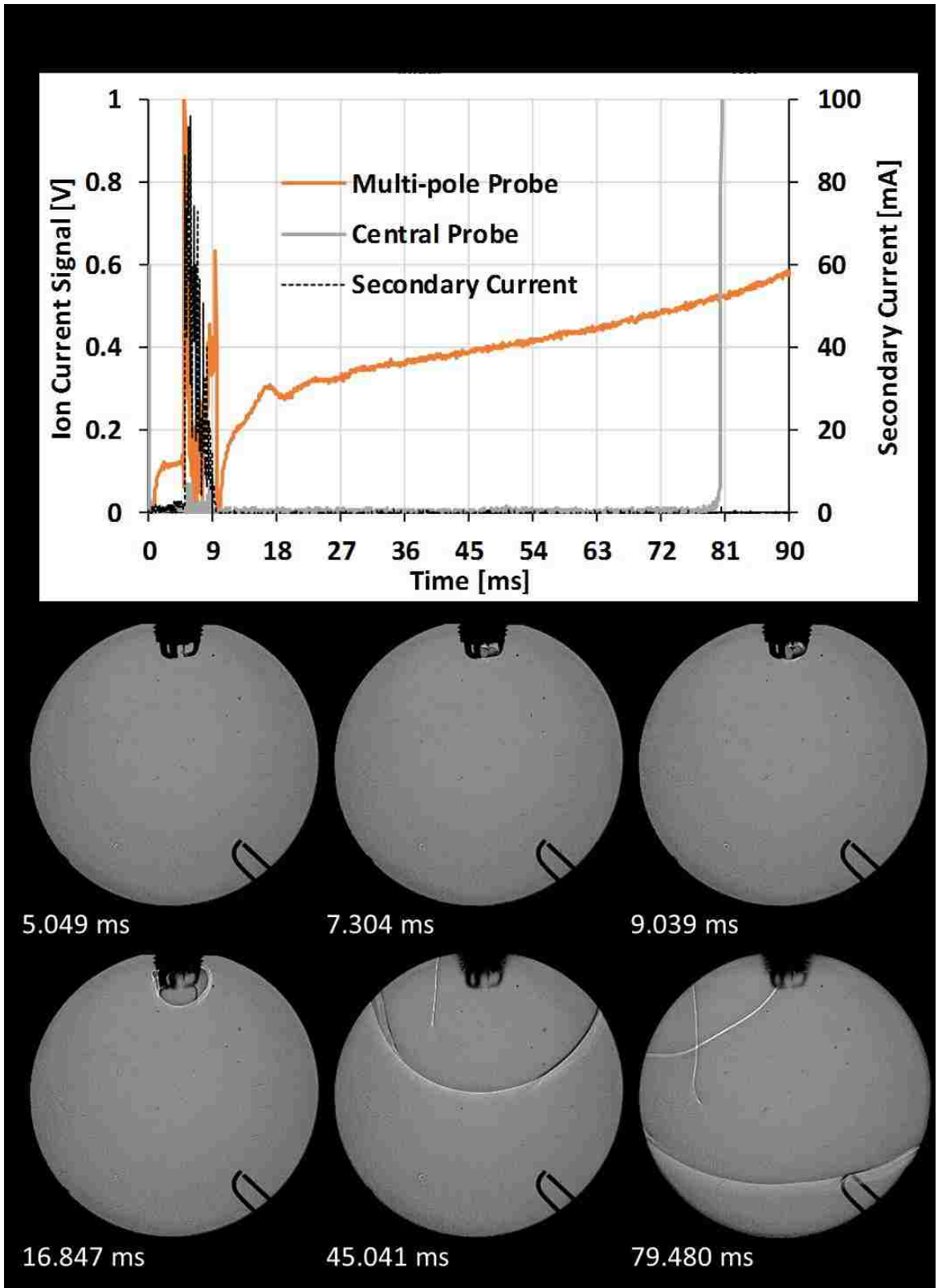


Figure 4-2. Ion current signal validation at  $\lambda=1.4$  with propane as fuel

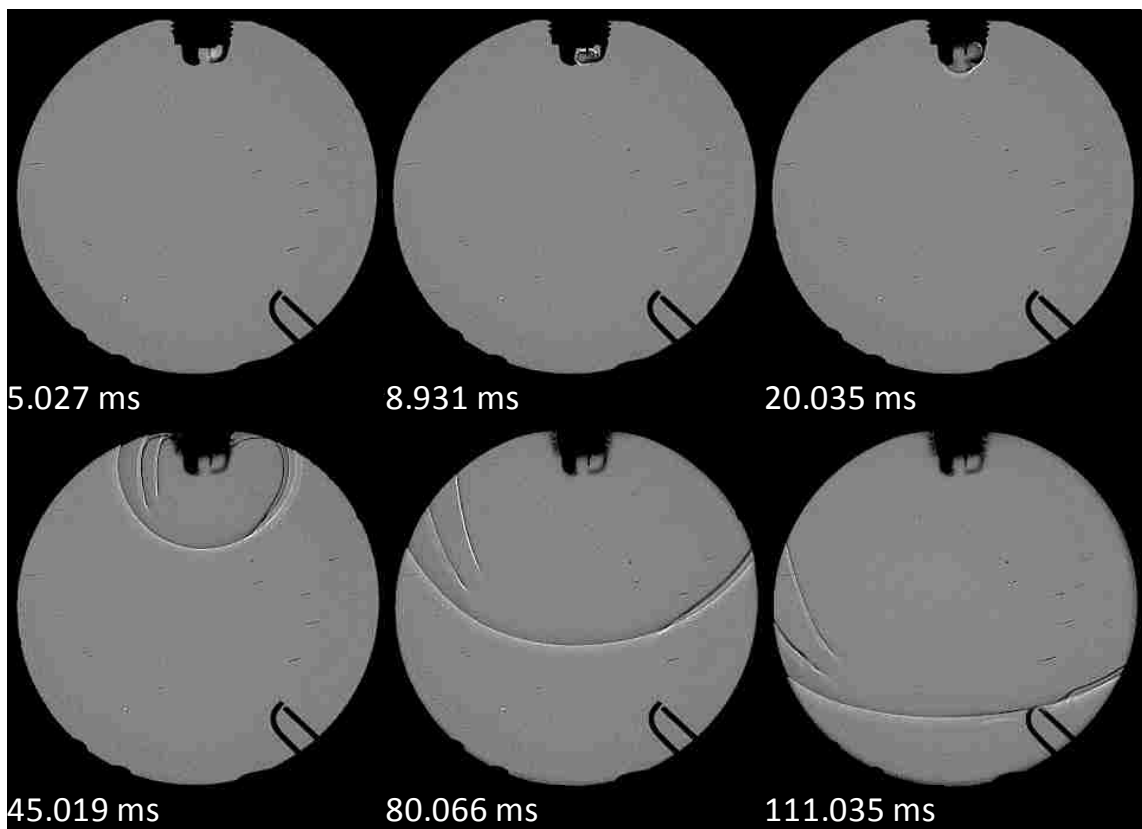
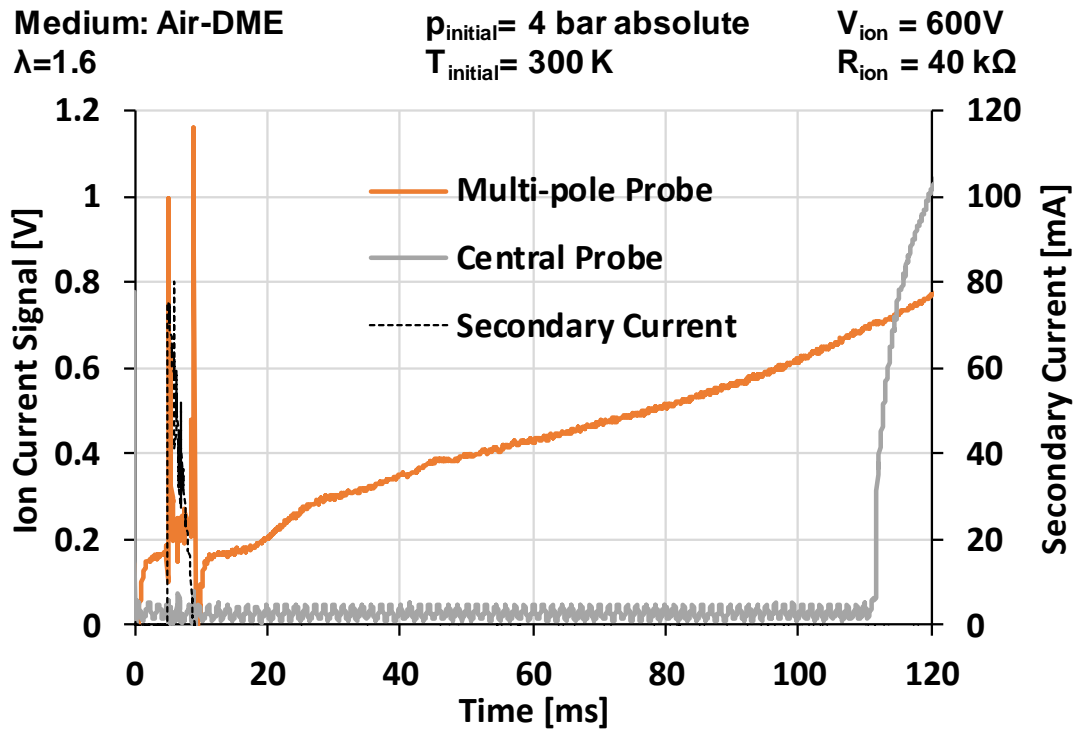


Figure 4-3. Ion current signal validation at  $\lambda=1.6$  with DME as fuel

## ■ Flame Propagation Study in Optical Chamber

In this section, the author describes the results of combustion tests performed in the CVCC using three fuels – methane, propane and DME at different excess air ratios. In order to study the effect of flow on the combustion and the flame propagation, the air-fuel mixture (hereafter referred to as charge) inside the chamber is stirred with a fan rotating at a constant speed (details of experimental setup explained in Chapter 3). Three types of data are analyzed – image frames from high speed shadowgraph imaging, pressure, and ion current. This section is further divided into two subsections. In the first subsection, the individual results of the three fuels from the lowest ( $\lambda=1.0$ ) to the highest ( $\lambda=1.4/1.6$ ) excess air ratios are presented. In the second subsection, a comparative analysis of the three fuels is provided. Each data point is an average of up to three combustion events.

### ■ Flame imaging analysis

The shadowgraph images are processed based on the method described in Chapter 3. Figure 4-4 shows an example of images at four instances of time from the rising edge of the spark trigger signal namely 5, 10, 15, and 20 ms for methane at  $\lambda=1.0$ . After the spark breakdown at the ~5 ms mark, the flame propagates outwardly from the spark plug symmetrically in the view plane when there is no charge motion – a typically laminar flame front. With charge motion, flame front and flame propagation are markedly different. The flame front is highly corrugated typical of turbulent flames, which increases the overall surface area, leading to faster flame propagation. When compared to the quiescent frames at the same time instance, the flame area is larger. After analysing the frame by frame data for different  $\lambda$ , the flame areas can be calculated as a function of time (Figure 4-5).

Medium: Air-Methane  
 $\lambda=1.0$

Fan Speed=1200 rpm

$p_{\text{initial}}= 4 \text{ bar absolute}$   
 $T_{\text{initial}}= 300 \text{ K}$

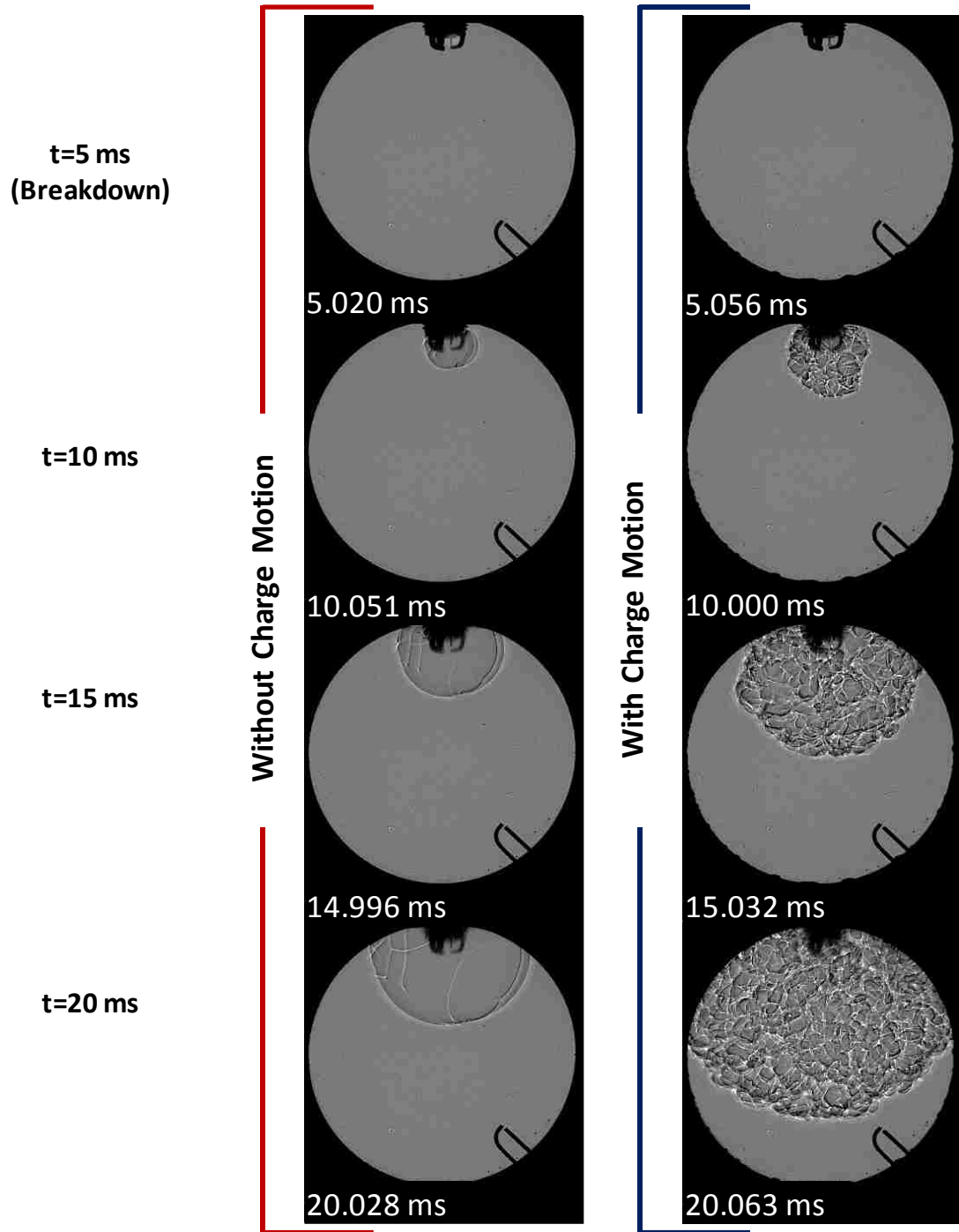


Figure 4-4. Image frames from methane combustion at  $\lambda=1.0$

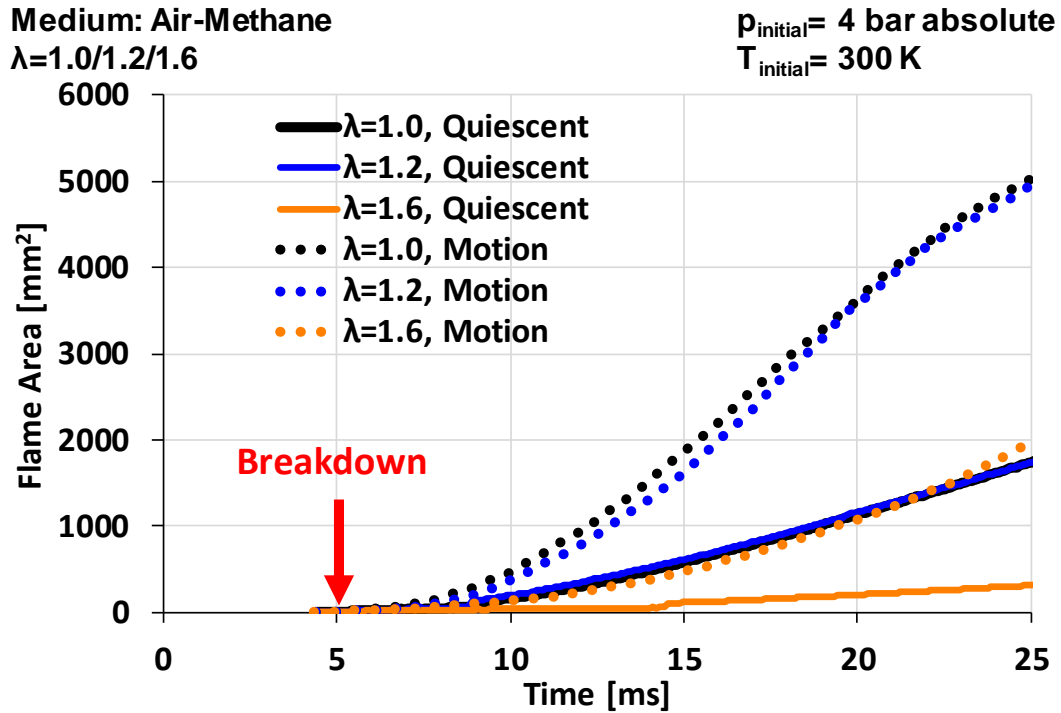


Figure 4-5. Flame area calculation of methane-air flames at varying  $\lambda$

The flame area can be correlated to the speed of combustion since it estimates the burned gas area. The results from this study cannot be directly correlated to classical literature results since the flame development in this chamber is not spherical, and other factors such as the effects of chamber walls, and flame quenching will influence the results. However, certain broad trends can be identified. The burning velocity is usually highest for slightly rich and stoichiometric methane-air mixtures at atmospheric pressures [26]. With increasing pressure and increasing excess air ratio, the burning velocity decreases [24-26]. For methane, under these experimental conditions, the  $\lambda$  of 1.0 and 1.2 have similar flame area profiles (Figure 4-5). However, as the mixture becomes leaner, the flame area decreases considerably. With the given disturbance in the form of charge motion, the flame area increases by more than 100% for the  $\lambda$  of 1.0 and 1.2 cases. For the  $\lambda=1.6$  case, with charge motion, the flame area increases by almost 800%. This brings the flame area profile

with respect to time more in line with the laminar flame propagation observed for  $\lambda$  of 1.0 and 1.2. The viewport is an 80 mm diameter circle, hence the maximum area estimation from the images is  $\sim 5024 \text{ mm}^2$ . When there is charge motion for  $\lambda=1.0$  and 1.2 methane cases, the flame front has propagated throughout the viewport by 25 ms. After the end of the glow phase at  $\sim 10$  ms, the effect of charge motion on increasing the flame area is more evident.

The effects of increasing  $\lambda$  and charge motion are similar for propane and DME. The leanest condition for propane charge was  $\lambda=1.4$  beyond which ignition was inconsistent. Example images are shown in Figure 4-6 and Figure 4-7 for propane and DME respectively at  $\lambda=1.0$ . The flame area estimations from the images are presented in Figure 4-8 and Figure 4-9 for propane and DME respectively. For both fuels, the laminar flame observed without charge motion propagates symmetrically in the viewing plane after the end of the glow phase ( $\sim 10$  ms).

For propane and DME, significant decreases in the flame areas with respect to time are observed when  $\lambda$  increases from 1.0 to 1.2. Further decreases are observed when  $\lambda$  increases to 1.4 (propane) or 1.6 (DME). For both propane and DME at  $\lambda=1.0$  with charge motion, the flame front travels across the viewport within the 20 ms mark. At  $\lambda=1.4$  for propane, the flame area increases by almost 100% by 25 ms when charge motion is used. For DME, the estimated flame area at  $\lambda=1.6$  is approximately  $100 \text{ mm}^2$ , with no significant effect of the charge motion at this  $\lambda$  till the 25 ms time instant (Figure 4-9). This could imply that since the initial flame propagation speed of DME at the leanest condition is slow and the flame remains near the spark plug, the given magnitude of charge motion may be insufficient to enhance the flame propagation speed.

Medium: Air-Propane  
 $\lambda=1.0$

Fan Speed=1200 rpm

$p_{\text{initial}}= 4 \text{ bar absolute}$   
 $T_{\text{initial}}= 300 \text{ K}$

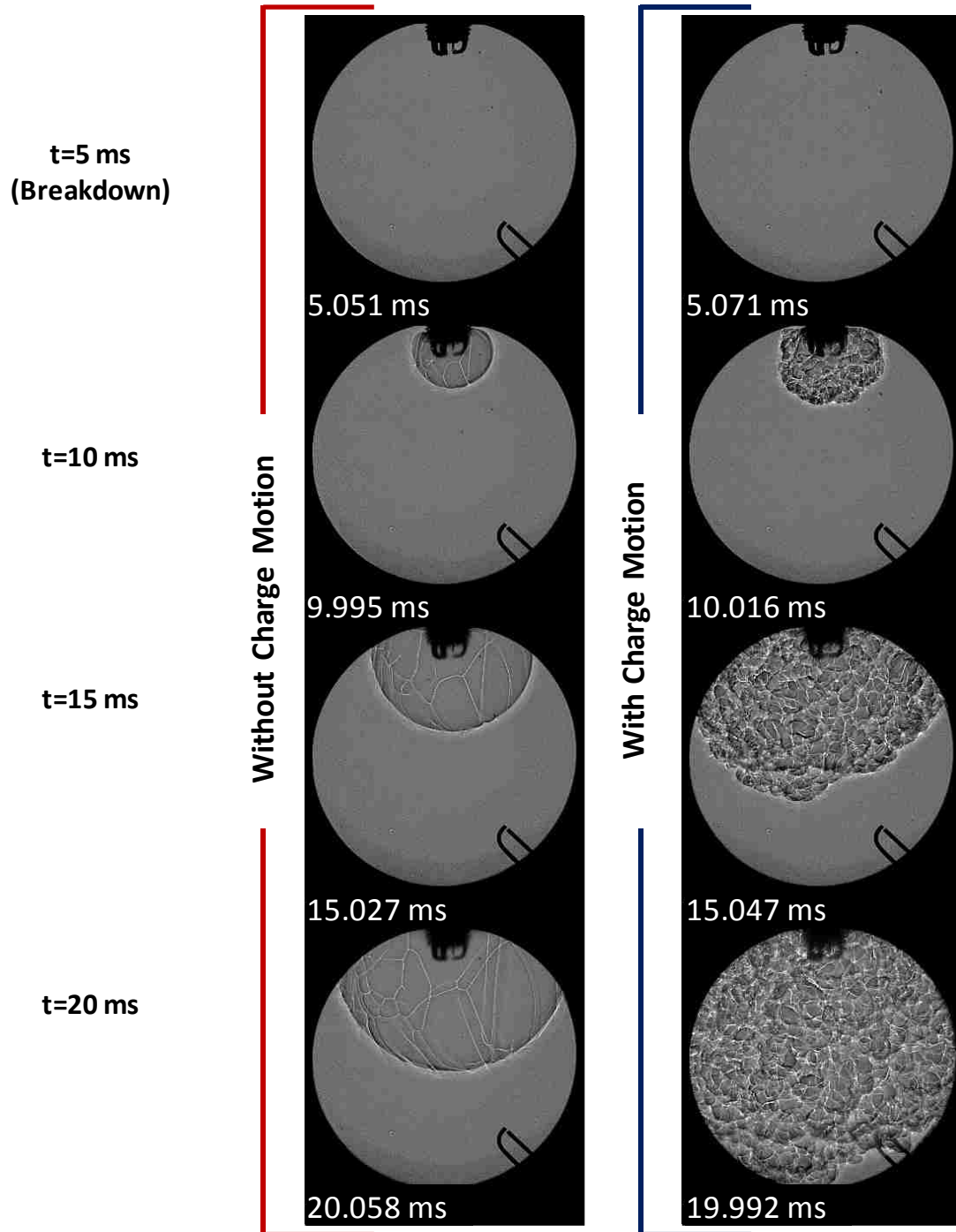


Figure 4-6. Image frames from propane combustion at  $\lambda=1.0$

Medium: Air-DME  
 $\lambda=1.0$

Fan Speed=1200 rpm

$p_{\text{initial}}= 4 \text{ bar absolute}$   
 $T_{\text{initial}}= 300 \text{ K}$

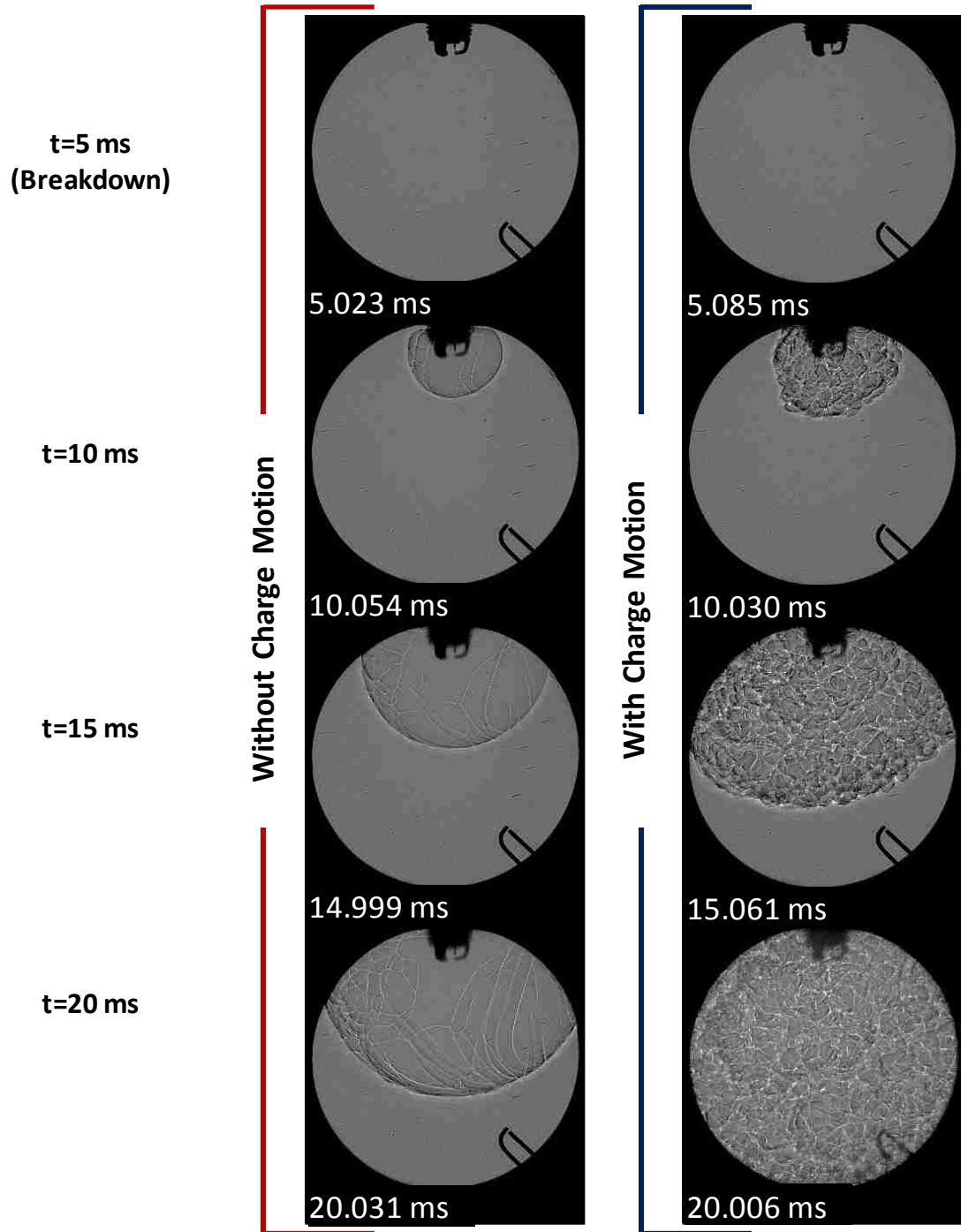


Figure 4-7. Image frames from DME combustion at  $\lambda=1.0$



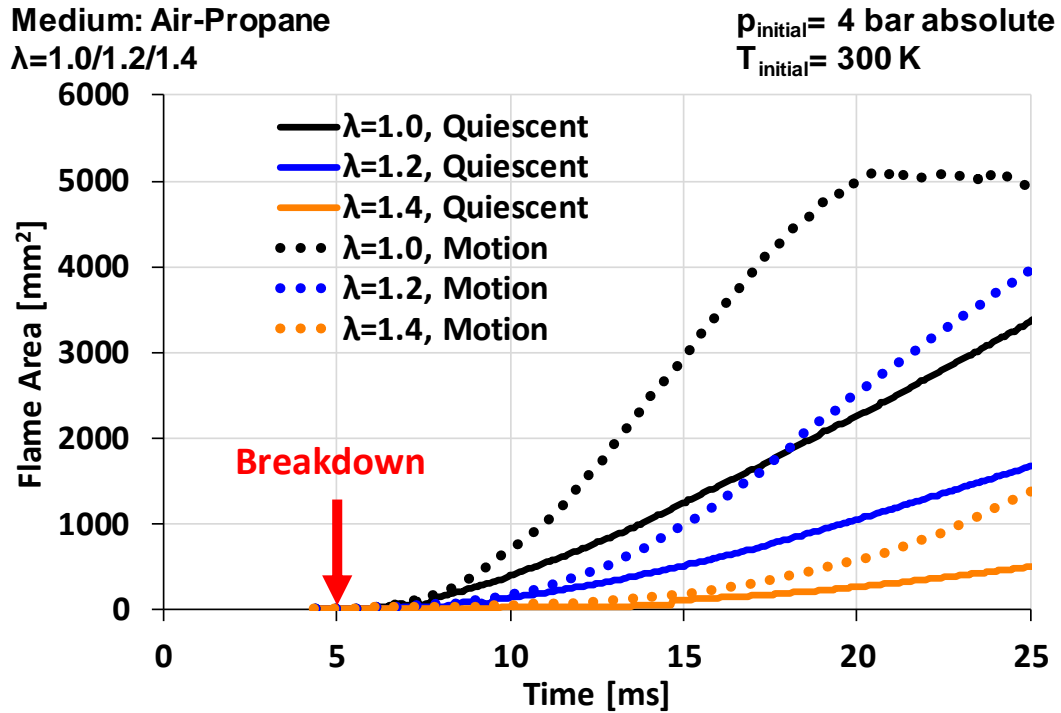


Figure 4-8. Flame area calculation of propane-air flames at varying  $\lambda$

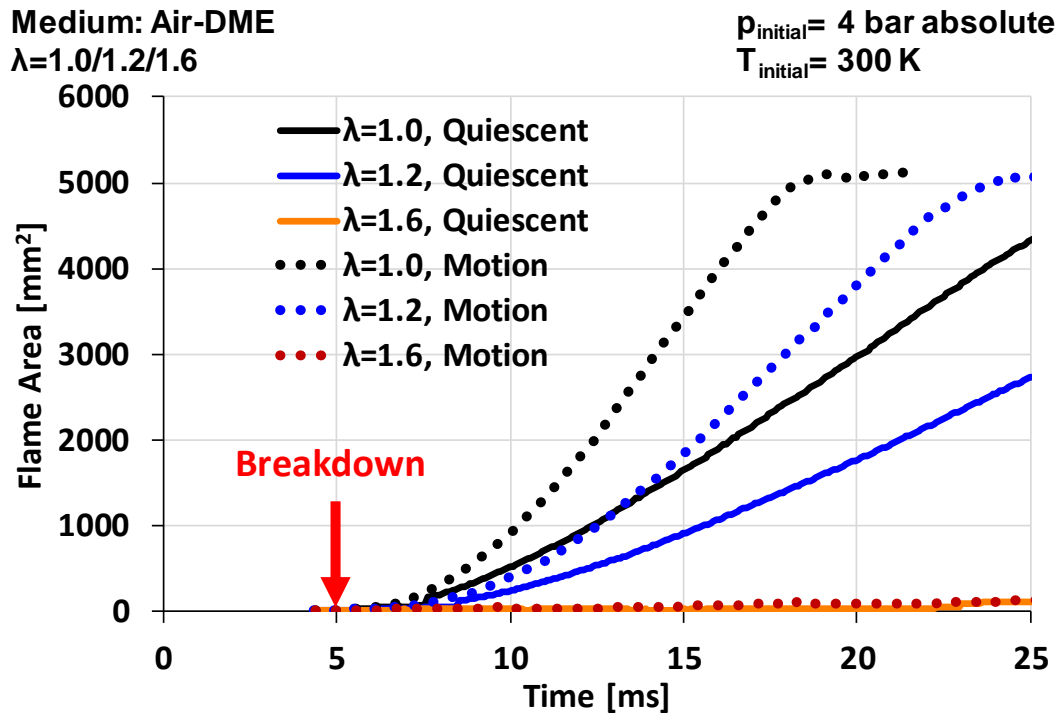


Figure 4-9. Flame area calculation of DME-air flames at varying  $\lambda$

## ■ Pressure and ion current analysis

The image analysis provides some clues on the effect of excess air ratio and charge motion on the combustion. One major disadvantage of the image analysis presented in this dissertation is that the flame is viewed in one plane only – two dimensions. Since the combustion in a CVCC or an IC engine is a three-dimensional phenomenon, additional measurements are necessary. The pressure signal processing is a more established method of analyzing combustion [112]. Additionally, in this study, ion current measurements are made at the multi-pole spark plug and the central region of the chamber.

The pressure and ion current measurements are made concurrently with the high-speed shadowgraph imaging. The pressure signal is the average gas pressure over the entire chamber volume, unlike the ion signal, which is localized in the region of the probe. The ion signal at the spark plug detects the initial flame kernel during which there wouldn't be a detectable change in the chamber pressure using the high range pressure transducer. Therefore, this signal is not expected to correlate with the pressure. However, when the flame front reaches the central ion probe, there should be a significant change in the chamber pressure. Hence, in following Figure 4-10, Figure 4-11 and Figure 4-12, the pressure and the ion central probe signal are illustrated for methane, propane and DME respectively at the stoichiometric and the leanest ( $\lambda=1.4$  or  $1.6$ ) test conditions.

Two general observations can be made for each fuel from the pressure traces. First, the peak pressure decreases when the charge becomes leaner though values at  $\lambda=1.0$  and  $\lambda=1.2$  are similar. The timing for this peak pressure is advanced as well. Second, at the same  $\lambda$ , with charge motion, the peak pressure increases and the timing for this peak is advanced as well. A higher peak pressure, and earlier peak pressure timing could indicate a faster

combustion. The significance of charge motion on lean combustion enhancement is evident especially for methane and propane (Figure 4-10 and Figure 4-11 respectively) when the charge motion can increase the peak pressure and peak pressure timing very close to stoichiometric case without air motion. Since a single fan speed was used for this study, the results should be viewed with that limitation. It is possible that further enhancement of flow can increase the speed of combustion further [37] or may cause the flame to be extinguished.

From DME imaging results at  $\lambda=1.6$  (Figure 4-9), it is evident that the flame area does not increase substantially within the 25 ms period from the rising edge of the spark trigger. This is further corroborated by the pressure signal (Figure 4-12) which does not show an increase till the ~50 ms mark even with charge motion. With charge motion, the rate of increase of pressure is higher, causing the peak pressure to occur at around 140 ms. This is much earlier compared to 300 ms for the quiescent  $\lambda=1.6$  case.

The central ion probe signal also shows certain similar attributes between the fuels. For fairness of comparison, the bias voltage and the measurement resistance are kept constant. First is the shape of the ion signal. As discussed in Section 5.1, the sharp rise in the central ion probe signal is related to the arrival of the flame at the probe location. In general, the signal remains high for the period over which the flame passes through the length of the probe. Then, it decreases, and increases again. This second peak is related to the post flame phase during which the thermal ionization is predominant [66]. For propane and DME at stoichiometric conditions, this thermal peak exceeds the limit of the measurement system; hence the curve is truncated at 50 volts. The high thermal ionization signal could indicate a higher temperature in the chamber. In general, this overvoltage is observed only for the

stoichiometric cases. The initial rise of the ion current is of interest since it is an approximate measure of the arrival of the flame front in that region of the chamber. The timing of the peak pressure and the timing of the corresponding first peak of the ion current are generally correlated. With charge motion, the flame propagates faster, which advances the first peak of the ion signal. The first peak of ion current timing is typically earlier than the peak pressure timing.

The second common attribute is the change in the magnitude of the first ion peak. The magnitude of the first peak of ion current is related to the peak pressure at the same  $\lambda$ . For instance, when charge motion is used, the ion current peak is higher. On a physical level, this may correspond to a faster rate of ion production due to the increase in the burning velocity. Moreover, there is a drastic decrease in the ion current magnitude with increase of  $\lambda$ . This highlights the difficulty in measuring ion current at lean conditions due to the decrease in the ion concentration. For the current experimental setup, discernible signal is observed even at  $\lambda=1.6$ . But owing to the small magnitude of the signal at  $\lambda=1.6$ , there is a possibility that during engine test, the system noise may make it difficult to distinguish the ion current. Therefore, a higher measurement resistance of 1 M $\Omega$  and a high range oscilloscope is used for engine tests.

An additional observation is the difference in the magnitude of the first peak of ion signal between the fuels. It is expected that due to the differences in the combustion chemistry, the ion concentration in the flame front could be different for each fuel [79]. For the given experimental conditions and setup, the magnitude of this first peak of signal is highest for propane, followed by DME, and finally methane at  $\lambda=1.0$ .

Medium: Air-Methane  
 $\lambda=1.0/1.6$

$p_{\text{initial}} = 4 \text{ bar absolute}$   
 $T_{\text{initial}} = 300 \text{ K}$

$V_{\text{ion}} = 600 \text{ V}$   
 $R_{\text{ion}} = 40 \text{ k}\Omega$

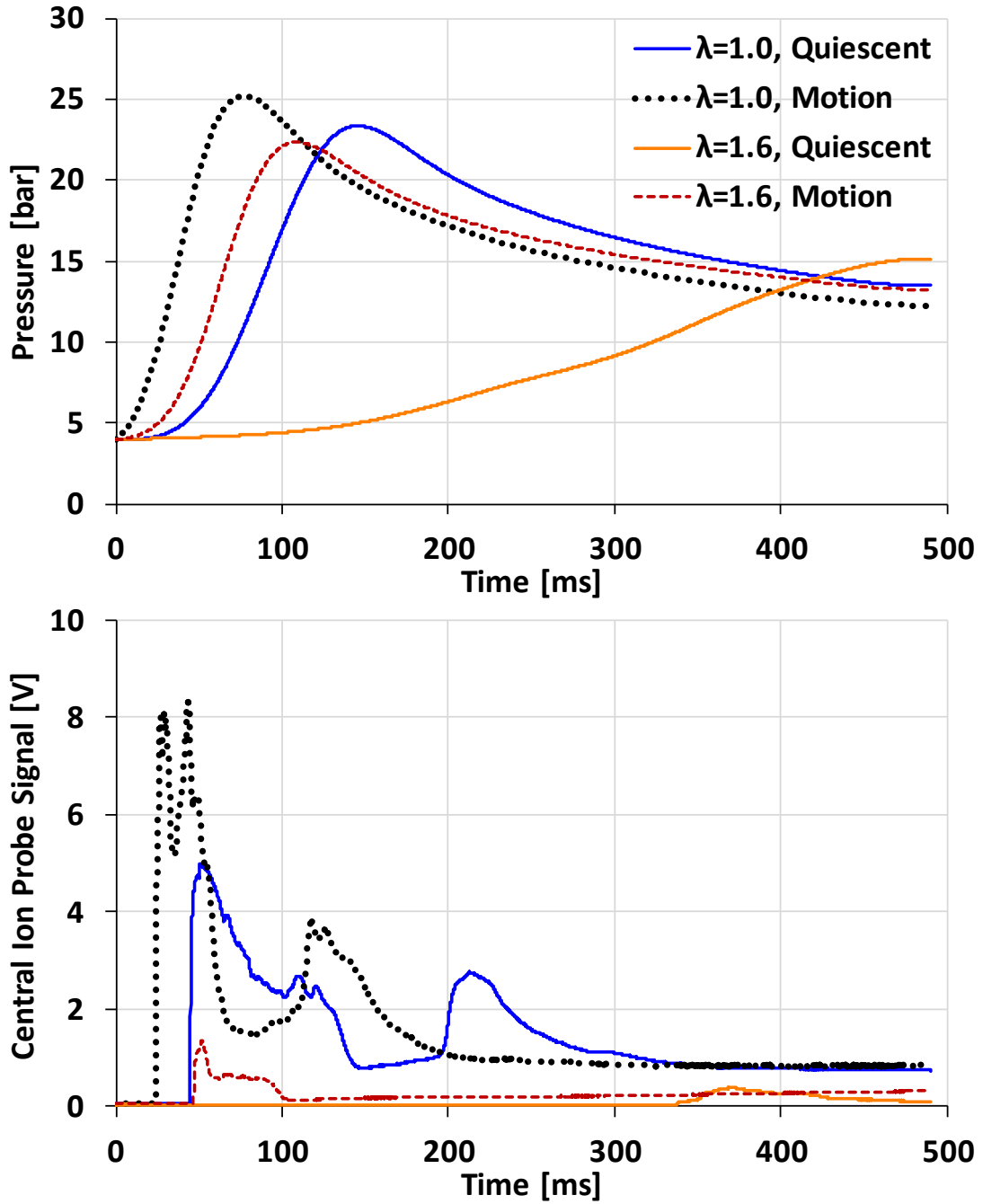


Figure 4-10. Air-methane flames – pressure traces (top) & ion probe signal (bottom)

Medium: Air-Propane  
 $\lambda=1.0/1.4$

$p_{\text{initial}} = 4 \text{ bar absolute}$   
 $T_{\text{initial}} = 300 \text{ K}$

$V_{\text{ion}} = 600 \text{ V}$   
 $R_{\text{ion}} = 40 \text{ k}\Omega$

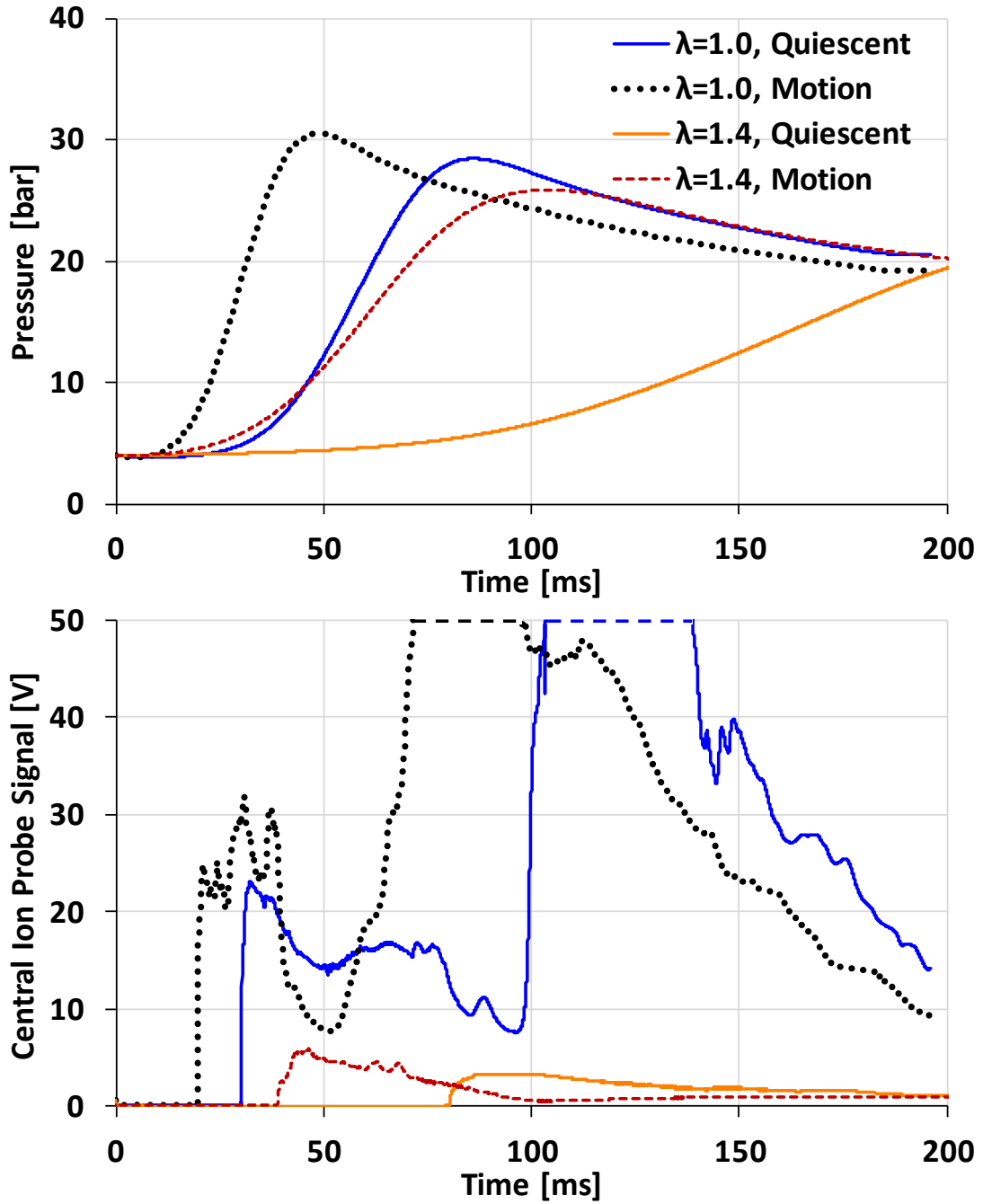


Figure 4-11. Air-propane flames – pressure traces (top) & ion probe signals (bottom)

Medium: Air-DME  
 $\lambda=1.0/1.6$

$p_{\text{initial}} = 4 \text{ bar absolute}$   
 $T_{\text{initial}} = 300 \text{ K}$

$V_{\text{ion}} = 600 \text{ V}$   
 $R_{\text{ion}} = 40 \text{ k}\Omega$

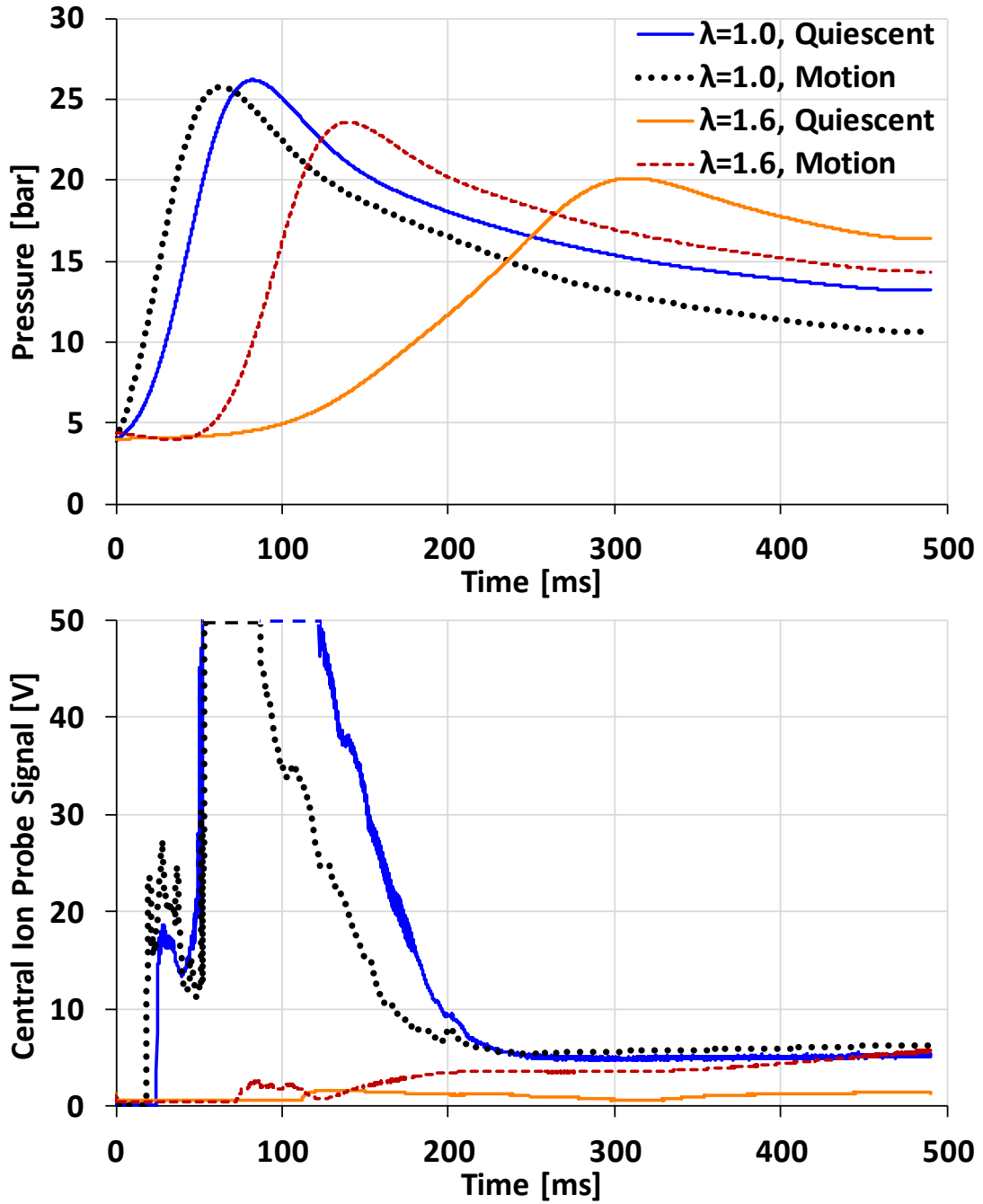


Figure 4-12. Air-DME flames – pressure traces (top) & ion probe signals (bottom)

## ■ Fuel Effect: A Comparison between Methane, Propane and DME

After a study of the individual attributes of combustion of each fuel in the CVCC in Section 4.2, the author provides a comparative analysis of the three fuels in this section. Since the shadowgraph frames at  $\lambda=1.0$  have been discussed previously, the combustion at the leanest condition ( $\lambda=1.6$  for methane and DME,  $\lambda=1.4$  for propane) is shown in Figure 4-13 and Figure 4-14 without and with charge motion respectively. After the breakdown at 5 ms and till 15 ms (Figure 4-13), the flame is in the periphery of the spark plug. At 40 ms, the differences in the flame area are more perceptible. With air-propane at  $\lambda=1.4$ , the flame is expected to be faster than that of methane and DME at  $\lambda=1.6$ . The DME flame area is lower than that of methane at 40 ms. However, by 60 ms, the DME flame area is greater than that of methane. This implies that DME flame propagation is initially slower, but then as the flame expands, the flame propagation speed increases. This may be explained by the fundamentals of flame propagation. The Markstein lengths (burned/unburned) for laminar flames at this pressure and  $\lambda$  are negative for methane and positive for DME [22-26, 117]. A negative Markstein length typically implies that the flame speed will increase with flame stretch. The flame stretch is highest at the lowest flame radius and decreases as the flame radius increases. Methane's Markstein length at  $\lambda=1.6$  and 4 bar absolute initial pressure is lower than -0.5 mm, while for DME, the Markstein length is approximately 0.5 mm [22, 117]. Hence, the higher stretch condition in the initial stage of the flame propagation is expected to increase the flame speed of methane. As the flame propagates, the stretch rate decreases, thereby decreasing the flame speed. The flame speed of DME on the other hand, due to the positive Markstein length, will increase as the flame stretch decreases with expanding flame radius.



Medium: Air-Methane/Propane/DME  
 $\lambda=1.6$  (Methane/DME) / 1.4 (Propane)

$p_{\text{initial}}= 4$  bar absolute  
 $T_{\text{initial}}= 300$  K

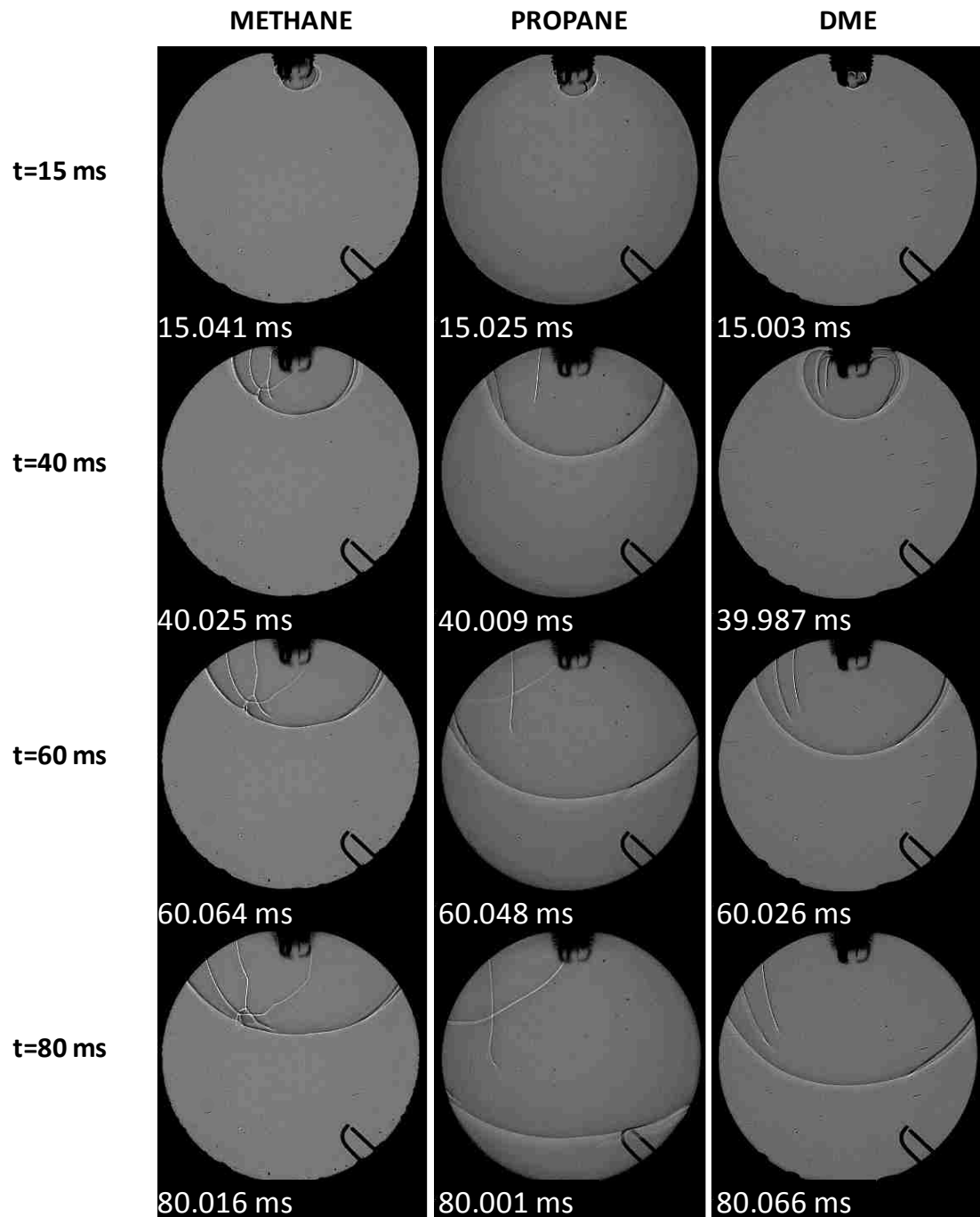


Figure 4-13. Image frames from combustion at  $\lambda=1.4/1.6$  under quiescent condition

With charge motion, the overall time scale of combustion is shorter. Unlike the quiescent cases, the flame front sweeps over the viewport within 40 ms for the methane and propane cases (Figure 4-14). Methane (at  $\lambda=1.6$ ) is marginally faster than propane (at  $\lambda=1.4$ ). For DME, the initial flame propagation is significantly slower, which again could be due to the positive Markstein length explained earlier.

To put these results into perspective from a practical standpoint, the time scales in these chamber tests at  $\lambda=1.4/1.6$  are much larger than those in an engine. Typically, combustion duration in an SI engine is of the order of a few milliseconds [113]. Therefore, the initial period of flame propagation in the 10-15 ms range after the spark breakdown warrants closer examination. In Figure 4-15 and Figure 4-16, the flame areas are plotted with respect to time for  $\lambda=1.0$  and  $\lambda=1.4/1.6$  respectively for all test fuels. At  $\lambda=1.0$ , DME flame area increases at the fastest rate, followed by propane and methane. With charge motion, all the curves shift upward but the order remains the same. At  $\lambda=1.0$ , the Markstein length for DME is negative, indicating that flame speed increases with increasing flame stretch.

At  $\lambda=1.6$ , the trends are reversed for the fuels (Figure 4-16). Under quiescent conditions, methane and propane have similar increases in flame areas with respect to time. With charge motion, methane is faster than propane. The flame area of DME does not increase significantly over the period under examination – both without and with charge motion. This could imply that under these experimental conditions, achieving fast flame propagation of DME would be a significant challenge with spark ignition.

Medium: Air-Methane/Propane/DME  
 $\lambda=1.6$  (Methane/DME) / 1.4 (Propane)

$p_{\text{initial}} = 4$  bar absolute  
 $T_{\text{initial}} = 300$  K

Fan Speed = 1200 rpm

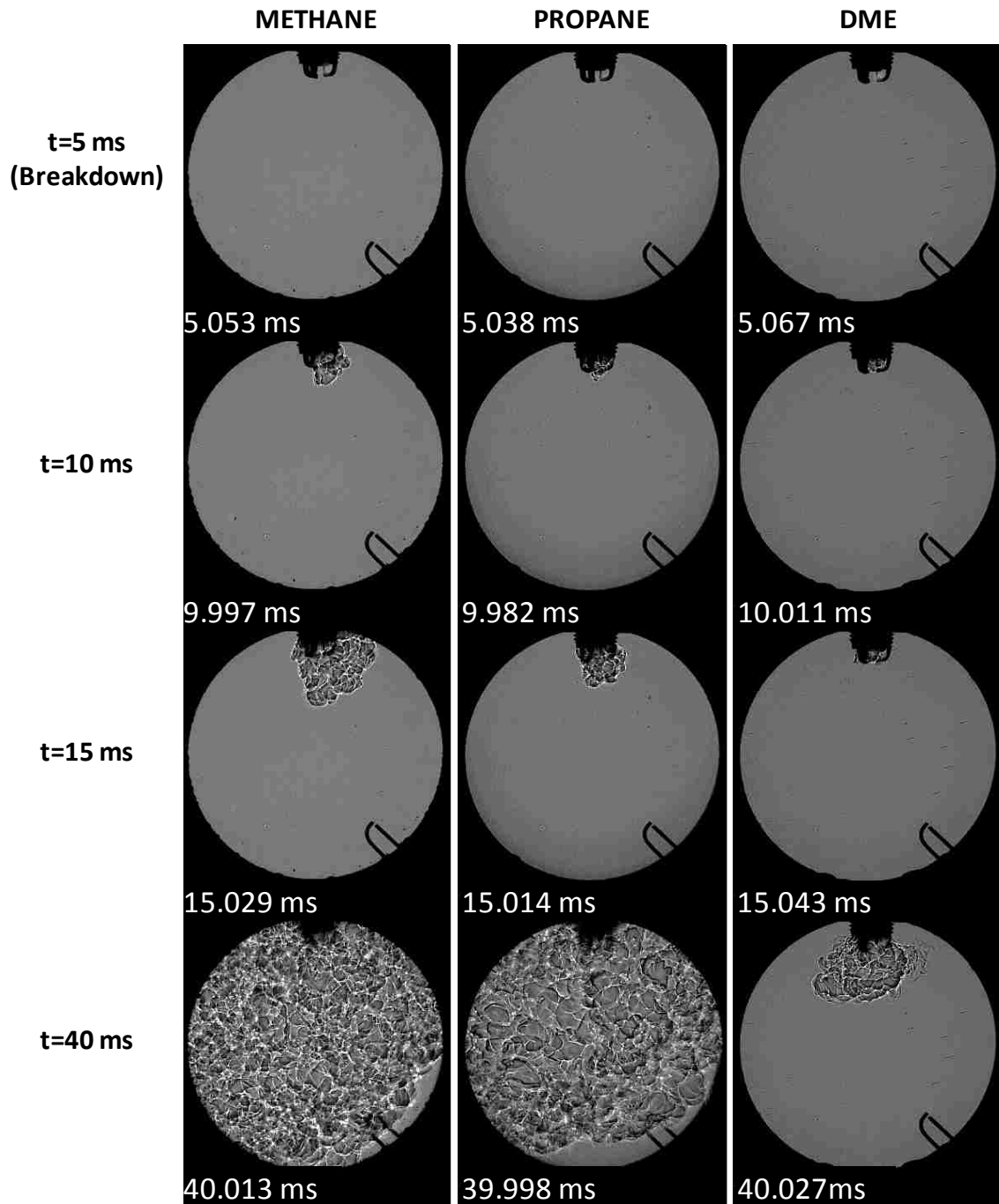


Figure 4-14. Image frames from combustion at  $\lambda=1.4/1.6$  under charge motion condition

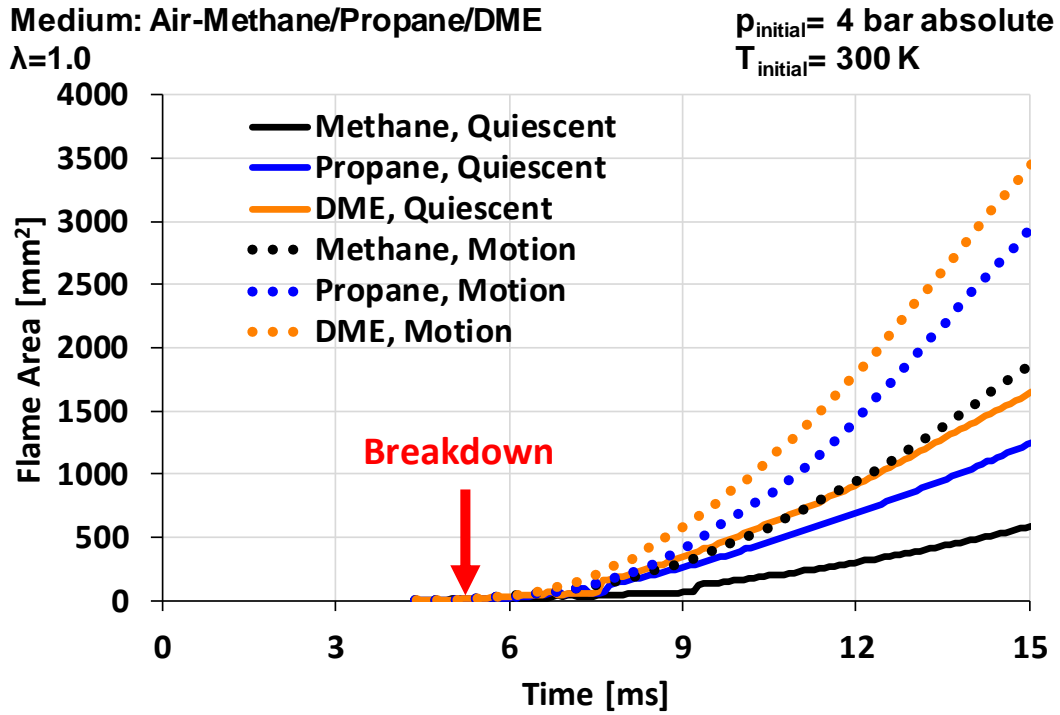


Figure 4-15. Flame area calculation at  $\lambda=1.0$

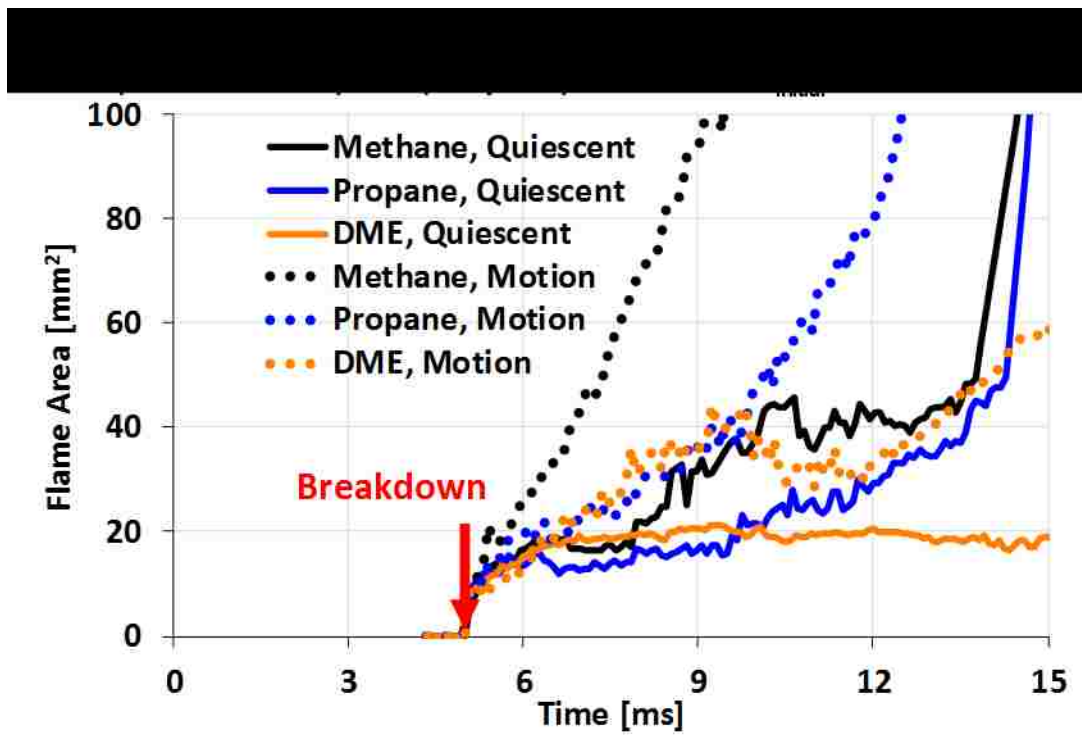


Figure 4-16. Flame area calculation at  $\lambda=1.4/1.6$

The 't<sub>5</sub>' time is determined from the pressure signal according to the procedure explained in Appendix B. This is an estimation of the period for 5% of mass fraction burned for a CVCC. A shorter t<sub>5</sub> would imply faster conversion of the unburned charge into burned gas during the early stage of combustion. The results for  $\lambda=1.0$  and  $\lambda$  of 1.4 (propane) and 1.6 (methane/DME) are presented in Figure 4-17 and Figure 4-18 respectively. The flame area estimations and the pressure-based analyses cannot be expected to match under all circumstances since the initial flame propagation will affect the area calculation, but it may not cause a detectable change in the chamber pressure. At  $\lambda=1.0$  under quiescent conditions, the t<sub>5</sub> is shortest for DME, followed by propane and methane. This correlates with the flame area estimations (Figure 4-15). With charge motion, t<sub>5</sub> of DME is shortest, followed by methane and propane.

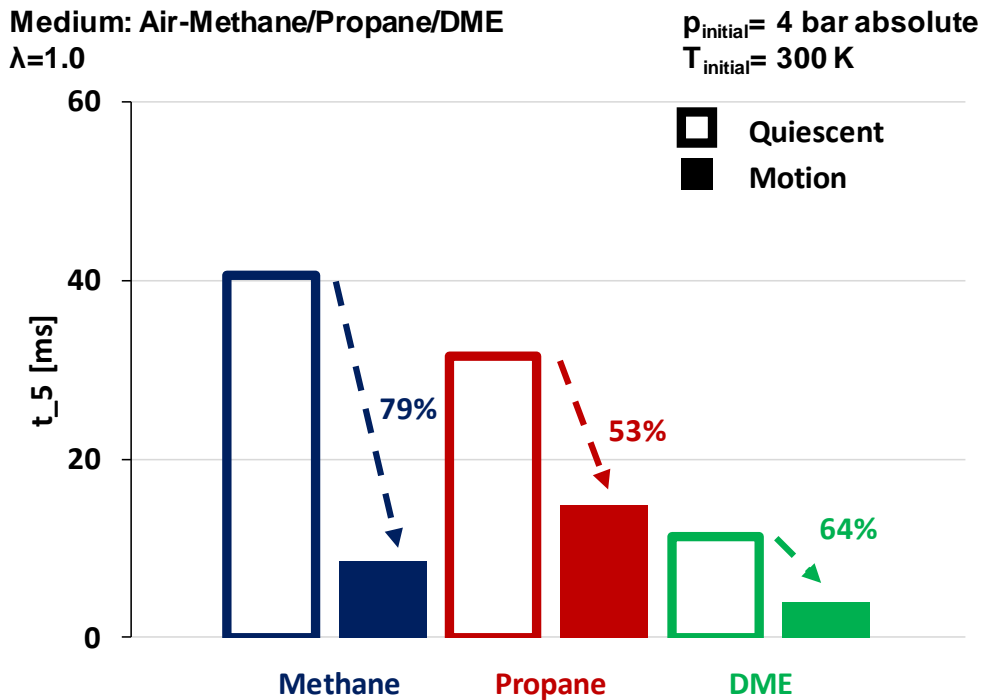


Figure 4-17. t<sub>5</sub> based on pressure at  $\lambda=1.0$

At  $\lambda=1.6$  and quiescent conditions,  $t_{5}$  is shortest for propane followed by methane and DME. With charge motion, the  $t_{5}$  is similar for methane and propane, and longest for DME. These trends broadly match the main conclusion from the image processing – DME SI combustion is the slowest of the three fuels at the leanest test conditions.

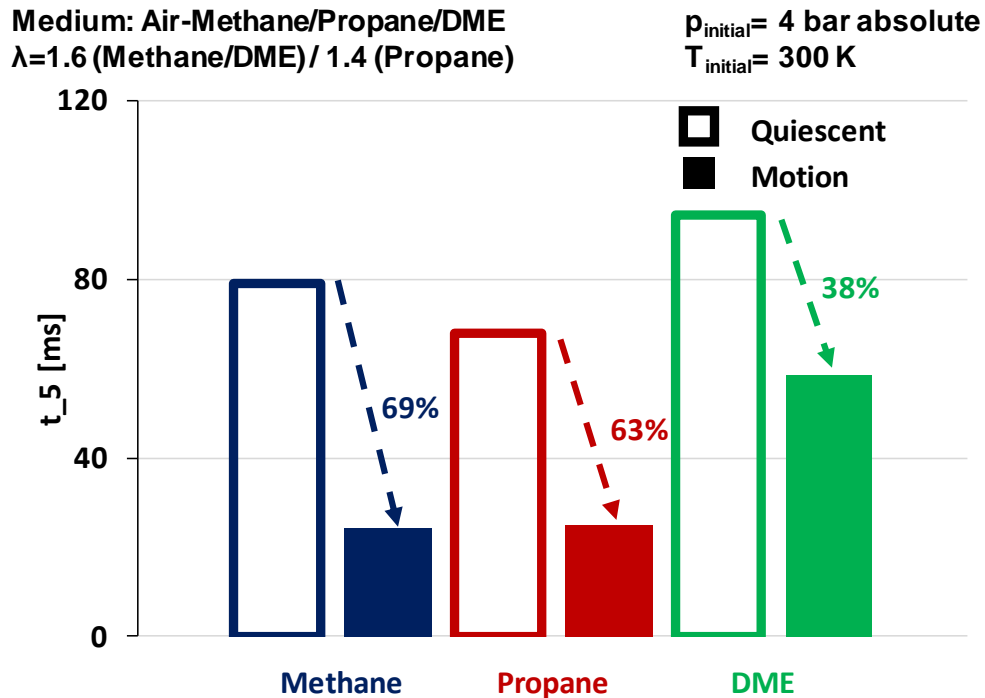


Figure 4-18.  $t_5$  based on pressure at  $\lambda=1.4/1.6$

### Directed Flow on Spark Gap

From the previous discussion, it can be concluded that charge motion has a significant impact on the flame propagation. Additionally, the spark discharge itself is expected to be affected by the charge motion. As explained previously in the literature review, the mean flow field inside the engine will constantly interact with the spark discharge and the flame kernel. Therefore, a two-step study is carried out to investigate this interaction. First, an experiment on the effect of directed flow on just the spark discharge is conducted under

ambient conditions. A Dantec Dynamics Hot-Wire Calibrator is used to direct a free stream air jet of known velocity towards the spark gap of a conventional resistive spark plug. Second, combustion tests are performed in the CVCC under lean conditions ( $\lambda=1.6$ ) with directed flow on the spark gap of a conventional resistive spark plug (uses a ceramic resistor to suppress ignition noise) to estimate the impact on the charge combustion.

A representation of the effect of flow on the discharge channel is shown in Figure 4-19. The arc is represented in light gray colour (enhanced perimeter for improved viewability) with an outline of the spark plug in the background. High speed direct imaging is used to capture the arc during the spark breakdown and glow phase. Increasing the flow velocity across the spark gap typically causes the discharge channel to increasingly stretch until it breaks and re-establishes [113]. This stretching of the discharge channel can impact combustion greatly [27, 114].

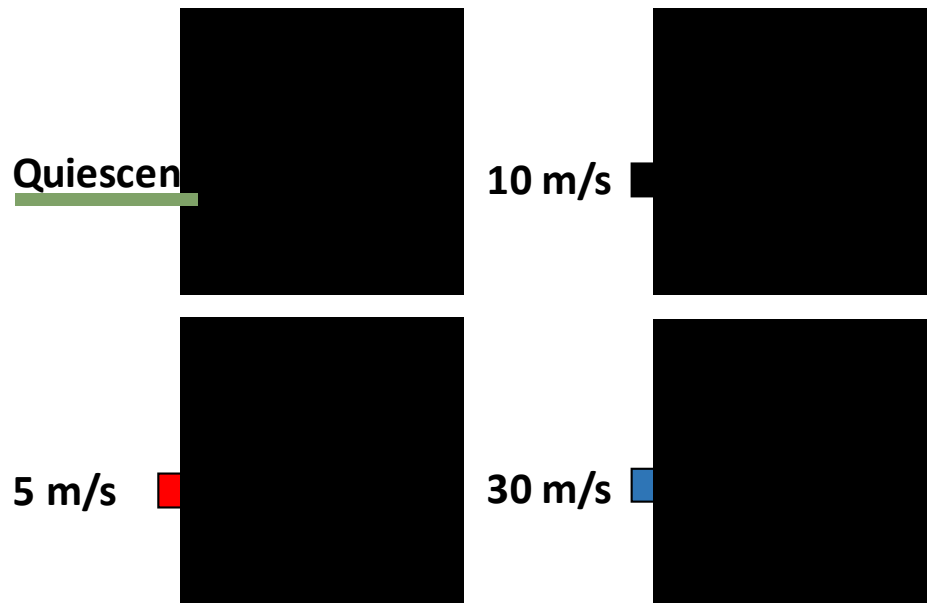


Figure 4-19. Stretching of the discharge channel under flow

Measurement of the discharge current provides further clues on the impact of flow on the discharge mechanism (Figure 4-20). The spark breakdown occurs at ~0 ms in the figure. The coil charging duration is 2 ms for all cases. The number of spikes in the discharge current increase with increasing flow velocity across the spark gap. These typically could correspond to the re-establishment of the discharge channel after it breaks off after stretching. The overall glow phase duration decreases with increasing cross flow velocity.

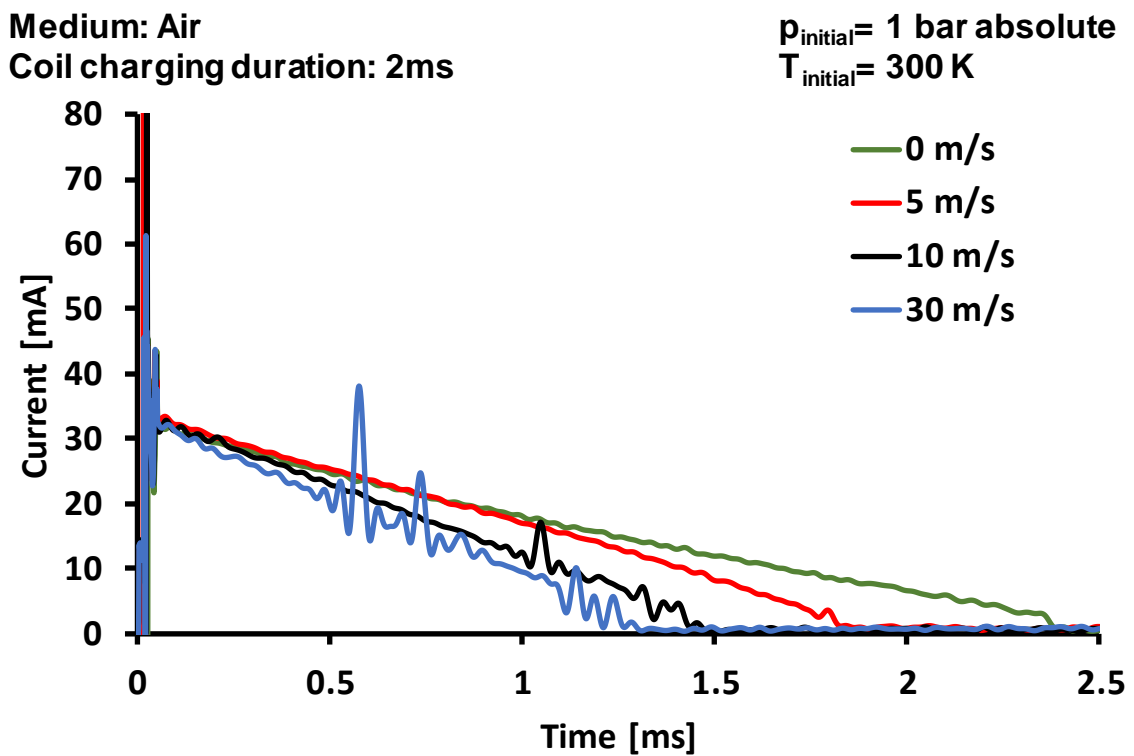


Figure 4-20. Discharge current vs. time at different gap velocities

Given the adverse impact of the spark gap flow velocity on the discharge current, it was desired to manipulate the discharge current level through a current management module developed at the author's laboratory. The current control module is independent of the transistor coil ignition (TCI) system used for spark breakdown previously. It consists of a high voltage isolated DC output power supply (~2000 VDC), a stabilizer capacitor, and an



IGBT to control the duration of the additional current supply. The module is activated during the glow phase to boost the discharge current from a decreasing waveform profile into a flatter square waveform profile under ideal and quiescent conditions. The actual current profile is expected to be irregular due to the charge motion. Average current levels of 100 to 400 mA may be provided through this module. Further details can be found in previous publications [113, 115]. Another way to manipulate the discharge current is to use two independent ignition coils and stagger the coil charging and discharging to provide a steady current supply. This ‘dual coil’ method can provide an average discharge current of up to 55 mA.

A comparison of the current profiles between conventional, dual coil (55 mA), and current control module (190 mA and 250 mA) are provided in Figure 4-21. This test is performed in the CVCC in an air-methane medium at  $\lambda=1.6$  with a conventional resistive spark plug (4.5 k $\Omega$ ). The flow into the spark gap is provided through a nozzle which is connected to a buffer volume containing air-methane charge at  $\lambda=1.6$ . The estimated flow velocity from particle image velocimetry (PIV) is approximately 25 m/s. The background pressure and temperature are identical to the test conditions in the previous sections. The coil charging duration for the TCI system is 2 ms. It can be seen from Figure 4-21 that the flow causes the current profile to increase and decrease over the current control duration of 1.8 ms. However, a significantly higher average discharge current (55, 190 or 250 mA) can be provided to the spark gap.

The consequent impact of the current modulation on the combustion of a lean mixture ( $\lambda=1.6$ ) at 55 mA, 190 mA, and 250 mA is shown in Figure 4-22. The corresponding flame area calculation result is given in Figure 4-23.

Medium: Air-Methane  
Coil charging duration: 2ms

$p_{\text{initial}} = 4 \text{ bar absolute}$   
 $T_{\text{initial}} = 300 \text{ K}$

Current Control Duration – 1.8 ms

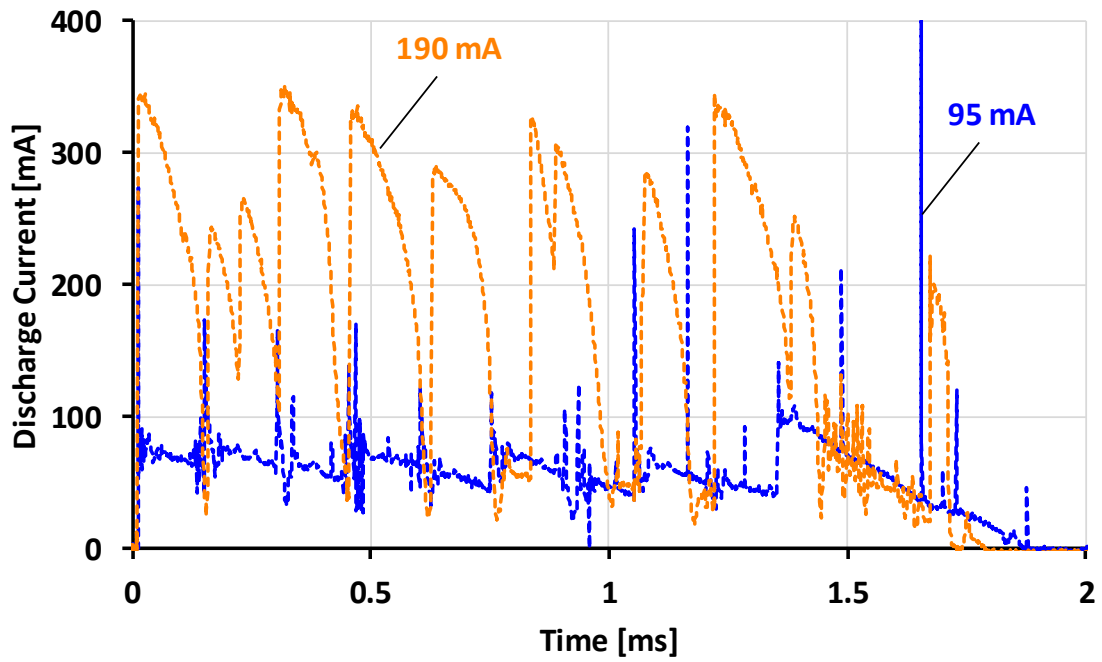
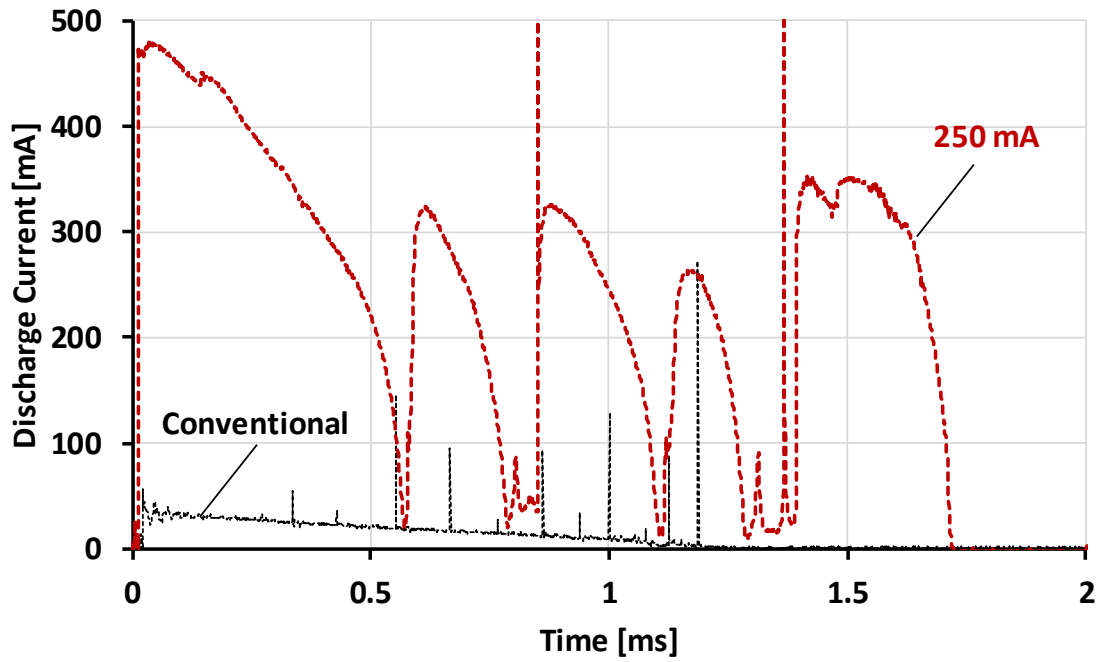


Figure 4-21. Discharge current manipulation using current control

Medium: Air-Methane     $\lambda=1.6$      $p_{\text{initial}}=4$  bar absolute     $T_{\text{initial}}=300$  K  
 Coil charging duration: 2 ms    Current control duration: 1.8 ms  
 Average Discharge Current

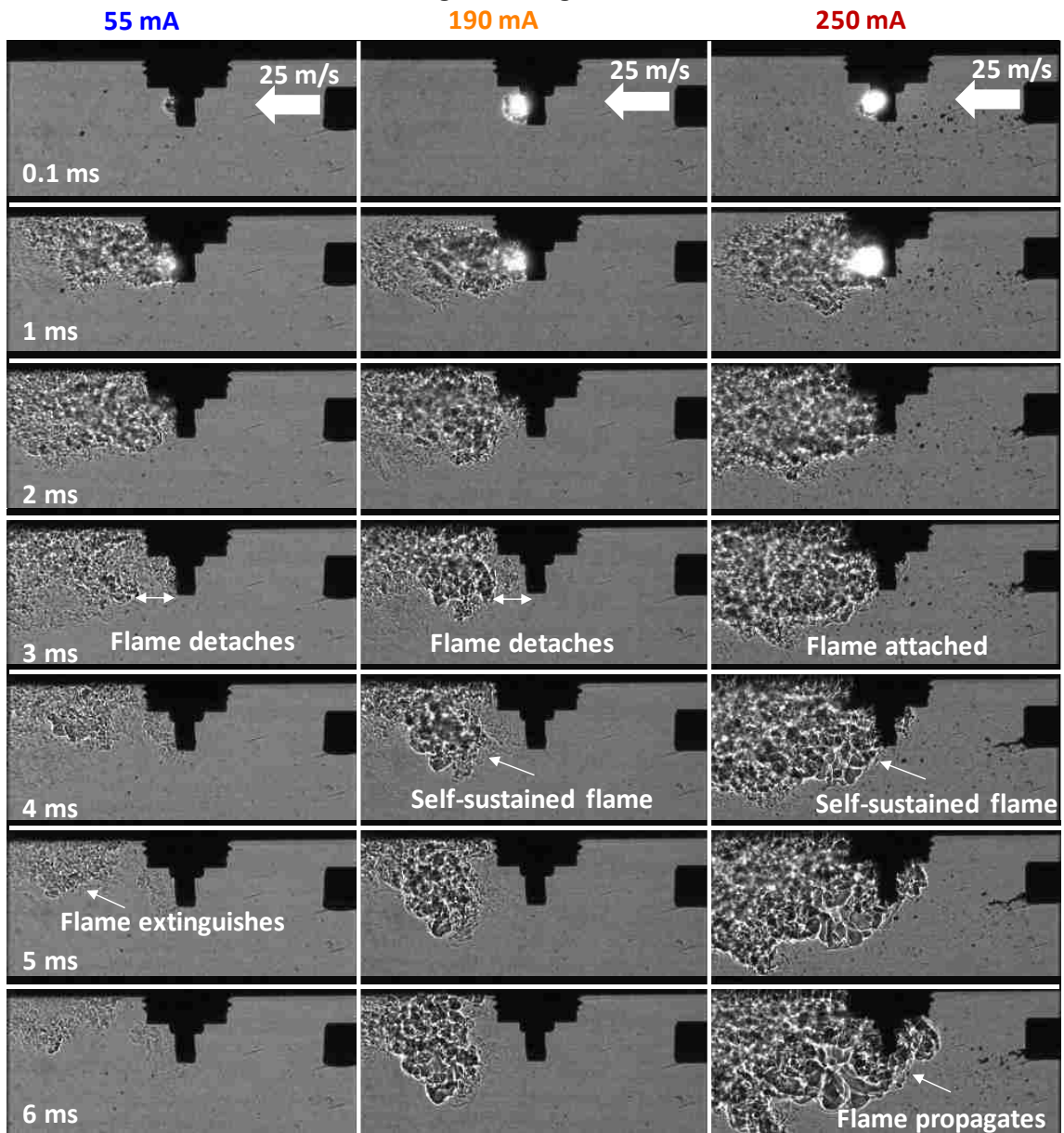


Figure 4-22. Combustion with directed flow – effect of current control

The result highlights the challenge of sustaining ignition and propagating the flame under flow conditions. Spark breakdown occurs at  $\sim 0$  ms. For all current levels, combustion is initiated, and an initial flame kernel is formed by 1 ms (Figure 4-22). However, for the 55

and 190 mA cases, the flame detaches from the spark gap at 3 ms from the spark breakdown. For the 55 mA case, the flame is extinguished by 5 ms, and the background mixture in the chamber does not ignite. This causes the flame area to decrease (Figure 4-23). In the 190 mA case, the detached flame is able to sustain, and eventually, the background mixture in the chamber is ignited. For 250 mA case, the flame remains attached to the spark gap, and eventually, causes combustion of the background mixture. This phenomenon of flame detaching has also been reported in [49].

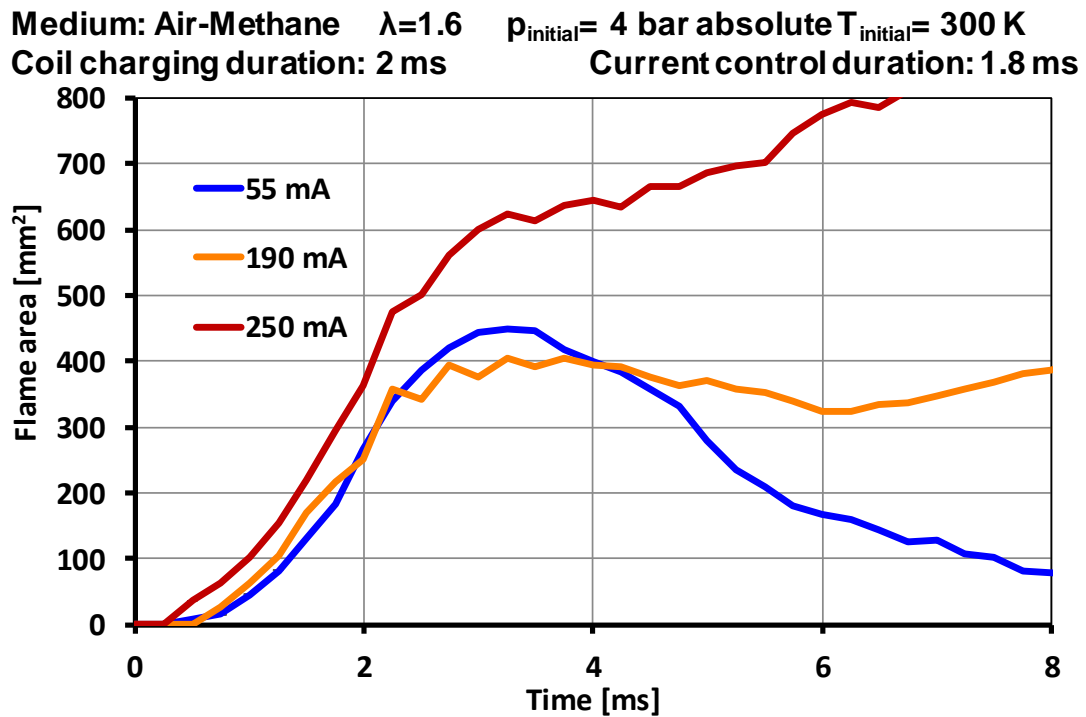


Figure 4-23. Flame area using current control at 25 m/s directed flow

### ■ Shock Accelerated Flame

The present CVCC experimental setup can provide limited charge motion which may not produce flame speeds relevant to engine conditions. Therefore, tests are performed using a shock tube to simulate higher speed flames to identify certain trends with respect to  $\lambda$  and

initial pressure. The operation of the ion current measurement system can also be tested under these high flow conditions. The experimental conditions are listed in Table 4-1.

Table 4-1. Experimental conditions for shock tube test

Fuel	Methane
Excess air ratio	1.0/1.2/1.4
Initial temperature	27 °C
Initial pressure	1.5 / 1.75 / 2.0 bar abs
Shock tube pressure ratio	~3-4
Ion current bias voltage	250 VDC
Estimated shock speed	~400-500 m/s

The driven section of the shock tube is filled with charge at a pressure of 1.5, 1.75 or 2.0 bar absolute and at a  $\lambda$  of 1.0, 1.2 or 1.4. The driven section is open to ambient air. When the charge is ignited, the pressure in the driver section increased which caused the diaphragm to suddenly burst (at ~3-4 bar) and a shockwave propagated in the driven section. This was followed by a freely propagating flame in the open ended driven section of the shock tube. A schematic diagram of the shock tube is shown in Figure 3-11.

The pressure profiles at  $\lambda=1.0$  for two initial pressure conditions are shown in Figure 4-24. When the diaphragm bursts, the pressure transducer in the driver section measures a sharp fall in pressure. Shortly after, the shockwave causes a sharp increase in pressure measured by the driven section pressure transducer. The distance between the pressure transducers and the time between the falling edge of the driver pressure and the rising edge of the driven pressure can be used to estimate the shockwave speed. For the given conditions, the shockwave speed is of the order of ~400 to 500 m/s depending on the diaphragm burst

pressure which is between ~3-4 bar. The flame speed is measured using two ion current probes – one each in the driver and the driven section. An example of ion current and pressure profiles is shown in Figure 4-25.

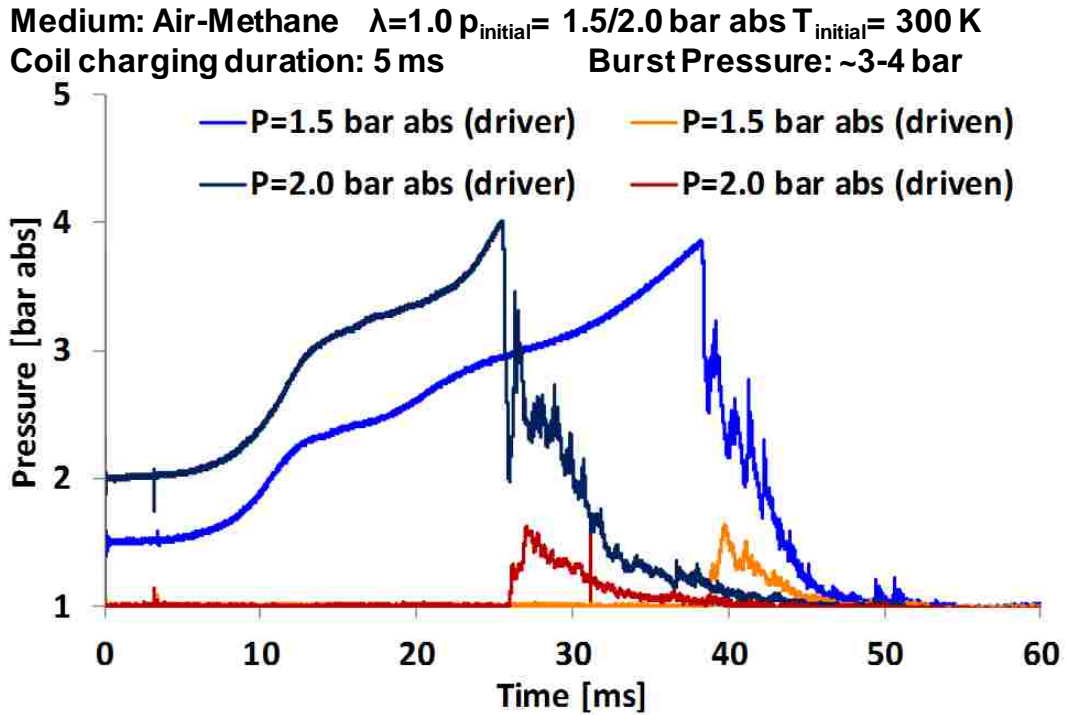


Figure 4-24. Driver and driven section pressure profiles

The ion signal peaks are used to estimate the flame propagation speed (Figure 4-25). The spark breakdown occurs at 0 ms. Thereafter, the flame propagates from the spark plug (SP) and registers the first peak in the driver section ion current probe (S1). Eventually, as the diaphragm breaks, the shock propagates first followed by the flame front which registers the peak in the driven section ion current probe (S2).

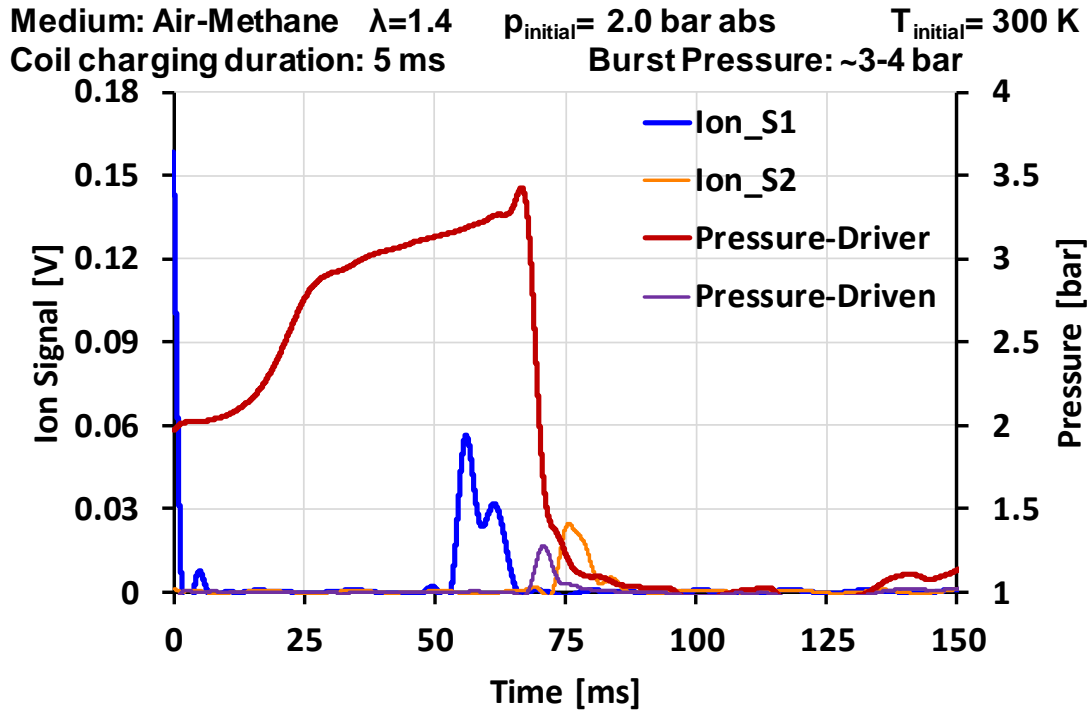


Figure 4-25. Ion and pressure signal profiles for  $\lambda=1.4$  and  $p_{\text{initial}}=2.0$  bar abs

Two types of flame speed estimations are made – from SP to S1, and from S1 to S2 based on the time instance of the ion signal peak. The results are shown in Figure 4-26 for two initial pressures of 1.5 and 2.0 bar absolute. The results for the 1.75 bar pressure case were intermediate of the two pressure conditions shown in Figure 4-26, and are therefore not shown. When the  $\lambda$  increases from 1.0 to 1.4, the flame speed from SP to S1 for  $p_{\text{initial}}=1.5$  bar decreases from ~9.6 m/s to ~3.2 m/s. The flame speed for  $p_{\text{initial}}=2.0$  is marginally lower and follows the same trend.

The flame front propagation from S1 to S2 is probably affected by two factors. The first is the passage of the shockwave, which would be followed by the passage of the gas interface. The second is the open ended driven section which would cause any flame to expand freely since there is no back pressure from the end wall (or the diaphragm in case of the driver

section). Hence, the flame speeds from S1 to S2 are observed to be significantly higher than that from SP to S1. The flame speed for the highest initial pressure case (2.0 bar) is almost double the lowest initial pressure case (1.5 bar). This could be due to the extra fuel energy that is put into the driver section when the initial pressure is higher. The overall decreasing trend in flame speed with increasing  $\lambda$  remains.

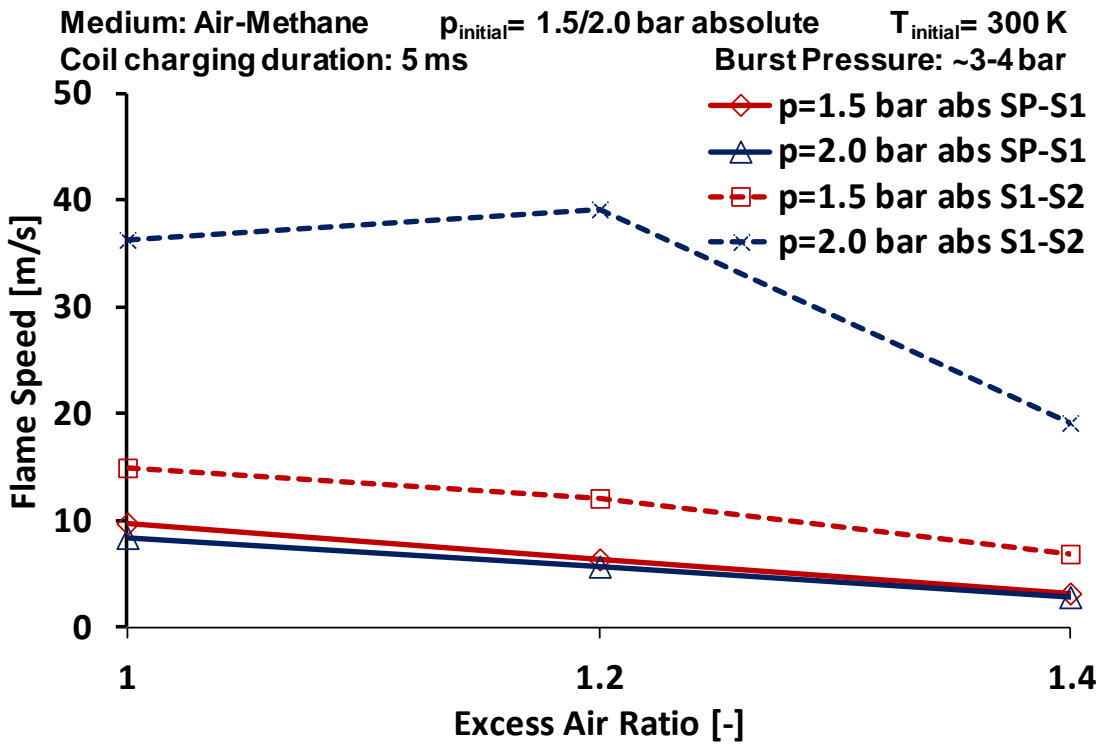


Figure 4-26. Flame speed estimation from ion current signal



## ■■■■■ CHARGE REACTIVITY IMPACT ON ENGINE COMBUSTION

In this chapter, the author describes the empirical work done on the Yanmar engine test cell. In addition to the typical instrumentation of a modern engine test cell, in-cylinder ion current measurement is also performed to provide further insight into the combustion. The broad objective is to study the effects of excess air ratio and intake temperature on combustion of the chosen test fuels. This chapter is organized into five sections. In the first section, the author presents the results of modifying the intake manifold to enhance the in-cylinder air motion. In the second section, an overview of combustion of the three test fuels (gasoline, ethanol, and DME) under low load is provided. As explained in Chapter 3, these fuels were chosen based on their availability and their varying reactivity. The effects of excess air ratio and intake temperature on the reactivity of each of these fuels is described in the third and fourth sections respectively. In the fifth section, extension of lean limit of DME HCCI with intake heating is briefly discussed.

### ■■■ Effect of Modifying Intake Flow

The intake manifold of the engine is modified by adding an insert with the objective to enhance the flow field during the intake stroke of the engine. Modification of the intake flow field can potentially affect the subsequent combustion. The insert was conceptualized in the author's laboratory. Details of the development project, simulation results, evaluation on a swirl measurement flow bench, and engine test results are provided in [29]. The impact of the intake insert is highlighted in the following figures. The first effect is on combustion stability quantified here by the coefficient of variation (COV) of indicated mean effective pressure (IMEP) shown in Figure 5-1. The insert has no significant impact on the COV of IMEP up to  $\lambda=1.4$ . At  $\lambda=1.6$ , using the insert reduces the COV of IMEP by

0.5% at advanced ignition timings, and by ~1-2% at the retarded ignition timings. Due to the increased stability, the ignition timing window can also be expanded beyond 330 °CA. In practice, at  $\lambda=1.6$ , enhanced air motion may increase the flame speed (CVCC results in Chapter 4). This in turn may allow more complete combustion for majority of the engine cycles. This can improve the load stability and decrease the COV of IMEP.

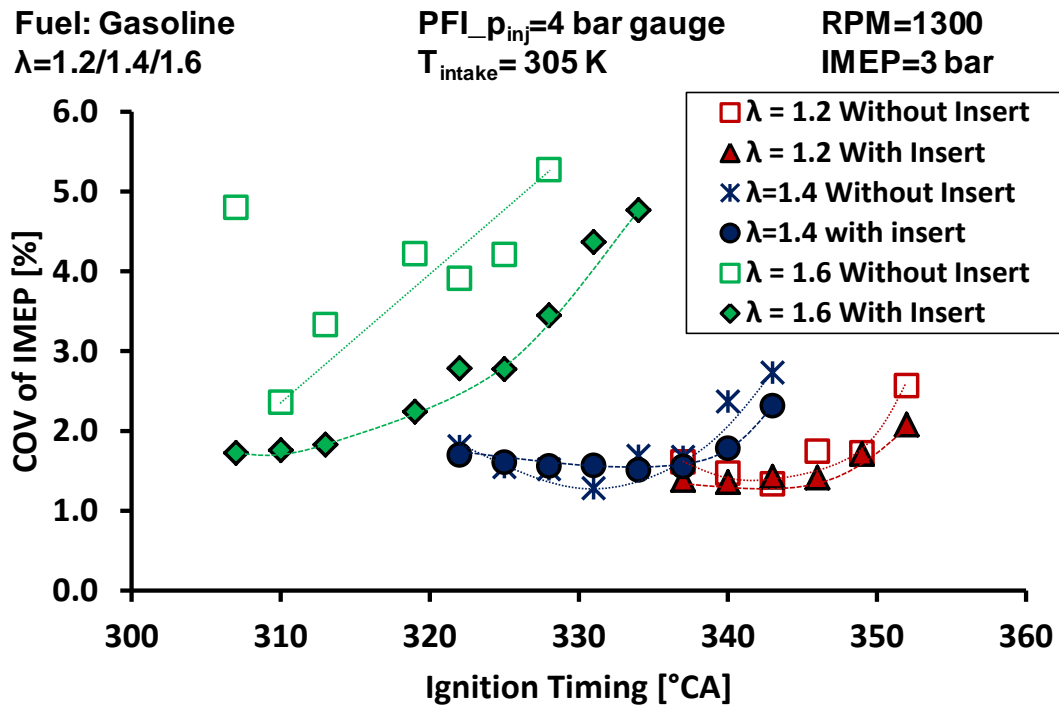


Figure 5-1. COV of IMEP without and with insert at varying  $\lambda$

In terms of start of combustion, using the insert causes the start of combustion (denoted by CA5) to advance by ~1-2 degree crank angle (°CA) at  $\lambda$  of 1.4, and by ~2-3 °CA at  $\lambda$  of 1.6 (Figure 5-2). This implies that the ignition delay is reduced by using the insert. A corresponding advance in the combustion phasing (denoted by CA50) is observed as well (Figure 5-3). If the CA50 is excessively delayed, there will be a drop in the combustion efficiency. Due to these benefits, the insert was used in subsequent engine tests.

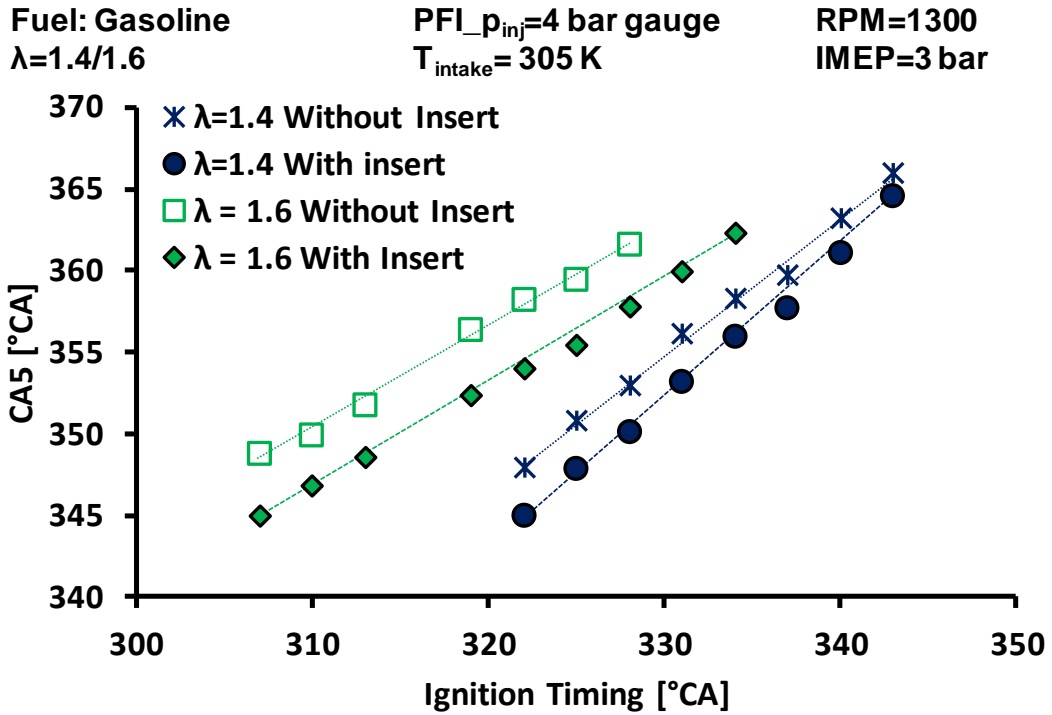


Figure 5-2. CA5 without and with insert at varying  $\lambda$

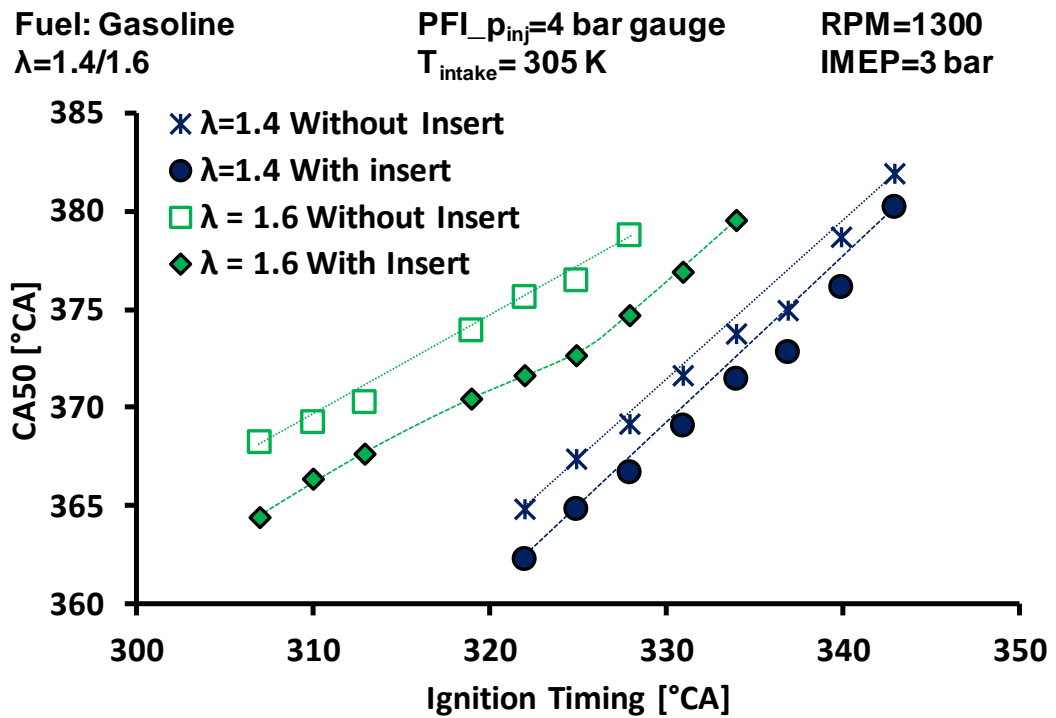


Figure 5-3. CA50 without and with insert at varying  $\lambda$

## ■ Test Matrix and Baseline Combustion Results

The engine test conditions are summarized in Table 5-1. Two main methods of changing charge reactivity are studied. First is changing excess air ratio of the charge from  $\lambda=1.0$  (stoichiometric) to  $\lambda=1.6$ . Second is increasing the intake temperature in two steps from the baseline of  $\sim 313\text{K}$  to  $333\text{ K}$  and  $393\text{ K}$ . This is performed at excess air ratios of 1.4 and 1.6 to understand the effect of temperature on the charge reactivity and combustion duration on the leanest combustion cases.

Table 5-1. Engine Test Conditions

Test type	Air-Fuel Ratio Effect	Temperature Effect
Fuel	Gasoline/Ethanol/DME	
Fuel mass per cycle	$\sim 18.4$ (gasoline) / $\sim 31.2$ (ethanol) mg/cycle	
Engine speed	1300 rpm	
Nominal load	$\sim 3$ bar IMEP	
Spark coil charge duration	5 ms (for gasoline and ethanol only)	
Port fuel injection pressure	4 bar gauge (gasoline and ethanol) / 7 bar gauge (DME)	
Excess Air Ratio ( $\lambda$ )	1.0 / 1.2 / 1.4 / 1.6	1.6 (gasoline and ethanol) $\sim 1.83$ DME
Intake Temperature	313 K	313 / 333 / 393 K

Three fuels are chosen for the engine test with different reactivities – gasoline, ethanol, and DME. The properties of the fuels and additional details on their choice are provided in Chapter 2. For the chosen test conditions, DME combustion does not require spark ignition since DME’s high cetane number causes it to auto-ignite. Therefore, DME combustion results presented in this dissertation are for HCCI type of combustion. Gasoline and ethanol are spark ignited with a constant spark coil charging duration of 5 ms. For the spark ignited tests, the ignition timing is swept between the advance and the retard limit timings for each

condition. These limit timings are based on the broad target of keeping the CA50 between 360 and 380 °CA. Based on experience, the thermal efficiency is usually maximum in this range for this engine setup. When CA50 is outside the 360-380 °CA limit, there is usually a significant drop in engine load (of the order of ~20-30%). The fuel amount is maintained constant for all test points to keep the load at 3 bar IMEP. For increasing the  $\lambda$ , the throttle is progressively opened to increase the mass air flow into the engine. The ignition timing usually must be advanced owing to the increase in the combustion duration as the charge becomes leaner. For increasing temperature, the intake heater power is ramped up and controlled with a PID heater controller.

In the Figures 5-4 to 5-7, the pressure and the heat release rate traces are shown for all three fuels at each of excess air ratios tested at baseline temperature. For ease of comparison, the ignition timings are identical for gasoline and ethanol. Each ignition timing corresponds to the shortest combustion duration observed for gasoline at a given  $\lambda$ . Certain characteristics become apparent. Gasoline and ethanol have similar single hump heat releases with ethanol combustion typically starting before gasoline for all  $\lambda$ . This is expected since the laminar flame speed of ethanol is usually higher than gasoline [100]. The peak pressure and peak heat release rate of ethanol are greater than gasoline for all  $\lambda$ . DME HCCI combustion cannot be directly compared with premixed SI combustion but the contrast between the two is evident. Two peaks of heat release are observed for DME HCCI combustion. The first peak corresponds to the low temperature reactions typically before compression TDC which eventually lead to the combustion of the bulk of the charge. Since combustion can initiate at multiple locations, the overall combustion duration is short, which causes a sharp peak in the heat release rate.

Ignition Timing=340 °CA IMEP=3 bar RPM=1300  $T_{intake}=313\text{ K}$   
 $\lambda=1.0$  PFI\_  $p_{inj}$ =4 (gasoline & ethanol) & 7 (DME) bar gauge

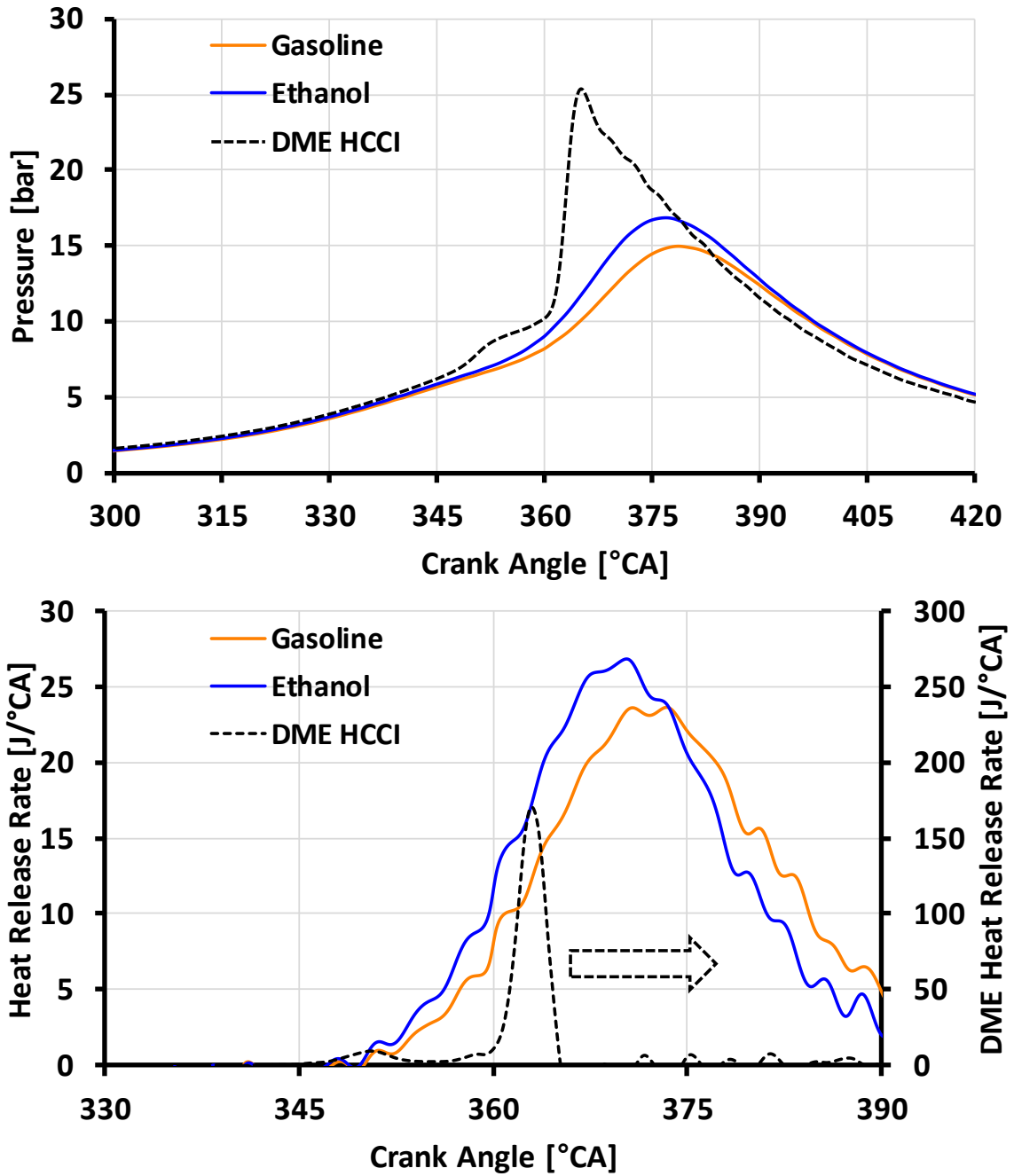


Figure 5-4. Pressure and HRR at  $\lambda=1.0$  for test fuels

Ignition Timing=330 °CA IMEP=3 bar RPM=1300  $T_{\text{intake}}=313\text{ K}$   
 $\lambda=1.2$  PFI\_  $p_{\text{inj}}=4$  (gasoline & ethanol) & 7 (DME) bar gauge

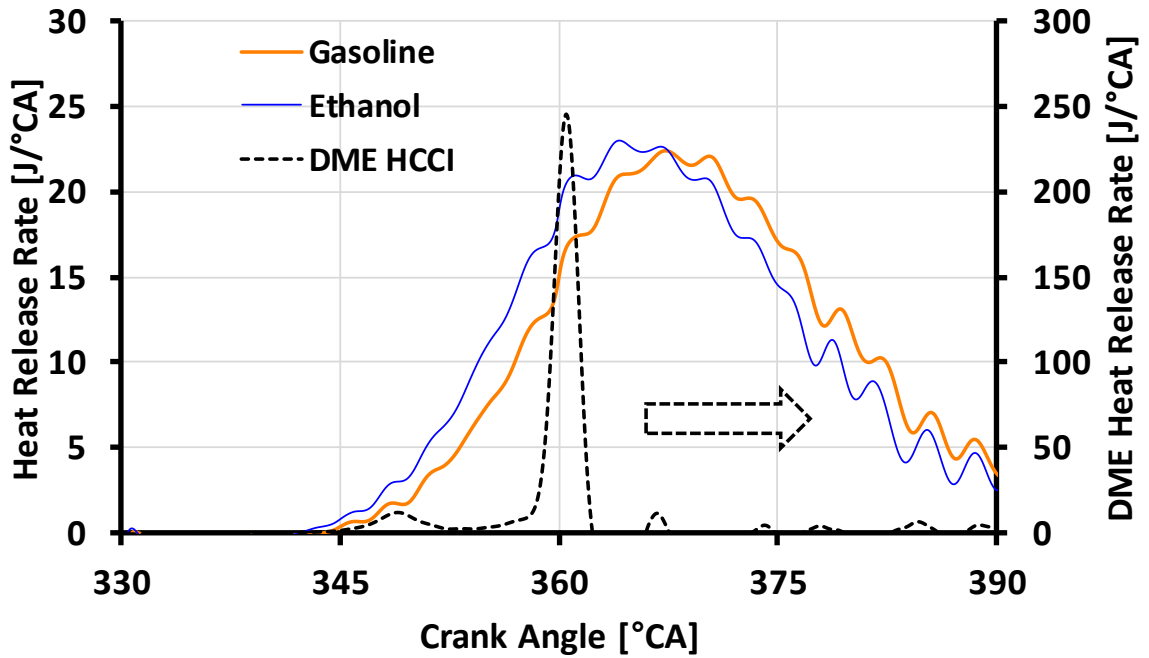
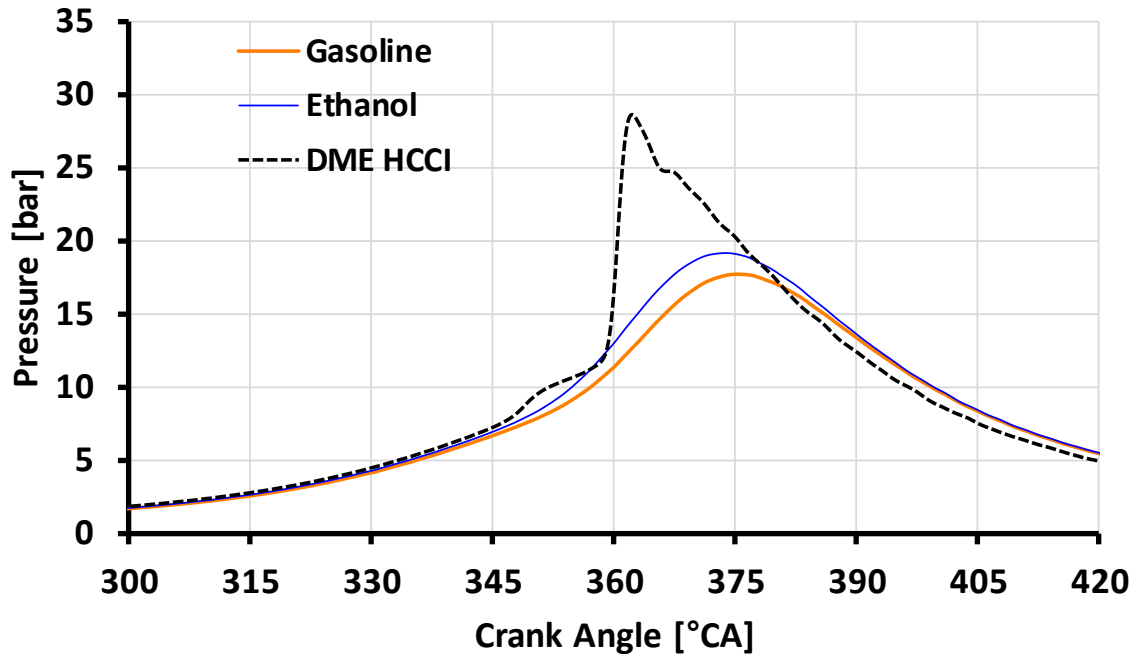


Figure 5-5. Pressure and HRR at  $\lambda=1.2$  for test fuels

Ignition Timing=315 °CA IMEP=3 bar RPM=1300  $T_{\text{intake}}=313\text{ K}$   
 $\lambda=1.4$  PFI\_ $p_{\text{inj}}$ =4 (gasoline & ethanol) & 7 (DME) bar gauge

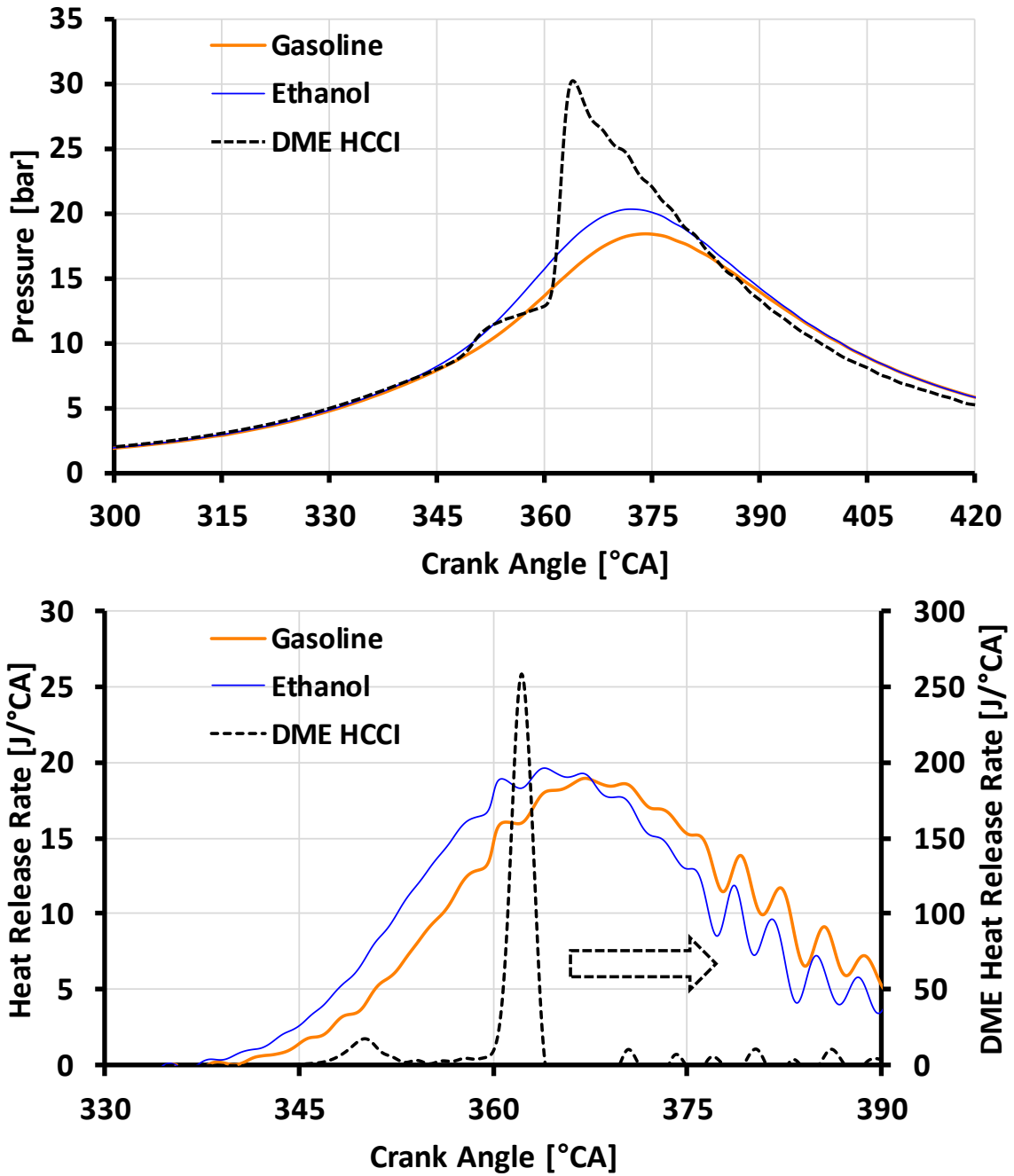


Figure 5-6. Pressure and HRR at  $\lambda=1.4$  for test fuels



Ignition Timing=310 °CA IMEP=3 bar RPM=1300  $T_{\text{intake}}=313\text{ K}$   
 $\lambda=1.6$  PFI\_  $p_{\text{inj}}=4$  (gasoline & ethanol) & 7 (DME) bar gauge

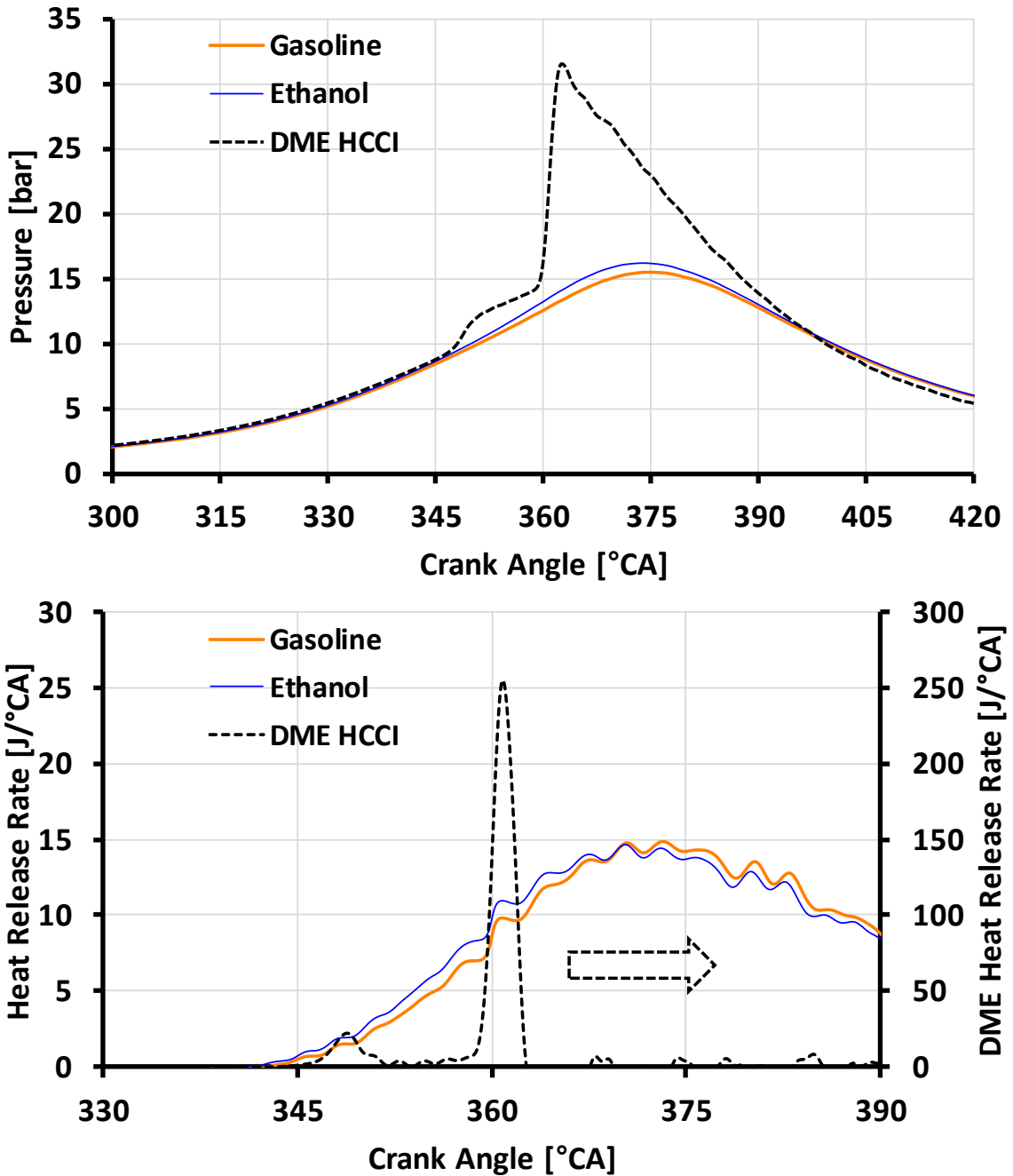


Figure 5-7. Pressure and HRR at  $\lambda=1.6$  for test fuels

The start of combustion (CA5), combustion phasing (CA50) and combustion duration (CA5 to CA95) for the four examples in Figures 5-4 to 5-7 are summarized in Table 5-2.

Table 5-2. Summary of CA5, CA50 and Combustion Duration

	Fuel	Excess Air Ratio ( $\lambda$ )			
		1.0	1.2	1.4	1.6
Ignition Timing [ $^{\circ}$ CA]	Gasoline	340	330	315	310
	Ethanol	340	330	315	310
	DME	HCCI			
CA5 [ $^{\circ}$ CA]	Gasoline	361.6	356.9	354.4	359.4
	Ethanol	359.8	354.8	351.2	358.6
	DME	350.4	350.1	350.4	349.1
CA50 [ $^{\circ}$ CA]	Gasoline	375.2	371.4	372.2	381.6
	Ethanol	372.3	369.1	368.5	380.3
	DME	358.3	359.2	361.7	361.2
Combustion Duration [ $^{\circ}$ CA]	Gasoline	65.0	62.2	63.7	74.9
	Ethanol	69.1	65.5	63.3	70.2
	DME	16.8	14.6	14.3	14.0

The author would like to emphasize that owing to the different ignition timings, the CA5 and CA50 results presented in Table 5-2 should not be used to compare between different excess air ratios. The purpose of presenting these numbers is to make some broad observations which are investigated further. The CA5 and CA50 of ethanol are more advanced compared to those of gasoline. The overall combustion duration of gasoline is however lower or similar to the combustion duration of ethanol except at  $\lambda=1.6$ . This suggests that the later half of gasoline combustion is faster than that of ethanol (period from

CA50 to CA95). At  $\lambda=1.6$ , even advancing the ignition timing of gasoline and ethanol to 310 °CA does not advance the CA5.

When the excess air ratio is increased by opening the throttle, the intake pressure increases from 0.4 bar absolute to 0.556 bar. Increase in the intake pressure can increase the fuel reactivity for HCCI combustion and advance the CA5 and CA50 [118]. For DME HCCI, the combustion duration decreases from  $\lambda=1.0$  to  $\lambda=1.6$ . No clear trend is observed for DME's CA5 and CA50 results summarized in Table 6-2.

### ■ Excess Air Ratio Effect

In this section, the effect of the excess air ratio is examined in detail through select results at baseline temperature. The results for gasoline and ethanol are presented in the form of ignition timing sweeps. The DME HCCI results are listed on each figure for reference. First, the analysis of the pressure-based signal is presented followed by the emission results. Finally, a brief description on the ion current results is provided.

The two important parameters of interest in this research are the start of combustion (CA5), and the combustion duration. They are illustrated in Figure 5-8 for three excess air ratios of 1.0, 1.2, and 1.6. With increasing excess air ratio, CA5 retards. The CA5 for ethanol is always earlier compared to gasoline for the same  $\lambda$  and ignition timing. With retardation of the ignition timing, the CA5 retards monotonically. The error bars in the figures represent the standard deviation of the data collected over 200 cycles. With increasing  $\lambda$ , the flame speed for SI combustion is expected to decrease provided there is no change in the background charge motion. The charge reactivity would decrease as  $\lambda$  increases. This may explain the retardation of the CA5 and CA50 with increasing  $\lambda$ .

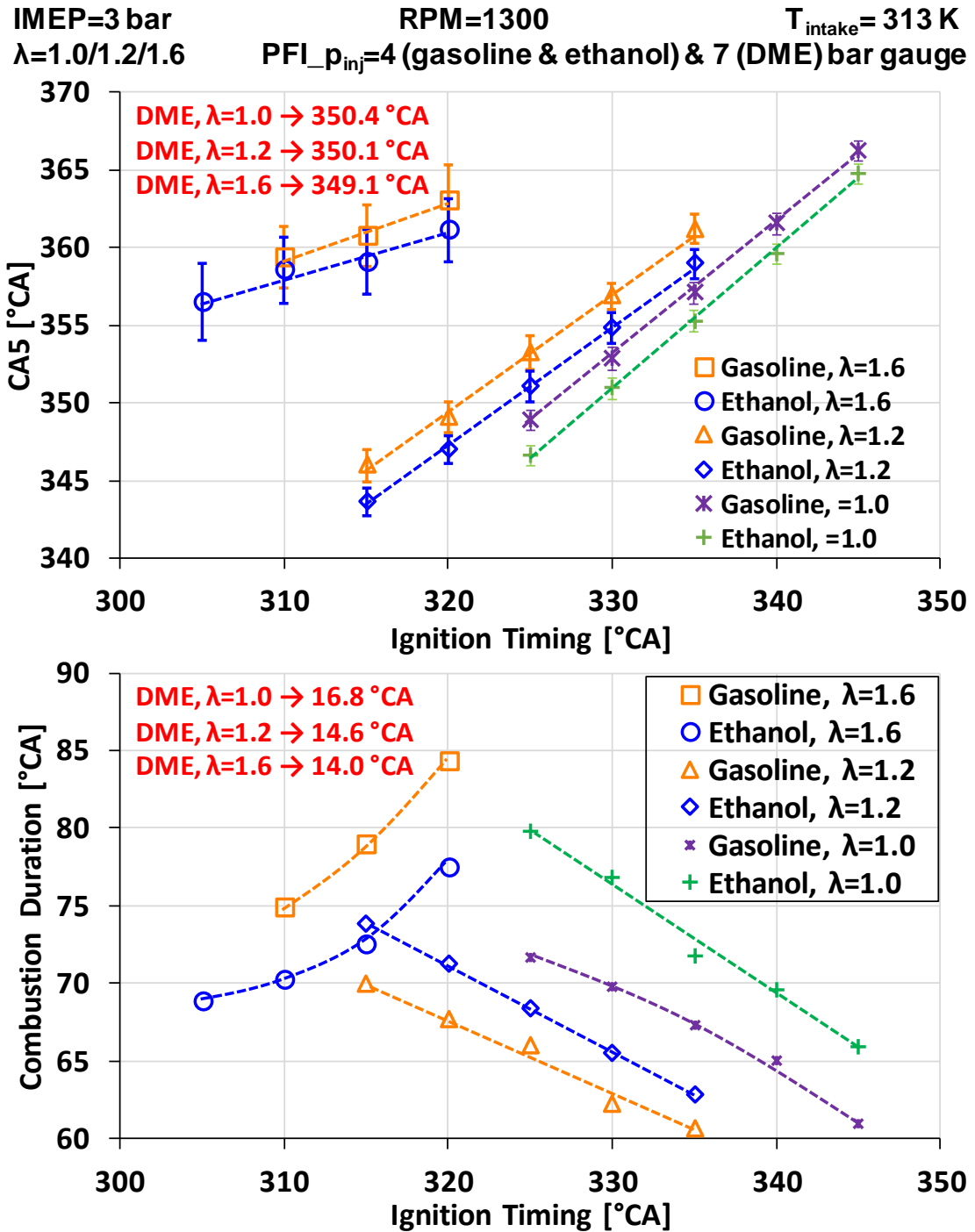


Figure 5-8. CA5 (top) and combustion duration (bottom) at 313 K

A few observations can be made of the combustion duration of gasoline and ethanol (Figure 5-8). First, the combustion duration of gasoline is shorter than that of ethanol for  $\lambda=1.0$  and  $\lambda=1.2$  over the entire range of ignition timing. The combustion durations of both fuels are

very similar at  $\lambda=1.4$  (not shown). The trend shifts when  $\lambda=1.6$ , with gasoline combustion duration significantly longer than that of ethanol. Second, for both ethanol (green) and gasoline (purple), the combustion duration at  $\lambda=1.0$ , is longer than at  $\lambda=1.2$ . Therefore, in the remaining figures of this section, comparisons of  $\lambda$  of 1.2 and 1.6 will be shown only since they represent the fastest and slowest combustion for this set of results. Third, at  $\lambda$  of 1.0 and 1.2, the combustion duration decreases as the timing is retarded. However, at  $\lambda=1.6$ , the combustion duration increases as the timing is retarded. This can be understood from the combustion phasing (CA50) plot shown in Figure 5-9.

When the ignition timing is retarded, the combustion phasing retards as well for  $\lambda=1.2/1.6$ . However, for  $\lambda=1.2$ , when the ignition timing is retarded, the CA50 gets retarded into the 360 to 380 °CA zone where the thermal efficiency is typically maximized for this test setup possibly due to the optimal combination of pressure and temperature. Flame speed usually decreases when pressure increases, and flame speed increases when temperature increases [24-25]. If the ignition timing is earlier, the flame may propagate in the increasing pressure environment prevailing in the cylinder as the piston approaches TDC. With a later timing, the flame propagation may still be in higher pressure environment, but the temperature is expected to be significantly higher than that at the compression TDC. For  $\lambda=1.6$ , when the ignition timing is retarded, the CA50 is retarded beyond 380 °CA. This can be caused by the lower reactivity of the charge under lean conditions. Moreover, later in the expansion stroke, the temperature may also not be sufficiently high to enhance the flame speed. The CA50 of ethanol is earlier for gasoline for  $\lambda=1.2/1.6$ . However, the end of combustion (CA95) for gasoline combustion is marginally earlier than that of ethanol at  $\lambda=1.2$  which suggests that the second half of the combustion is faster for gasoline at  $\lambda=1.2$ . At  $\lambda=1.6$ ,

gasoline's CA95 is more than 5 °CA later than the CA95 of ethanol. These observations will be further discussed in the next chapter using chemical kinetic simulations.

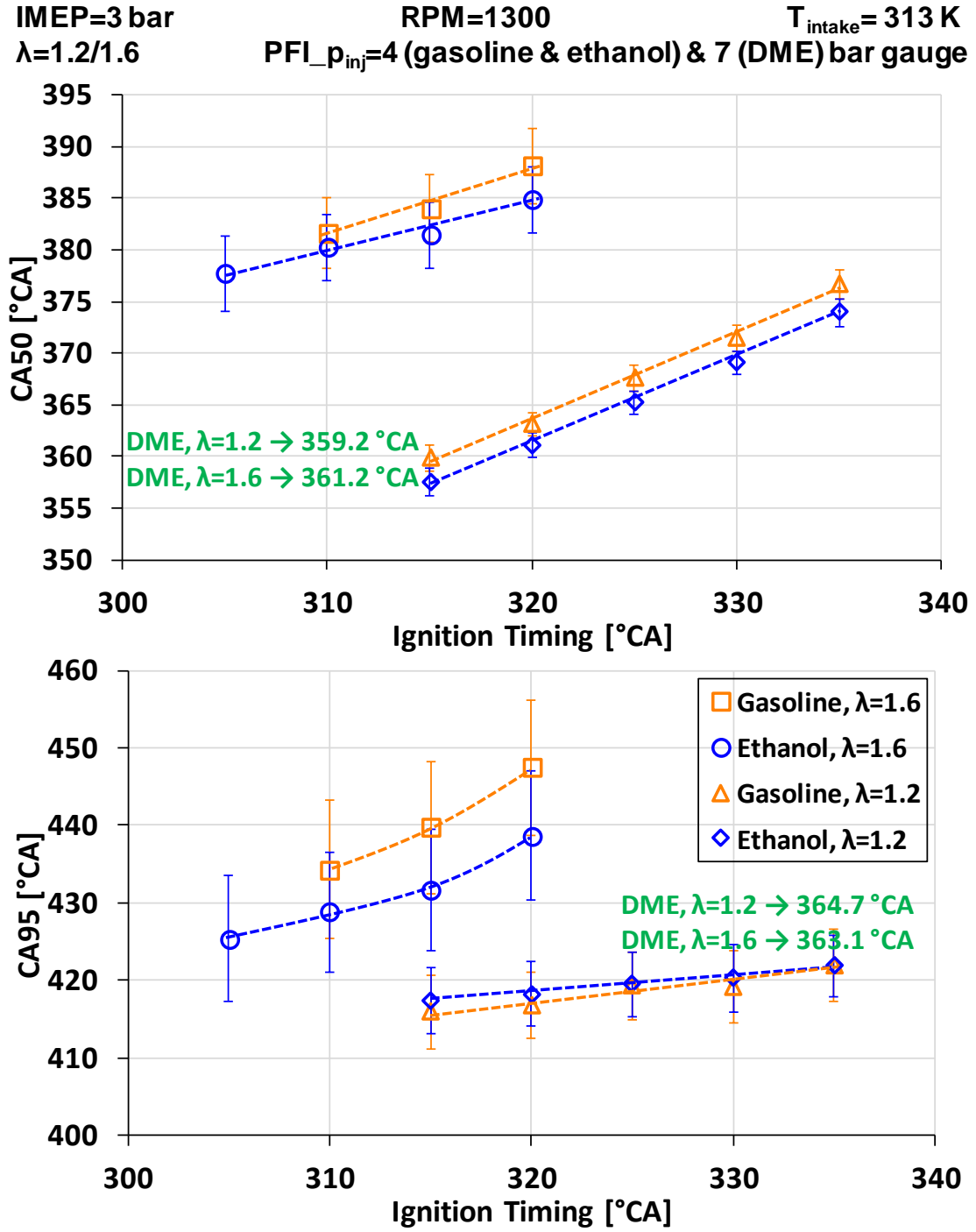


Figure 5-9. CA50 (top) and CA95 (bottom) at 313 K

In the figures above and the following, the DME HCCI results are also listed. The ignition timing is not applicable as there is no spark, hence, they are not plotted on the individual figure. HCCI combustion is very different from the SI combustion of gasoline and ethanol but the purpose of showing these values is to provide a context for the subsequent numerical analysis of DME HCCI (Section 6.1.3).

The primary purpose of the engine tests is to study the impact on combustion duration, and no attempts are made to mitigate the regulated components of the engine exhaust. However, a brief description of the NO<sub>x</sub> and CO emissions (Figure 5-10) is provided here to further understand the implications of lean combustion. One of the main advantages of using a leaner charge in an SI engine is the reduction of NO<sub>x</sub>. From  $\lambda=1.2$  to  $\lambda=1.6$ , there is approximately a tenfold reduction in NO<sub>x</sub> emission. Ethanol's NO<sub>x</sub> emission is observed to be lower than gasoline which could be due to the higher heat of evaporation which reduces charge temperature during the intake stroke when the ethanol spray evaporates.

CO is typically a product of incomplete combustion. The trends for CO are shown in Figure 5-10 as well. CO is observed to be lower for gasoline at  $\lambda=1.2/1.6$  compared to CO for ethanol. The CO emission at  $\lambda=1.2$  is higher than  $\lambda=1.6$ . This could be due to the higher availability of oxygen at lean conditions which can oxidize the CO. As the timing is retarded, CO emission tends to increase which could be due to insufficient time for complete combustion. DME HCCI's NO<sub>x</sub> and CO emissions are similar to those of gasoline at the same  $\lambda$ . The difference in the CO emission between the fuels and at different excess air ratios will be discussed further in the chemical kinetic simulations in the next chapter.

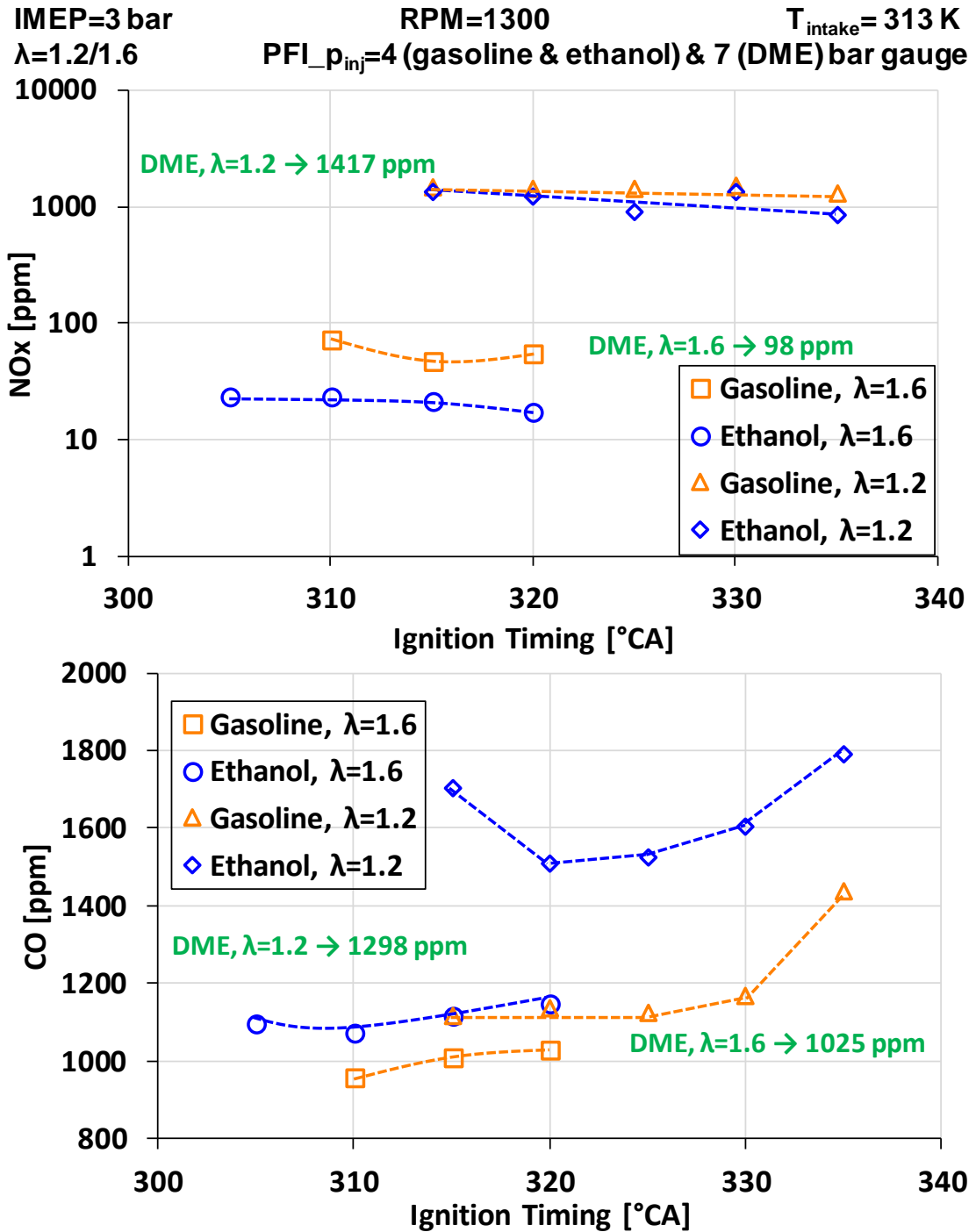


Figure 5-10. NOx emission (top) and CO emission (bottom) at 313 K

The indicated thermal efficiency (ITE) can be calculated from the fuel measurement and the IMEP. The results are presented in Figure 5-11. The ITE is between 28 to 33.5% for all cases. The ITE for ethanol is lower than gasoline. For  $\lambda=1.2$ , it is evident that a very



advanced or a very retarded timing will cause a drop in the load. This trend is observed for both gasoline and ethanol. Though the combustion duration decreases (Figure 5-8), the rise in CO emission could indicate a drop in the combustion efficiency. For  $\lambda=1.6$ , retarding the ignition timing causes the thermal efficiency to drop, which is probably caused by the delayed CA50.

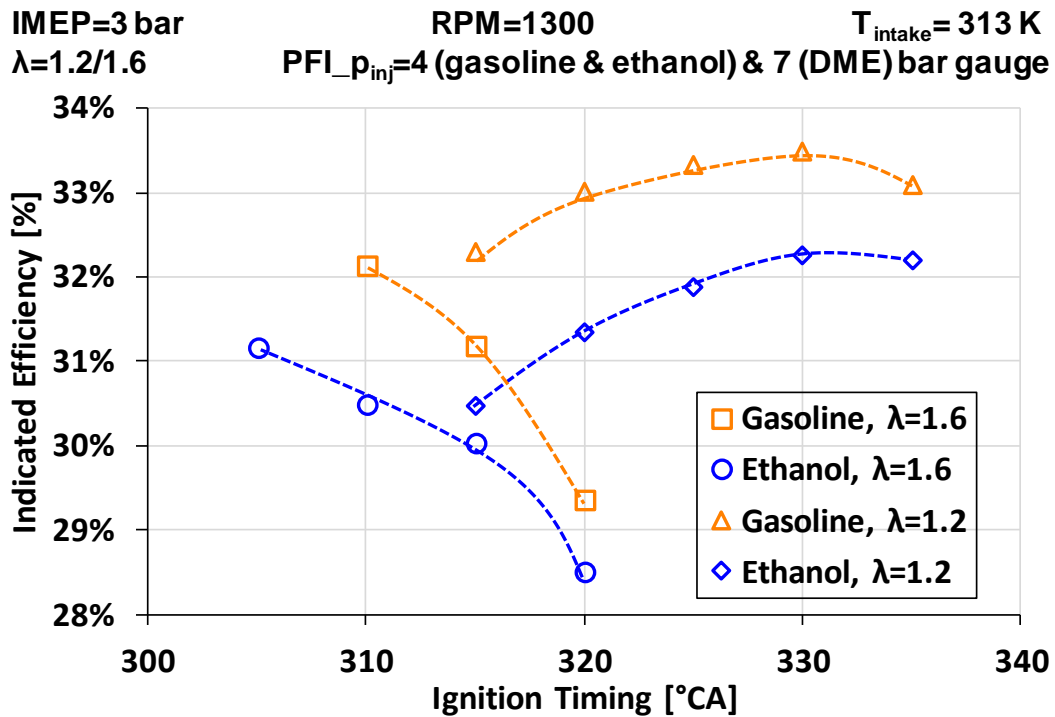


Figure 5-11. Indicated thermal efficiency at 313 K

The ion current signal is processed according to the method explained in Chapter 3. There are two locations – plug probe (in the spark breakdown vicinity) and the auxiliary probe located 25.6 mm from the spark plug on the cylinder head (Figure 3-5). The crank position for the ion signal peaks for gasoline (denoted by ‘g’ followed by  $\lambda$ ) and ethanol (denoted by ‘e’ followed by  $\lambda$ ) at various excess air ratios and ignition timings are plotted against CA5. Unlike the CA5, which is derived from the cylinder averaged pressure signal, the ion signal reflects more localized phenomena.

Ignition Timing Sweep  
 $\lambda=1.0/1.2/1.4/1.6$

PFI\_p<sub>inj</sub>=4 bar gauge  
T<sub>intake</sub>= 313 K

RPM=1300  
IMEP=3 bar

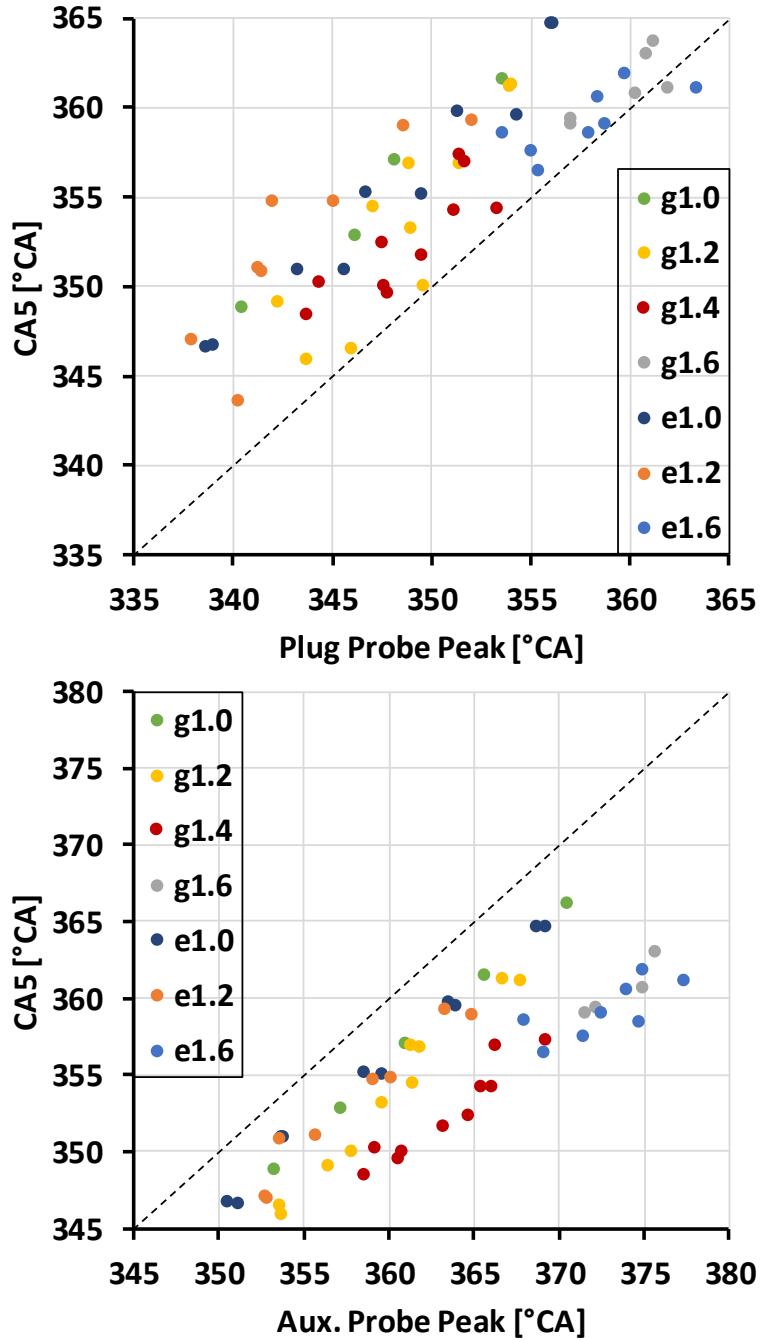


Figure 5-12. Scatter of ion current peak position – plug and auxiliary probe

The peak of the spark probe ion signal is more advanced than the CA5 as shown in Figure 5-12. This peak could be caused by the growth of the initial flame kernel which may not

be a detectable change for the wide range pressure transducer. Conversely, the peak of the auxiliary probe is retarded compared to the CA5. This could be due to flame propagation away from the spark plug which has caused a significant change in the cylinder pressure. Since the first peaks of the ion signals can represent passage of the flame front (Chapter 4), the time difference between the two peaks ( $T_{ion\_diff}$ ) could provide some information on the general in-cylinder flame propagation. The  $T_{ion\_diff}$  for gasoline combustion at various excess air ratios is shown in Figure 5-13. A lower value of  $T_{ion\_diff}$  could indicate faster flame propagation between the ion probes. The results correspond with the combustion duration results in terms of the  $\lambda$  trends (Figure 5-8). The trend with respect to ignition timing is not clear especially for  $\lambda=1.0/1.2$ . The lowest and highest durations of 8 ( $\lambda=1.2$ ) and 17.5 ( $\lambda=1.6$ ) °CA can roughly translate to a flame propagation speed of 25 and 11.4 m/s between the two probe locations.

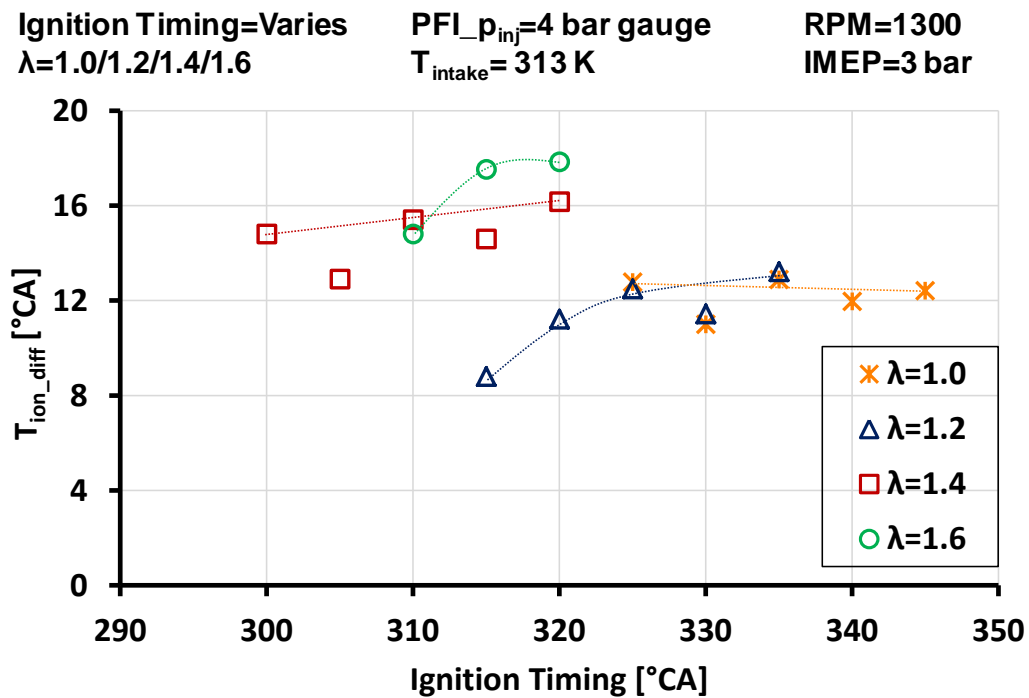


Figure 5-13. Ion signal peak difference for gasoline combustion at 313 K

## ■ Temperature Effect

A method to increase the charge reactivity under lean conditions is increasing the initial temperature of the charge ( $T_{\text{intake}}$ ). This method is applied to study the effect of intake temperature on the start of combustion and combustion duration for gasoline and ethanol at the leanest condition of  $\lambda=1.6$ . Two increments of intake temperature above the baseline are made for this study – 20 K ( $T_{\text{intake}}=333$  K) and 80 K ( $T_{\text{intake}}=393$  K), both achieved through intake heating. This range of increase in intake temperature is possible in modern engines without additional heating by using EGR.

Gasoline (Figure 5-14) and ethanol (Figure 5-15) show similar trends. The first increment of 20 K to raise the intake temperature to 333 K has a marginal effect on advancing the CA5 – approximately 1-2 °CA. The CA50 follows a similar trend to the CA5 (not shown). For the given experimental setup and test conditions, at 333 K, the CA50 advances into the 360-380 °CA band for gasoline. The overall decrease in the combustion duration is more significant – of the order of 5-10 °CA. Further increase in the intake temperature to 393 K causes the CA5 to advance to  $\lambda=1.0$  levels. Gasoline's combustion duration is longer than that of ethanol at the baseline temperature. However, it is observed that gasoline's change in combustion duration with increasing temperature is more significant compared to ethanol. At 393 K, the advance in the ignition timing has a stronger tendency to advance the CA5 compared to the lower temperatures. Additionally, at 393 K, change in the ignition timing doesn't have a major effect on the overall combustion duration.

Fuel=Gasoline  
 $\lambda=1.6$

PFI\_p<sub>inj</sub>=4 bar gauge  
T<sub>intake</sub>= 313/333/393 K

RPM=1300  
IMEP=3 bar

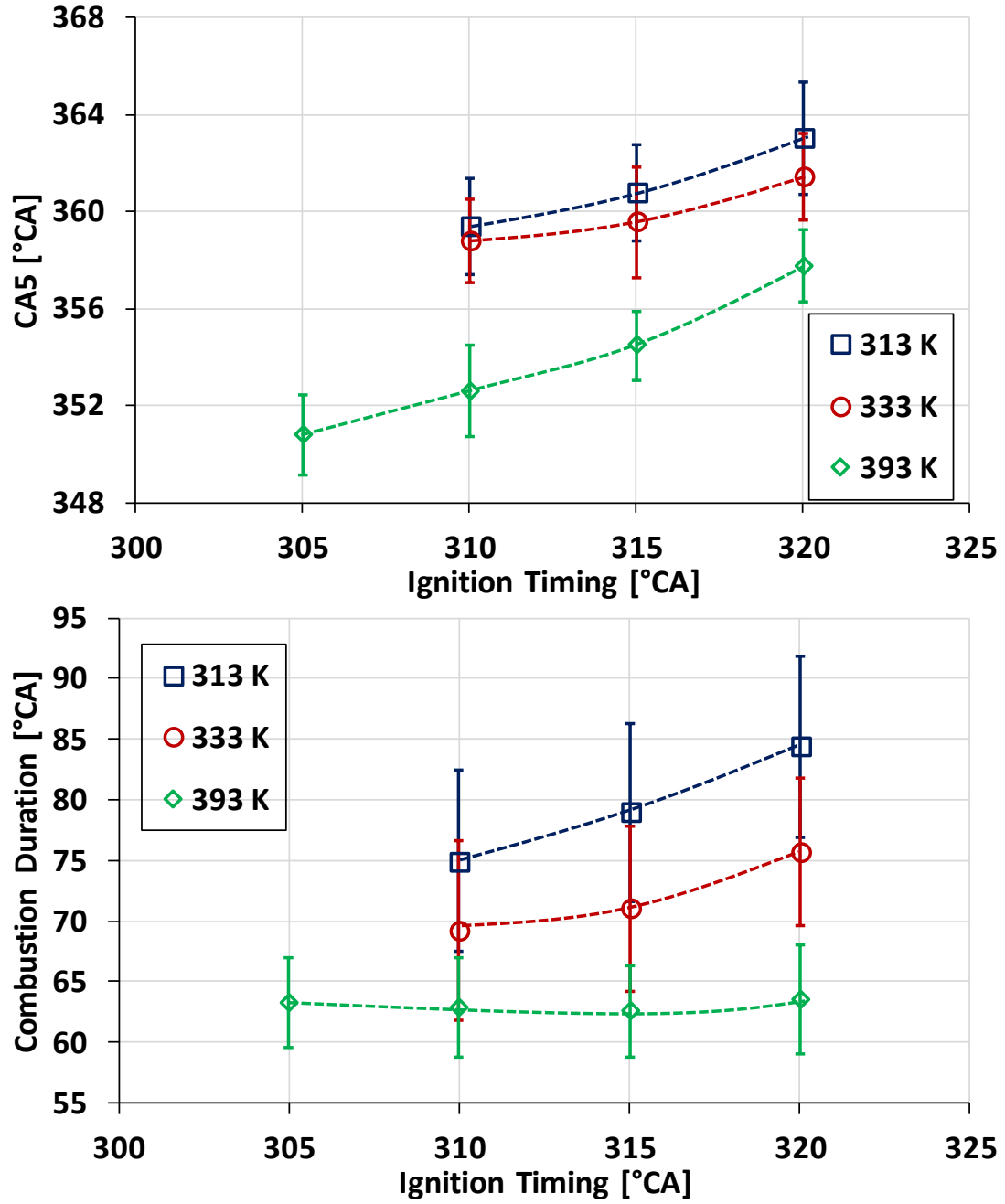


Figure 5-14. Intake heating (gasoline): CA5 (top) and combustion duration (bottom)

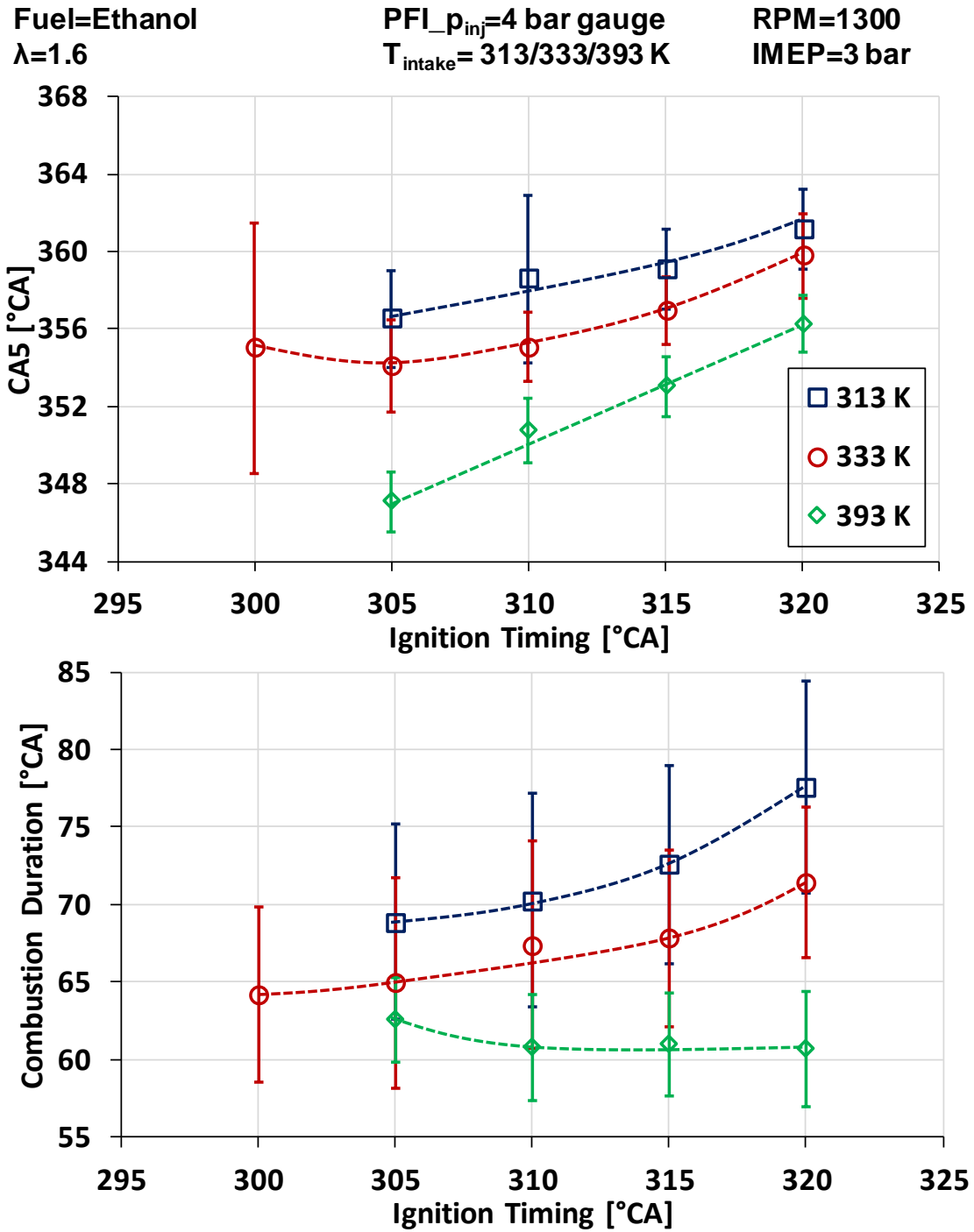


Figure 5-15. Intake heating (ethanol): CA5 (top) and combustion duration (bottom)

The time difference between the ion current peak signals,  $T_{ion\_diff}$ , is shown in Figure 5-16. The trends match the corresponding trends in the combustion duration. For instance, at an ignition timing of 320 °CA, the combustion duration decreases by approximately 20 °CA and the  $T_{ion\_diff}$  decreases by ~8 °CA.

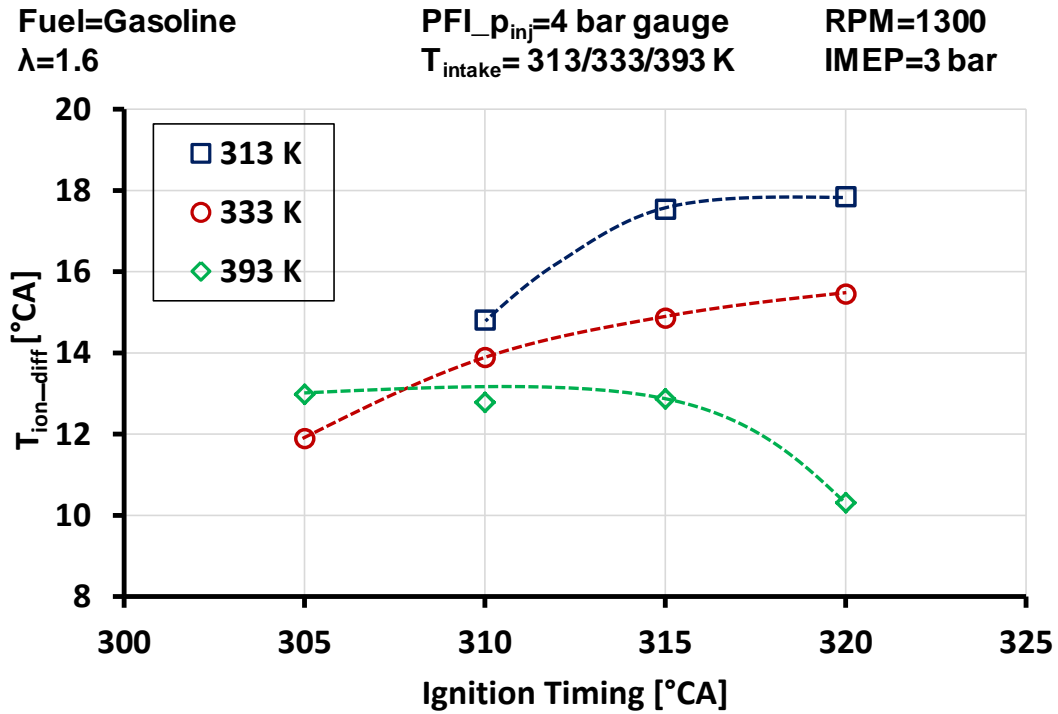


Figure 5-16. Ion signal peak difference for gasoline combustion with intake heating

Two broad conclusions can be made about the flame propagation speed from the engine test results. First, the increase in the excess air ratio reduces the flame propagation speed. The overall trends are similar for each of the gasoline and ethanol test fuels. However, increasing  $\lambda$  may not have equal effect on the charge reactivity for both the fuels. Second, at the leanest condition ( $\lambda=1.6$ ), increase in the intake temperature may cause the flame propagation speed to increase to levels observed at near stoichiometric conditions ( $\lambda=1.2$ ). The temperature effect on NOx and CO emissions is illustrated in Figure 5-17 for gasoline and ethanol at  $\lambda$  of 1.2 ( $T_{intake}=313$  K) and 1.6 ( $T_{intake}=313$  K).

IMEP=3 bar  
 $\lambda=1.2/1.6$   
 RPM=1300  
 PFI\_  $p_{inj}$ =4 (gasoline & ethanol) bar gauge  
 $T_{intake}=313/393$  K

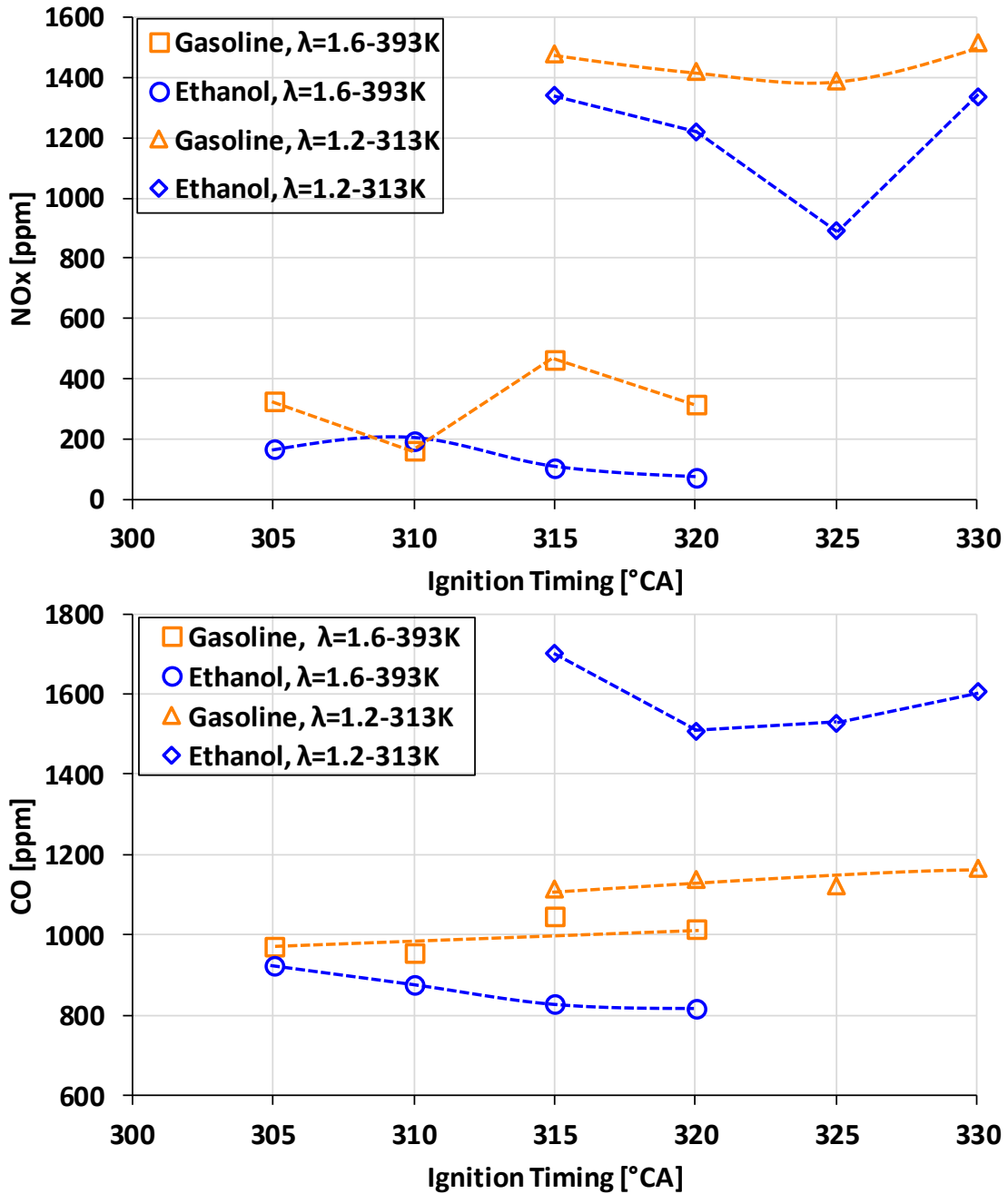


Figure 5-17.  $T_{intake}$  effect on NOx emission (top) and CO emission (bottom)

At  $\lambda=1.6$  and  $T_{intake}=393$  K, the NOx emission is significantly lower than that at  $\lambda=1.2$  and  $T_{intake}=313$  K (Figure 5-17). This trend is consistent for both gasoline and ethanol. Ethanol case's NOx emission at elevated temperatures is marginally lower than gasoline which



agrees with the results presented in Section 5.3 at baseline temperature. However, when intake temperature is increased at  $\lambda=1.6$ , the NO<sub>x</sub> emission increases. This is probably due to the increase in the peak cylinder temperature. CO emissions are also lower for  $\lambda=1.6$  at  $T_{\text{intake}}=393$  K when compared to  $\lambda=1.2$  at  $T_{\text{intake}}=313$  K (Figure 5-17). In fact, the CO emissions do not change significantly when  $T_{\text{intake}}$  is increased from 313 to 393 K at  $\lambda=1.6$ . An additional advantage of increasing  $T_{\text{intake}}$  at  $\lambda=1.6$  is the decrease in the COV of IMEP. This is illustrated in Figure 5-18 for gasoline. Similar trend is observed for ethanol (not shown). The COV of IMEP at  $\lambda=1.6$  decreases from ~15% to ~5% when  $T_{\text{intake}}$  increases from 313 K to 393 K. At the baseline temperature, the high COV of IMEP at  $\lambda=1.6$  could be caused by partial or complete misfire cycles which may also lower the indicated thermal efficiency as discussed previously (Figure 5-11). Therefore, in practice, increasing  $T_{\text{intake}}$  at  $\lambda=1.6$  may provide certain benefits if the heating process does not consume fuel.

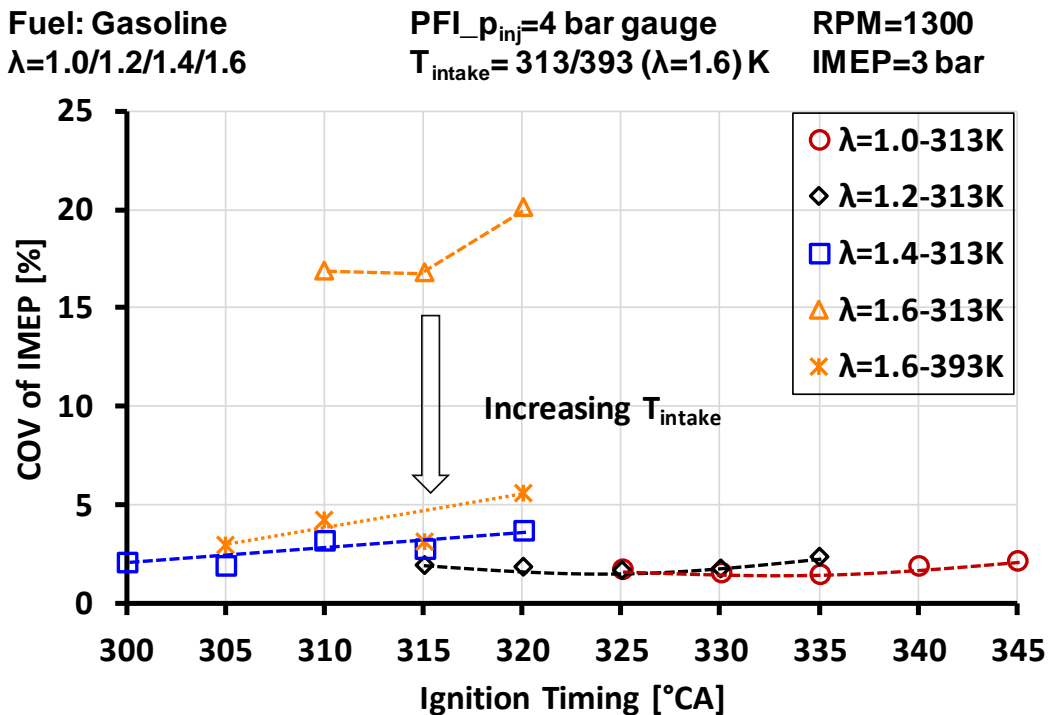


Figure 5-18. COV of IMEP – changing  $\lambda$  and  $T_{\text{intake}}$

## ■ Extending Lean Limit of DME HCCI

A brief description of  $\lambda$  and  $T_{\text{intake}}$  effects on DME HCCI is provided in this section. Owing to its high cetane number, DME undergoes compression ignition under the given experimental conditions. The overall combustion duration of DME is much shorter compared to the SI combustion of gasoline and ethanol. At the baseline intake temperature of 313 K, with increase in excess air ratio, the combustion duration decreases up to  $\lambda=1.6$  (Figure 5-19). The COV of IMEP decreases as well. The CA5 is advanced and the CA50 is retarded (Figure 5-20). These observations may be explained by two factors. First, the intake pressure increases with increasing throttle opening which can advance the start of combustion for HCCI combustion due to enhancement of the low temperature reaction rates [118]. Second, the retardation of the CA50 with increase in  $\lambda$  would suggest that the duration of the first half of combustion (CA5 to CA50) increases with increasing  $\lambda$ . However, the overall combustion duration decreases with increasing  $\lambda$  (up to  $\lambda=1.6$ ) since the duration of the second half of the combustion (CA50 to CA95) becomes shorter with increasing  $\lambda$ . The second half of combustion typically occurs during the expansion stroke when cylinder temperature is increasing and is probably a consequence of the high temperature reactions associated with DME oxidation.

Due to the high reactivity of DME, the excess air ratio can be increased to  $\lambda=1.7$  at which a significant increase in the combustion duration is observed (Figure 5-19). Since there is no major change in the CA5 or the CA50 (Figure 5-20), this suggests that again, the duration of the second half of the combustion (CA50 to CA95) becomes longer. Therefore, for the given experimental setup and test conditions, combustion duration and the CA50-CA95 period are the shortest at  $\lambda=1.6$ . With increasing intake temperature, the combustion

duration can be decreased while the  $\lambda$  can be increased further to  $\sim 1.8$ . The extension of  $\lambda$  is limited by the COV of IMEP which increases drastically at the leanest condition of  $\lambda=1.83$  even with  $T_{\text{intake}}$  at 393 K. CA5 and CA50 are both advanced with increasing  $T_{\text{intake}}$ .

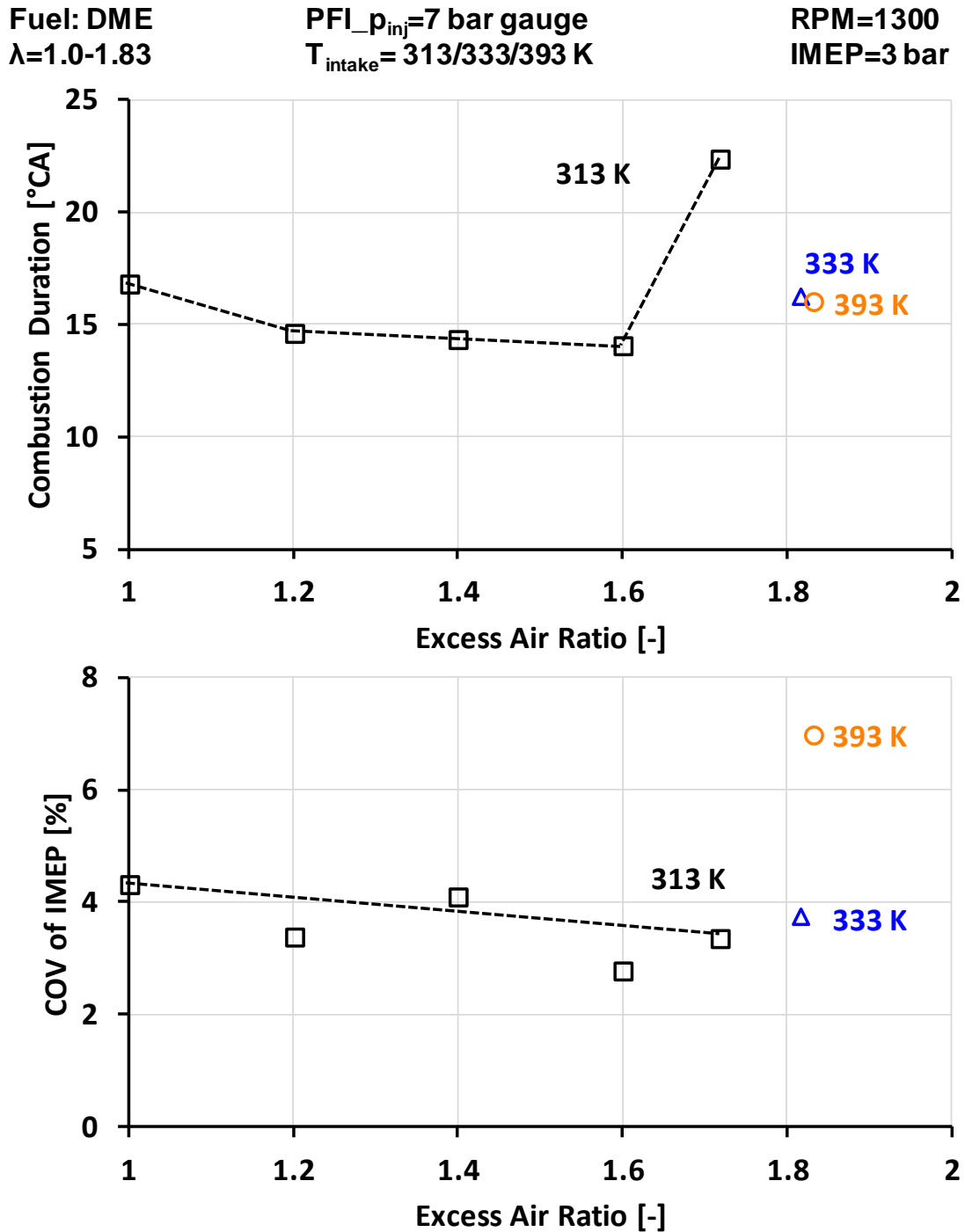


Figure 5-19. Effect of increasing  $\lambda$  on CD and COV of IMEP for DME

Fuel: DME  
 $\lambda=1.0-1.83$

PFI\_  $p_{inj}$  = 7 bar gauge  
 $T_{intake} = 313/333/393$  K

RPM=1300  
IMEP=3 bar

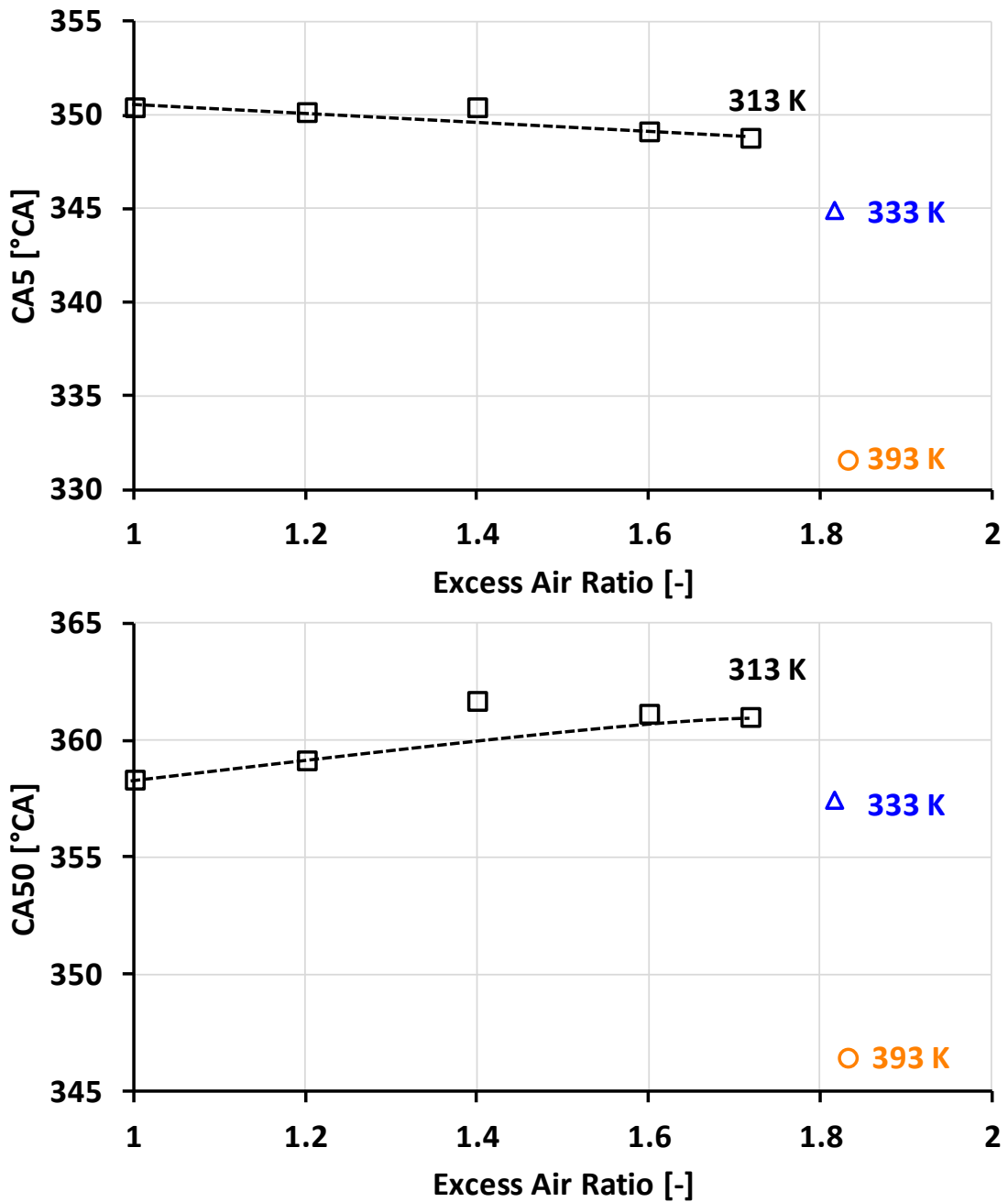


Figure 5-20. Effect of increasing  $\lambda$  on CA5 and CA50 for DME

The NOx and CO emissions are shown in Figure 5-21 – both NOx and CO emissions decrease with increasing  $\lambda$ . When  $T_{\text{intake}}$  is increased, even though  $\lambda$  is higher, the NOx emission increases while the CO emission decreases.

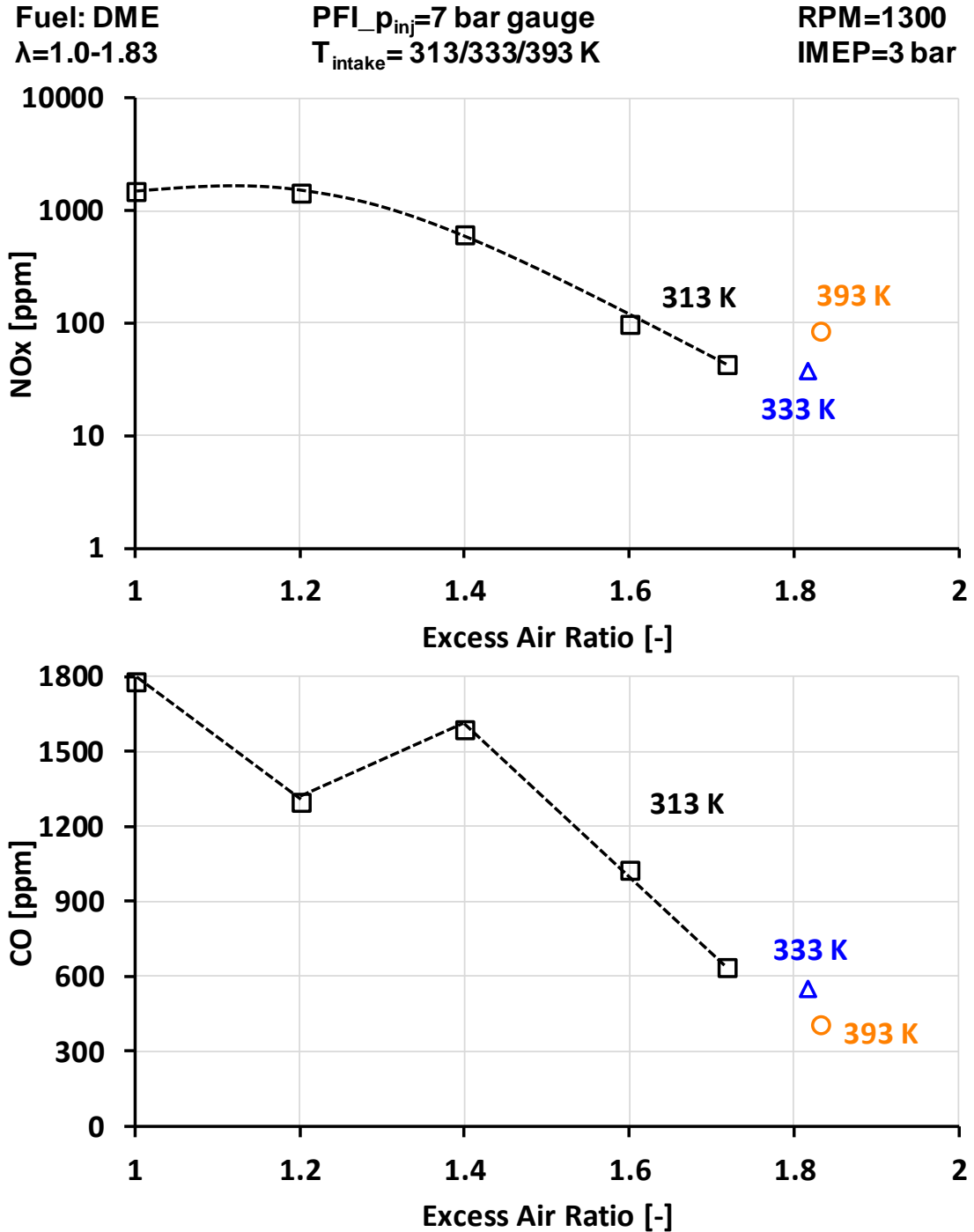


Figure 5-21. Effect of increasing  $\lambda$  on NOx and CO emissions for DME

## ■ Summary of Engine Test Results

The effects of changing the experimental variables are summarized in Table 5-3. These may only be valid for the given experimental conditions and test setup.

Table 5-3. Impact summary of experimental variables

<b>Action</b>	<b>Start of Combustion</b>	<b>Combustion Duration</b>	<b>COV<sub>IMEP</sub></b>	<b>NO<sub>x</sub></b>	<b>CO</b>
<b>Intake Flow Modification</b>	Advance	Decrease	Decrease	No major effect	No major effect
<b>Increase <math>\lambda</math> – SI Combustion</b>	Retard	Increase	Increase	Decrease	Decrease
<b>Increase <math>\lambda</math> – DME HCCI Combustion</b>	Advance	Decrease	Decrease	Decrease	Decrease
<b>Increase T<sub>intake</sub> at <math>\lambda=1.6</math> – SI Combustion</b>	Advance	Decrease	Decrease	Increase	Decrease

## ANALYSIS OF CHARGE REACTIVITY AND FLOW FIELDS

Two software simulation tools are used in this study. The first is the ANSYS CHEMKIN version 19, which is used to study the chemical kinetics under lean and premixed conditions for the test fuels. The objective is to develop some understanding of the underlying chemical mechanisms which could explain the results of the engine tests. The second tool is the 3-dimensional computational fluid dynamics (CFD) suite Converge which is used to simulate the in-cylinder flow field with additional emphasis on the region in the vicinity of the spark plug. The purpose of the CFD simulation is to estimate the flow velocities in the cylinder during the time of ignition.

### Chemical Simulations

CHEMKIN simulations are performed under different excess air ratios to determine the overall scheme of reactions. Two types of 0-dimensional models are used. The Spark Ignition Engine Zonal model is used for gasoline and ethanol, while the Closed Internal Combustion HCCI Engine model is used for DME. The main purpose of these simulations is to understand the effects of change in excess ratio and initial temperature on the combustion chemistry.

The SI and the HCCI engine model inputs are setup using the following methods. The geometric parameters are based on the Yanmar engine used for the engine tests. The simulation period is from the compression BDC to 120 °CA after the compression TDC. The initial pressure is determined from the empirical data. The initial temperature is set to the empirical intake temperatures for the SI model (313 K and 393 K) and to 400 K for the HCCI model. In theory (and practice), DME is the most reactive of the three test fuels. However, for the purposes of the simulation, the initial temperature had to be set to 400 K

for combustion to occur. This is a deviation from the baseline engine test conditions and can probably be attributed to the temperature thresholds in the reaction mechanism.

The heat transfer parameters are tuned to match the experimental motoring pressure for each excess air ratio. The heat transfer parameters are listed in Table D-1 and Table D-2 of Appendix-D for gasoline/ethanol and DME respectively. The dimensionless heat transfer correlation and the Woschini correlation for average cylinder gas velocity are used. The parameters for the Woschini correlation are assumed to be uniform throughout each stroke of the cycle. The SI engine model consists of two homogeneous zones – the unburned and burned. Initially, all the gas is in the unburned zone. The mass exchange between the unburned and burned zone is controlled by the Wiebe function whose parameters are also adjusted. The start of combustion and the combustion duration input for the SI engine model are based on empirical data. A further assumption is a burning efficiency of 100%. The heat transfer and Wiebe function parameters are tuned by comparing the simulation and experimental pressure curves. The default or initial values are obtained from the software manual [119].

The motoring and firing validation results are provided in Appendix D. In general, the motoring and firing pressure traces between the simulation and the experimental results show reasonable correlation with respect to peak pressures and start of combustion. Details of the simulation parameters are summarized in Table 6-1. Each fuel is described separately. Results are shown for three excess air ratios – 1.0, 1.2, and 1.6.  $\lambda=1.4$  was also simulated but has not been presented here since the results were always intermediate of  $\lambda=1.2$  and  $\lambda=1.6$  for all test fuels.



Table 6-1. Parameters for CHEMKIN simulations

Fuel	Gasoline	Ethanol	DME
Reactor Type	SI Dual Zone		HCCI Engine
Geometry	Yanmar NFD-170		
Engine Speed	1300 rpm		
Simulation Period	180 to 480 °CA		
Excess Air Ratio	1.0/1.2/1.4/1.6		
Initial Temperature	313 K / 393 K		400 K
Initial Pressure	Empirical data		
Model Ref.	Mehl <i>et al.</i>	Marinov	Fischer <i>et al.</i>
Heat Transfer	Generalized convective heat transfer coefficient Woschini correlation of average cylinder gas velocity		

### ■ Gasoline surrogate SI combustion

The gasoline surrogate skeletal mechanism consists of 312 species and 1488 reactions. Details of the mechanism can be found in [120-121]. For this research, gasoline is modelled as a mixture of iso-octane ( $iC_8H_{18}$ ) and normal heptane ( $nC_7H_{16}$ ) molecules. The molar ratio of octane and heptane is 9:1, which roughly correlates to the octane number of the fuel used in the experiments. The pressure, temperature, and mole fraction of the primary fuel molecule – iso-octane, are shown in Figure 6-1. All the results are zone-averaged, meaning they are averaged values from the burned and unburned zones of the SI dual zone model. From the pressure traces, it is found that the peak pressure is highest for  $\lambda=1.2$ , followed by  $\lambda=1.0$  and  $\lambda=1.6$ . The temperature rise is earlier for  $\lambda=1.2$ , but the highest bulk gas temperature is estimated for  $\lambda=1.0$ . There is a significant decrease in peak temperature with increase of  $\lambda$ , of the order of  $\sim 500$  K. This could explain the drop in the NO<sub>x</sub> emissions observed in the test results (Figure 5-10).

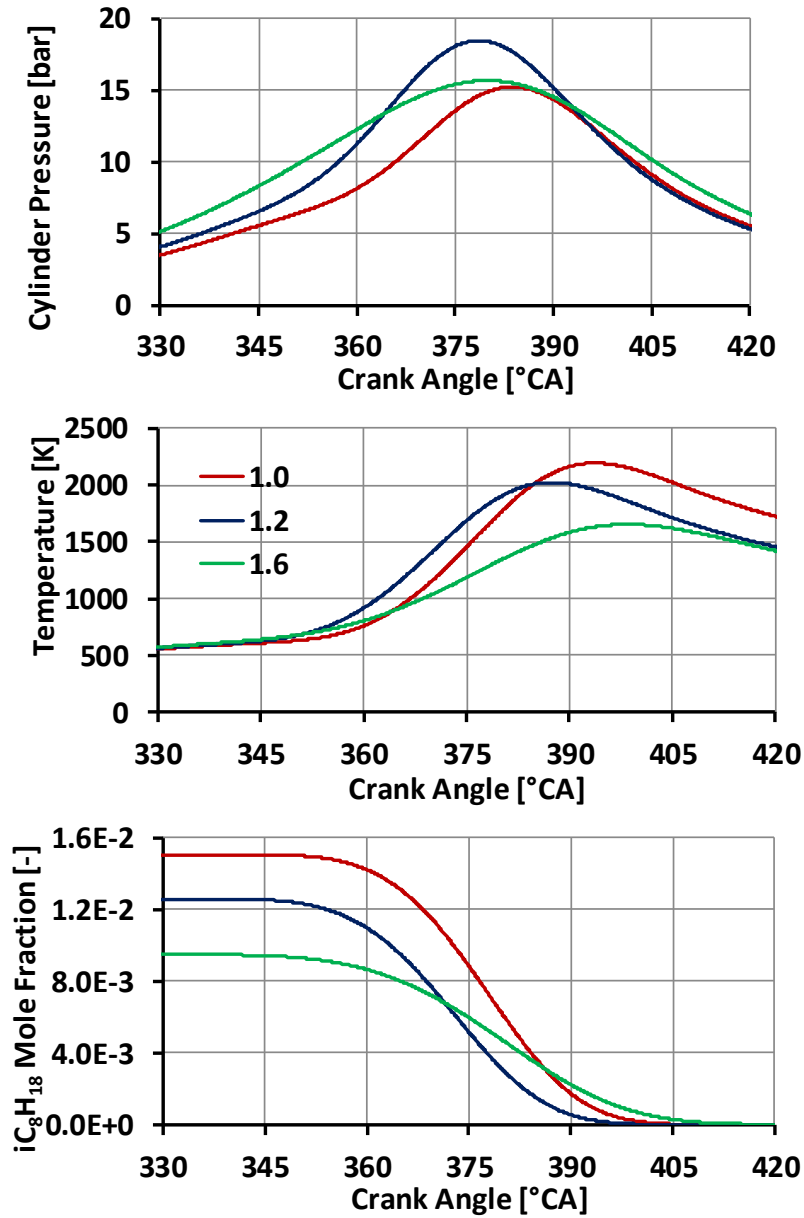


Figure 6-1. Gasoline surrogate – Cylinder pressure, temperature &  $Y_{iC_8H_{18}}$

The mole fractions of each species will be denoted by the symbol  $Y$  followed by the specie in the subscript. For iso-octane, from the mole fraction denoted by  $Y_{iC_8H_{18}}$ , it is estimated that iso-octane is consumed faster at  $\lambda=1.2$ , compared to  $\lambda=1.0$ . This implies that the combustion duration at  $\lambda=1.2$  is shorter than the combustion duration at  $\lambda=1.0$ . This agrees

with the test results (Figure 5-8). Iso-octane oxidation is facilitated by a few key chemical reactions which are listed in Table D-3 (based on [121]).

Figure 6-2 shows the mole fractions of  $\dot{\text{O}}\text{H}$  (hydroxyl),  $\dot{\text{H}}$  (hydrogen),  $\text{H}\dot{\text{O}}_2$  (hydroperoxyl), and  $\dot{\text{C}}\text{H}_3$  (methyl) radicals with respect to crank angle at varying  $\lambda$ . These radicals participate in the chain branching reactions. A few observations can be made. First,  $\lambda=1.6$  produces the lowest concentration of all the radicals shown in the figure. Second, the maximum  $\text{H}\dot{\text{O}}_2$  and  $\dot{\text{C}}\text{H}_3$  radical concentrations at  $\lambda=1.2$  are higher than that at  $\lambda=1.0$ . The methyl radical formation begins later for  $\lambda=1.2$ , compared to  $\lambda=1.0$ , but quickly increases after. Third, the  $\dot{\text{O}}\text{H}$  and  $\dot{\text{H}}$  radical concentrations are highest for  $\lambda=1.0$  though the formation of  $\dot{\text{O}}\text{H}$  starts later when compared to the  $\dot{\text{O}}\text{H}$  formation at  $\lambda=1.2$ . It may then be possible that the  $\text{H}\dot{\text{O}}_2$  and  $\dot{\text{C}}\text{H}_3$  radicals would not be as active in hydrogen abstraction at  $\lambda=1.0$  in comparison to  $\lambda=1.2$ . Fourth, the  $\dot{\text{C}}\text{H}_3$  radical may not play a significant role in the hydrogen abstraction at  $\lambda=1.6$ . Two of the main intermediates are iso-butene ( $\text{iC}_4\text{H}_8$ ) and propene ( $\text{C}_3\text{H}_6$ ). These are typically products of the unimolecular decomposition. Mole fractions of  $\text{iC}_4\text{H}_8$ ,  $\text{C}_3\text{H}_6$ ,  $\text{CH}_4$  (methane), and  $\text{CO}$  are illustrated in Figure 6-3. The concentrations of iso-butene and propene are highest for  $\lambda=1.2$  (Figure 6-3), and very similar for  $\lambda$  of 1.0 and 1.6. This may indicate that unimolecular decomposition is more prevalent for  $\lambda=1.2$  compared to  $\lambda$  of 1.0 and 1.6. The concentration of methane is also highest for  $\lambda=1.2$  followed by  $\lambda=1.0$ , and negligible for  $\lambda=1.6$ .  $\text{CO}$  on the other hand, has the highest concentration for  $\lambda=1.0$ . This is expected since the lower oxygen availability will reduce conversion of  $\text{CO}$  into carbon dioxide ( $\text{CO}_2$ ). At  $\lambda=1.6$ , the  $\text{CO}$  concentration is lowest, and agrees with the trends of the experimental results (Figure 5-10).

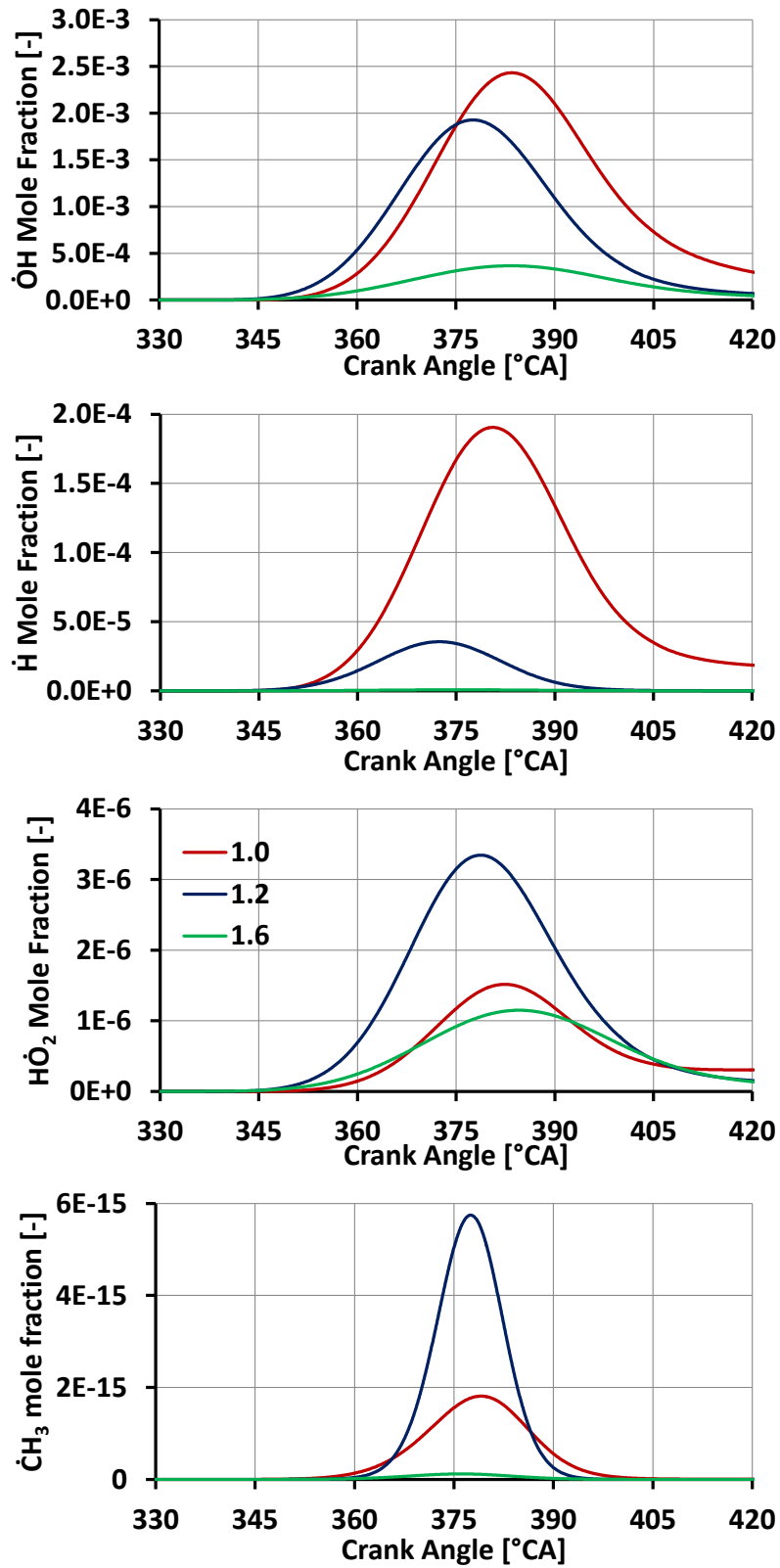


Figure 6-2. Gasoline surrogate –  $Y_{OH}$ ,  $Y_H$ ,  $Y_{HO_2}$ , and  $Y_{CH_3}$

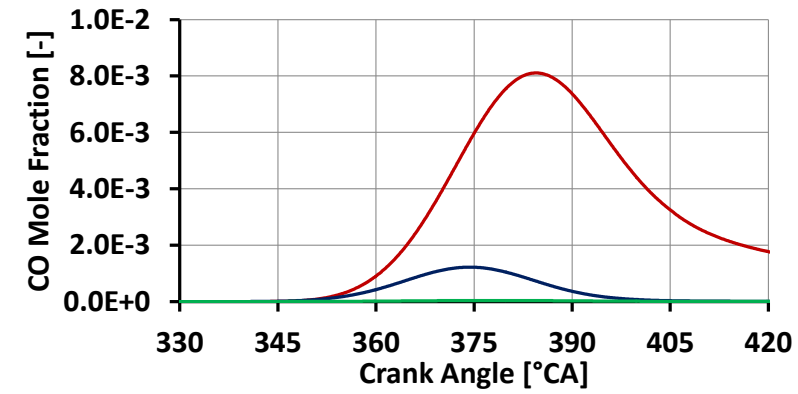
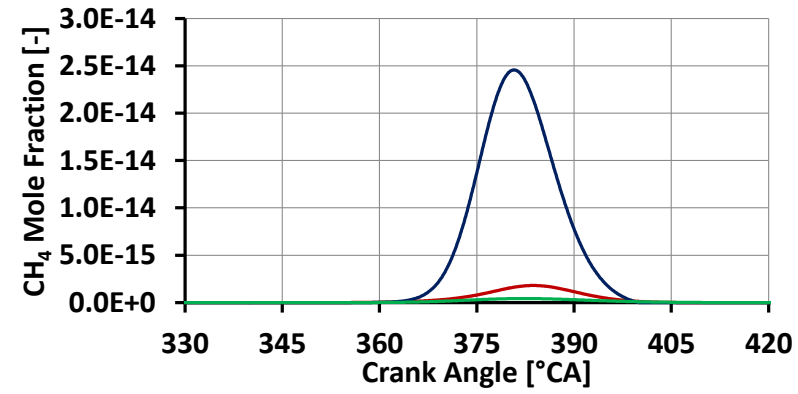
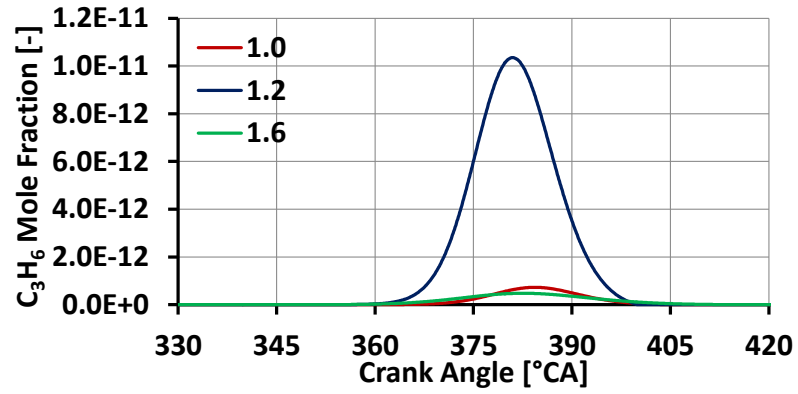
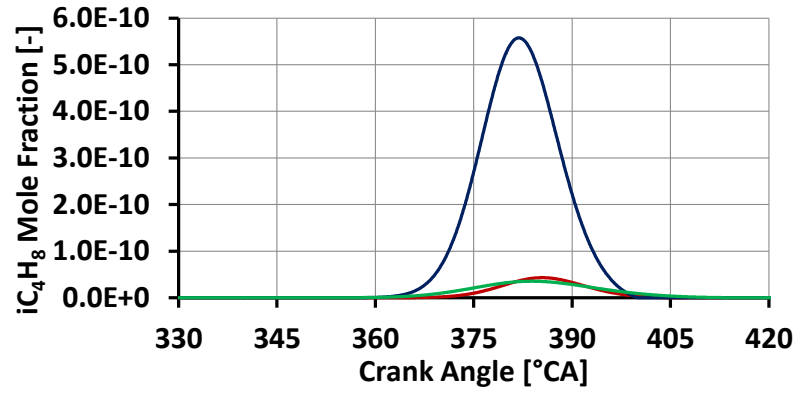


Figure 6-3. Gasoline surrogate –  $Y_{iC_4H_8}$ ,  $Y_{C_3H_6}$ ,  $Y_{CH_4}$  and  $Y_{CO}$

## Ethanol SI combustion

The reaction mechanism used for ethanol analysis consists of 57 species and 383 reactions. Details of the mechanism can be found in [122]. Some of the key oxidation reactions are listed in Table D-4. The cylinder pressure, bulk gas temperature, and ethanol consumption are shown in Figure 6-4 which follow the same trends as gasoline.

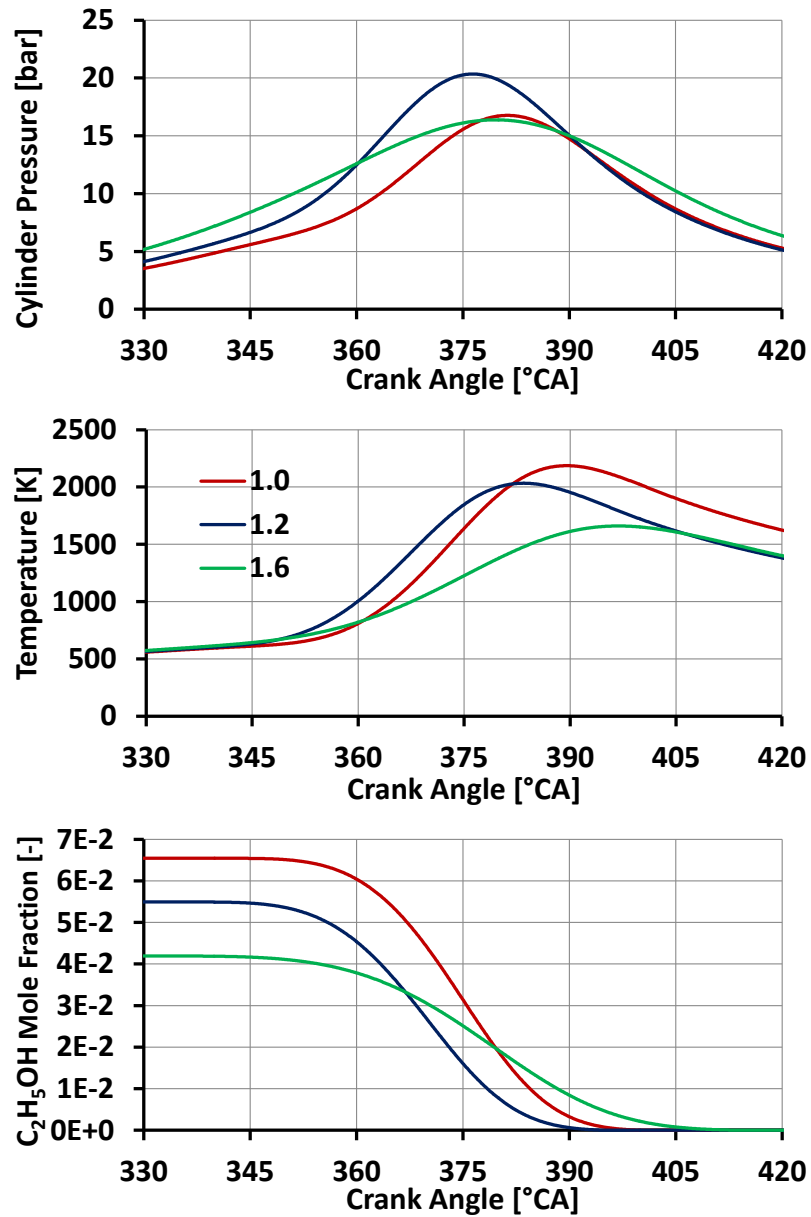


Figure 6-4. Ethanol – Cylinder pressure, temperature &  $Y_{C_2H_5OH}$

According to the engine results, gasoline and ethanol follow similar trends when the  $\lambda$  is increased. This similarity may be explained by the similar trends seen in the formation and consumption of the radicals such as  $\dot{\text{O}}\text{H}$ ,  $\dot{\text{H}}$ ,  $\text{H}\dot{\text{O}}_2$ , and  $\dot{\text{C}}\text{H}_3$  (Figure 6-5). Formation of  $\dot{\text{O}}\text{H}$  and  $\dot{\text{H}}$  radicals are highest for  $\lambda=1.0$ , and decrease with increase in  $\lambda$ . At  $\lambda=1.2$ , formation of  $\text{H}\dot{\text{O}}_2$  and  $\dot{\text{C}}\text{H}_3$  radicals are highest out of all the  $\lambda$ . At  $\lambda=1.6$ , the  $\dot{\text{H}}$  radical formation is almost negligible when compared to the  $\dot{\text{H}}$  formation at lower excess air ratios.

The mole fractions of major intermediate species such as ethene ( $\text{C}_2\text{H}_4$ ), methane ( $\text{CH}_4$ ), formaldehyde ( $\text{CH}_2\text{O}$ ) and carbon monoxide ( $\text{CO}$ ) are illustrated in Figure 6-6. Formaldehyde and carbon monoxide formation are highest at  $\lambda=1.0$  and comparatively negligible for  $\lambda=1.6$ . This could indicate that the homolytic scission of the carbon-carbon bond (Reaction 1 in Table D-4) is favored over the homolytic scission of the carbon-oxygen bond. Ethene is an intermediate in the homolytic scission of the carbon-oxygen bond. At  $\lambda=1.2$ , the higher mole fractions of ethene and methane are estimated when compared to the those at  $\lambda=1.0/1.6$ . This may imply that the homolytic scission of the carbon-oxygen bond is more prevalent at  $\lambda=1.2$  than at  $\lambda=1.0/1.6$ . Peak  $\text{CO}$  formation decreases with increasing excess air ratio probably due to increased oxidation of  $\text{CO}$  to  $\text{CO}_2$ .

From the gasoline and ethanol simulation results, some correlation can be made to the engine test results in terms of combustion duration and carbon monoxide formation. The differences in the radical formation and consumption between  $\lambda=1.0$  and  $\lambda=1.2$  may provide some insight into why combustion is fastest for  $\lambda=1.2$ . At  $\lambda=1.6$ , there is a sharp drop in concentration of most of the major reactivity enhancing radicals which may cause the longest combustion durations.

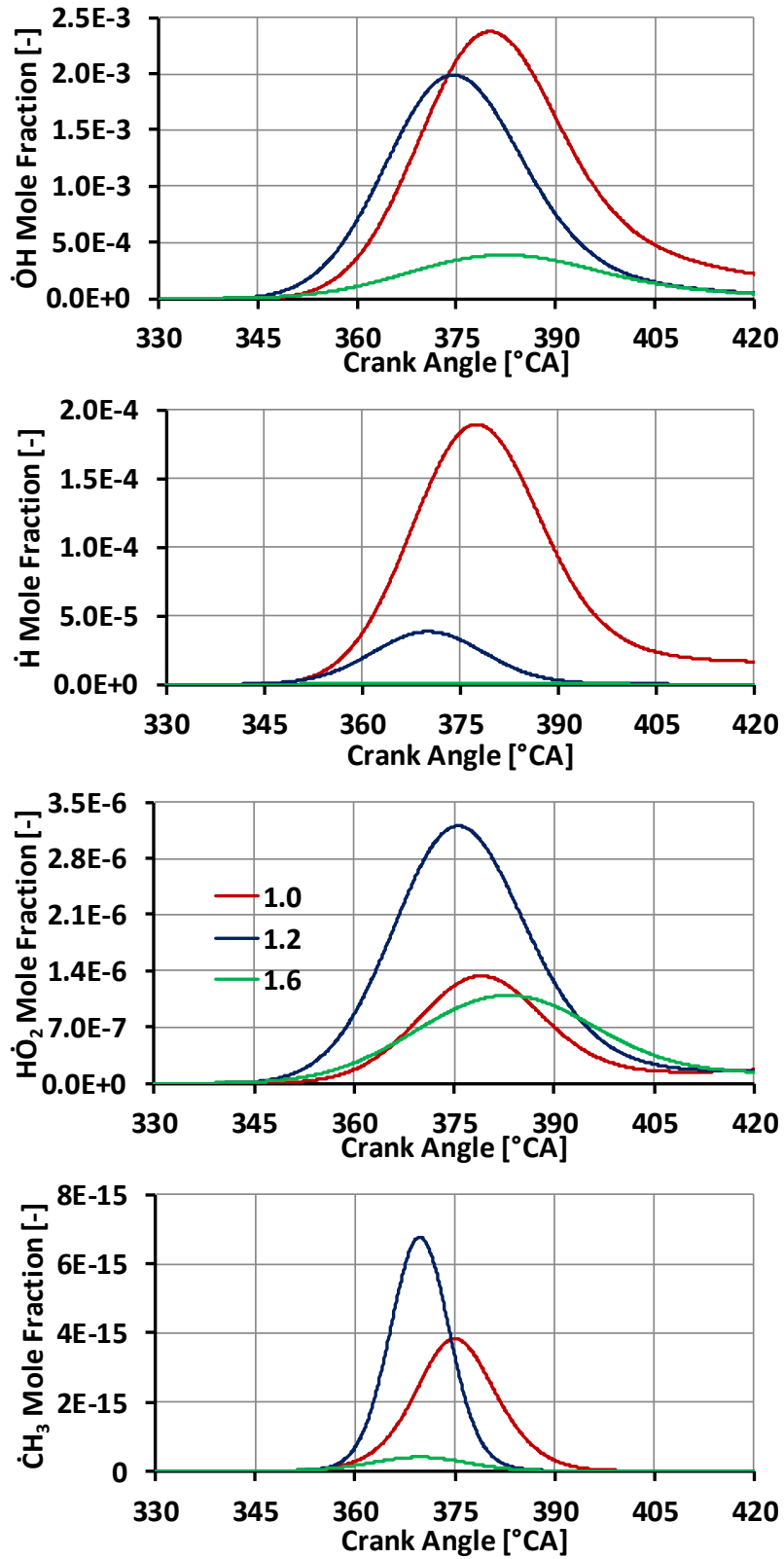


Figure 6-5. Ethanol –  $Y_{\dot{O}H}$ ,  $Y_{\dot{H}}$ ,  $Y_{\dot{H}O_2}$ , and  $Y_{\dot{C}H_3}$



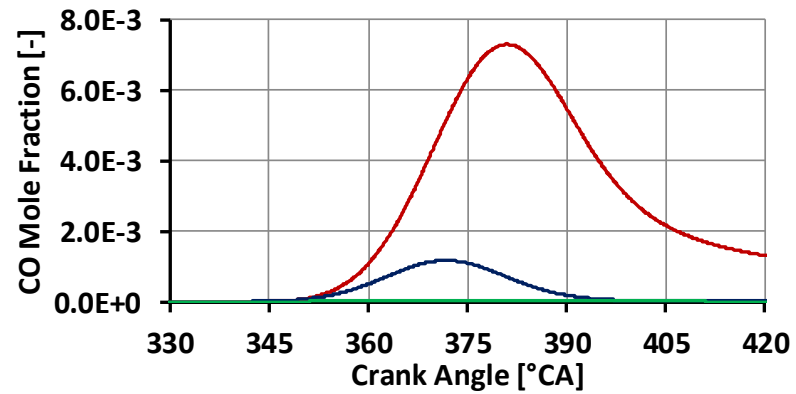
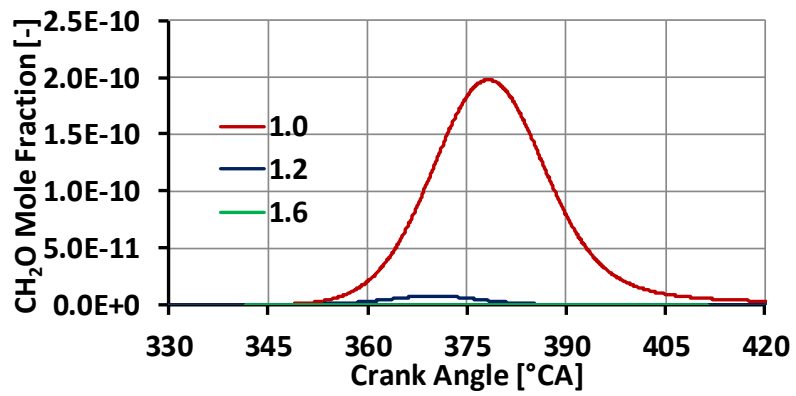
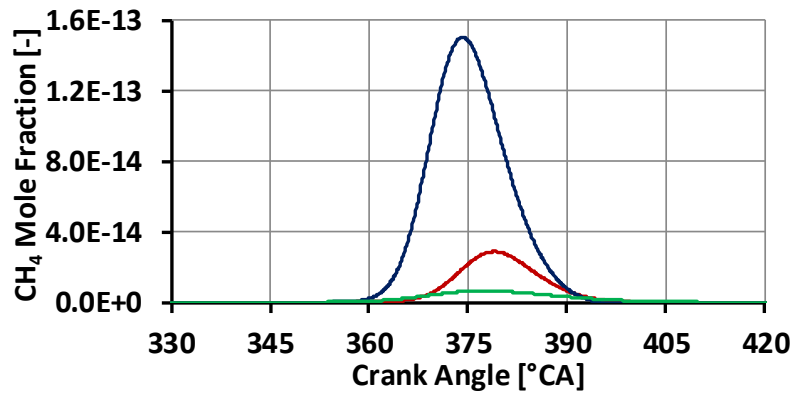
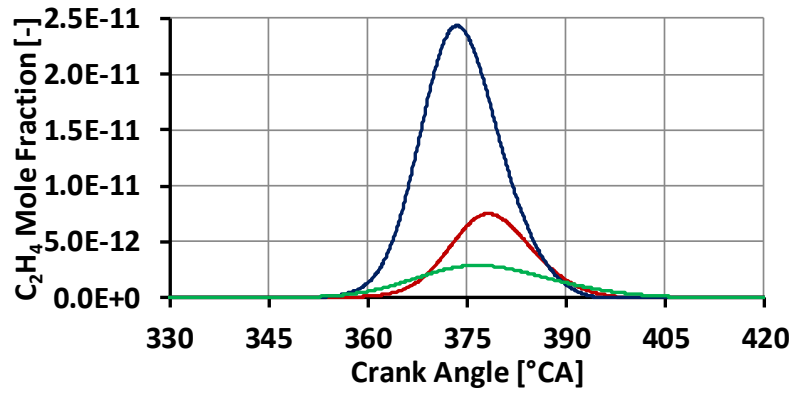


Figure 6-6. Ethanol –  $Y_{C_2H_4}$ ,  $Y_{CH_4}$ ,  $Y_{CH_2O}$  and  $Y_{CO}$

## ■ Intake temperature effect

The intake temperature (denoted by  $T_{\text{intake}}$ ) was found to affect the combustion significantly during the engine test results. The overall trend was similar for both gasoline and ethanol – with increasing  $T_{\text{intake}}$ , the combustion advanced and the combustion duration decreased. In this subsection, the temperature effect will be examined through chemical simulations at  $\lambda=1.6$  at  $T_{\text{intake}}$  of 313 and 393 K. In the following figures, simulation results for  $\lambda=1.2$  at  $T_{\text{intake}}=313$  K will also be shown for comparison. The simulated and experimental pressures traces are shown in Figure D-6 and Figure D-7 in Appendix-D at  $T_{\text{intake}}=393$  K for gasoline and ethanol.

The pressure, temperature, and iso-octane mole fraction are shown in Figure 6-7. The peak pressure at  $\lambda=1.6$  at  $T_{\text{intake}}=393$  K (denoted by  $\lambda=1.6-393$  K) is marginally higher than the  $\lambda=1.2$  (denoted by  $\lambda=1.2-313$  K) case, congruent to the experimental results. The peak in-cylinder temperature is higher for  $\lambda=1.2$  compared to  $\lambda=1.6$  with intake heating. This prediction may also be true if the measured exhaust NO<sub>x</sub> emissions are indicative of it. The measured NO<sub>x</sub> emission for  $\lambda=1.2$  is greater than 1000 ppm while the measured NO<sub>x</sub> emission for  $\lambda=1.6$  at 393 K is less than 700 ppm. The initial iso-octane mole fraction is lower when  $\lambda=1.6$  at 393 K in comparison to  $\lambda=1.2$ , but the consumption of iso-octane is completed within similar durations. The iso-octane consumption is slowest for  $\lambda=1.6$  at the baseline temperature (denoted by  $\lambda=1.6-313$  K). Increasing temperature is expected to increase the rate of reactions of key oxidation reactions. Consequently, there will be an impact on the formation of main chain branching radicals. The peak mole fractions of  $\dot{\text{O}}\text{H}$ ,  $\dot{\text{H}}$ , and  $\text{H}\dot{\text{O}}_2$  radicals increase when  $T_{\text{intake}}$  increases from 313 to 393 K at  $\lambda=1.6$  though the highest concentration is at  $\lambda=1.2$  at the baseline temperature (Figure 6-8). There is marginal

effect of increase in  $T_{\text{intake}}$  on the  $\dot{H}$  formation. However, the peak  $\dot{C}H_3$  mole fraction is a few orders of magnitude higher for the  $\lambda=1.6$ -393 K case compared to the other baseline temperature cases at  $\lambda$  of 1.2 and 1.6. Formation of  $\dot{C}H_3$  also starts earlier when the intake temperature is higher. Ethanol shows similar trends for pressure, temperature, ethanol mole fraction, and radical formation, and are not shown here for the sake of brevity.

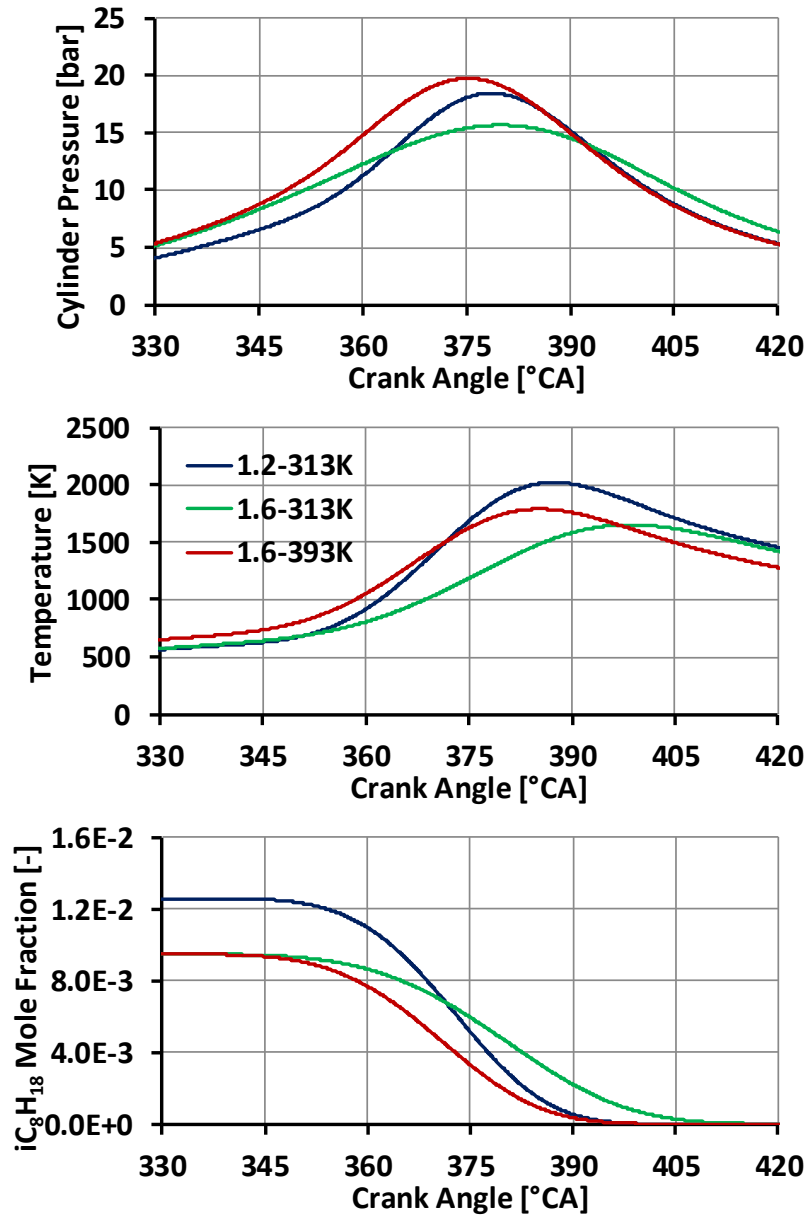


Figure 6-7.  $T_{\text{intake}}$  effect (gasoline) – Cylinder pressure, temperature &  $Y_{iC_8H_{18}}$

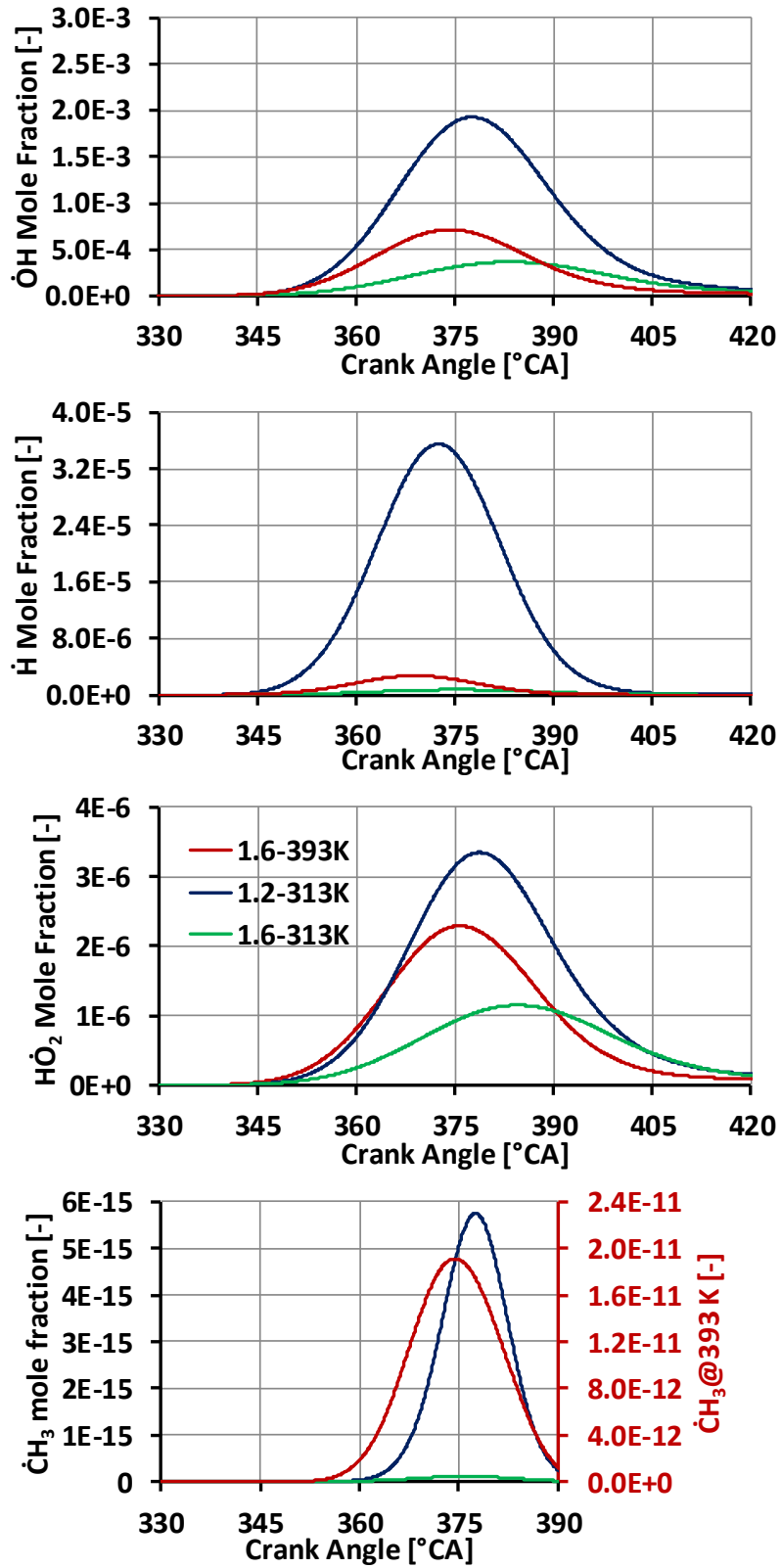


Figure 6-8.  $T_{\text{intake}}$  effect (gasoline) –  $Y_{\text{OH}}$ ,  $Y_{\text{H}}$ ,  $Y_{\text{HO}_2}$ , and  $Y_{\text{CH}_3}$

From the experimental results (Figure 5-8 and Figure 5-14), it is found that increasing the intake temperature to 393 K at  $\lambda=1.6$  reduces the combustion duration to periods equivalent to  $\lambda=1.2$  at 313 K. The enhancement of the charge reactivity with increase in the  $T_{\text{intake}}$  may be due to the enhancement of certain key reactions. Figure 6-9 and Figure 6-10 show the trends for major intermediate species for gasoline and ethanol respectively. Carbon monoxide formation shows a marginal increase at  $\lambda=1.6$  when the  $T_{\text{intake}}$  is increased to 393 K. At the leanest conditions, since oxygen is freely available, carbon monoxide would be expected to be oxidized to carbon dioxide with ease. Another common major intermediate species for both the fuels is methane. Methane formation increases by a few orders of magnitude for both fuels when the intake temperature is increased to 393 K at  $\lambda=1.6$ .

In general, a similar increase in the peak concentration of the major intermediate species is observed for both fuels when  $T_{\text{intake}}$  is increased at  $\lambda=1.6$ . Moreover, the start of formation of these intermediate species is advanced as well. For gasoline for instance, increasing the intake temperature at  $\lambda=1.6$  increases the iso-butene and propene formation by a few orders of magnitude (Figure 6-9). This prediction along with the increase in the  $\dot{C}H_3$  would indicate that the tendency for the unimolecular dissociation of iso-octane would increase with increase in temperature (Table D-3). For ethanol, the peak ethene concentration is increased by two orders of magnitude and ethene formation starts earlier (comparing  $\lambda=1.6$ -393 K with  $\lambda=1.2$ -313 K in Figure 6-10) which would suggest a greater tendency for homolytic scission of the carbon-oxygen bond (Table D-4). At  $\lambda=1.6$ -313 K, no formaldehyde formation is predicted. The peak formaldehyde concentration at  $\lambda=1.6$ -393 K is of the order of  $\lambda=1.0$  (Figure 6-6) and an order greater than  $\lambda=1.2$ -313 K though the start of formation is later.

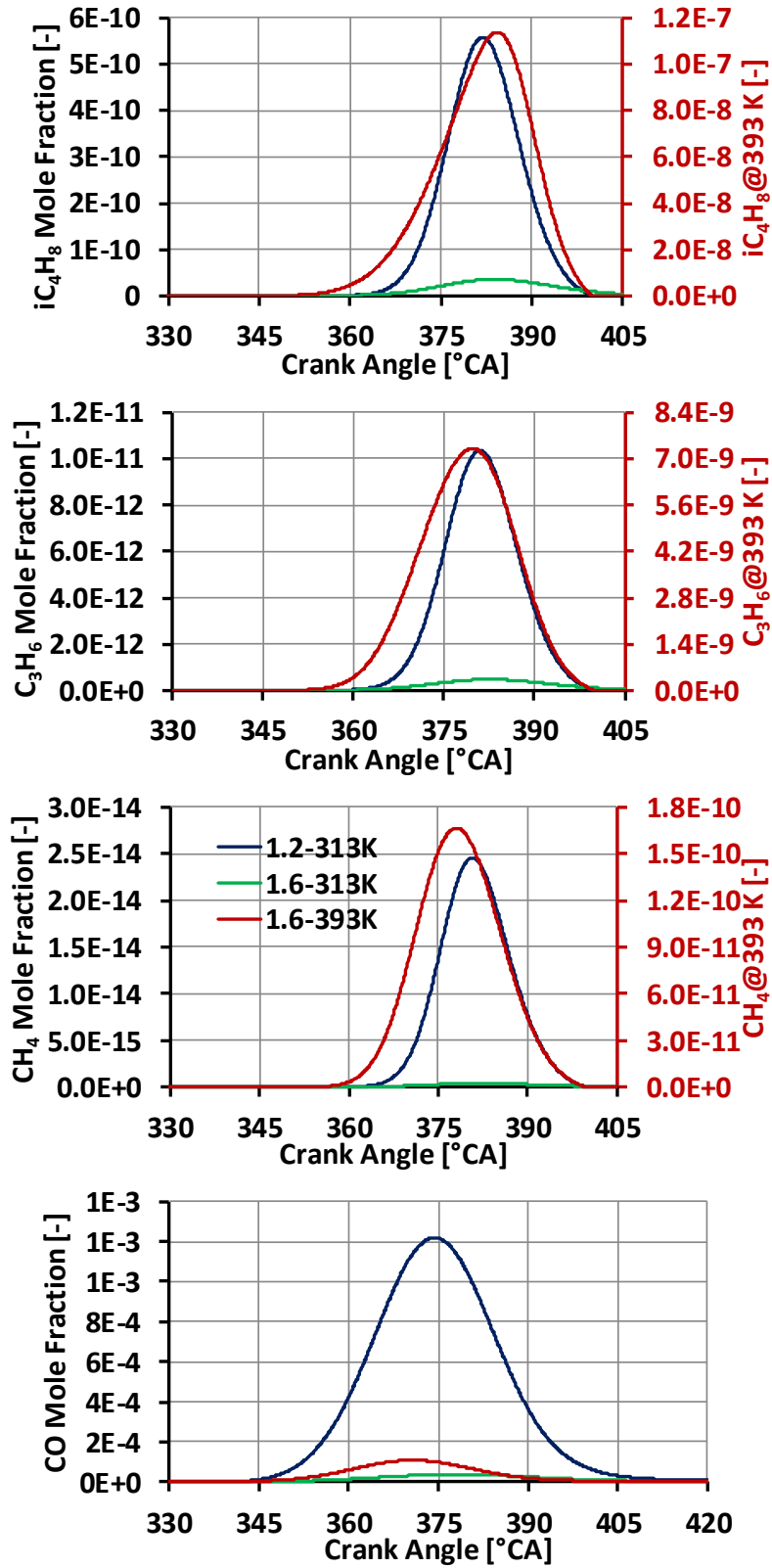


Figure 6-9.  $T_{intake}$  effect (gasoline) –  $Y_{iC_4H_8}$ ,  $Y_{C_3H_6}$ ,  $Y_{CH_4}$  and  $Y_{CO}$

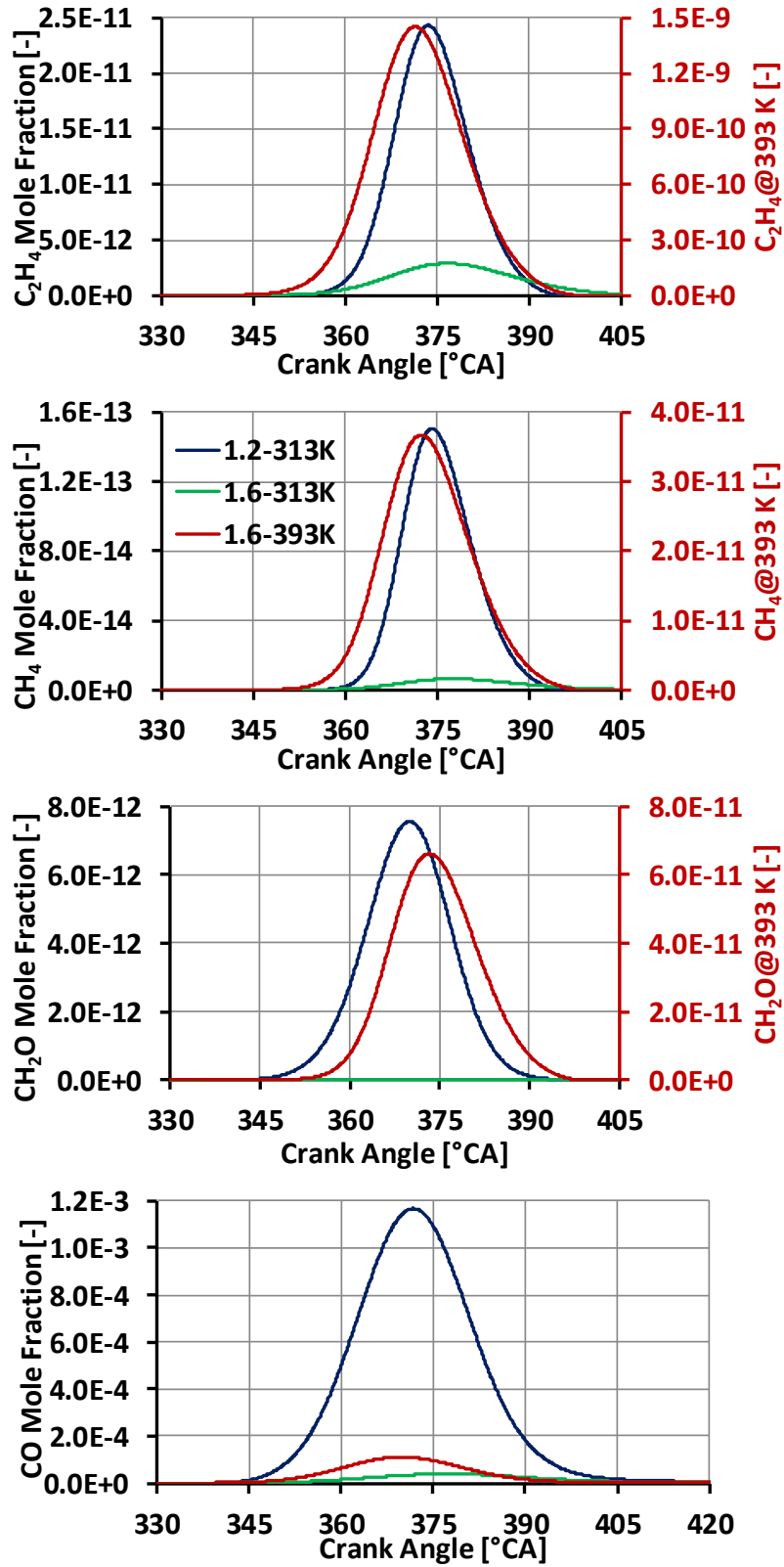


Figure 6-10.  $T_{\text{intake}}$  effect (ethanol) –  $Y_{\text{C}_2\text{H}_4}$ ,  $Y_{\text{CH}_4}$ ,  $Y_{\text{CH}_2\text{O}}$  and  $Y_{\text{CO}}$

## ■ DME HCCI combustion

DME simulation results are not a direct comparison to the gasoline and ethanol results owing to the difference in the reactor model used. The reaction mechanism consists of 79 species and 351 reactions. Details are provided in [123-125]. The key reactions are listed in Table D-5.

The motoring pressure was a reasonable match with the simulated motoring pressure which was used to validate the heat transfer parameters. The simulated firing pressure curve deviated from the experimental results. The pressure rise from the low temperature reactions matched that from the experiments. However, the second pressure rise corresponding to the high temperature reactions was later than that from the experiments. Therefore, the results presented here should be viewed only in terms of trends and may not directly correspond to the engine test results of Chapter 5. Validation curves are provided in Appendix D.



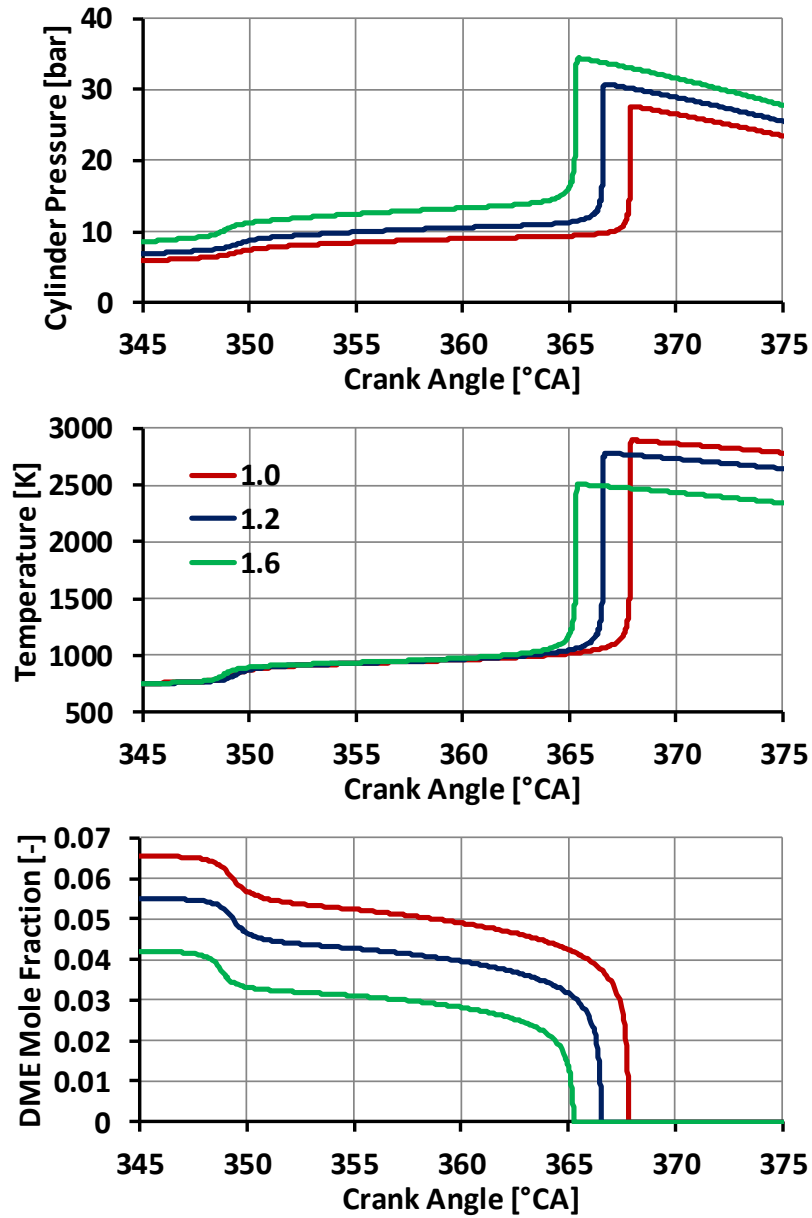


Figure 6-11. DME – Cylinder pressure, temperature &  $Y_{\text{CH}_3\text{OCH}_3}$

The estimated cylinder pressure, temperature, and DME mole fraction are shown in Figure 6-11. The simulation parameters are set in accordance with the engine tests. With increasing  $\lambda$ , the intake pressure is increased as the fuel amount is kept constant. The peak pressure increases with increasing  $\lambda$ . This agrees with the engine test results. The chemical simulation also captures the low temperature reactions which start before compression

TDC with corresponding changes in the pressure, temperature and DME mole fraction. The timing for the start of the low temperature reactions is marginally retarded by increase in  $\lambda$ . Rate of DME consumption increases with increasing  $\lambda$ .

Unlike gasoline or ethanol, DME HCCI follows the trends of species monotonically. The concentration plots of reactivity enhancing radicals –  $\dot{\text{O}}\text{H}$ ,  $\dot{\text{H}}$ ,  $\dot{\text{H}}\text{O}_2$ , and  $\dot{\text{C}}\text{H}_3$  are shown in Figure 6-12. From the simulation, it is estimated that the low temperature reactions (LTRs) before TDC which eventually initiate the high temperature reactions (HTRs) are controlled by the  $\dot{\text{H}}\text{O}_2$  and  $\dot{\text{C}}\text{H}_3$  radicals. The start of formation of these radicals starts at the same time as the start of the first heat release.  $\lambda=1.0/1.2$  cases have similar concentration profiles of  $\dot{\text{H}}\text{O}_2$  and  $\dot{\text{C}}\text{H}_3$  radicals in the low temperature regime. When  $\lambda$  is increased to 1.6, the peak concentrations of  $\dot{\text{H}}\text{O}_2$  and  $\dot{\text{C}}\text{H}_3$  are advanced in both the LTR and HTR periods which may be due to increase in oxygen availability as well as start of pyrolysis. During the start HTR period (typically after TDC),  $\dot{\text{H}}$  and  $\dot{\text{O}}\text{H}$  concentration peaks increase, and the timings of these peaks retard when the  $\lambda$  is increased. Large increases in the radical pool are expected with further chain branching to cause the HTRs to progress even faster. The  $\text{CH}_3\dot{\text{O}}$ ,  $\text{CH}_4$ ,  $\text{CH}_2\text{O}$ , and  $\text{CO}$  intermediate formation and consumption are advanced with increasing  $\lambda$ .  $\text{CH}_3\dot{\text{O}}$  is highest during the LTR period probably due to the high concentrations of the  $\dot{\text{H}}\text{O}_2$  and the  $\dot{\text{C}}\text{H}_3$  radicals (Reaction 10 in Table D-5). The other three intermediates increase as the HTRs start. The formaldehyde concentration is especially high during the entire combustion duration owing to it being a common by product of several reactions (Reactions 1a, 2a, and 6 in Table D-5).

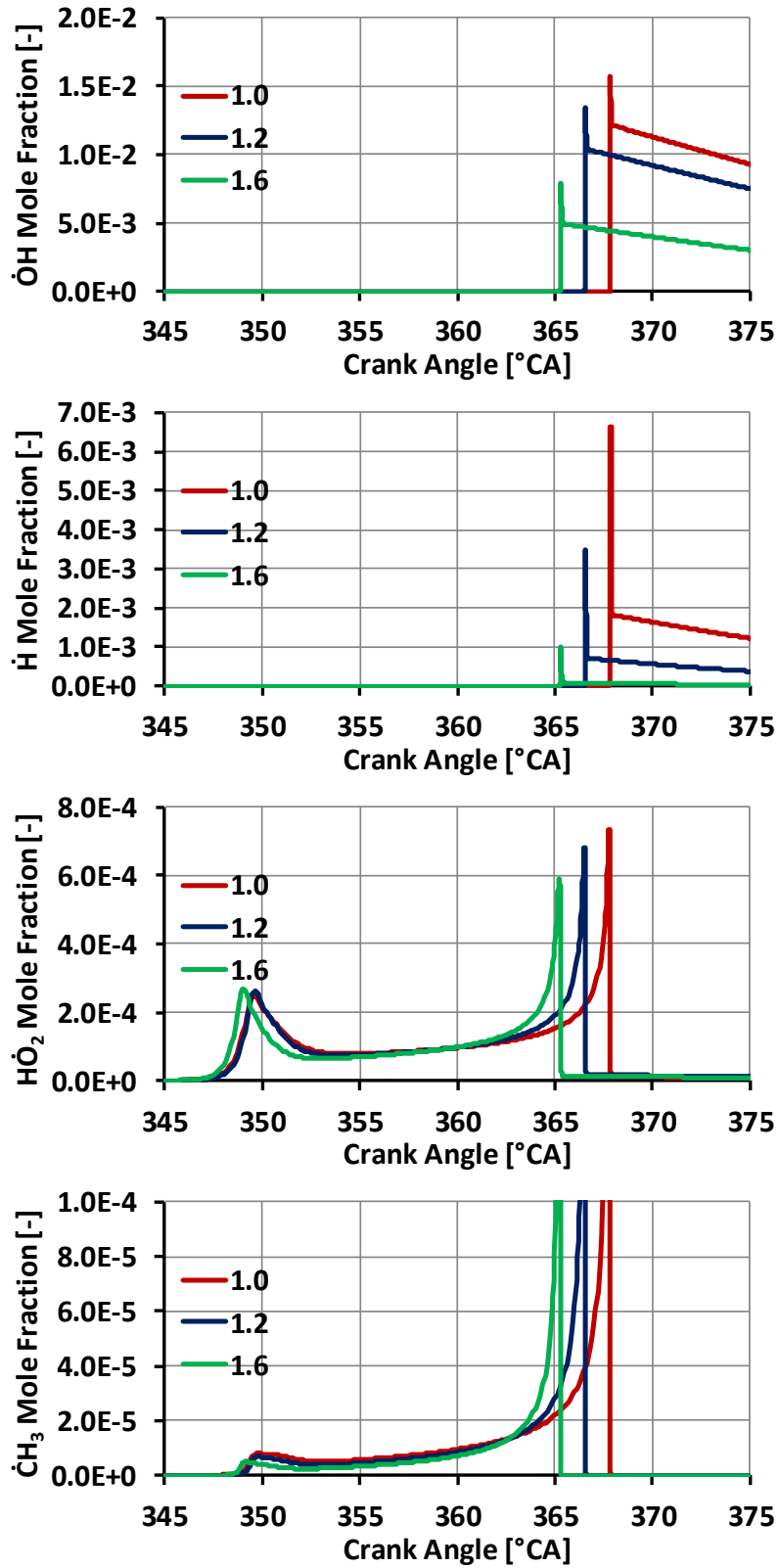


Figure 6-12. DME –  $Y_{OH}$ ,  $Y_H$ ,  $Y_{HO_2}$ , and  $Y_{CH_3}$

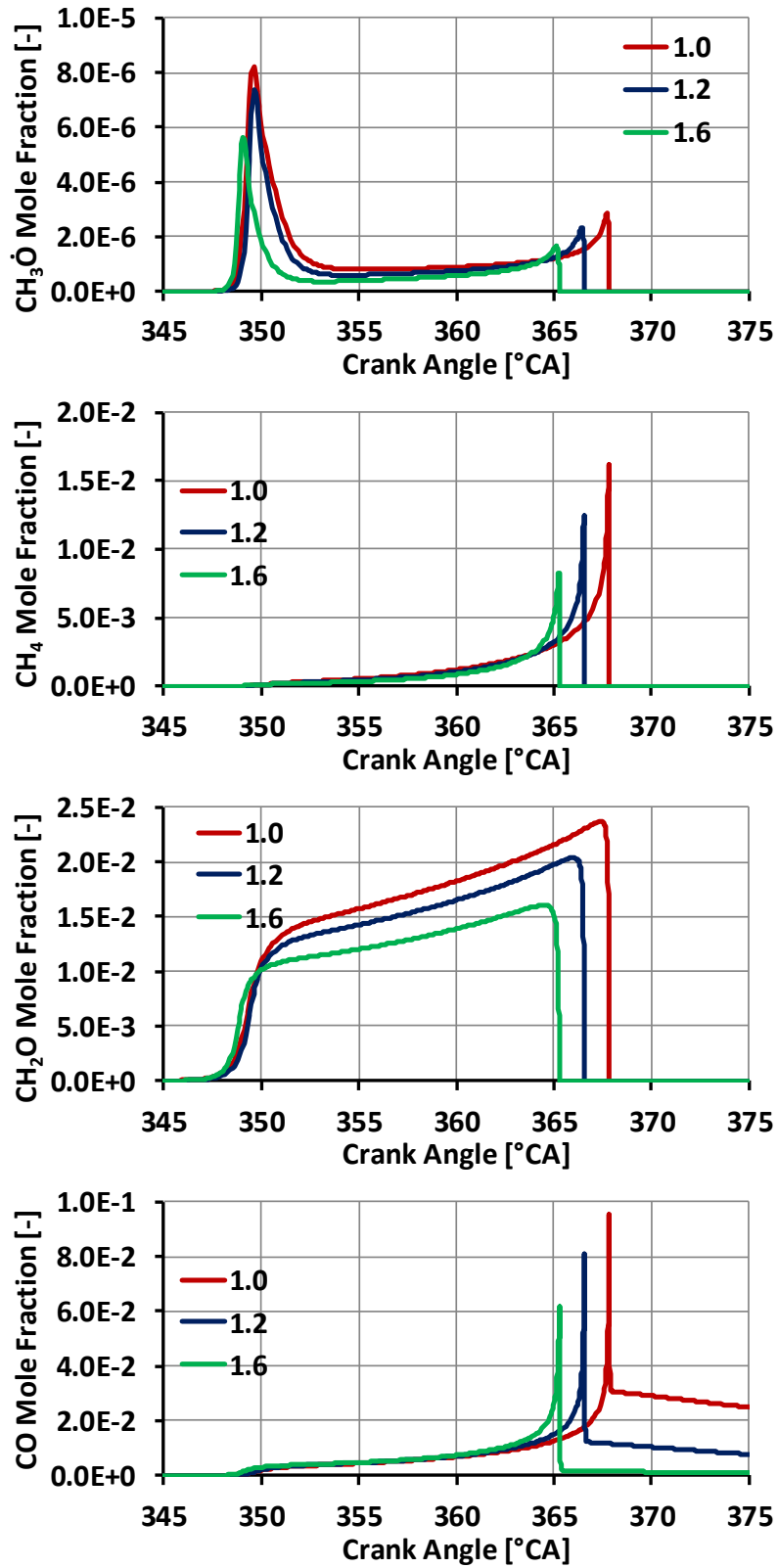


Figure 6-13. DME –  $Y_{CH_3O}$ ,  $Y_{CH_4}$ ,  $Y_{CH_2O}$  and  $Y_{CO}$

## ■ In-cylinder Flow-field Simulations

This section describes the three-dimensional computational fluid dynamics simulations undertaken to estimate the flow field in the cylinder under engine motoring conditions. As emphasized previously, the flow-field is a critical element in the development of the flame. Simulation parameters are described in the first sub-section. The simulation results for the effect of intake flow rate on the in-cylinder flow field are discussed in the second sub-section. Details on the flow field near the spark plug are described in the third sub-section.

### ■ Simulation parameters

The geometry input for Converge® version 2.3 is shown in Figure 6-14 showing some of the main boundaries. The geometry is based on the Yanmar NFD-170 stationary diesel engine used for the engine tests. It also includes the insert in the intake manifold. A flexible foam mold of the helical intake port is made using the cylinder head. This mold is then laser scanned in 3-D, and from the scan, the corresponding surface file is generated for intake port [29]. This surface file is incorporated in the overall geometry input file. A single motoring engine cycle is simulated from 0 to 720 °CA. The primary variable for the CFD simulations is the mass air flow rate. Four increasing flow rates corresponding to  $\lambda=1.0/1.2/1.4/1.6$  are simulated to estimate the in-cylinder flow field during the spark breakdown and early flame propagation period of 300 to 360 °CA.

The simulation parameters are summarized in Table 6-2. Since the main purpose of the simulations is to estimate the flow, the input parameters especially those related to the flow, are selected carefully to mirror the engine operating conditions. The intake pressure measured at a resolution of 0.1 °CA during engine motoring (empirical data) is used as the boundary condition for the inflow boundary of the intake port. The cylinder region

boundary temperature is set to 373 K to match the empirical motoring pressure. Finally, the experimental and simulated motoring pressure traces are compared to validate the gas exchange process (Figure E-1, Appendix E). The intake and exhaust valve profiles are determined through physical measurement on the engine.

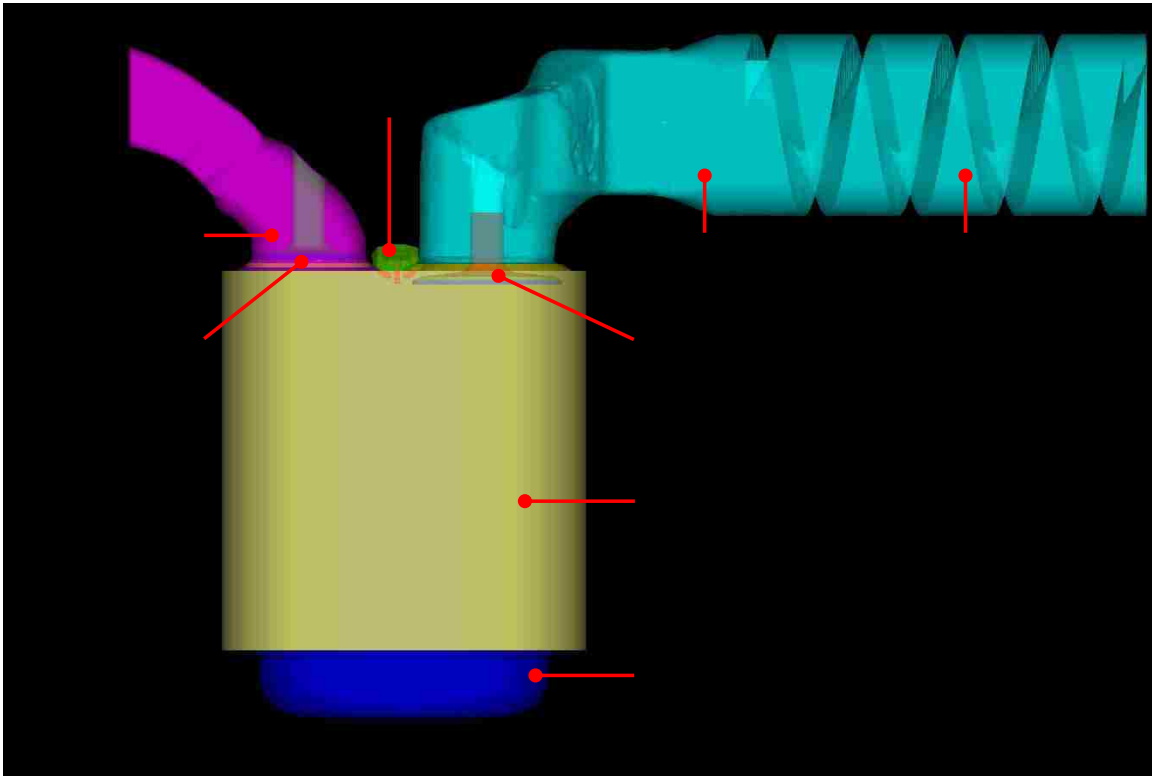


Figure 6-14. Converge geometry input showing the main features and boundaries

The base grid size refers to the edge length of cube shaped cells. Time varying grid refinement is used. During the intake stroke, the grid size in the region around the intake valve is reduced to 1 mm. The grid size in the cylinder region is reduced to 1 mm till the start of the spark window at 291 °CA. During the spark and the early flame propagation window of 291 to 370 °CA, which is the main period of interest, the grid size is 0.5 mm. Thereafter, the grid size in the cylinder region is again increased to 1 mm. For the spark plug vicinity flow field simulations, the grid size is reduced further to 0.25 mm over a 20

mm radius and 20 mm height cylindrical region centered around the sparking electrode of the multi-pole plug. This is of the order of the spark gap (0.86 mm) and air gap (~0.8 mm) between the spark plug ceramic insulator and the metal ground shell. The grid size is decided based on successive reduction of the grid size until no further improvement is observed in the resolution of the velocity profile. The average root mean square of the fluctuating velocity,  $u'$  (defined in Section 1.5) and the swirl ratio (ratio of average rotational velocity about the cylinder axis and the engine speed) for the cells in the cylinder are very similar for two grid sizes of 0.5 and 0.25 mm (Figure 6-15). Therefore, there may not be any major improvement in the computational accuracy with further grid refinement.

Table 6-2. Converge simulation parameters

<b>Parameter</b>	<b>Value</b>
Intake temperature	313 K
Boundary temperature	373 K
Intake pressure profile	Input from empirical data
Cell size (edge length)	4 mm (max) / 0.25 mm (min)
Turbulence model	Renormalized Group k- $\epsilon$
Engine geometry	Yanmar NFD-170
Bore	102 mm
Stroke	105 mm
Engine speed	1300 rpm
Compression ratio	9.2:1
Intake valve open (IVO)	-10 °CA
Intake valve close (IVC)	225 °CA
Intake lift	10.46 mm
Exhaust valve open (EVO)	495 °CA
Exhaust valve close (EVC)	14 °CA
Exhaust lift	10.46 mm

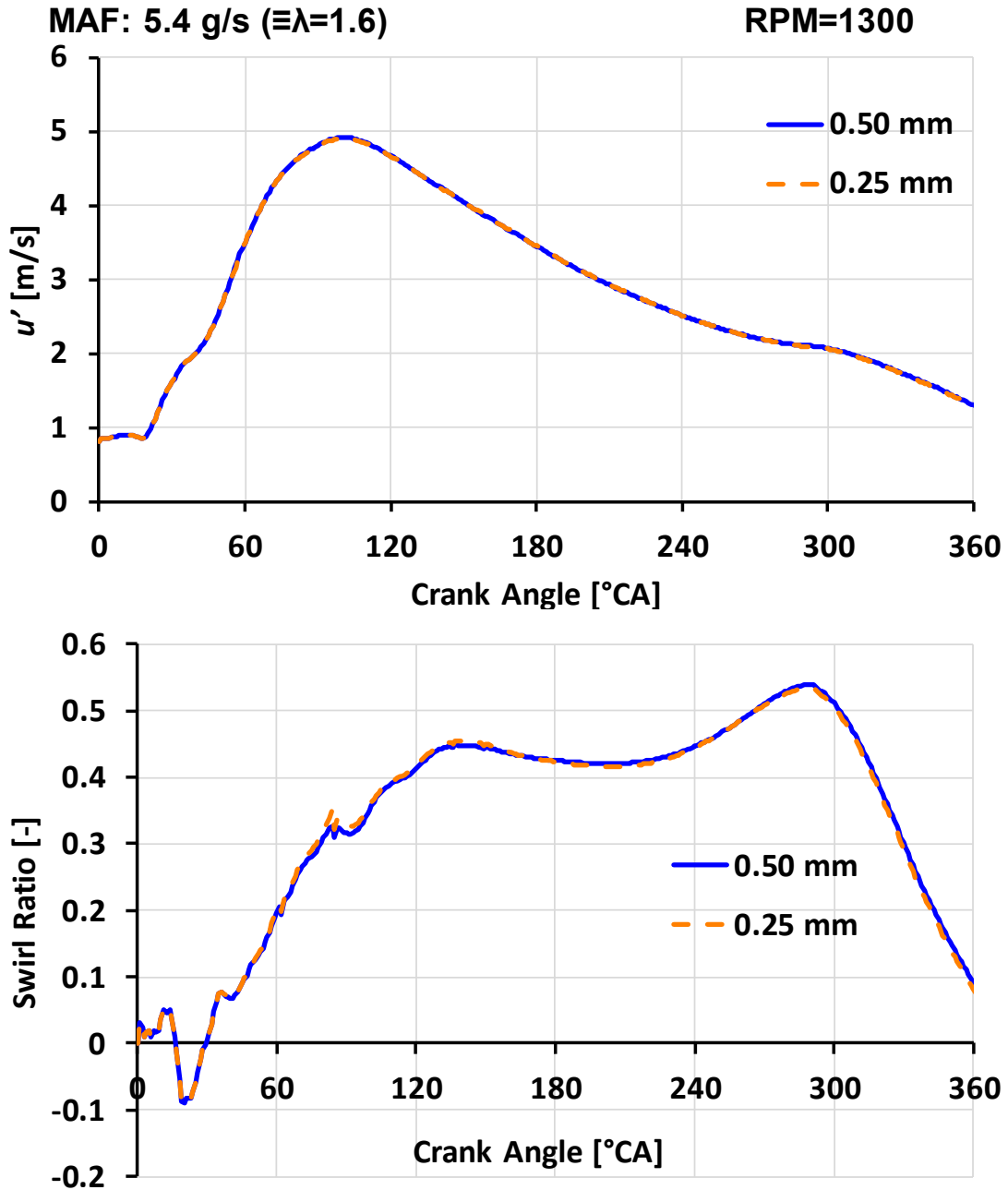


Figure 6-15. Effect of cell size on turbulent velocity and swirl ratio

The Renormalized Group (RNG)  $k$ - $\epsilon$  turbulence model is used since it has been shown to estimate engine flows with reasonable accuracy [126-128]. The major input files with details of all input parameters are provided in Appendix E. Theory and recommended input parameters for the turbulence model can be found in the software manual [129] and



literature [126, 128]. The simulation data is post-processed using Ansys Enight 10.1. Two viewing planes are defined as shown in Figure 6-16 for presenting the results. These planes bisect the sparking electrode of the multi-pole spark plug. In this manner, the region closest to the spark kernel can be examined. The plane which views the spark gap from the front is defined as ‘Gap Plane’ and the plane which views the spark gap from the side (and intersects the ground electrode completely) is defined as ‘Ground Plane’. The purpose of the simulations is to obtain an estimate of the order of the in-cylinder flow velocities which could not be measured directly. Moreover, the author would like to emphasize that two-dimensional representations of complex three-dimensional phenomena such as in-cylinder flows can only be used to draw broad conclusions on the in-cylinder flow structure. Since the spark gap is small (of the order of ~1 mm), this approximation may be acceptable. The simulated flow field should be validated with empirical studies in the future.

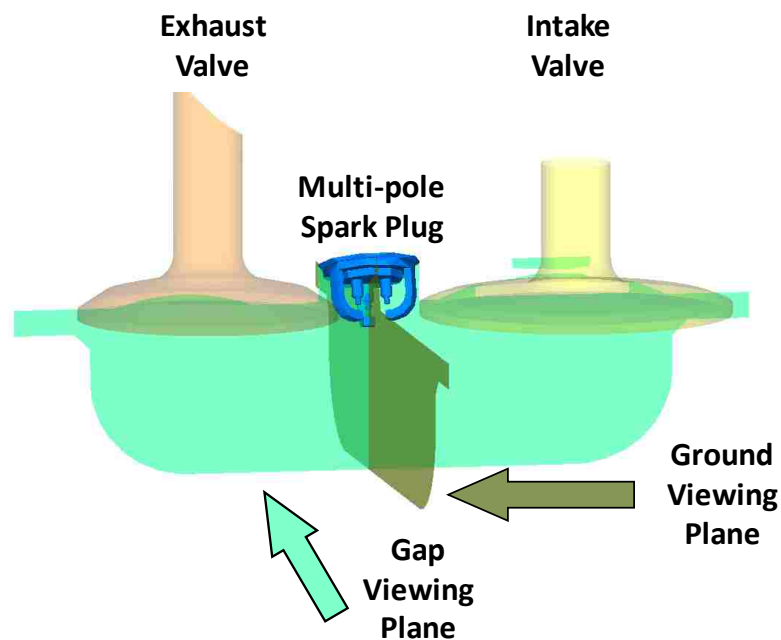


Figure 6-16. Viewing planes for the CFD results

## Effect of intake flow rate on in-cylinder flow field

In this section, the author presents the results for the estimation of the in-cylinder flow field velocity at two intake air flow rates of 4.2 and 5.4 g/s. These match with the MAF at  $\lambda=1.2$  and  $\lambda=1.6$  for the engine test and correspond to the shortest and longest combustion durations that were observed during the engine tests.

The figures are to be read in terms of the velocity magnitude and the velocity direction. The colour in the background corresponds to the velocity magnitude for the cells which the viewing plane intersects. This is calculated using the three directional components of the velocity for each of these cells. The no-slip boundary layer calculation is not shown in the figures. The direction of the arrow in the foreground corresponds to the direction of the cell velocity projected on viewing plane. For clarity, select cells are demarcated with their corresponding velocity arrow to illustrate the velocity flow-field. The length of the arrow has no physical significance.

Each of the following figures, Figure 6-17-Figure 6-20 is at 325, 335, 345, and 355 °CA crank position respectively. The top two insets show the gap plane velocity at the two MAFs, and the bottom two show the ground plane velocity at the same MAFs. For the gap plane plots, the intake valve is on the right, and the exhaust valve is on the left. The colour bar for the velocity magnitude ranges from 0 to 14 m/s.

From 325 °CA onwards (Figure 6-17), some similarities can be observed between the two MAF cases in the gap and the ground planes. First, the overall velocity magnitudes between the two MAF cases are similar with the velocity magnitude in most of the cells in the range of ~6-8 m/s. Second, there is a developed recirculation zone of low velocity that is between

the intake valve and the spark plug in the gap plane. The charge velocity is lower in this zone (~2-4 m/s). As the piston moves towards TDC, this zone moves closer towards the spark gap (Figure 6-18). By 345 °CA (Figure 6-19), for the 4.2 g/s MAF case, the recirculation zone in the gap plane is inside the perimeter of the spark plug. For 5.4 g/s MAF case, this low velocity recirculation zone is inside the spark plug perimeter by 355 °CA (Figure 6-20). Third, in the ground plane, the flow is directed towards the ground electrode for both MAF cases at 325 °CA (from left to right in the images). As the piston approaches TDC, the flow direction in the ground plane shifts towards the spark plug axis (bottom left to top right in the images). This shift is apparent earlier in the 4.2 g/s MAF case in comparison to the 5.4 g/s case. The velocity magnitude in this plane is ~6-8 m/s near the spark gap and decreases as the piston approaches TDC. Fourth, the simulation predicts formation of multiple recirculation zones in the ground plane as the piston approaches 355 °CA, with the structures resembling typical compression squish.

From these estimations, two main conclusions can be drawn. First, there are no major differences in the in-cylinder flow field structure when the MAF is increased from 4.2 to 5.4 g/s. Second, the flow field changes with crank position especially near the spark plug. Hence, the grid near the spark plug is refined further and analyzed in greater detail. In addition to the spark gap, the flow in the gap between the ground metal shell and the ceramic insulator is of interest since this flow can affect the surface temperature of the spark plug. The surface temperature of the spark plug may be associated with combustion abnormalities [130].

MAF: 4.2/5.4 g/s ( $\equiv \lambda = 1.2/1.6$ )

RPM=1300

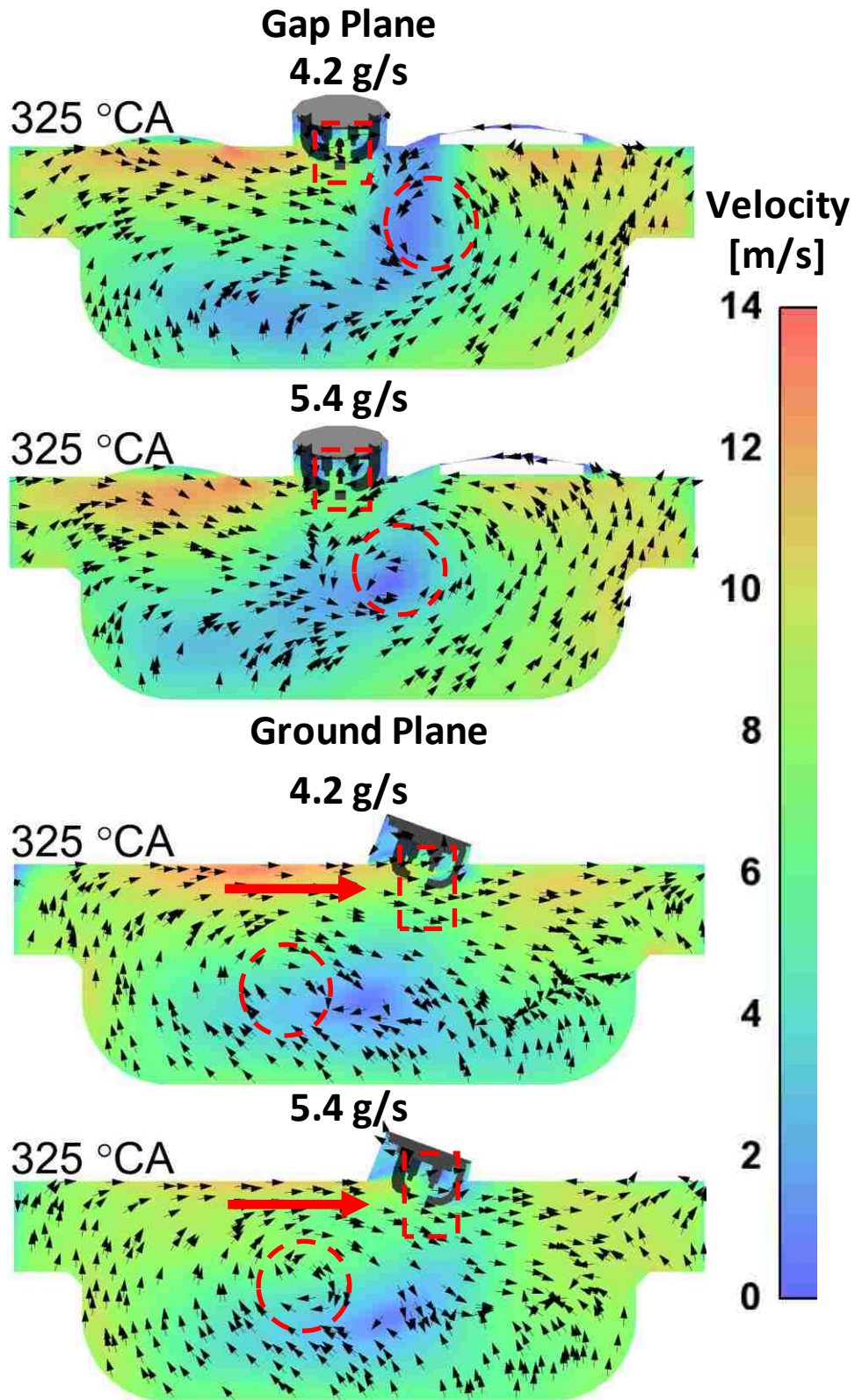


Figure 6-17. Flow field comparison at 325 °CA between MAF of 4.2 and 5.4 g/s

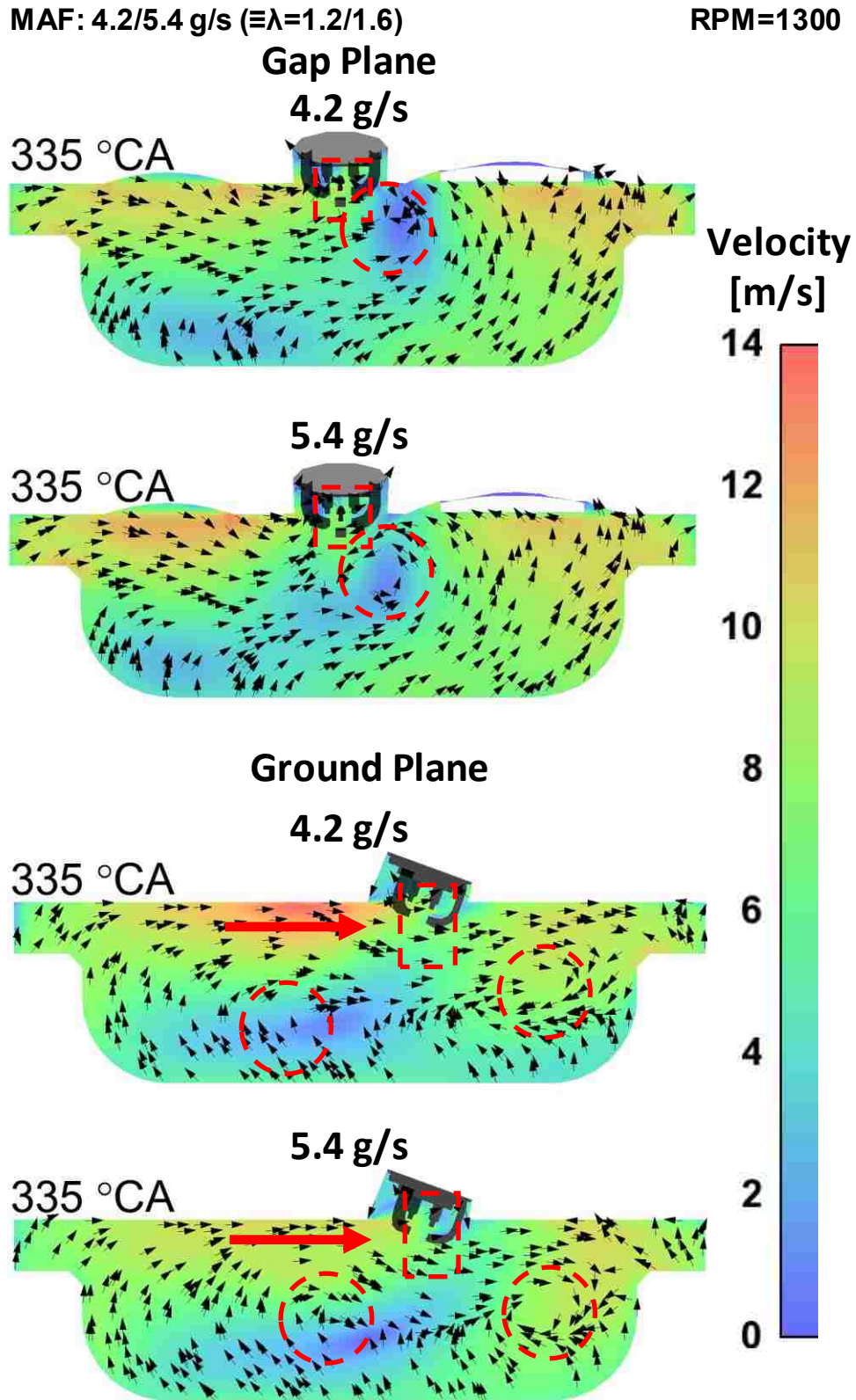


Figure 6-18. Flow field comparison at 335 °CA between MAF of 4.2 and 5.4 g/s

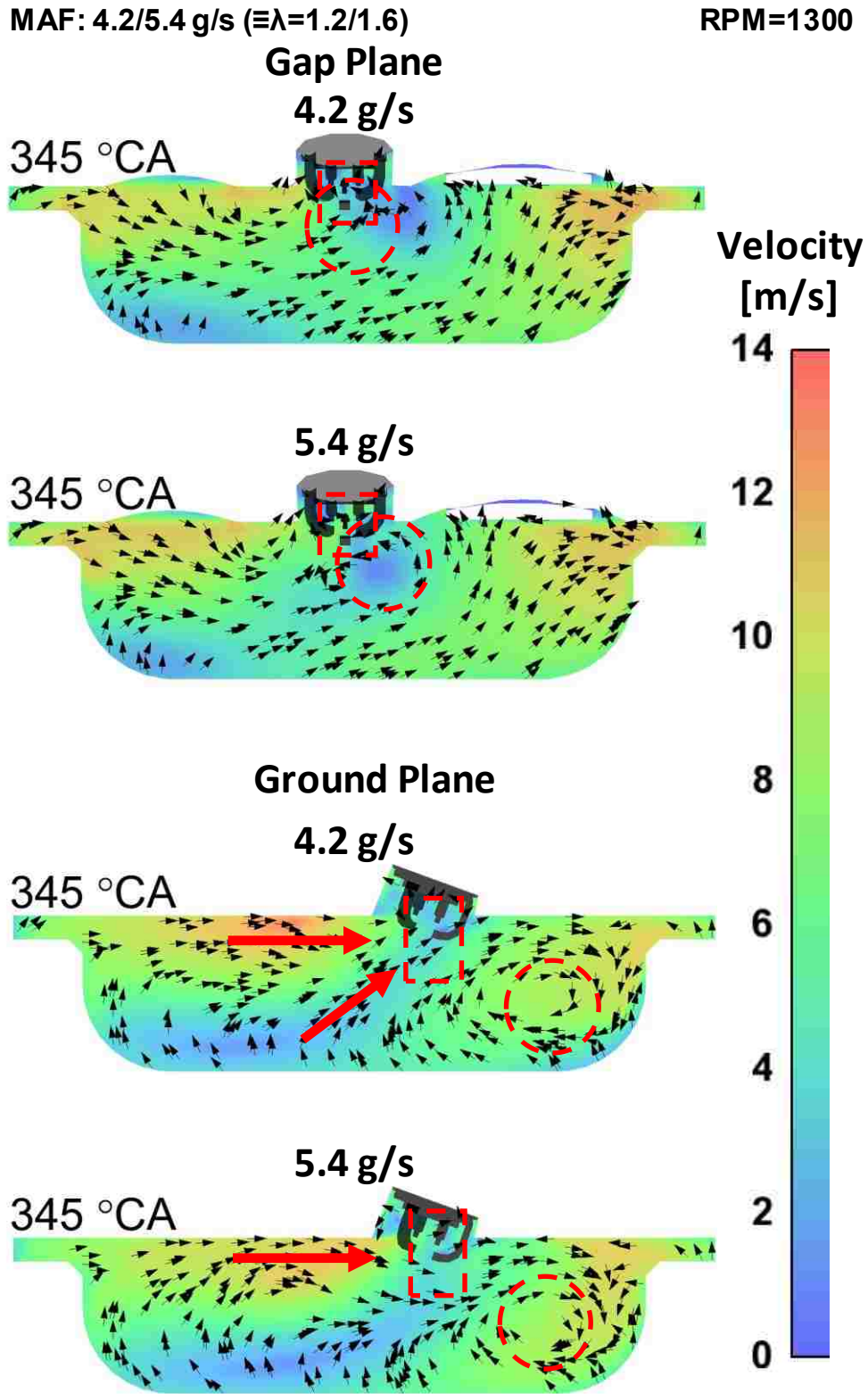


Figure 6-19. Flow field comparison at 345 °CA between MAF of 4.2 and 5.4 g/s

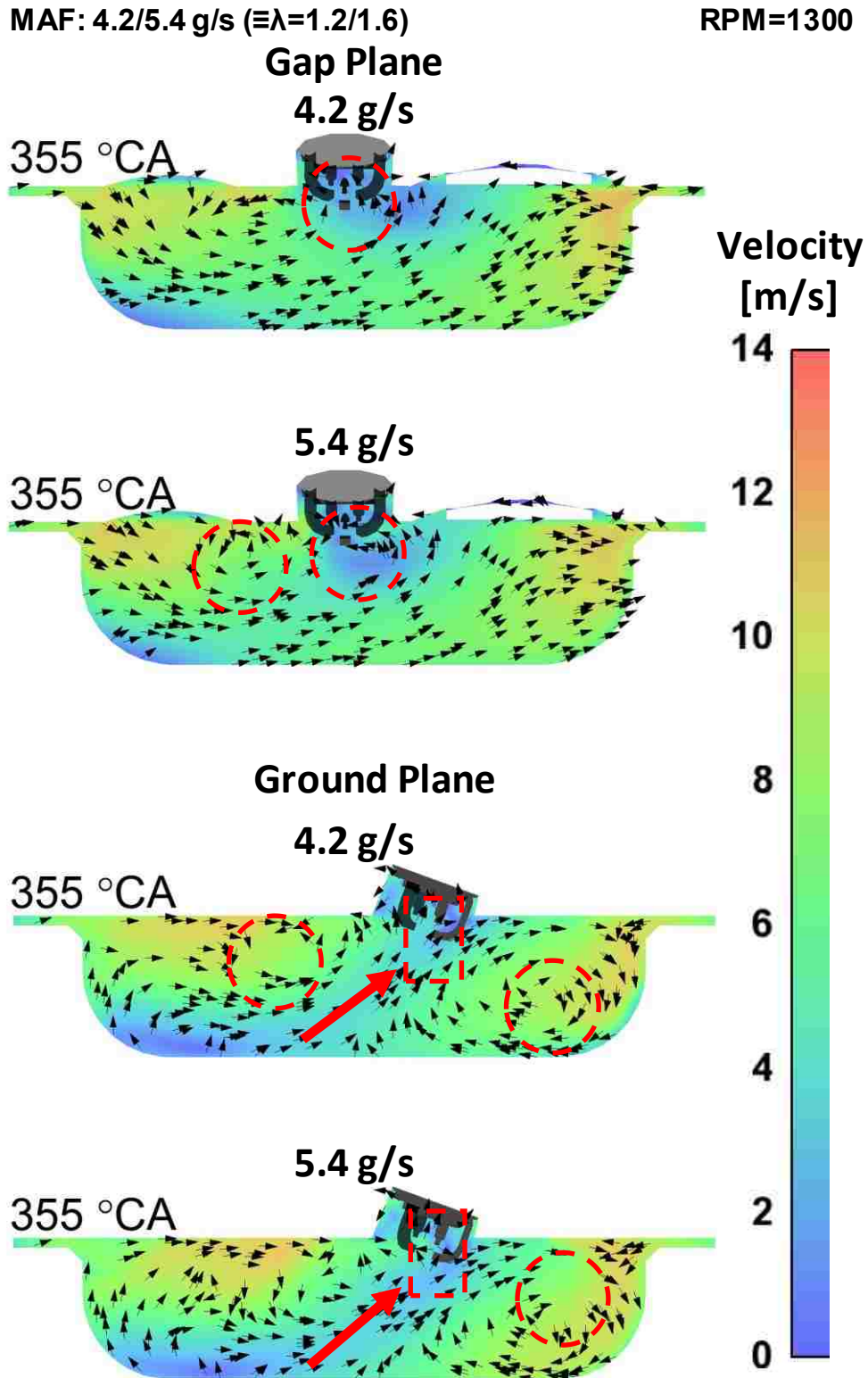


Figure 6-20. Flow field comparison at 355 °CA between MAF of 4.2 and 5.4 g/s

## ■ Flow profile in the spark plug vicinity

From the results presented in section 6.2.2, it can be concluded that the flow field near the spark plug changes significantly over the ignition timing window of this study – 300 to 360 °CA. Hence, a more detailed analysis of the flow profile near the spark plug is undertaken for the MAF of 5.4 g/s corresponding to the leanest test condition ( $\lambda=1.6$ ).

The gap plane and ground plane results are shown in Figure 6-21 and Figure 6-22 from 315 to 365 °CA at 10 °CA intervals. The ignition timing at this  $\lambda$  for the engine test was varied from 305 to 325 °CA. In this timing range, there is no significant difference in the flow field in the spark gap. The average velocity magnitude in the spark gap is ~6-8 m/s. In the ground plane, the flow is directed towards the spark gap. The sparking central electrode acts as a bluff body causing a recirculation zone formation between the central and the ground electrode. Again, by 345 °CA, the velocity magnitude in the gap decreases in both the planes, and the flow direction in the ground plane changes direction.

According to the chamber test, with charge motion, the propane flame is still around the perimeter of the multi-pole spark plug 5 ms after the spark breakdown (Figure 4-14). At an ignition timing of 320 °CA, the in-cylinder pressure of the engine at  $\lambda=1.6$  is ~3.6 bar absolute. This is slightly lower than the CVCC initial pressure of 4 bar absolute. However, a reasonable assumption would be that the flame kernel is still around the spark perimeter 5 ms after the breakdown, which is ~39 °CA. This is supported by the plug probe ion signal data and further by the cylinder pressure signal since the CA5 is later at 363 °CA (Figure 5-8 for gasoline at  $\lambda=1.6$ ). Therefore, the flow field around the spark plug at ~359 °CA (320+39 °CA) should play an important role in increasing the area of the flame as it expands away from the plug.



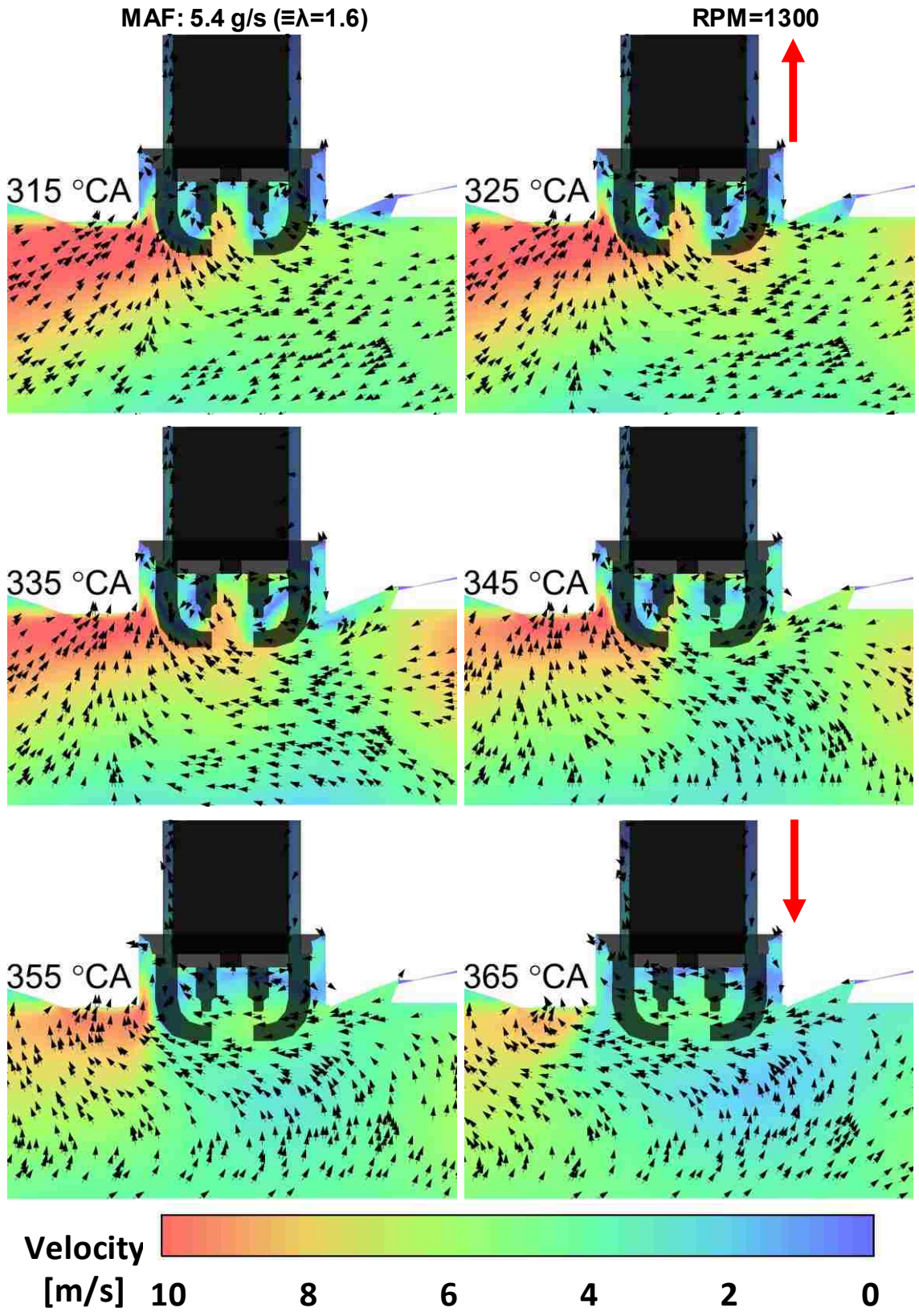


Figure 6-21. Detailed flow field in the spark vicinity at 5.4 g/s for gap plane

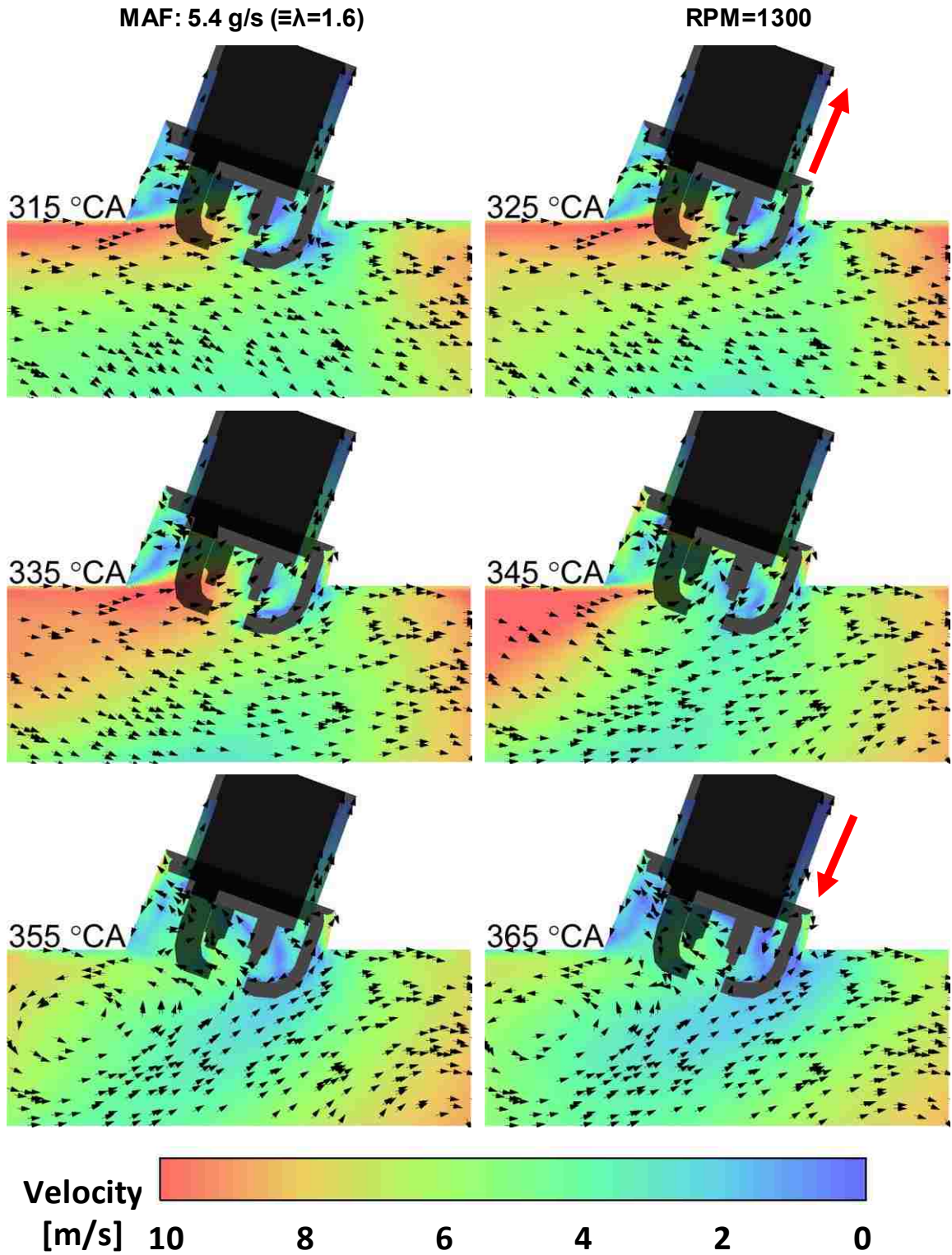


Figure 6-22. Detailed flow field in the spark vicinity at 5.4 g/s for ground plane

The lower flow velocities estimated between 355-365 °CA may not aid in flame expansion. Incidentally, advancing the ignition timing to 310 °CA decreases the combustion duration in comparison to ignition timing of 320 °CA. The flame could then be outside the perimeter of the spark plug by ~349 °CA.

In addition to the flow field in the spark gap region, for the given conditions, there is no major flow in the gap between the ground metal shell and the ceramic insulator. The flow velocity is of the order of less than 1 m/s. However, as the piston approaches TDC, the direction of the velocity starts to shift from upward into the gap to downward away from the gap. This is probably due to the downward motion of the piston causing the in-cylinder gas to expand outward with respect to the axis of the cylinder.

## CONCLUSIONS AND FUTURE WORK

A study of premixed and lean combustion relevant to spark ignition engines operating under low load and low speed was conducted. The effects of charge motion and charge reactivity were investigated through empirical and numerical methods on a variety of research platforms. Certain trends were identified and compared with published research. The significance of a comprehensive approach to analysis of lean combustion was highlighted. In this chapter, the author provides a summary of the research undertaken and the main conclusions. Recommendations are also made for future research.

### Combustion Chamber Flame Propagation Studies

Tests are conducted in a CVCC and shock tube to study some of the fundamental parameters governing premixed flame propagation including fuel property, excess air ratio, charge motion, and discharge current profile. Three different gaseous fuels are tested – methane, propane and DME. Concurrent high-speed shadowgraph imaging, pressure, and ion current measurements are made. The main conclusions of this research are –

- The ion current measurement system developed during this research can detect the propagating flame front under various operating conditions. The system is validated using simultaneous optical measurements. Flame front detection during the glow phase is also possible with the ion current system using the multi-pole spark plug. A conventional spark plug typically cannot measure ion current during the glow phase.
- Shadowgraph images are processed to differentiate between flame propagation at various excess air ratios and fuels with and without charge motion. Flame areas

decrease with increasing  $\lambda$ , but with charge motion, the flame area at the leanest conditions can match that of laminar flames at stoichiometric conditions.

- With decreasing  $\lambda$ , the peak pressure increases and the timing for this pressure advances. The ion current signal shows a similar trend. The effect of charge motion in increasing the flame speed is also evident from the pressure and ion signals. However, at the highest tested  $\lambda$  of 1.6, the magnitude of the ion current is much lower than that at  $\lambda=1.0$ , which is probably caused by the decrease in the ion concentration.
- The flame areas for each fuel can be correlated to the differences in the Markstein lengths. At  $\lambda=1.6$  and with charge motion, for the given test setup, spark ignited DME flame propagation is the slowest of the three test fuels.
- Directed flow on the spark gap demonstrated the increasing stretch of the discharge channel with increasing flow velocity. The effective discharge duration decreases as well. Increasing the average discharge current can prevent blow-out of the flame kernel (and consequent misfire) under flow conditions with a lean background mixture ( $\lambda=1.6$ ).
- Shock accelerated high speed flames of methane were generated in a shock tube with an open ended driven section. This allowed sudden free propagation of the flame. Flame speeds of up to  $\sim 39$  m/s were estimated using the ion current probes. The flame propagation in the driver section, which is akin to a chamber, was not affected significantly by the initial unburned gas pressure. However, the freely propagating flame behind the shock tube was strongly influenced by the initial

unburned gas pressure probably due to increased fuel energy content. Overall, flame speeds typically decreased with increasing  $\lambda$  for all cases.

### ■ Charge Reactivity Impact on Engine Combustion

Charge reactivity impact tests are conducted on a single cylinder SI research engine under low load and low speed. First, the effect of an insert in the intake manifold is evaluated. Second, gasoline and ethanol fuels are tested under different excess air ratios and intake temperatures. DME HCCI tests are also conducted under similar operating conditions to contrast low fuel reactivity (gasoline and ethanol) with high fuel reactivity (DME). The main conclusions of this research are –

- A helical insert placed in the intake manifold can lower the combustion variability especially under lean conditions. It may also advance the start of combustion (CA5) and combustion phasing (CA50).
- The peak pressure and peak heat release rate for ethanol combustion are greater than those for gasoline. DME HCCI has a double hump heat release corresponding to low temperature reactions and high temperature reactions respectively. Owing to probably multiple locations of combustion initiation, the overall combustion duration is significantly shorter than ethanol and gasoline.
- For all SI gasoline and ethanol cases, the CA5 retards monotonically with retardation of the ignition timing. The combustion duration is shortest at  $\lambda=1.2$ . CA5 and CA50 of ethanol at all excess air ratios are earlier than those for gasoline, but the overall combustion duration (CA5-CA95) is lower for gasoline except at  $\lambda=1.6$ . This implies that the second half of combustion of gasoline (developed flame) may be faster than ethanol.

- With increasing  $\lambda$ , NO<sub>x</sub> and CO emissions tend to decrease probably due to reduced flame temperature and additional oxygen supply respectively. Ethanol NO<sub>x</sub> emissions are lower than gasoline probably due to the lowering of the initial charge temperature when liquid ethanol evaporates. Lowering of the in-cylinder temperature with ethanol may also reduce CO oxidation rate. CO emissions were lower for gasoline.
- The plug ion current probe and the auxiliary ion current probe signals show some correlation with the pressure signal based CA5. The plug probe's response is found to be faster than the pressure signal probably due to the detection of the initial flame kernel which may not cause a detectable change in pressure. The period between the peaks of plug probe and the auxiliary probe can be used to make a rough estimate of the flame propagation between these two locations. With increasing  $\lambda$ , the period increases, indicating slower flame propagation.
- Increasing the intake temperature at  $\lambda=1.6$  advances the CA5 and shortens the combustion duration for both gasoline and ethanol fuels. At the highest intake temperature of 393 K, the combustion duration tends to become independent of the ignition timing. The ion signals also indicate faster flame propagation with increasing temperature.
- Though the combustion duration is similar, NO<sub>x</sub> and CO emissions at  $\lambda=1.6$  and  $T_{\text{intake}}=393$  K are lower than those at  $\lambda=1.2$  and  $T_{\text{intake}}=313$  K. The COV of IMEP is also reduced when  $T_{\text{intake}}$  is increased at  $\lambda=1.6$  from 313 to 393 K.
- For DME HCCI, increasing  $\lambda$  from 1.0 to 1.6 causes a decrease in the combustion duration.  $\lambda$  can be extended to 1.83 at which the COV of IMEP starts increasing.

## ■ Simulation Studies for Combustion Chemistry and In-cylinder Flow Field

Numerical analysis of the combustion chemistry and in-cylinder flow field is conducted using CHEMKIN and Converge CFD suite respectively. The main conclusions are –

### ■ Chemical simulations

- Start of reactions is earliest for  $\lambda=1.2$  and latest for  $\lambda=1.6$  for both gasoline and ethanol. Cylinder pressure is also highest at  $\lambda=1.2$  for both fuels though the bulk gas temperature is highest at  $\lambda=1.0$ . At  $\lambda=1.6$ , the peak bulk gas temperature reduces by  $\sim 500$  K which could explain the lower NO<sub>x</sub>.
- Various radicals are identified that are most instrumental in causing the oxidation of the fuel by assisting with chain branching. The  $\dot{O}H$  and  $\dot{H}$  radical concentrations are highest for  $\lambda=1.0$  and decrease with increasing  $\lambda$ . However, the  $\dot{O}H$  radical formation starts earliest for  $\lambda=1.2$ . The  $\dot{H}O_2$  and the  $\dot{C}H_3$  mole fractions are highest at  $\lambda=1.2$  and lowest at  $\lambda=1.6$ . These trends are common for both fuels. These analyses may provide some clues on why combustion duration is shortest at  $\lambda=1.2$ , and longest at  $\lambda=1.6$ .
- For gasoline reactions, the highest concentration of intermediate species such as iso-butene and propene may indicate a greater tendency for unimolecular decomposition at  $\lambda=1.2$  in comparison to  $\lambda=1.0/1.6$ .
- For ethanol reactions, the higher concentrations of ethene and methane intermediates at  $\lambda=1.2$  may indicate a greater tendency for homolytic scission of the carbon-oxygen bond, rather than the carbon-carbon bond at  $\lambda=1.0$ .



- With increased initial temperature at  $\lambda=1.6$ , there is a sharp rise in the  $\dot{\text{C}}\text{H}_3$  radical formation for both ethanol and gasoline, accompanied by an increase in concentration of certain intermediate species by a few orders of magnitude.
- For DME HCCI, the peak cylinder pressure increases with increasing  $\lambda$  since the intake pressure increases. The increasing intake pressure probably advances the start of combustion and shortens the overall combustion duration.
- The low temperature reactions for DME HCCI combustion may be controlled by the formation of the  $\dot{\text{H}}\text{O}_2$  and  $\dot{\text{C}}\text{H}_3$  radicals. During high temperature reactions when the bulk of the charge is combusted, the  $\dot{\text{H}}$  and  $\dot{\text{O}}\text{H}$  concentrations usually reach their peak.
- Increasing  $\lambda$  for DME HCCI combustion also advances the formation of intermediates such as  $\text{CH}_3\dot{\text{O}}$ ,  $\text{CH}_4$ ,  $\text{CH}_2\text{O}$ , and  $\text{CO}$ .

### ■ In-cylinder flow-field simulations

- No major differences in the velocity magnitudes are observed between the two MAF (4.2 and 5.4 g/s) cases at which the experimental combustion durations are shortest and longest respectively. The velocity magnitudes in the cylinder are estimated to be of the order of  $\sim 6\text{-}8$  m/s as the piston approaches TDC.
- Recirculating flow structures resembling compression squish may be identified as the piston moves towards TDC in the ignition timing zone. One of these flow structures in the gap plane approaches the spark gap as the piston reaches TDC. The velocity in this zone is lower, of the order of  $\sim 2\text{-}4$  m/s which may aid in flame kernel formation if the ignition timing is appropriate.

## ■ Recommendations for Future Work

The author attempted to make a comprehensive analysis of premixed and lean combustion from the perspective of charge motion and charge reactivity. However, the present understanding cannot be deemed comprehensive. The following recommendations are made for future work –

- Stronger flows relevant to engine conditions must be generated in the chamber to further the understanding of flow on the flame propagation. CVCC tests at higher pressures and higher temperatures of the unburned gas are required since they will be more relevant to the conditions found in modern gasoline engines. The ignitability challenges should be addressed with further studies on the spark current profile control, and spark discharge energy.
- Use of EGR under lean combustion should be explored in greater detail in terms of balancing emission reduction and improving thermal efficiency.
- The ion current measurement using multi-pole plug shows potential as a future diagnostic for early detection of combustion especially during the glow phase, and efforts must be made to use this measurement for intra-cycle control.
- The numerical analyses related to the chemical reactions and the flow field require further validation. In-cylinder direct gas sampling may be one way to determine the in-cylinder gas composition to determine differences in the underlying chemistry with changes in  $\lambda$ . Though the gas exchange process is validated, the flow-field is not. Optical studies may yield more information.

## REFERENCES

1. Yang, Z., and A. Bandivadekar, "2017 Global Update: Light-Duty Vehicle Greenhouse Gas and Fuel Economy Standards," ICCT, 2017.
2. An, F., R. Earley, and L. Green-Weiskel, "Global Overview on Fuel Efficiency and Motor Vehicle Emission Standards: Policy Options and Perspectives for International Cooperation," The Innovation Center for Energy and Transportation, 2011.
3. "US: Light-Duty: Fuel Economy and GHG," Accessed from <http://www.transportpolicy.net/standard/us-light-duty-fuel-economy-and-ghg/> on June 25, 2018
4. "Canada: Light-Duty: Fuel Economy and GHG," Accessed from <https://www.transportpolicy.net/standard/canada-light-duty-fuel-consumption-and-ghg/> on June 25, 2018.
5. "IA-HEV Outlook," International Energy Agency, 2013.
6. "Global EV Outlook 2017: Two Million and Counting," International Energy Agency, 2017.
7. Schreffler, R., "BEVs, Batteries and The Electrification Future," Wards Auto Special Report, 2017.
8. Seddon, D., "Gas Usage and Values: The Technology and Economics of Natural Gas Use in the Process Industries," PennWell Books, 2006.
9. <https://pubchem.ncbi.nlm.nih.gov/>. Accessed on July 03, 2018.
10. <https://www.atsdr.cdc.gov/>. Accessed on July 03, 2018.
11. [https://www.dieselnet.com/tech/fuel\\_cng.php](https://www.dieselnet.com/tech/fuel_cng.php). Accessed on July 03, 2018.
12. Nitta, N., F. Wu, J. T. Lee, and G. Yushin, "Li-Ion Battery Materials: Present and Future," *Materials Today* 18 (5):252–64, 2015.
13. Budde-Meiwes, H., J. Drillkens, B. Lunz, J. Muennix, S. Rothgang, J. Kowal, and D. U. Sauer, "A Review of Current Automotive Battery Technology and Future Prospects," *Proceedings of the Institution of Mechanical Engineers, Part D: Journal of Automobile Engineering* 227 (5):761–76, 2013.
14. Blomgren, G. E., "The Development and Future of Lithium Ion Batteries," *Journal of The Electrochemical Society* 164 (1):A5019–25, 2017.

15. Thackeray, M. M., C. Wolverton, and E. D. Isaacs, "Electrical Energy Storage for Transportation—Approaching the Limits of, and Going beyond, Lithium-Ion Batteries," *Energy & Environmental Science* 5 (7): 7854-63, 2012.
16. Johnson, T., and A. Joshi, "Review of Vehicle Engine Efficiency and Emissions," SAE Technical Paper 2018-01-0329, 2018.
17. John, J., "Lean Burn Engine Concepts-Emissions and Economy," SAE Technical Paper 750930, 1975.
18. Germane, G. J., C. G. Wood, and C. C. Hess, "Lean Combustion in Spark-Ignited Internal Combustion Engines - A Review," SAE Technical Paper 831694, 1983.
19. Peters, B. D., and A. A. Quader, "'Wetting' the Appetite of Spark Ignition Engines for Lean Combustion," SAE Technical Paper 780234, 1978.
20. Noguchi, M., S. Sanda, and N. Nakamura, "Development of Toyota Lean Burn Engine," SAE Technical Paper 760757, 1976.
21. Manivannan, A, and R. Ramprabhu, "Lean Burn Natural Gas Spark Ignition Engine – An Overview," SAE Technical Paper 2003-01-0638, 2003.
22. Gu, X. J., M. Z. Haq, M. Lawes, and R. Woolley, "Laminar Burning Velocity and Markstein Lengths of Methane–Air Mixtures," *Combustion and Flame* 121 (1-2):41-58, 2000.
23. Stone, R., A. Clarke, and P. Beckwith, "Correlations for the Laminar-Burning Velocity of Methane/Diluent/Air Mixtures Obtained in Free-Fall Experiments," *Combustion and Flame* 114 (3-4):546-555, 1998.
24. Elia, M., M. Ulinski, and M. Metghalchi, "Laminar Burning Velocity of Methane–Air–Diluent Mixtures," *Journal of Engineering for Gas Turbines and Power* 123 (1):190-196, 2001.
25. Bradley, D., M. Lawes, and M. S. Mansour, "Explosion Bomb Measurements of Ethanol–air Laminar Gaseous Flame Characteristics at Pressures up to 1.4MPa." *Combustion and Flame* 156 (7):1462–1470, 2009.
26. Taylor, S. C., "Burning Velocity and the Influence of Flame Stretch," PhD Dissertation, University of Leeds, 1991.

27. Aleiferis, P. G., A. M. K. P. Taylor, J. H. Whitelaw, K. Ishii, and Y. Urata, "Cyclic Variations of Initial Flame Kernel Growth in a Honda VTEC-E Lean-Burn Spark-Ignition Engine," SAE Technical Paper 2000-01-1207, 2000.
28. Lee, K., C. Bae, and K. Kang, "The Effects of Tumble and Swirl Flows on Flame Propagation in a Four-Valve S.I. Engine," *Applied Thermal Engineering* 27 (11–12): 2122–30, 2007.
29. Ives, M. E., "Enhancement of Intake Generated Swirl to Improve Lean Combustion," MSc Thesis, University of Windsor, 2017.
30. Hopkinson, B., "The Effect of Mixture Strength and Scavenging upon Thermal Efficiency," *Proceedings of the Institution of Mechanical Engineers* 74 (1):417-89, 1908.
31. Quader, A. A., "What Limits Lean Operation in Spark Ignition Engines-Flame Initiation or Propagation?" SAE Technical Paper 760760, 1976.
32. Wray, H. A., "Manual on Flash Point Standards and their Use: Methods and Regulations," No. 9, ASTM International, 1992.
33. Ting, D., "Some Basics of Engineering Flow Turbulence," Naomi Ting's Books, 2011.
34. Gulder, O., "Turbulent Premixed Flames," Lecture notes, University of Toronto, Accessed from [https://experimentsitestoil.weebly.com/uploads/1/0/1/9/10190142/combustion\\_of\\_aer.pdf](https://experimentsitestoil.weebly.com/uploads/1/0/1/9/10190142/combustion_of_aer.pdf) on July 25, 2018.
35. Strehlow, R. A., and L. D. Savage, "The Concept of Flame Stretch," *Combustion and Flame* 31: 209–11, 1978.
36. Karpov, V. P., A. N. Lipatnikov, and P. Wolanski, "Finding the Markstein Number Using the Measurements of Expanding Spherical Laminar Flames," *Combustion and Flame* 109 (3): 436–48, 1997.
37. Bradley, D., M. Lawes, and M. S. Mansour, "Correlation of Turbulent Burning Velocities of Ethanol–air, Measured in a Fan-stirred Bomb up to 1.2MPa." *Combustion and Flame* 158 (1):123–138, 2011.
38. "Engine Turbulence," Indian Institute of Technology, accessed from [web.iitd.ac.in/~pmvs/courses/mel345/engine-turbulence.pdf](http://web.iitd.ac.in/~pmvs/courses/mel345/engine-turbulence.pdf) on December 05, 2014.

39. Herweg, R., P. Begleris, A. Zettlitz, and G. F. W. Ziegler, "Flow Field Effects on Flame Kernel Formation in a Spark-Ignition Engine," *Journal of Fuels and Lubricants* 97 (3): 826-46, 1988.
40. Ohigashi, S., Y. Hamamoto, and A. Kizima, "Effects of Turbulence on Flame Propagation in Closed Vessel," *Bulletin of JSME* 14 (74): 849-58, 1971.
41. Moriyoshi, Y., H. Morikawa, and E. Komatsu, "Analysis of Turbulent Combustion in Simplified Stratified Charge Conditions," *JSME International Journal Series B Fluids and Thermal Engineering* 46 (1):86-91, 2003.
42. Lee, K., and J. Ryu, "An Experimental Study of the Flame Propagation and Combustion Characteristics of LPG Fuel," *Fuel* 84 (9):1116–27, 2005.
43. Bradley, D., M. Z. Haq, R. A. Hicks, T. Kitagawa, M. Lawes, C.G.W. Sheppard, and R. Woolley, "Turbulent Burning Velocity, Burned Gas Distribution, and Associated Flame Surface Definition," *Combustion and Flame* 133 (4):415–30, 2003.
44. Bradley, D., M. Lawes, K. Liu, and R. Woolley, "The Quenching of Premixed Turbulent Flames of Iso-octane, Methane and Hydrogen at High Pressures," *Proceedings of the Combustion Institute* 31 (1):1393–1400, 2007.
45. Bradley, D., M. Lawes, and M. S. Mansour, "Flame Surface Densities During Spherical Turbulent Flame Explosions," *Proceedings of the Combustion Institute* 32 (1):1587–93, 2009.
46. Bradley, D., M. Lawes, and M. S. Mansour, "Measurement of Turbulent Burning Velocities in Implosions at High Pressures," *Proceedings of the Combustion Institute* 33 (1):1269–75, 2011.
47. Haq, M. Z., C. G. W. Sheppard, R. Woolley, D. A. Greenhalgh, and R. D. Lockett, "Wrinkling and Curvature of Laminar and Turbulent Premixed Flames," *Combustion and Flame* 131 (1–2):1–15, 2002.
48. Jiang, L. J., S. Shy, M. T. Nguyen, S. Y. Huang, and D. W. Yu, "Spark Ignition Probability and Minimum Ignition Energy Transition of the Lean Iso-Octane/Air Mixture in Premixed Turbulent Combustion," *Combustion and Flame* 187:87–95, 2018.

49. Sayama, S., M. Kinoshita, Y. Mandokoro, and T. Fuyuto, "Spark Ignition and Early Flame Development of Lean Mixtures under High-Velocity Flow Conditions: An Experimental Study," *International Journal of Engine Research*:1-11, 2017.
50. Lipatnikov, A. N., and J. Chomiak, "Effects of Premixed Flames on Turbulence and Turbulent Scalar Transport," *Progress in Energy and Combustion Science* 36 (1):1–102, 2010.
51. Brequigny, P., Christine M-R., F. Halter, B. Moreau, and T. Dubois. "Impact of Fuel Properties and Flame Stretch on the Turbulent Flame Speed in Spark-Ignition Engines," SAE Technical Paper 2013-24-0054, 2013.
52. Ihracska, B., T. Korakianitis, P. Ruiz, D. R. Emberson, R. J. Crookes, A. Diez, D. Wen, "Assessment of Elliptic Flame Front Propagation Characteristics of Iso-octane, Gasoline, M85 and E85 in an Optical Engine," *Combustion and Flame* 161:696–710, 2014.
53. Ikeda, Y., A. Nishiyama, T. Baritaud, "Flame Speed Measurement of a Racing Engine by IR Method and Chemiluminescence Method," 14th Int. Symposium on Applications of Laser Techniques to Fluid Mechanics, Lisbon, Portugal, 2008.
54. Mounaïm-Rousselle, C., L. Landry, F. Halter, F. Foucher, "Experimental Characteristics of Turbulent Premixed Flame in a Boosted Spark-Ignition Engine," *Proceedings of the Combustion Institute* 34:2941–49, 2013.
55. Le Coz, J. F. "Cycle-to-Cycle Correlations Between Flow Field and Combustion Initiation in an S.I. Engine," *SAE Transactions*:954-66, 1992.
56. Li, Y., S. Liu, S-X. Shi, M. Feng, and X. Sui. "An Investigation of In-Cylinder Tumbling Motion in a Four-Valve Spark Ignition Engine," *Proceedings of the Institution of Mechanical Engineers, Part D: Journal of Automobile Engineering* 215(2), 273-284, 2001.
57. Morse, A. P., and J. H. Whitelaw, "Measurements of the In-Cylinder Flow of a Motored Four-Stroke Reciprocating Engine," *Proceedings of the Royal Society of London Series A, Mathematical and Physical Sciences* 377(1770):309-29, 1981.
58. Ting, D. S-K., M. D. Checkel, and B. Johansson, "The Importance of High-Frequency, Small-Eddy Turbulence in Spark Ignited, Premixed Engine Combustion," SAE Technical Paper 952409, 1995.

59. Catania, A. E., C. Dongiovanni, and A. Mittica, "Further Investigation into the Statistical Properties of Reciprocating Engine Turbulence," *JSME International Journal. Ser. 2, Fluids Engineering, Heat Transfer, Power, Combustion, Thermophysical Properties* 35(2):255-65, 1992.
60. Jung, D., K. Sasaki, K. Sugata, M. Matsuda, T. Yokomori, and N. Iida, "Combined Effects of Spark Discharge Pattern and Tumble Level on Cycle-to-Cycle Variations of Combustion at Lean Limits of SI Engine Operation," *SAE Technical Paper 2017-01-0677*, 2017.
61. Settles, G. S., and M. J. Hargather, "A Review of Recent Developments in Schlieren and Shadowgraph Techniques," *Measurement Science and Technology* 28 (4), 2017.
62. Parsinejad, F., J. C. Keck, and H. Metghalchi, "On the Location of Flame Edge in Shadowgraph Pictures of Spherical Flames: A Theoretical and Experimental Study," *Experiments in Fluids* 43 (6):887-94, 2007.
63. "Introduction to Schlieren and Shadowgraph," Module 5, Lecture 26, 2012. Accessed from [https://nptel.ac.in/courses/112104039/pdf\\_version/lecture26.pdf](https://nptel.ac.in/courses/112104039/pdf_version/lecture26.pdf) on July 10, 2018.
64. Mehresh, P., J. Souder, D. Flowers, U. Riedel, and R. W. Dibble, "Combustion Timing in HCCI Engines Determined by Ion-Sensor: Experimental and Kinetic Modeling," *Proceedings of the Combustion Institute* 30 (2): 2701-09, 2005.
65. Stenl   s, O., P. Einewall, R. Egnell, and B. Johansson, "Measurement of Knock and Ion Current in a Spark Ignition Engine with and without NO Addition to the Intake Air," *SAE Technical Paper 2003-01-0639*, 2003,
66. Andersson, I., and L. Eriksson, "Ion Sensing for Combustion Stability Control of a Spark Ignited Direct Injected Engine," *SAE Technical Paper 2000-01-0552*, 2000.
67. Zhu, G. G., D. D. Hung, and J. Winkelman, "Combustion Characteristics Detection for Low Pressure Direct Injection Engines Using Ionization Signal," *SAE Technical Paper 2006-01-3317*, 2006.
68. Ohashi, Y., M. Koiwa, K. Okamura, and A. Ueda, "The Application of Ionic Current Detection System for the Combustion Condition Control," *SAE Technical Paper 1999-01-0550*, 1999.



69. Suzuki, T., H. Ohara, A. Kakishima, K. Yoshida, and H. Shoji, "A Study of Knocking Using Ion Current and Light Emission," SAE Technical Paper 2003-32-0038, 2003.
70. Daniels, C.F., G.G. Zhu, and J. Winkelman, "Inaudible Knock and Partial-burn Detection Using In-cylinder Ionization Signal," SAE Technical Paper 2003-01-3149, 2003.
71. Merola, S. S., and B. M. Vaglieco, "Knock Investigation by Flame and Radical Species Detection in Spark Ignition Engine for Different Fuels," *Energy Conversion and Management* 48 (11): 2897-910, 2007.
72. Shimasaki, Y., H. Maki, J. Sakaguchi, K. Nishizawa, A. Kato, H. Suzuki, N. Kondo, and T. Yamada, "Study on Combustion Monitoring System for Formula One Engines Using Ionic Current Measurement," SAE Technical Paper 2004-01-1921, 2004.
73. Cavina, N., G. Po, and L. Poggio "Ion Current Based Spark Advance Management for Maximum Torque Production and Knock Control," *Proc. of Eighth Biennial ASME Conference on Engineering Systems Design and Analysis*:537-545, 2006.
74. Clements, R. M., and P. R. Smy, "The Variation of Ionization with Air/Fuel Ratio for a Spark Ignition Engine," *Journal of Applied Physics* 47 (2):505-509, 1976.
75. Dev, S., N. Sandhu, M. Ives, S. Yu, M. Zheng J. Tjong, "Ion Current Measurement of Diluted Combustion Using a Multi-Electrode Spark Plug," SAE Technical Paper 2018-01-1134, 2018.
76. Gürbüz, H., "Parametrical Investigation of Heat Transfer with Fast Response Thermocouple in SI Engine," *Journal of Energy Engineering* 142 (4), 2016.
77. Gao, Z., B. Li, C. Li, B. Liu, S. Liu, X. Wu, and Z. Huang, "Investigation on Characteristics of Ion Current in a Methanol Direct-Injection Spark-Ignition Engine," *Fuel* 141:185-191, 2015.
78. Einewall, P., P. Tunestål, and B. Johansson, "The Potential of Using the Ion-Current Signal for Optimizing Engine Stability-Comparisons of Lean and EGR (Stoichiometric) Operation," SAE Technical Paper 2003-01-0717, 2003.
79. Dong, G., Y. Chen, Z. Wu, L. Li, and R. Dibble, "Study on the Phase Relation between Ion Current Signal and Combustion Phase in an HCCI Combustion Engine," *Proceedings of the Combustion Institute* 35 (3):3097-105, 2015.

80. Farrell, J. T., J. G. Stevens, and W. Weissman, "A Second Law Analysis of High Efficiency Low Emission Gasoline Engine Concepts," SAE Technical Paper 2006-01-0491, 2006.
81. Arcoumanis, C., C. S. Bae, and Z. Hu, "Flow and Combustion in a Four-Valve, Spark-Ignition Optical Engine," SAE Transactions:197-211, 1994.
82. Arcoumanis, C., C. S. Bae, J. H. Whitelaw, and H. M. Xu, "Imaging of Lean Premixed Flames in Spark-Ignition Engines," SAE Transactions:1820-36, 1994.
83. Le, M. K., T. Furui, A. Nishiyama, and Y. Ikeda, "Application of High-Speed PIV Diagnostics for Simultaneous Investigation of Flow Field and Spark Ignited Flame inside an Optical SI Engine," SAE International Journal of Engines 10 (3), 2017.
84. Aleiferis, P. G., A. M. K. P. Taylor, K. Ishii, and Y. Urata, "The Nature of Early Flame Development in a Lean-Burn Stratified-Charge Spark-Ignition Engine," Combustion and Flame 136 (3):283-302, 2004.
85. Lee, D., J. Shakal, S. Goto, H. Ishikawa, H. Ueno, and N. Harayama, "Observation of Flame Propagation in an LPG Lean Burn SI Engine," SAE Technical Paper 1999-01-0570, 1999.
86. Kang, K-Y., S-M. Oh, J-W. Lee, K-H. Lee, and C-S. Bae, "The Effects of Tumble Flow on Lean Burn Characteristics in a Four-Valve SI Engine," SAE Technical Paper 970791, 1997.
87. Einewall, P., P. Tunestål, and B. Johansson, "Lean Burn Natural Gas Operation vs. Stoichiometric Operation with EGR and a Three Way Catalyst," SAE Technical Paper 2005-01-0250, 2005.
88. Lumsden, G., D. Eddleston, and R. Sykes, "Comparing Lean Burn and EGR," SAE Technical Paper 970505, 1997.
89. Saanum, I., M. Bysveen, P. Tunestål, and B. Johansson. "Lean Burn Versus Stoichiometric Operation with EGR and 3-Way Catalyst of an Engine Fueled with Natural Gas and Hydrogen Enriched Natural Gas," SAE Technical Paper 2007-01-0015, 2007.
90. Kharas, K. C. C., R. G. Silver, H. J. Robota, and J. F. Skowron, "The Catalytic Implications of Lean Burn Engines: An Analysis of Factors Required to Meet Overall Emissions Requirements," SAE Technical Paper 932762, 1993.

91. Ratnak, S., J. Kusaka, Y. Daisho, K. Yoshimura, and K. Nakama, "Experiments and Simulations of a Lean-Boost Spark Ignition," *SAE Int. J. Engines* 9 (1):379-96, 2016.
92. Iida, N. "Research and Development of Super-Lean Burn for High Efficiency SI Engine: Challenge for Innovative Combustion Technology to Achieve 50% Thermal Efficiency," *The Proceedings of the International Symposium on Diagnostics and Modeling of Combustion in Internal Combustion Engines* 9, 2017.
93. Ishii, K., T. Sasaki, Y. Urata, K. Yoshida, and T. Ohno, "Investigation of Cyclic Variation of IMEP Under Lean Burn Operation in Spark-Ignition Engine" *SAE Technical Paper* 972830, 1997.
94. Takagi, Y, and S. M. Skippon, "Effects of In-Cylinder Fuel Spray Formation on Emissions and Cyclic Variability in a Lean-Burn Engine. Part 1: Background and Methodology," *SAE Technical Paper* 982618, 1998.
95. Jung, D., and N. Iida, "An Investigation of Multiple Spark Discharge Using Multi-Coil Ignition System for Improving Thermal Efficiency of Lean SI Engine Operation." *Applied Energy* 212:322–32, 2018.
96. Hanabusa, H., T. Kondo, K. Hashimoto, H. Sono, and M. Furutani, "Study on Homogeneous Lean Charge Spark Ignition Combustion," *SAE Technical Paper* 2013-01-2562, 2013.
97. Badr, O., N. Alsayed, and M. Manaf. "A Parametric Study On The Lean Misfiring And Knocking Limits Of Gas-Fueled Spark Ignition Engines," *Applied Thermal Engineering* 18 (7):579-94, 1998.
98. Russ, S., "A Review of the Effect of Engine Operating Conditions on Borderline Knock," *SAE Technical Paper* 960497, 1996.
99. Sjöberg, M., W. Zeng, D. Singleton, J. M. Sanders, and M. A. Gundersen, "Combined Effects of Multi-Pulse Transient Plasma Ignition and Intake Heating on Lean Limits of Well-Mixed E85 DISI Engine Operation," *SAE International Journal of Engines* 7 (4):1781–1801, 2014.
100. Aleiferis, P.G., J. Serras-Pereira, and D. Richardson, "Characterisation of Flame Development with Ethanol, Butanol, Iso-Octane, Gasoline and Methane in a Direct-Injection Spark-Ignition Engine." *Fuel* 109: 256–78, 2013.

101. Moxey, B. G., A. Cairns, and H. Zhao, "A Study of Turbulent Flame Development with Ethanol Fuels in an Optical Spark Ignition Engine," SAE Technical Paper 2014-01-2622, 2014.
102. Aleiferis, P. G., and M. K. Behringer, "Flame Front Analysis of Ethanol, Butanol, Iso-Octane and Gasoline in a Spark-Ignition Engine Using Laser Tomography and Integral Length Scale Measurements," *Combustion and Flame* 162 (12):4533–52, 2015.
103. Aleiferis, P.G., J. Serras-Pereira, Z. van Romunde, J. Caine, and M. Wirth, "Mechanisms of Spray Formation and Combustion from a Multi-Hole Injector with E85 and Gasoline," *Combustion and Flame* 157 (4):735–56, 2010.
104. Zhuang, H., D. Hung, M. Xu, H. Chen, T. Li, Y. Zhang, J. Yang, and Y. Men, "Flame Area Correlations with Heat Release at Early Flame Development of Combustion Process in a Spark-Ignition Direct-Injection Engine Using Gasoline, Ethanol and Butanol," SAE Technical Paper 2013-01-2637, 2013.
105. Costa, R. B. R. da, F. A. R. Filho, C. J. R. Coronado, A. F. Teixeira, and N. A. D. Netto, "Research on Hydrous Ethanol Stratified Lean Burn Combustion in a DI Spark-Ignition Engine," *Applied Thermal Engineering* 139:317–24, 2018.
106. Arcoumanis, C., C. Bae, R. Crookes, and E. Kinoshita, "The Potential of Di-Methyl Ether (DME) as an Alternative Fuel for Compression-Ignition Engines: A Review," *Fuel* 87 (7):1014–30.
107. Park, S. H., and Chang S. L., "Applicability of Dimethyl Ether (DME) in a Compression Ignition Engine as an Alternative Fuel," *Energy Conversion and Management* 86:848–63, 2014.
108. Shi, L., C. Ji, S. Wang, X. Cong, T. Su, and D. Wang. "Combustion and Emissions Characteristics of a S.I. Engine Fueled with Gasoline-DME Blends under Different Spark Timings." *Fuel* 211:11–17, 2018.
109. Ying, W., He L., Zhou J., and Zhou L., "Study of HCCI-DI Combustion and Emissions in a DME Engine." *Fuel* 88 (11):2255–61, 2009.
110. Kong, S-C., "A Study of Natural Gas/DME Combustion in HCCI Engines Using CFD with Detailed Chemical Kinetics," *Fuel* 86 (10–11):1483–89, 2007.

111. Zheng, M., S. Yu., and K. Xie, "Multi-coil Spark Ignition System," U.S. Patent 9,441,604, issued September 13, 2016.
112. Usman, A., "Advanced Diagnostics, Control and Testing of Diesel Low Temperature Combustion," PhD Thesis, University of Windsor, 2009
113. Yu, X., Z. Yang, S. Yu, M. Ives, and M. Zheng, "Discharge Characteristics of Current Boosted Spark Events under Flow Conditions," ASME 2017 Internal Combustion Engine Division Fall Technical Conference, 2017.
114. Ballal, D. R., and A. H. Lefebvre, "The Influence of Spark Discharge Characteristics on Minimum Ignition Energy in Flowing Gases," *Combustion and Flame* 24: 99–108, 1975.
115. Yang, Z., X. Yu, S. Yu, J. Chen, G. Chen, M. Zheng, G. T. Reader, D. S-K. Ting, "Impacts of Spark Discharge Current and Duration on Flame Development of Lean Mixtures under Flow Conditions," ASME 2018 Internal Combustion Engine Division Fall Technical Conference, 2018. (Under publication).
116. Davidson, D. F., and R. K. Hanson, "Interpreting Shock Tube Ignition Data," *International Journal of Chemical Kinetics* 36 (9):510–23, 2004.
117. Qin, X. and Y. Ju, "Measurements of Burning Velocities of Dimethyl Ether and Air Premixed Flames at Elevated Pressures," *Proceedings of the Combustion Institute* 30 (1):233-40, 2005.
118. Zheng, M., X. Han, U. Asad, and J. Wang. "Investigation of Butanol-fuelled HCCI Combustion on a High Efficiency Diesel Engine." *Energy Conversion and Management* 98:215-24, 2015.
119. "CHEMKIN Tutorial Manual", December 2011, Accessed from [https://www.ems.psu.edu/~radovic/ChemKin\\_Tutorial\\_2-3-7.pdf](https://www.ems.psu.edu/~radovic/ChemKin_Tutorial_2-3-7.pdf) on July 30, 2018.
120. Mehl M., W. J. Pitz, C. K. Westbrook, H. J. Curran, "Kinetic Modeling of Gasoline Surrogate Components and Mixtures under Engine Conditions", *Proceedings of the Combustion Institute* 33:193-200, 2011.
121. Curran, H. J., P. Gaffuri, W. J. Pitz, and C. K. Westbrook, "A Comprehensive Modeling Study of Iso-octane Oxidation," *Combustion and Flame* 129 (3): 253-80, 2002.

122. Marinov, N. M., "A Detailed Chemical Kinetic Model for High Temperature Ethanol Oxidation," *Int. Journal of Chemical Kinetics* 31:183-220, 1999.
123. Fischer, S. L., F. L. Dryer, and H. J. Curran, "The Reaction Kinetics of Dimethyl Ether. I: High-Temperature Pyrolysis and Oxidation in Flow Reactors," *Int. Journal of Chemical Kinetics* 32:713–40, 2000.
124. Curran, H. J., S. L. Fischer, and F. L. Dryer, "The Reaction Kinetics of Dimethyl Ether. II: Low-Temperature Pyrolysis and Oxidation in Flow Reactors," *Int. Journal of Chemical Kinetics* 32:741–59, 2000.
125. Kaiser, E. W., T. J. Wallington, M. D. Hurley, J. Platz, H. J. Curran, W. J. Pitz, and C. K. Westbrook, "Experimental and Modeling Study of Premixed Atmospheric-Pressure Dimethyl Ether-Air Flames," *Journal of Physical Chemistry A* 104 (35): 8194-8206, 2000.
126. Yakhot, V., S.A. Orszag, S. Thangam, T.B. Gatski, and C.G. Speziale, "Development of Turbulence Models for Shear Flows by a Double Expansion Technique", *Physics of Fluids* 4 (7):1510-20, 1992.
127. El Tahry, S. H., and D. C. Haworth, "Directions in Turbulence Modeling for In-Cylinder Flows in Reciprocating Engines." *Journal of Propulsion and Power* 8 (5): 1040–48, 1992.
128. Reitz, R. D., F. E. Corcione, and G. Valentino. "Interpretation of K- $\epsilon$  Computed Turbulence Length-Scale Predictions for Engine Flows." *Int. Symposium on Combustion*, 26:2717–23, 1996.
129. "Converge CFD Manual Series – Version 2.3", 2016.
130. Inoue, T., Y. Inoue, and M. Ishikawa, "Abnormal Combustion in a Highly Boosted SI Engine – The Occurrence of Super Knock," *SAE Technical Paper* 2012-01-1141, 2012.
131. Jeftic, M., "Strategies for Enhanced After-Treatment Performance: Post Injection Characterization and Long Breathing with Low NO<sub>x</sub> Combustion," PhD Thesis, University of Windsor, 2016.

APPENDIX A: Specifications of Key Equipment

Table A-1. Yanmar Engine Cylinder Pressure Measurement [112]

Hardware	Piezo electric Cylinder Pressure Transducer	Charge Amplifier
Model	Kistler 6043A60	Kistler 5010B
Measurement Range	0-250 bar	10-999000 pC
Sensitivity	20 pC/bar	0.01-9990 pC/bar
Output	–	±10 V
Accuracy	<±0.5%	<±0.5%

Table A-2. Air Flow and Fuel Flow Measurement [112]

Hardware	Air Flow	Fuel Flow
Model	Dresser Roots Meter 5M175	Ono Sokki FP-213
Measurement Range	2.36 m <sup>3</sup> /min 11.9 bar g maximum	1-1000 ml/min
Resolution	2.622 x 10 <sup>-4</sup> m <sup>3</sup>	0.01 ml
Output	Pulse output	0.01 ml/pulse
Accuracy	<0.3%	<±0.5%

Table A-3. CAI emission analyzer details

Species	Model	Working Principle	Range Used	Resolution	Noise/Zero- Span Drift
CO	600- NDIR/Oxygen	Non-dispersive infrared (NDIR)	0-1%	0.001%	<1%
CO <sub>2</sub>	600- NDIR/Oxygen	Non-dispersive infrared (NDIR)	0-20%	0.02%	<1%
O <sub>2</sub>	600- NDIR/Oxygen	Paramagnetic	0-25%	0.025%	<1%
NO/NO <sub>2</sub> / NO <sub>x</sub>	600-HCLD	Chemiluminescence	0-3000 ppm	0.01 ppm	<1%
HC	300M-HFID	Heated flame ionization detector	0-3000 ppm	0.01 ppm	<1%

Table A-4. PicoScope Oscilloscope Specifications

Model	4425	4824
Channels	4	8
Sampling rate	20 million samples/second (USB 3.0)	10 million samples/second
Input ranges	±50 mV to ±200 V in 12 ranges	±10 mV to ±50 V in 12 ranges
Bandwidth	20 MHz (100 mV to 200 V ranges) 10 MHz (50 mV range)	20 MHz (50 mV to 50 V ranges) 10 MHz (10 and 20 mV ranges)
DC accuracy	±1% of full scale	±1% of full scale
Input characteristics	1 MΩ in parallel with 24 pF	1 MΩ in parallel with 19 pF
Input type	Floating, BNC connector	Floating, BNC connector
Buffer memory	250 million samples shared between active channels	256 million samples shared between active channels
Time base ranges	100 ns/div to 5000 s/div	20 ns/div to 5000 s/div
Noise	220 μV RMS on 50 mV range	45 μV RMS on 10 mV range



## APPENDIX B: Pressure Signal Based Combustion Metrics

### ■ Pressure measurement in chamber

Initial chamber pressure =  $p_{\text{initial}}$

Peak chamber pressure =  $p_{\text{max}}$

$t_{100}$  = Time at which pressure signal is maximum

$t_0$  = Zero of time scale for data acquisition system

$t_5$  = Time at which pressure is  $p_{\text{initial}} + 5\%$  of  $(p_{\text{max}} - p_{\text{initial}})$

$t_{50}$  = Time at which pressure is  $p_{\text{initial}} + 50\%$  of  $(p_{\text{max}} - p_{\text{initial}})$

$t_{90}$  = Time at which pressure is  $p_{\text{initial}} + 90\%$  of  $(p_{\text{max}} - p_{\text{initial}})$

### ■ Pressure measurement in engine

Heat Release Rate (derivation and assumptions in [112, 131])

$$\frac{dQ}{d\theta} = \left[ \frac{1}{\gamma - 1} \right] \left[ V \frac{dp}{d\theta} + p\gamma \frac{dV}{d\theta} \right]$$

Definition for Start of Combustion

CA5 = Crank angle for 5% of mass fraction burned [ $^{\circ}$ CA]

Definition for Combustion Phasing

CA50 = Crank angle for 50% of mass fraction burned [ $^{\circ}$ CA]

Definition for End of Combustion

CA95 = Crank angle for 95% of mass fraction burned [ $^{\circ}$ CA]

Combustion Duration

Combustion Duration (CD) = CA95 - CA5 [ $^{\circ}$ CA]

Fuel: Gasoline  
 $\lambda=1.0/1.2/1.4/1.6$

PFI\_  $p_{inj}$  = 4 bar gauge  
 $T_{intake} = 313$  K

RPM=1300  
IMEP=3 bar

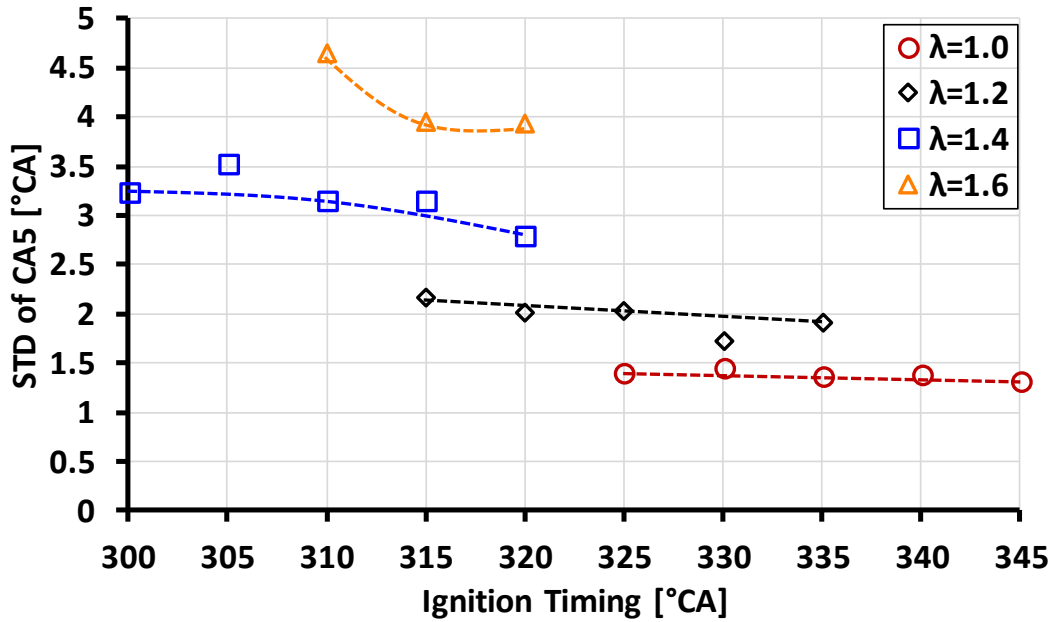


Figure B-1. Standard deviation of CA5

Fuel: Gasoline  
 $\lambda=1.0/1.2/1.4/1.6$

PFI\_  $p_{inj}$  = 4 bar gauge  
 $T_{intake} = 313$  K

RPM=1300  
IMEP=3 bar

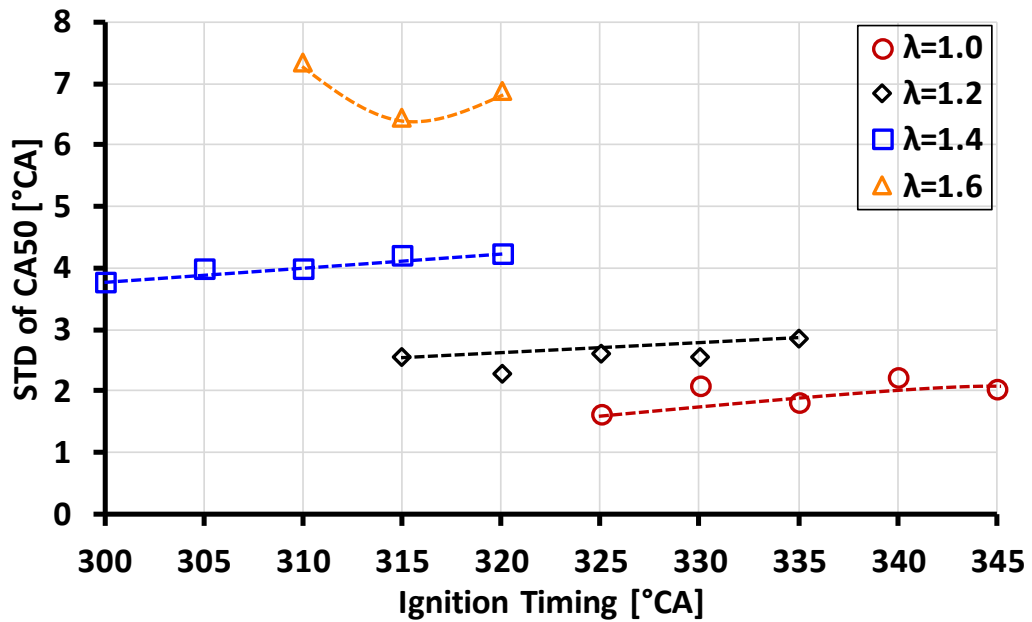


Figure B-2. Standard deviation of CA50

## APPENDIX C: Ion Current Signal Processing Method

■ Ion current profiles for two pole measurement using multi-pole spark plug

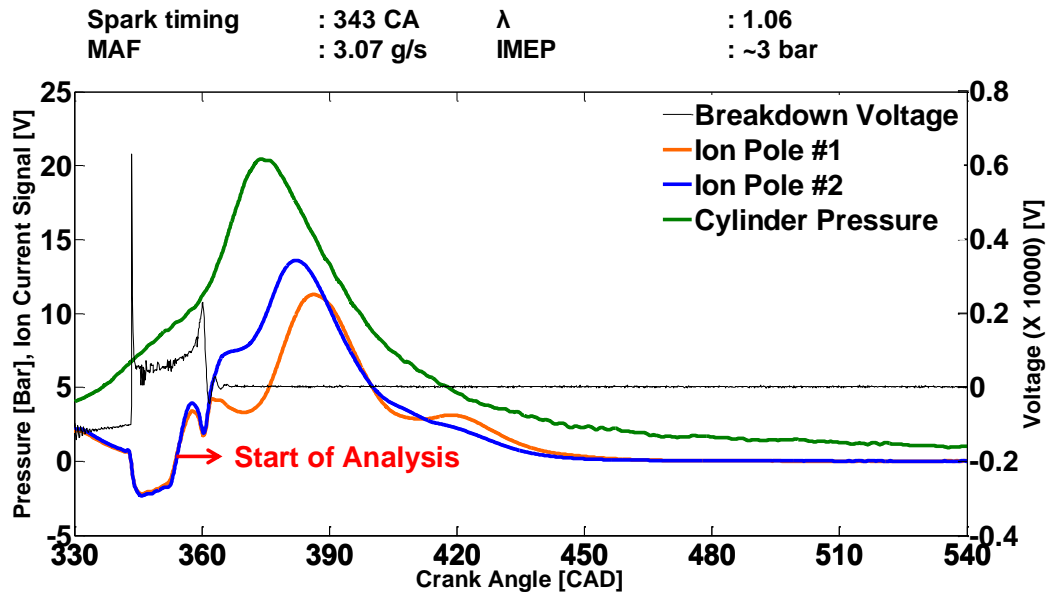


Figure C-1. Typical raw ion current profiles for a firing cycle

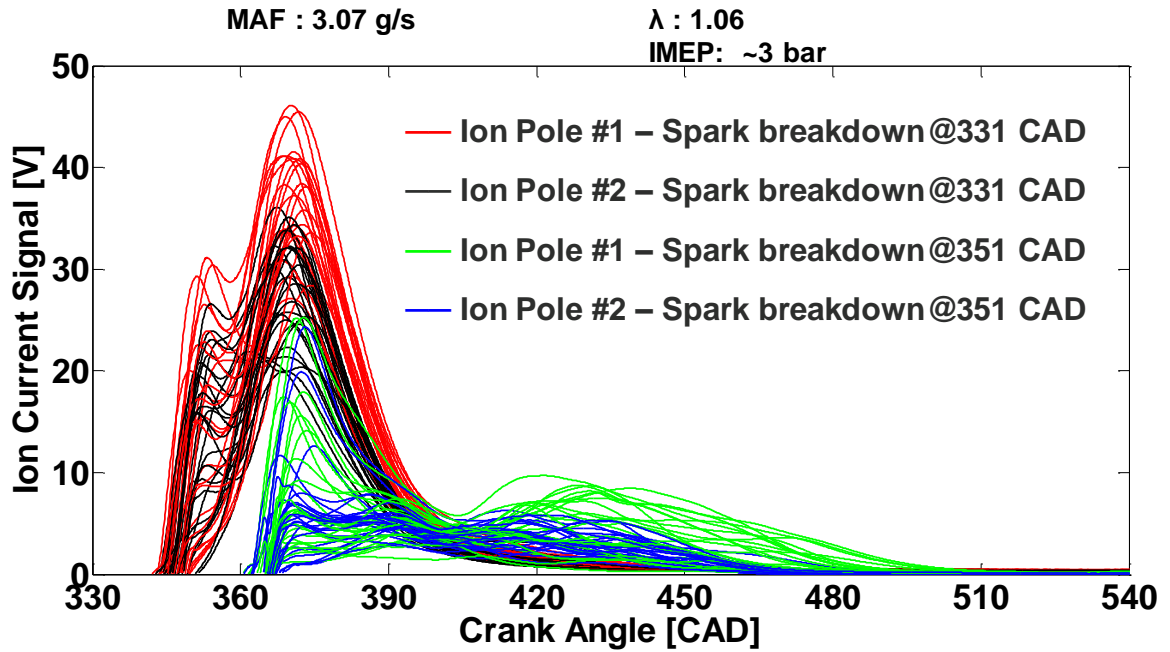


Figure C-2. Processed signal at two breakdown timings

## ■ Matlab processing program for determining signal peaks

```
clear variables
close all
clc

load('comb_cad_sig_ethanol.mat');
datastart=input('Enter start DP ');
dataend=input('Enter end DP ');

for j=datastart:1:dataend
k=comb_sig_cad_data(:,j);
cntr=1;
figure1 = figure('units','inches');
% axes1 = axes('Parent',figure1,'XTick',[300 310 320 330 340 350 360 370 380],...
%   'FontWeight','bold',...
%   'FontName','Times New Roman','FontSize',18);
% % Uncomment the following line to preserve the X-limits of the axes
% xlim(axes1,[300 380]);
% box(axes1,'on');
% hold(axes1,'all');

for i=1:20:141
[hax hl1 hl2]=plotyy(k(1:3600,i),k(1:3600,i+1),k(1:3600,i),k(1:3600,i+2)*(-1));
hold all
xlim(hax(1),[300 380]);
xlim(hax(2),[300 380]);
hax(1).XTick=300:10:380;
hax(2).XTick=300:10:380;
ylim(hax(1),[0 10]);
ylim(hax(2),[0 10]);
hax(1).YTick=0:1:10;
hax(2).YTick=0:1:10;
hl1.Color=[0 0 0];
hl2.Color=[1 0 0];
hold all
% plot(k(1:3600,i),k(1:3600,i+2),'Color',[1 0 0]);
% hold all
% plot(k(1:3600,16),k(1:3600,18));
% hold all
[dypks_s1,ix_s1] = findpeaks(k(1:3600,i+1), 'MinPeakDistance',5, 'MinPeakHeight',0.7);
[dypks_s2,ix_s2] = findpeaks(k(1:3600,i+2)*(-1), 'MinPeakDistance',5,
'MinPeakHeight',2);

% ix=findchangepts(k(1:3600,i+2),'Statistic','linear','MinThreshold',var(s1));
```

```

%
ix_s2=findchangepts(k(1:3600,i+2),'Statistic','linear','MinThreshold',var(k(1:3600,i+2)));

hold(hax(1),'on')
scatter(hax(1),k(ix_s1,i),dypks_s1);
hold(hax(2),'on')
scatter(hax(2),k(ix_s2,i),dypks_s2);
% hold all
% scatter(hax(2),k(ix_s2,i),k(ix_s2,i+2));

% t_s1=find((k(ix_s1,i)>limit), 1, 'first');
% t_s2=find((k(ix_s2,i)>limit), 1, 'first');
% ind_s1(cntr)=k(ix_s1(t_s1),i);
% ind_s2(cntr)=k(ix_s2(t_s2),i);
% cntr=cntr+1;
end

limit=input('Set min CAD limit for peak search ');
close all

for i=1:5:156
plot(k(1:3600,i),k(1:3600,i+1),'Color',[0 0 0]);
hold all
plot(k(1:3600,i),k(1:3600,i+2)*(-1),'Color',[1 0 0]);
hold all
% plot(k(1:3600,16),k(1:3600,18));
% hold all
[dypks_s1,ix_s1] = findpeaks(k(1:3600,i+1), 'MinPeakDistance',5, 'MinPeakHeight',0.7);
[dypks_s2,ix_s2] = findpeaks(k(1:3600,i+2)*(-1), 'MinPeakDistance',5,
'MinPeakHeight',2);
% ix=findchangepts(k(1:3600,i+2),'Statistic','linear','MinThreshold',var(s1));
% ix=findchangepts(k(1:3600,i+1),'Statistic','linear','MinThreshold',var(k(1:3600,i+1)));
%
ix_s2=findchangepts(k(1:3600,i+2),'Statistic','linear','MinThreshold',var(k(ix_s2,i+2)));
% scatter(k(ix_s1,i),dypks_s1);
% hold all
% scatter(k(ix_s2,i),dypks_s2);
% hold all
t_s1=find((k(ix_s1,i)>limit), 1, 'first');
t_s2=find((k(ix_s2,i)>limit)&(k(ix_s2,i+2)*(-1)>0.2), 1, 'first');
if isempty(t_s1)==1
    ind_s1(cntr,j)=0;
else
    ind_s1(cntr,j)=k(ix_s1(t_s1),i);
end
if isempty(t_s2)==1

```

```

    ind_s2(cntr,j)=0;
else
    ind_s2(cntr,j)=k(ix_s2(t_s2),i);
end
cntr=cntr+1;
end

diff_s2_s1(:,j)=ind_s2(:,j)-ind_s1(:,j); % take difference
diffind=find(diff_s2_s1(:,j)<1|ind_s1(:,j)==0|ind_s2(:,j)==0);
ind_s1(diffind,j)=0;
ind_s2(diffind,j)=0;
diff_s2_s1(diffind,j)=0;

mean_ind_s1(j)=sum(ind_s1(:,j))./sum(ind_s1(:,j)~=0);
mean_ind_s2(j)=sum(ind_s2(:,j))./sum(ind_s2(:,j)~=0);
mean_diff(j)=sum(diff_s2_s1(:,j))./sum(diff_s2_s1(:,j)~=0);
% mean_s2(j)=sum(ind_s2(:,j))./sum(ind_s2(:,j)~=0);
end

comb_ion_data_peak=zeros(32,dataend-datastart+1);
cntr2=datastart;
for a=1:3:(((dataend-datastart)+1)*3)-2
    comb_ion_data_peak(:,a)=ind_s1(:,cntr2);
    comb_ion_data_peak(:,a+1)=ind_s2(:,cntr2);
    comb_ion_data_peak(:,a+2)=diff_s2_s1(:,cntr2);
    cntr2=cntr2+1;
end

mean_data=[mean_ind_s1(datastart:dataend)'          mean_ind_s2(datastart:dataend)'
mean_diff(datastart:dataend)'];
% save('comb_ion_pk_21_30.mat','comb_ion_data_peak');

```

APPENDIX D: Validation and Input Parameters – CHEMKIN

■ Motoring cases for validation of heat transfer parameters

Table D-1. Heat transfer parameters for Gasoline and Ethanol

Parameter	Value
Heat Transfer Correlation	
Coefficient a	0.2
Coefficient b	0.8
Coefficient c	0.0
Wall Temperature	400 K
Woschni Correlation of Average Cylinder Gas Velocity	
Coefficient C11	2.28
Coefficient C12	0.318
Coefficient C2	0.324 cm/sec-K
Combustion-Expansion Transition Temperature	650 K

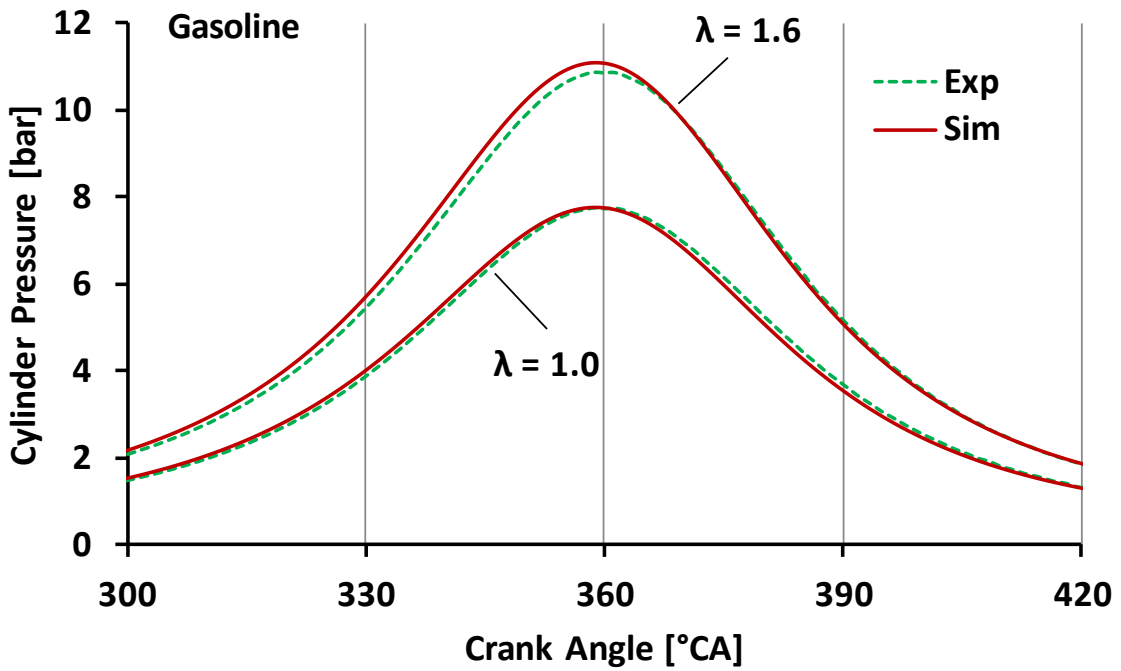


Figure D-1. Gasoline motoring in CHEMKIN – Experiment vs. Simulation

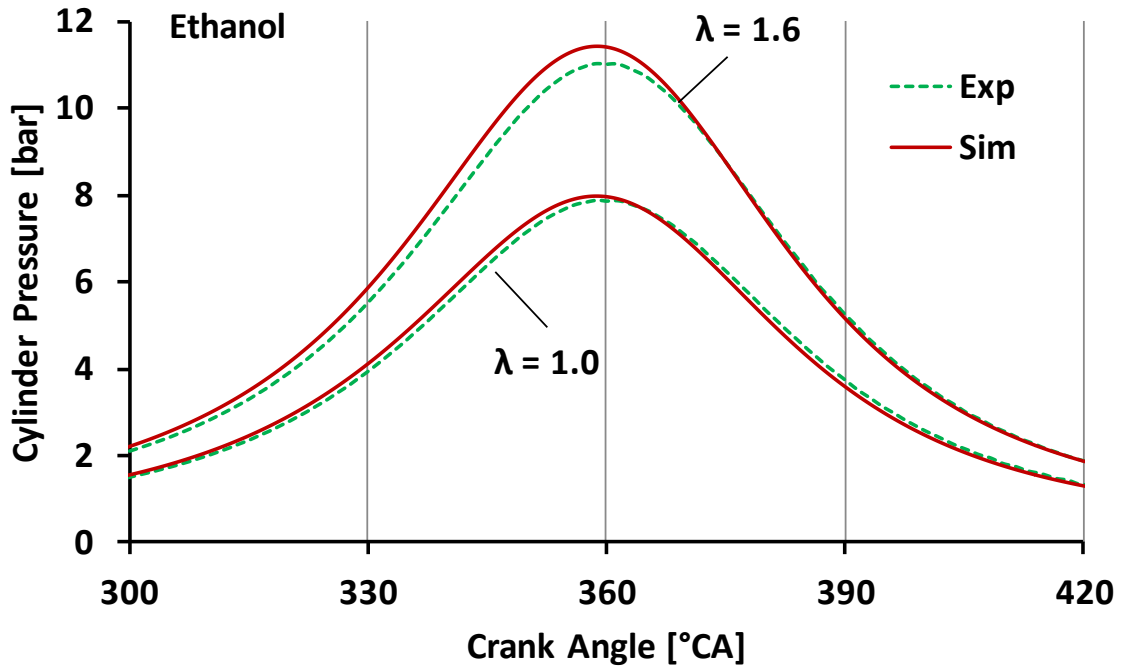


Figure D-2. Ethanol motoring in CHEMKIN – Experiment vs. Simulation

Table D-2. Heat transfer parameters for DME

Parameter	Value
Dimensionless Heat Transfer Correlation	
Coefficient a	0.035
Coefficient b	0.71
Coefficient c	0.0
Wall Temperature	400 K
Chamber Bore Diameter	102 mm
Woschni Correlation of Average Cylinder Gas Velocity	
Coefficient C11	2.28
Coefficient C12	0.308
Coefficient C2	3.24 cm/sec-K
Combustion-Expansion Transition Temperature	650 K



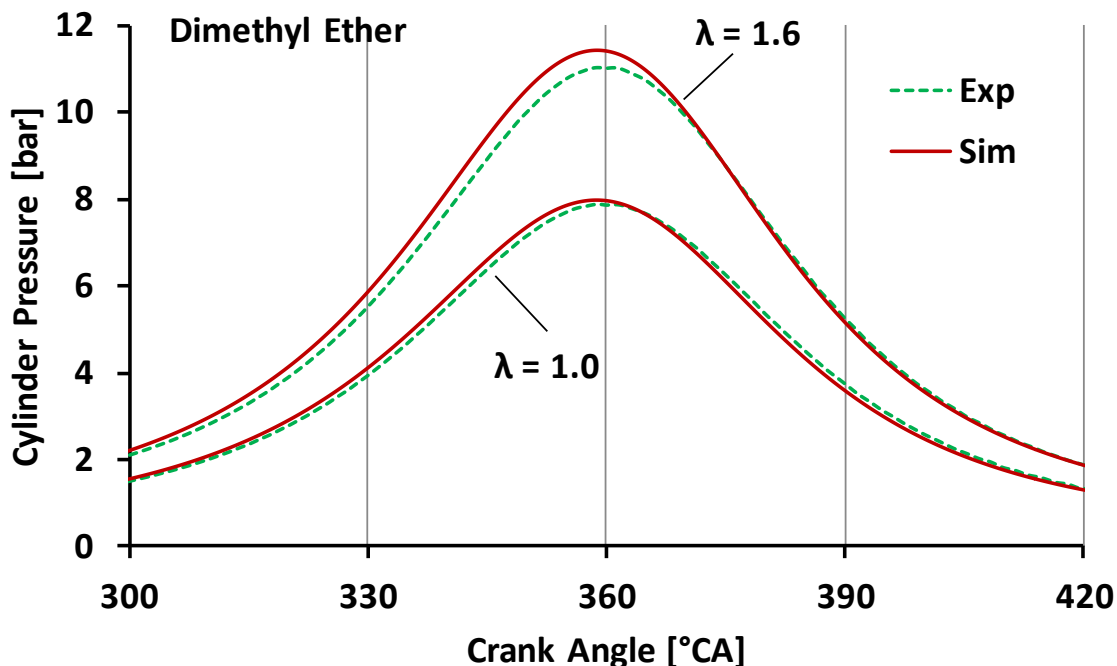


Figure D-3. DME motoring in CHEMKIN – Experiment vs. Simulation

#### Chemical mechanisms – main reactions

The purpose of listing these reactions is to highlight some of the important species involved in the oxidation of iso-octane. This list is not exhaustive.

The most dominant reaction is the unimolecular fuel decomposition (Reaction 1) of iso-octane into tert-butyl radical ( $\text{tC}_4\text{H}_9$ ). The radical further dissociates into iso-butene ( $\text{iC}_4\text{H}_8$ ) and hydrogen radical (Reaction 1a). Another pathway of iso-octane consumption is abstraction of hydrogen atom from the iso-octane molecule to form the  $\text{aC}_8\text{H}_{17}$  radical and hydrogen molecule (Reaction 2).  $\text{aC}_8\text{H}_{17}$  breaks up into iso-butene and iso-butyl radical (Reaction 2a). This iso-butyl radical ( $\text{iC}_4\text{H}_9$ ) further dissociates into propene and methyl radical (Reaction 2b). Reaction 3 is alkyl decomposition which breaks up the iso-octane molecule into the heptyl radical and the methyl radical. In reactions 4 and 5, the iso-octane molecule breaks up into isomers of  $\text{C}_8\text{H}_{17}$  radical which further dissociate into isobutene.

Consequently, iso-butene and propene are the primary intermediates of the reaction. Additionally, in hydrocarbon combustion reactions, the hydroperoxyl radical chemistry plays an important role in controlling the overall reactivity (Reactions 6 to 9). The chain branching reaction to form the hydroxyl ( $\dot{\text{O}}\text{H}$ ) and  $\dot{\text{O}}$  radicals increases the overall reactivity (Reaction 6) since it increases the number of radicals. Hydrogen abstraction from iso-octane is facilitated by the hydroxyl and the hydroperoxyl ( $\text{H}\dot{\text{O}}_2$ ) radicals (Reactions 7-8). Moreover, reaction of the methyl ( $\dot{\text{C}}\text{H}_3$ ) radical with the hydroperoxyl radical to form the methoxy and hydroxyl radicals (Reaction 9) promotes reactivity since it maintains the number of radicals.

Table D-3. Key iso-octane oxidation reactions [121]

Serial No.	Reaction
<b>Oxidation</b>	
1	$\text{iC}_8\text{H}_{18} \rightarrow \text{t}\dot{\text{C}}_4\text{H}_9 + \text{t}\dot{\text{C}}_4\text{H}_9$
1a	$\text{t}\dot{\text{C}}_4\text{H}_9 \rightarrow \text{iC}_4\text{H}_8 + \dot{\text{H}}$
2	$\text{iC}_8\text{H}_{18} + \dot{\text{H}} \rightarrow \text{a}\dot{\text{C}}_8\text{H}_{17} + \text{H}_2$
2a	$\text{a}\dot{\text{C}}_8\text{H}_{17} \rightarrow \text{iC}_4\text{H}_8 + \text{i}\dot{\text{C}}_4\text{H}_9$
2b	$\text{i}\dot{\text{C}}_4\text{H}_9 \rightarrow \text{C}_3\text{H}_6 + \dot{\text{C}}\text{H}_3$
3	$\text{iC}_8\text{H}_{18} \rightarrow \text{y}\dot{\text{C}}_7\text{H}_{15} + \dot{\text{C}}\text{H}_3$
4	$\text{iC}_8\text{H}_{18} + \dot{\text{H}} \rightarrow \text{c}\dot{\text{C}}_8\text{H}_{17} + \text{H}_2$
5	$\text{iC}_8\text{H}_{18} + \dot{\text{H}} \rightarrow \text{b}\dot{\text{C}}_8\text{H}_{17} + \text{H}_2$
<b>Hydroperoxyl radical</b>	
6	$\dot{\text{H}} + \text{O}_2 \rightarrow \dot{\text{O}} + \dot{\text{O}}\text{H}$
7	$\text{iC}_8\text{H}_{18} + \dot{\text{O}}\text{H} \rightarrow \text{x}\dot{\text{C}}_8\text{H}_{17} + \text{H}_2\text{O}$
8	$\text{iC}_8\text{H}_{18} + \text{H}\dot{\text{O}}_2 \rightarrow \text{x}\dot{\text{C}}_8\text{H}_{17} + \text{H}_2\text{O}_2$
9	$\dot{\text{C}}\text{H}_3 + \text{H}\dot{\text{O}}_2 \rightarrow \text{CH}_3\dot{\text{O}} + \dot{\text{O}}\text{H}$

One common aspect between the ethanol and gasoline reaction mechanisms is the hydrogen and oxygen chain branching (Reaction 3) which produces two active radicals to promote subsequent reactions. The main source of radicals which initiate the ignition are

the homolytic scissions of the ethanol molecule (Reactions 1 and 2). Reaction 1 is homolytic scission of the carbon-carbon bond, while reaction 2 is for the homolytic scission of the carbon-oxygen bond. The products of these reactants undergo further reactions. For instance, the methyl ( $\dot{\text{C}}\text{H}_3$ ) radical reacts with the hydroperoxyl ( $\text{H}\dot{\text{O}}_2$ ) radical to form methoxy radical and hydroxyl radical (Reaction 1a). The methoxy radical further dissociates into formaldehyde ( $\text{CH}_2\text{O}$ ) and hydrogen atom (Reaction 1b). The hydroxymethylene ( $\dot{\text{C}}\text{H}_2\text{OH}$ ) radical reacts with oxygen to form formaldehyde and hydroperoxyl (Reaction 1c). Homolytic scission of the carbon-oxygen (Reaction 2) bond leads to formation of ethyl radical ( $\dot{\text{C}}_2\text{H}_5$ ). The ethyl radical finally dissociates into ethene ( $\text{C}_2\text{H}_4$ ) and hydrogen atom (Reaction 2a). The formyl radical ( $\text{H}\dot{\text{C}}\text{O}$ ) reacts to form hydrogen atom and carbon monoxide.

Table D-4. Key ethanol oxidation reactions [122]

Serial No.	Reaction
1	$\text{C}_2\text{H}_5\text{OH} (+\text{M}) \leftrightarrow \dot{\text{C}}\text{H}_3 + \dot{\text{C}}\text{H}_2\text{OH} (+\text{M})$
1a	$\dot{\text{C}}\text{H}_3 + \text{H}\dot{\text{O}}_2 \leftrightarrow \text{CH}_3\dot{\text{O}} + \dot{\text{O}}\text{H}$
1b	$\text{CH}_3\dot{\text{O}} (+\text{M}) \leftrightarrow \text{CH}_2\text{O} + \dot{\text{H}} (+\text{M})$
1c	$\dot{\text{C}}\text{H}_2\text{OH} + \text{O}_2 \leftrightarrow \text{CH}_2\text{O} + \text{H}\dot{\text{O}}_2$
2	$\text{C}_2\text{H}_5\text{OH} (+\text{M}) \leftrightarrow \dot{\text{C}}_2\text{H}_5 + \dot{\text{O}}\text{H} (+\text{M})$
2a	$\dot{\text{C}}_2\text{H}_5 (+\text{M}) \leftrightarrow \text{C}_2\text{H}_4 + \dot{\text{H}} (+\text{M})$
3	$\text{O}_2 + \dot{\text{H}} \leftrightarrow \dot{\text{O}} + \dot{\text{O}}\text{H}$
4	$\text{H}\dot{\text{C}}\text{O} + \text{M} \leftrightarrow \dot{\text{H}} + \text{CO} + \text{M}$

The key DME reactions are summarized in Table D-5. Again, this list is not exhaustive and only presents some of the more important species which affect the fuel reactivity. The reactions can be divided into two processes – DME pyrolysis and DME oxidation. Both processes begin with the unimolecular decomposition of the DME molecule (Reaction 1). In case of an established radical pool, H atom abstraction may occur through the  $\dot{\text{H}}$ ,  $\dot{\text{C}}\text{H}_3$ ,

$\dot{\text{O}}$  or the  $\text{OH}\dot{\text{H}}$  radicals (Reactions 2, 3, 4 and 5 respectively). The  $\text{OH}\dot{\text{H}}$  radical reaction with DME molecule is only under oxidation.

Table D-5. Key DME oxidation reactions [123-124]

Serial No.	Reaction
<b>High temperature pyrolysis</b>	
1	$\text{CH}_3\text{OCH}_3 \rightarrow \text{CH}_3\dot{\text{O}} + \dot{\text{C}}\text{H}_3$
1a	$\text{CH}_3\dot{\text{O}} \rightarrow \text{CH}_2\text{O} + \dot{\text{H}}$
2	$\text{CH}_3\text{OCH}_3 + \dot{\text{H}} \rightarrow \text{CH}_3\text{O}\dot{\text{C}}\text{H}_2 + \text{H}_2$
3	$\text{CH}_3\text{OCH}_3 + \dot{\text{C}}\text{H}_3 \rightarrow \text{CH}_3\text{O}\dot{\text{C}}\text{H}_2 + \text{CH}_4$
2a/3a	$\text{CH}_3\text{O}\dot{\text{C}}\text{H}_2 \rightarrow \text{CH}_2\text{O} + \dot{\text{C}}\text{H}_3$
<b>Oxidation</b>	
4	$\text{CH}_3\text{OCH}_3 + \dot{\text{O}}\text{H} \rightarrow \text{CH}_3\text{O}\dot{\text{C}}\text{H}_2 + \text{H}_2\text{O}$
5	$\text{CH}_3\text{OCH}_3 + \dot{\text{O}} \rightarrow \text{CH}_3\text{O}\dot{\text{C}}\text{H}_2 + \dot{\text{O}}\text{H}$
6	$\dot{\text{C}}\text{H}_3 + \text{O}_2 \rightarrow \text{CH}_2\text{O} + \dot{\text{O}}\text{H}$
7	$\text{CH}_2\text{O} + \dot{\text{C}}\text{H}_3 \rightarrow \text{H}\dot{\text{C}}\text{O} + \text{CH}_4$
7a	$\text{H}\dot{\text{C}}\text{O} + \text{O}_2 \rightarrow \text{CO} + \text{H}\dot{\text{O}}_2$
7b	$\text{H}\dot{\text{C}}\text{O} \rightarrow \dot{\text{H}} + \text{CO}$
8	$\text{O}_2 + \dot{\text{H}} \rightarrow \dot{\text{O}} + \dot{\text{O}}\text{H}$
9	$\dot{\text{H}} + \text{O}_2 (+\text{M}) \rightarrow \text{H}\dot{\text{O}}_2 (+\text{M})$
10	$\dot{\text{C}}\text{H}_3 + \text{H}\dot{\text{O}}_2 \rightarrow \text{CH}_3\dot{\text{O}} + \dot{\text{O}}\text{H}$

The methoxy ( $\text{CH}_3\dot{\text{O}}$ ) radical formed from the pyrolysis converts to formaldehyde ( $\text{CH}_2\text{O}$ ) and hydrogen atom (Reaction 1a). The methoxymethyl ( $\text{CH}_3\text{O}\dot{\text{C}}\text{H}_2$ ) radical may also undergo beta scission to create formaldehyde and methyl radical (Reaction 2a/3a). Formaldehyde is also formed as an intermediate in the reaction of methyl radical with oxygen (Reaction 6). Methyl radical and formaldehyde may react to form the formyl ( $\text{H}\dot{\text{C}}\text{O}$ ) radical and methane (Reaction 7). The formyl radical can react with oxygen to form carbon monoxide and generate the hydroperoxyl radical (Reaction 7a). The formyl radical may also decompose into hydrogen atom and carbon monoxide (Reaction 7b). Higher oxygen

typically increases the  $\text{HO}_2$  formation (Reactions 7a and 9). Consequently, this may increase the formation of the methoxy radical. Hence, the intermediates of interest are identified as follows – methoxy radical, methane, formaldehyde, and carbon monoxide.

#### ■ Firing cases for validation

This section presents a comparison of the pressure profiles for the combustion cases.  $\lambda=1.2/1.6$  experimental pressures are compared with the CHEMKIN results. With increasing  $\lambda$ , the intake pressure increases because the throttle is opened further. Simulation maximum pressures are marginally higher than experimental measurements for all cases. Start of combustion is typically matched for all cases ( $\pm 2$  °CA) as well including start of low temperature reactions of DME. Overall combustion duration is longer for simulation than experiments for DME due to a longer calculated period for high temperature reactions. However, the simulations follow the trends with respect to  $\lambda$ .

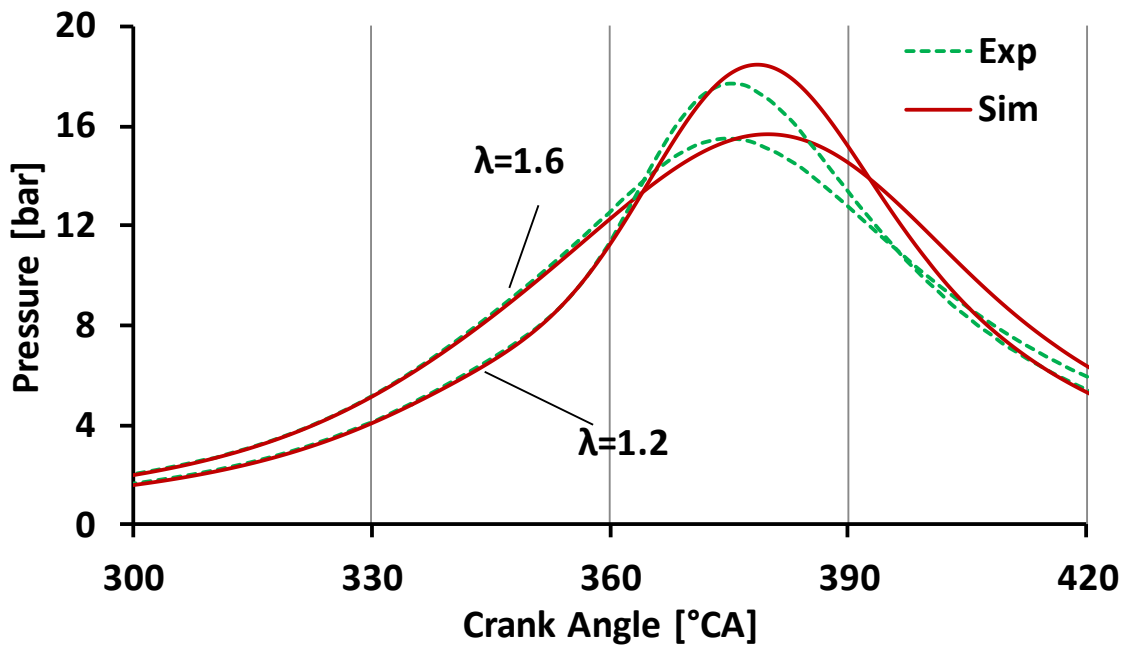


Figure D-4. Gasoline firing in CHEMKIN – Experiment vs. Simulation

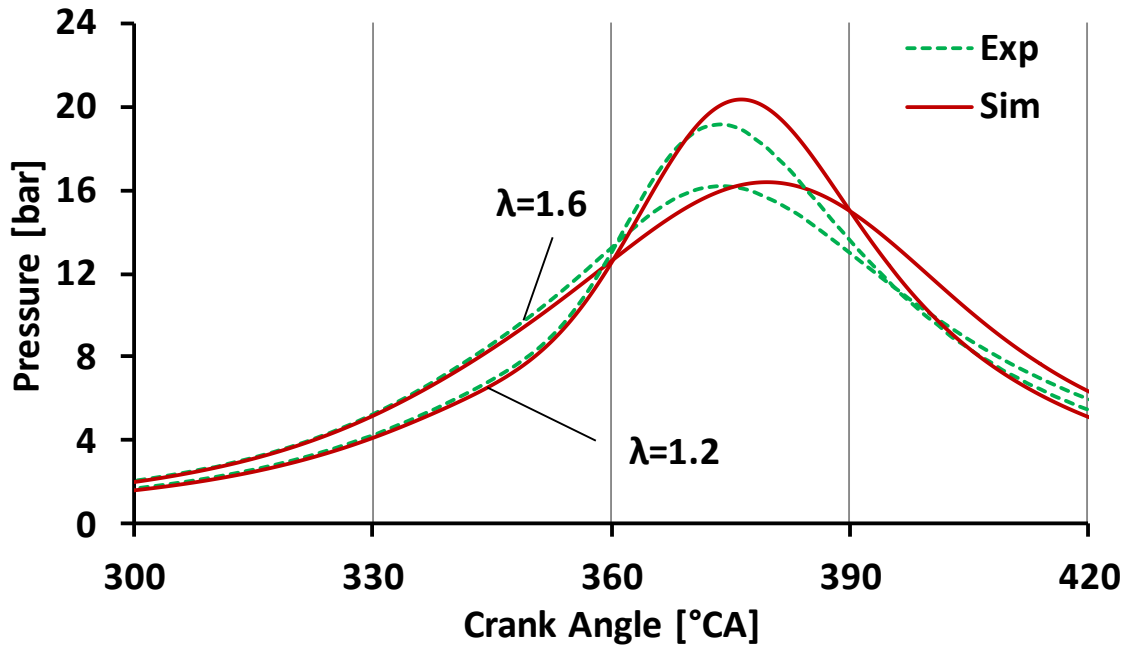


Figure D-5. Ethanol firing in CHEMKIN – Experiment vs. Simulation

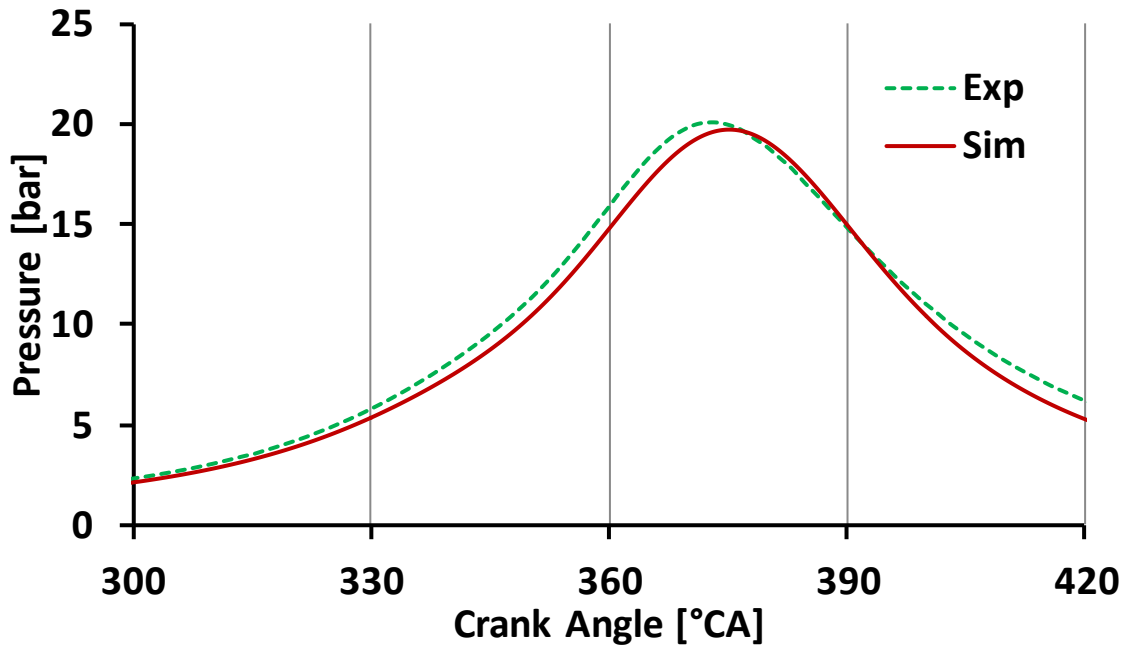


Figure D-6. Gasoline firing in CHEMKIN ( $T_{\text{intake}}=393$  K) – Experiment vs. Simulation

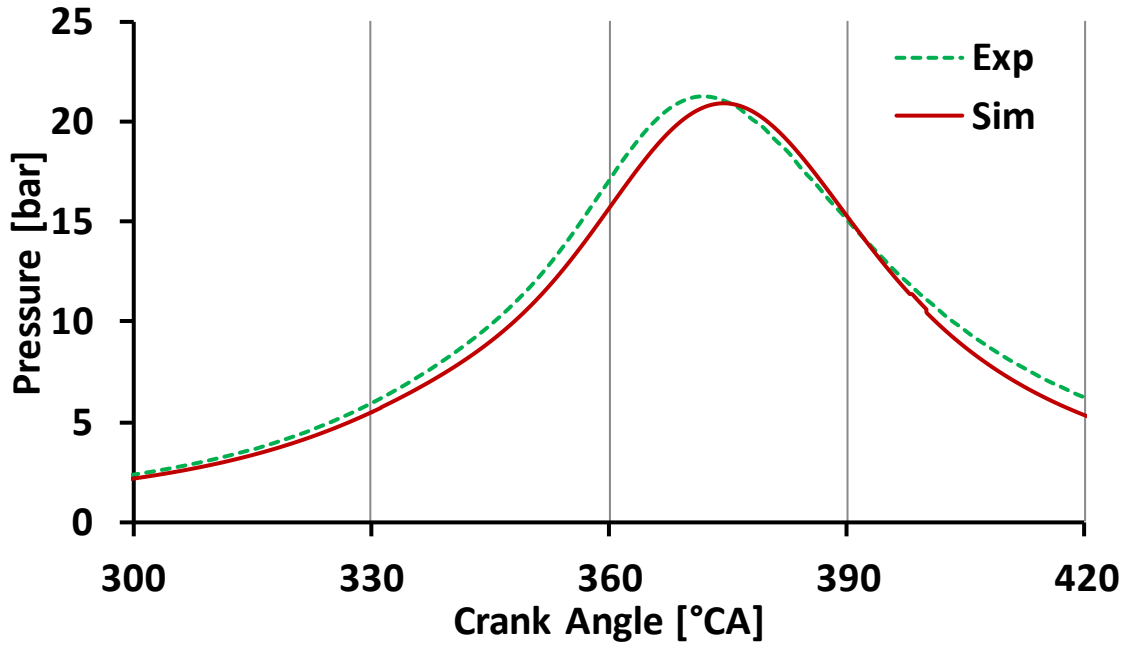


Figure D-7. Ethanol firing in CHEMKIN ( $T_{\text{intake}}=393$  K) – Experiment vs. Simulation

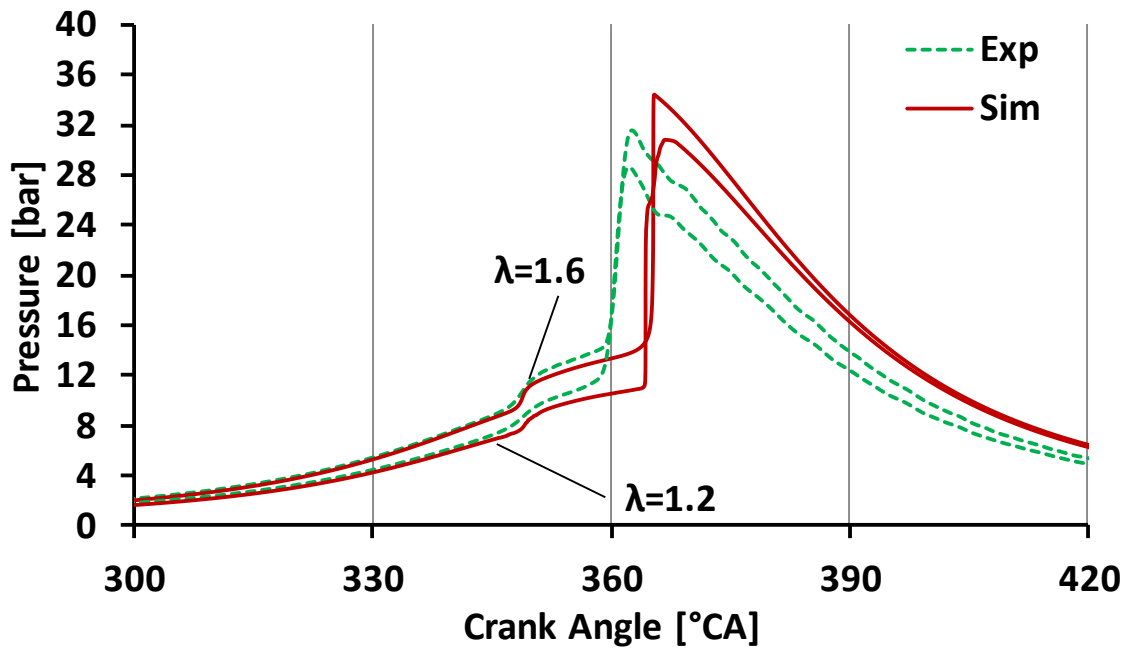


Figure D-8. DME firing in CHEMKIN – Experiment vs. Simulation

APPENDIX E: Validation and Input Parameters – Converge

■ Boundary conditions

Table E-1. Types of boundaries

Boundary	Boundary Condition
Intake/exhaust port	No-slip stationary wall
Cylinder head	No-slip stationary wall
Inflow	Manifold pressure
Outflow	Zero-gradient pressure
Intake/exhaust valves	No-slip moving wall
Spark plug	No-slip stationary wall
Cylinder	No-slip stationary wall
Piston	No-slip moving wall

■ Embedding parameters

```

# Embedding 3
#-----
BOUND          embedded_type
                12 boundary_id
                2  embed_scale
                3  num_embed

SEQUENTIAL
    -364 start_time
    -134 end_time

#-----
# Embedding 4
#-----
REGION          embedded_type
                0  region_id
                2  embed_scale

SEQUENTIAL
    -360 start_time
    -69  end_time

#-----
# Embedding
4@
#-----
REGION          embedded_type
                0  region_id
    
```

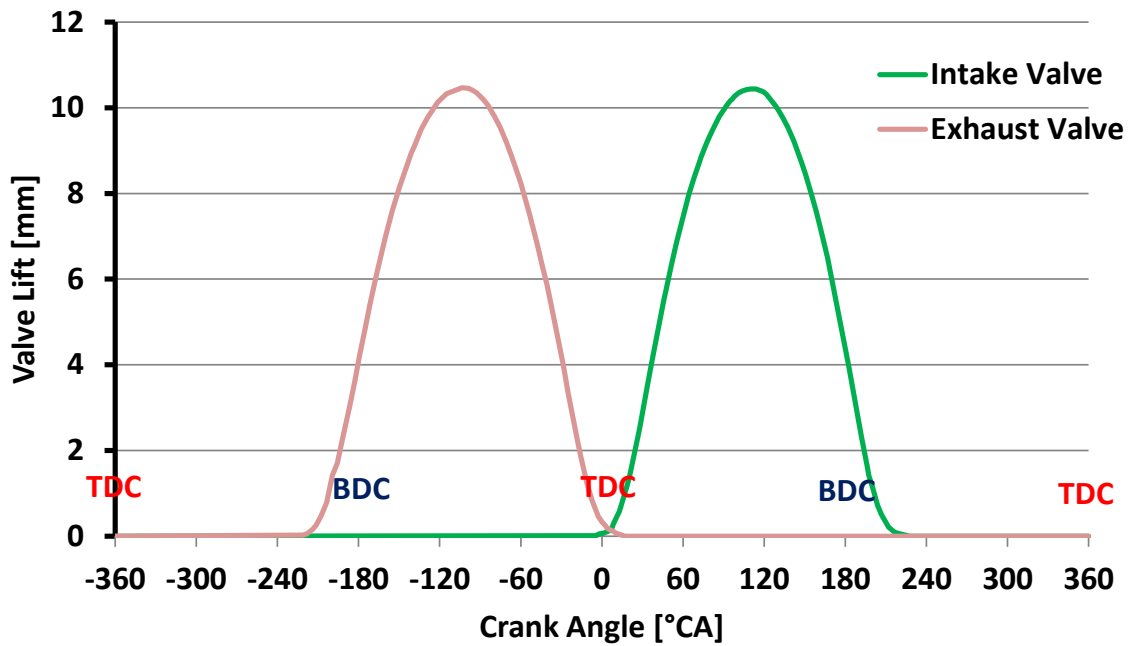


```

3 embed_scale
SEQUENTIAL
-70 start_time
10 end_time
#-----
# Embedding 5
#-----
REGION embedded_type
0 region_id
2 embed_scale
SEQUENTIAL
11 start_time
200 end_time

```

■ Valve lifts (measured)



■ Input parameters

surface.dat	surface_filename
1	crank_flag
-360	start_time
180	end_time
1	rstrflg

2	rstrtnum
0	mapflag
0	nohydro
-1	parallel_scale
100	load_cyc
1	reread_input
0	random_seed
# grid	
0.004	dx_base
0.004	dy_base
0.004	dz_base
0	grid_scale
0	amr_flag
1	embedded_flag
1	events_flag
0.0005	seal_tol
# output control	
2	screen_print_level
twrite.in	twrite_post
5	twrite_transfer
1	twrite_files
60	twrite_restart
3	num_restart_files
0	write_map_flag
0	wall_output_flag
0	transfer_flag
0	mixing_output_flag
0	species_output_flag
1	inter_regions_flow_flag
1	dynamic_flag
0	mpi_write_flag
# timestep control	
1	timeflag
1.00E-07	dtstart
1.00E-08	dt
0.0001	dt_max
1.00E-08	dt_min
1.5	mult_dt_spray
9999	mult_dt_evap
0.5	mult_dt_chem

0.5	mult_dt_coll_mesh
1	max_cfl_u
2	max_cfl_nu
50	max_cfl_mach
# solver flags	
1	momentum_solver
1	energy_solver
1	species_solver
1	turbulence_solver
0	steady_solver
100	min_cycles_steady
0	monitor_steady_state_flag
# properties	
1	gas_compressible_flag
0	liquid_compressible_flag
1	eos_flag
0	real_gas_prop_flag
6	max_reduced_pres
133	crit_temp
3770000	crit_pres
0.035	acentric_factor
0	species_diffusion_model
0.71	prandtl
0.78	schmidt
10	min_temp
60000	max_temp
10	max_visc
0	gravity_x
0	gravity_y
0	gravity_z

#### ■ Solver parameters

20	tol_scale
2	piso_itmin
9	piso_itmax
0.001	piso_tol
0	flux_scheme_mom
0.5	fv_upwind_factor_mom
1	muscl_blend_factor_mom

step	flux_limiter_mom
0	flux_scheme_global
0.5	fv_upwind_factor_global
1	muscl_blend_factor_global
step	flux_limiter_global
0	flux_scheme_turb
1	fv_upwind_factor_turb
1	muscl_blend_factor_turb
step	flux_limiter_turb
1.00E-05	monotone_tolerance
0	upwind_all_dir_flag
1	impl
1	conserve
1	strict_conserve_flag
1	rc_flag
0.7	omega_presrat
0.2	omega_p_steady
0	mom_solver_type
1.00E-05	mom_tol
0	mom_itmin
30	mom_itmax
1	mom_omega
0	mom_preconditioner
0	pres_solver_type
1.00E-08	pres_tol
2	pres_itmin
500	pres_itmax
1.3	pres_omega
0	pres_preconditioner
0	density_solver_type
0.0001	density_tol
0	density_itmin
2	density_itmax
1	density_omega
0	density_preconditioner
0	energy_solver_type
0.0001	energy_tol
0	energy_itmin
2	energy_itmax
1	energy_omega
0	energy_preconditioner
0	species_solver_type
0.0001	species_tol

0	species_itmin
2	species_itmax
1	species_omega
0	species_preconditioner
0	passive_solver_type
1.00E-05	passive_tol
0	passive_itmin
30	passive_itmax
1	passive_omega
0	passive_preconditioner
0	tke_solver_type
0.001	tke_tol
2	tke_itmin
30	tke_itmax
0.7	tke_omega
0	tke_preconditioner
0	eps_solver_type
0.001	eps_tol
2	eps_itmin
30	eps_itmax
0.7	eps_omega
0	eps_preconditioner
0	omega_solver_type
0.001	omega_tol
2	omega_itmin
30	omega_itmax
0.7	omega_omega
0	omega_preconditioner
0	rad_solver_type
1.00E-08	rad_tol
0	rad_itmin
2500	rad_itmax
1	rad_omega
0	rad_preconditioner

■ Turbulence parameters

	2	turbulence_model
# 1 = k-eps,	2	= rng k-eps, 3 = rapid distortion rng
# 6 = standa	rd	k-omega 1998, 7 = standard k-omega 200
# 0 = upwind	LES,	12 = Smagorinsky model, 21 = dynami
# 11 = 1-equ	ation	eddy viscosity LES, 22 = dynamic st

```

# k-eps RANS      model constants
0.0845 keps_cmu
1.39 keps_rpr_tke
1.42 keps_ceps1
1.68 keps_ceps2
-1 keps_ceps3
1.39 keps_rpr_eps
0.012 keps_rng_beta
4.38 keps_rng_eta0
# k-omega RANS model constants
0.09 komega_cmu
0.85 komega_rpr_tke
0.5 komega_rpr_omega
0.556 komega_alpha
0.075 komega_beta
0.875 komega_clim
0.31 komega_sst_a1
1 komega_rpr_tke_outer
0.856 komega_rpr_omega_outer
0.44 komega_alpha_outer
0.0828 komega_beta_outer
0 komega_near_wall_treatment
# Wall modeling
11 heat_model
0.42 law_kappa
5.5 law_b
# Other physics effects
0 discrete_c_s
0.03 discrete_c_ps
0 buoyancy_flag
# Turbulence Statistics
0 turb_stat_flag
-999999 turb_stat_start_time
-999999 turb_stat_end_time
0.0001 turb_stat_tol

```

■ Converge motoring simulation

The gas exchange process is validated by comparison of simulation results with experimental pressure measurements

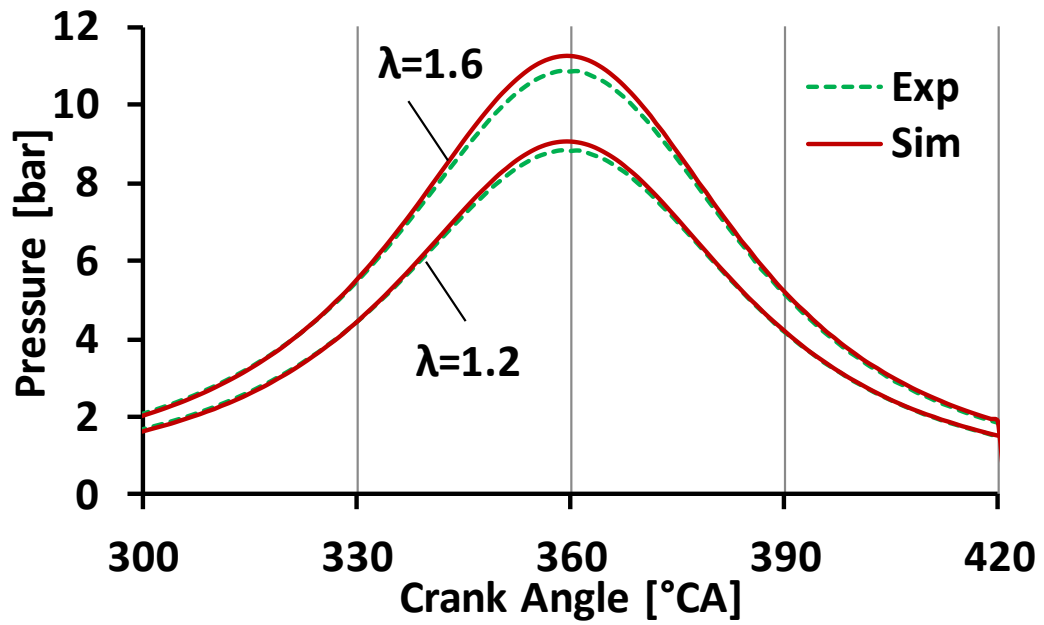


Figure E-1. Converge motoring – Experiment vs. Simulation

## APPENDIX F: Copyright Permissions

### ELSEVIER LICENSE TERMS AND CONDITIONS

Aug 02, 2018

This Agreement between Mr. Shouvik Dev ("You") and Elsevier ("Elsevier") consists of your license details and the terms and conditions provided by Elsevier and Copyright Clearance Center.

License Number	4400840425332
License date	Aug 02, 2018
Licensed Content Publisher	Elsevier
Licensed Content Publication	Applied Thermal Engineering
Licensed Content Title	A parametric study on the lean misfiring and knocking limits of gas-fueled spark ignition engines
Licensed Content Author	O. Badr,N. Alsayed,M. Manaf
Licensed Content Date	Jul 1, 1998
Licensed Content Volume	18
Licensed Content Issue	7
Licensed Content Pages	16
Start Page	579
End Page	594
Type of Use	reuse in a thesis/dissertation
Portion	figures/tables/illustrations
Number of figures/tables/illustrations	1
Format	both print and electronic
Are you the author of this Elsevier article?	No
Will you be translating?	No
Original figure numbers	Figure 11
Title of your thesis/dissertation	An Investigation of Premixed and Lean Combustion in Engines
Expected completion date	Sep 2018
Estimated size (number of pages)	200
Requestor Location	Mr. Shouvik Dev [REDACTED] [REDACTED] Attn: Mr. Shouvik Dev
Publisher Tax ID	GB 494 6272 12
Total	0.00 CAD



## VITA AUCTORIS

NAME: Shouvik Dev

PLACE OF BIRTH: Kolkata, India

YEAR OF BIRTH: 1986

EDUCATION: High School, BGKV, Kolkata, India, 2004  
B. E., Jadavpur University, Kolkata, India, 2008  
M. A. Sc., University of Windsor,  
Windsor, Canada, 2013

## LIST OF PUBLICATIONS

### Patent

1. Zheng, M., Dev, S., Wang, M., “Engine Cylinder Combustion Feedback Control Device,” China Utility Patent Application No. 201621178843.1, Authorized on 2017-05-31.

### Journal Publications

1. Dev, S., Gao, T., Ives, M., Yu, X., Zheng, M., “Fuel Stratification and Partially Premixed Combustion with Neat N-Butanol in a Compression Ignition Engine,” *Journal of Engineering for Gas Turbines and Power*, GTP-18-1069, 2018.
2. Yanai, T., Bryden, G., Dev, S., Reader, G.T. and Zheng, M., “Investigation of Ignition Characteristics and Performance of a Neat n-Butanol Direct Injection Compression Ignition Engine at Low Load,” *Fuel* 208:137-148, 2017.
3. Yang, Z., Dev, S., Jeftic, M., Aversa, C. *et al.*, "Preliminary Investigation of Exhaust Pressure Waves in a Single Cylinder Diesel Engine and the Impacts on Aftertreatment Sprays," *SAE International Journal of Engines* 10(2):2017.
4. Yanai, T., Aversa, C., Dev, S., Reader, G. T., Zheng, M., "Investigation of Fuel Injection Strategies for Direct Injection of Neat n-Butanol in a Compression Ignition Engine," *SAE International Journal of Engines* 9(3), 2016.
5. Dev, S., Divekar, P., Xie, K., Han, X., Chen, X., Zheng, M., “A Study of Combustion Inefficiency in Diesel Low Temperature Combustion and Gasoline-Diesel RCCI Via Detailed Emission Measurement,” *ASME Journal of Engineering for Gas Turbines and Power*, GTP-15-1087, 2015.

6. Yanai, T., Dev, S., Han, X., Zheng, M., Tjong, J., “Impact of Fuelling Techniques on Neat n-Butanol Combustion and Emissions in a Compression Ignition Engine,” SAE International Journal of Engines 8(2):735-746, 2015.
7. Sandhu, N., Dev, S., Purohit, D., Yang, Z., Zheng, M., Ting, D., “Preliminary Simulation Study of Flow Field around a Spark Plug under Ambient and Engine Conditions,” Energy and Sustainability, 2018.
8. Yang, Z., Han, X., Yu, S., Dev, S., Reader, G. T., Ting, D., Zheng, M., “Combustion Characteristics and Emissions of Direct Injection Neat N-Butanol in a Compression Ignition Engine,” Energy and Sustainability, 2018.

#### **Papers in Refereed Conference Proceedings**

1. Dev, S., Sandhu, N. S., Ives, M., Yu, S., Zheng, M., Tjong, J., “Ion Current Measurement of Diluted Combustion Using a Multi-Electrode Spark Plug,” SAE Technical Paper 2018-01-1134, 2018.
2. Yu, S., Dev, S., Yang, Z., Leblanc, S., Yu, X., Han, X., Li, T., Zheng, M., “Fuel Injection Strategies for Reactivity Control in Dual-fuel Low Temperature Combustion Engine,” SAE Technical Paper 2018-01-0265, 2018.
3. Dev, S., Gao, T., Yu, X., Ives, M., Zheng, M., “Fuel Stratification and Partially Premixed Combustion with Neat N-Butanol in a Compression Ignition Engine,” ASME Internal Combustion Engine Division Fall Technical Conference, Volume 1: Large Bore Engines; Fuels; Advanced Combustion, Seattle, Washington, USA, October 15–18, 2017.

4. Dev, S., Divekar, P., Yanai, T., Chen, X., Zheng, M., "Hydrocarbon Speciation of Diesel Ignited Ethanol and Butanol Engines," SAE Technical Paper 2016-01-0773, 2016.
5. Yanai, T., Dev, S., Han, X., Zheng, M., Tjong, J., "Impact of Fuelling Techniques on Neat n-Butanol Combustion and Emissions in a Compression Ignition Engine," SAE paper 2015-01-0808, 2015.
6. Dev, S., Divekar, P., Xie, K., Han, X., Chen, X., Zheng, M., "A Study of Combustion Inefficiency in Diesel-gasoline LTC via Detailed Emission Measurement," Proceedings of the ASME 2014 ICEF Fall Technical Conference, Columbus, IN, USA.
7. Divekar, P., Dev., S., Han, X., Zheng, M., Chen, X., "Study of Exhaust Gas Recirculation – a Low Temperature Combustion Enabler," Proceedings of the Canadian Society for Mechanical Engineering International Congress 2014, Toronto, ON, Canada.

#### **Papers in Non-refereed Conference Proceedings**

1. Ives, M., Dev, S., and Zheng, M., "Preliminary Investigation of Intake Swirl Motion in a Compression Ignition Engine," Proceedings of Combustion Institute – Canadian Section Spring Technical Meeting, 6 Pages, 2016, Waterloo, ON.
2. Dev S., Han Q., Xie K., Zheng M., Henshaw P., "A study of diesel engine intake flow field to improve in-cylinder air motion," Proceedings of Combustion Institute – Canadian Section Spring Technical Meeting, 2013.
3. Yanai, T., Dev, S., Han, X., Zheng, M., "Investigation of the Combustion Characteristics and Performance in a Compression Ignition Engine Fuelled with Neat n-Butanol," Proceedings of the Combustion Institute – Canadian Section, Windsor, ON, Canada, 2014.

4. Yanai, T., Dev, S., Han, X., Tjong, J., Zheng, M., “Investigation of Combustion and Emission Characteristics of Neat n-Butanol in an HCCI Engine,” Proceedings of the Combustion Institute – Canadian Section, Saskatchewan, Canada, 2015.

### **Poster Presentations**

1. Han Q., Divekar P., Dev S., “2<sup>nd</sup> Generation biofuels for sustainable transportation,” AUTO21 HQP Conference, May 29-31 2012 at Montreal, QC.
2. Divekar P., Dev S., Grignon D., “Flexible operation of HCCI combustion using intelligent control,” AUTO21 HQP Conference, May 29-31 2012 at Montreal, QC.
3. Dev S., Han Q., Xie K., “Measurement of engine intake flow field,” Green Auto Power Train –Annual General Meeting, November 16, 2012 at University of Windsor
4. Dev S., “CFD simulation to support diesel engine experimental research,” Green Auto Power Train –Annual General Meeting, November 16, 2012 at University of Windsor
5. Divekar, P., Dev, S., Tan, Q., Yang, Z., “Exhaust Gas Recirculation for Ultra-low NOx Emissions,” CREATE Summer School 2015, Windsor, ON